

https://dspace.org/

Laser engineered net shaping technology to manufacture tungsten carbide in a steel binder

Molobi, Emma

2021
https://hdl.handle.net/10539/32970

Downloaded from a DSpace repository. https://dspace.org/



UNIVERSITY OF THE
WITWATERSRAND,
JOHANNESBURG

LASER ENGINEERED NET SHAPING TECHNOLOGY TO MANUFACTURE TUNGSTEN CARBIDE IN A STEEL BINDER

EMMA MOLOBI

A thesis submitted to the Faculty of Engineering and the Built Environment, University of the Witwatersrand, Johannesburg, in fulfilment of the requirements for the degree of Doctor of Philosophy.

Johannesburg, October 2021

DECLARATION

I declare that this thesis is my own, unaided work. It is being submitted to the Degree of Doctor of Philosophy at the University of the Witwatersrand, Johannesburg. It has not been submitted before for any degree or examination at any other University.



……
Emma Molobi

……14th…… day of ……October……,…… Year……2021……

ABSTRACT

In this research work the feasibility of using direct energy deposition by means of Laser Engineered Net Shaping® technology in the manufacturing of WC-FeCr hardmetals was investigated. A martensitic stainless steel (AISI 420-FeCr) alloy was chosen as the binder material to cement the tungsten carbide (WC) particles. This steel was chosen for its corrosion resistance, high hardness and toughness at elevated temperatures. A comprehensive analysis into the deposition of the WC-10wt%FeCr (AISI 420) alloy was conducted by carrying out a full factorial design of experiments (DOE) to fabricate thin wall samples and optimization models were used in order to establish near optimal parameters. Continuous refinement of the laser power, traverse speed, powder feed rate and the z-increment by the use of ANOVA regression analysis, single objective optimization and multi-objective optimization techniques were used. The required sample height, lowest porosity combination was obtained at a laser power of 200 W, traverse speed of 3.2 mm/s, powder feed rate of 12.2 g/min and a z-increment of 0.2 mm which yielded a porosity of 2.80 %. Samples with a cube geometry were deposited onto a substrate for further refinement of the process parameters and in conjunction to the thin wall samples the lowest porosity of 2.87% was attained at the same process parameters. The porosity was a result of both lack of fusion and gas entrapment during deposition. Inhomogeneous bimodal microstructures composed of spherical WC with a surface reaction zone, herringbone carbides at the bottom of the sample, trapezoidal and stripe shaped carbides in the middle and top of the sample and partially melted columnar grains at the top of the sample were observed. The different reaction phases were inhomogeneous across the sample built and were also dependent on the process parameters. The variations in the microstructure led to the variation in the hardness profile of the samples from the substrate end to the top layers and was dependent on process parameters. Different crack restraining methods were investigated after initial depositions showed a high crack intensity. Preheating the substrate to 250 °C and laser re-melting resulted in the reduction of cracks. The LENS® process was also used to fabricate a prototype cylindrical rotary burr which was tested against a conventionally manufactured component in terms of its ability to remove previously deposited welds. The conventionally manufactured component performed far better than the prototype. Further work is required in order to improve the prototype's material properties and performance.

DEDICATION

I would like to dedicate this work to my beloved parents, Mr Julian Molobi and Mrs Clara Molobi for their continued support, constant motivation and for being my well of wisdom and strength. Thank you for staying up until late to keep me company during the write up of this thesis and constantly believing in me.

ACKNOWLEDGEMENTS

Firstly, I would like to thank God for the gift of life, health and courage to overcome all difficulties experienced and thankful for all the successes encountered.

Professor N. Sacks, for giving me the opportunity to pursue my studies under her supervision. Her continued guidance, support and patience throughout this research work. I truly appreciated your supervision, mentorship and allowing me the opportunity to carry out my research work.

Ms. M. Theron, for her guidance and assistance in using the LENS® machine at the Council for Scientific and Industrial Research (CSIR), National Laser Centre (NLC). I appreciate your advice and support during my experimental trials.

Mr N. Arthur, for his technical support and knowledge on the LENS® machine.

The National Laser Centre (NLC) at the Council for Scientific and Industrial Research (CSIR), for use of the LENS® machine

Professor A. Ziegler, for my training on the microscopy facilities and constant availability when I needed assistance.

Microscopy and Microanalysis Unit (MMU), University of the Witwatersrand, for the use of the microscopy equipment.

School of Chemical and Metallurgical Engineering Staff, University of the Witwatersrand, Mr B. Mothibedi (Lab Manager) for allowing me after hour's usage of the laboratories, Mr S. Moqabolane for assistance in metallographic preparation.

The Department of Science and Innovation (DSI) and the National Research Foundation (NRF), South Africa, for supporting the DSI/NRF Centre of Excellence in Strong Materials, for financial support and granting me the opportunity to pursue my postgraduate studies. I am grateful for the opportunity granted.

Table of Contents

DECLARATION ii

ABSTRACT iii

DEDICATION iv

ACKNOWLEDGEMENTS v

LIST OF FIGURES xi

LIST OF TABLES xix

CHAPTER 1 Introduction 1

1.1 Background and Motivation for the Research 1

1.2 Research Aim and Objectives 3

1.3 Contribution to Knowledge 4

1.4 Structure of the Thesis 4

CHAPTER 2 Literature Review 6

2.1 Tungsten Carbide History 6

2.2 Additive Manufacturing 11

2.2.1 General additive manufacturing 11

2.2.2 Laser Engineered Net Shaping (LENS®) 13

2.2.3 Additive manufacturing of hardmetals 31

2.3 Binder Systems for Hardmetals 42

2.3.1 Cobalt binders 42

2.3.2 Nickel binders 46

2.3.3 Iron binders 48

2.4 Phase Equilibria of the W-Fe-Cr-C Hardmetals 57

2.4.1 W-C system 58

2.4.2 Fe-C system 59

2.4.3 Fe-W system 60

2.4.4 Fe-Cr-C system 61

2.4.5 W-Fe-C system 63

2.4.6 W-Fe-Cr-C system 64

2.5 Summary 65

CHAPTER 3 Experimental Procedures 66

3.1 Introduction 66

3.2 Feedstock Powders 66

3.3 Substrate 67

3.4 LENS® Equipment 67

3.5 LENS® Production of WC-FeCr Hardmetals 70

3.5.1 Design of Experiments Matrix and Optimization 70

3.5.2 Thin wall and cube depositions 74

3.5.3 Crack restraining methods 77

3.5.4 Cylindrical rotary burr prototype 78

3.6 Material Characterization Tests 82

3.6.1 Powder particle size characterization 82

3.6.2 Sample cutting 83

3.6.3 Sample height measurements 83

3.6.4 Surface roughness 83

3.6.5 WC-FeCr hardmetal sample preparation 83

3.6.6 Powder morphology 84

3.6.7 Porosity 84

3.6.8 WC-FeCr hardmetal microstructure 85

3.6.9 Elemental chemical analysis 85

3.6.10 Phase analysis 85

3.6.11 Hardness 86

3.6.12 Fracture toughness 86

3.6.13 Density 87

3.6.14 Thermal profiling 88

3.6.15 Liquid dye penetrant testing 91

CHAPTER 4 Characterization of Feedstock Powders 92

4.1 Introduction 92

4.2 Particle Size Distribution (PSD) 92

4.3 Morphology 94

4.4 Chemical Composition 95

4.5 Phase Analysis 98

4.6 Porosity Analysis 99

CHAPTER 5 Thin wall and Cube Deposition Results and Analyses 101

5.1 Introduction 101

5.2 Optimization of Sample Height 101

5.2.1 Sample profile 101

5.2.2 Effect of process parameters on sample height 102

5.2.3 Regression analysis and parameter optimization 106

5.3 Optimization of Sample Height and Porosity Simultaneously 111

5.3.1 Effect of process parameters on sample porosity 111

5.3.2 Parameter optimization 116

5.4 Optimization of the Z-increment 118

5.4.1 Effect of the z-increment on sample height 118

5.4.2 Effect of the z-increment on porosity 120

5.5 Optimization of Cube Samples 124

CHAPTER 6 Material Characterization Results and Analysis 127

6.1 Introduction 127

6.2 Microstructure 127

6.2.1 Microstructure of the thin wall samples 127

6.2.2 Effects of process parameters on microstructure 132

6.2.3 Microstructure of the FeCr Cube Sample 141

6.2.4 Microstructure of the cube sample 143

6.3 Constituent Phases 153

6.3.1 Phases present in thin wall samples 153

6.3.2 Phases present in the FeCr cube sample 156

6.3.3 Phases present in the optimum cube sample 157

6.4 Hardness Properties 158

6.4.1 Influence of process parameters on the thin wall sample hardness 158

6.4.2 Hardness profile of the thin wall samples 160

6.4.3 Hardness of reaction phases in thin wall samples 161

6.4.4 Hardness of the optimum cube sample 162

6.5 Fracture Toughness of the Cube Sample 162

6.6 Effect of Laser Heat Input on the Surface Roughness of Thin Wall Samples 163

6.7 Analysis of Thin Wall Thermal Profiles 164

CHAPTER 7 Results and Analysis of Crack Restraining Methods 166

7.1 Introduction 166

7.2 Cube Sample without Crack Restraining 166

7.3 Effect of FeCr Buffer Layer on Crack Formation 167

7.4 Effect of Ni-Alloy Buffer Layer on Crack Formation 169

7.5 Effect of Laser Re-Melting On Crack Formation 171

7.6 Effect of Preheat on Crack Formation 172

7.7 Comparison of Crack Restraining Methods 173

7.7.1 Crack analysis 173

7.7.2 Effects of crack restraining methods on hardness 173

7.7.3 Effects of crack restraining methods on phase formation 174

CHAPTER 8 Rotary Burr Prototype Results and Analysis 176

8.1 Introduction 176

8.1 CAD Model of the Rotary Burr 177

8.2 LENS® Deposition of a Cylindrical Rotary Burr 178

8.3 Finite Element Analysis (FEA) 181

8.4 Field Testing of the Prototype Burr 182

CHAPTER 9 Discussion 186

9.1 Introduction 186

9.2 Influence of Feedstock Powders on Deposition Process and Composite Properties 186

9.3 Influence of Deposition Parameters on WC-FeCr Hardmetal Sample Height and Porosity 188

9.4 Microstructure of LENS® Manufactured WC-FeCr Hardmetals 193

9.5 Influence of Crack Restraining Methods on Crack Prevention During Deposition 198

9.6 Assessment of Prototype WC-FeCr Hardmetal Rotary Burr 200

CHAPTER 10 Conclusions and Recommendations 202

10.1 Introduction 202

10.2 Recommendations for future research 203

REFERENCES 204

APPENDIX A Tungsten and Iron-Chromium LENS® Parameters from Literature 222

APPENDIX B Cylindrical Rotary Burr Application and Design 223

APPENDIX C ANOVA Regression Analysis 226

APPENDIX D PUBLICATIONS AND CONFERENCES 228

LIST OF FIGURES

Figure 1-1: Flow diagram overview of various additive manufacturing processes [1]..... 1
Figure 2-1: Historical developments of hardmetals [23]..... 7
Figure 2-2: The foundation of hardmetal companies [24]..... 8
Figure 2-3: Relationship between toughness, hardness and wear resistance of tungsten carbide coatings [27]..... 8
Figure 2-4: Flowchart of hardmetal production [29]..... 9
Figure 2-5: Plot of % densification vs. temperature for the four grades of WC-Co samples, i.e., 50nm, 200nm, 800nm, 1000nm [31]..... 10
Figure 2-6: Roadmap of AM [34]..... 12
Figure 2-7: Additive manufacturing process chain [36]..... 13
Figure 2-8: Schematic representation of the LENS® process [42]..... 15
Figure 2-9: LENS® repair of motor blower fan blade (left) and Ti airfoils [43]..... 18
Figure 2-10: LENS® manufactured Inconel 625 free-forms [38]..... 18
Figure 2-11: Comparison of gas atomized powder size requirements for different AM processes [49]..... 19
Figure 2-12: Powder injection configurations [52]..... 20
Figure 2-13: Powder flow from a coaxial nozzle [60]..... 22
Figure 2-14: Metallurgical zones developed in a weld [61]..... 23
Figure 2-15: Energy intensity of different welding processes [62]..... 23
Figure 2-16: Divergent Marangoni flow [61]..... 25
Figure 2-17: Convergent Marangoni flow [61]..... 25
Figure 2-18: Characteristic pores in laser-based powder bed fusion parts: (A) entrapped gas porosity; (B) incomplete melting-induced porosity, (C) lack of fusion with un-melted particles inside large irregular pores and (D) cracks [64]..... 26
Figure 2-19: Influence of process parameters on lack of fusion and gas porosity [66]..... 28
Figure 2-20: Changes in porosity with: (a) powder feed rate, (b) linear mass density for various velocities in AISI 420 stainless steel [67]..... 29
Figure 2-21: Influence of scan speed and energy density on porosity [69]..... 30
Figure 2-22: Process window for SLM of Ti-6Al-4V [68]..... 30
Figure 2-23: Layer delamination and cracking [48]..... 30

Figure 2-24: SEM images of: (a) sample sintered at 1450 °C for 1 hour with a few pores; (b) Laser deposited sample at 200W showing a dense microstructure [71]. 31
Figure 2-25: Hardness profile of a LENS® deposited hardmetals [8]. 32
Figure 2-26: Influence of powder feed rate on sample height: (a) 11 g/min, (b) 12.4 g/min, (c) 14.9 g/min, (d) 20.4 g/min [70]. 32
Figure 2-27: Influence of traverse speed on sample height: (a) 4.2 mm/s, (b) 6.4 mm/s, (c) 10.6 mm/s [70]. 33
Figure 2-28: Relationship between laser intensity, laser spot size and working distance [58]. 34
Figure 2-29: Experimental setup showing the thermal measurement system [72]. 35
Figure 2-30: A thermal image of a WC-Co thick wall sample [72]. 35
Figure 2-31 : BSE image of the as-built sample showing round shape un-melted WC/W2C particle, prismatic carbide (circled), dendritic carbide (site A), and Ni binder (dark grey regions) [73]. 36
Figure 2-32: (a) As polished, (b) etched, optical micrograph of the hardmetal top surface [74]. 37
Figure 2-33: Morphology of the coatings; (a) before laser re-melting, (b) after laser re-melting [78]. 39
Figure 2-34: (a) Micro-cracks cross through WC particles, (b) micro-cracks inside the WC particle, (c) macro-cracks cross through WC particles, (d) high magnification of (b) [80]. 41
Figure 2-35: Vickers indentation and Palmqvist cracks on hardmetal [81]. 42
Figure 2-36: WC-Co hardmetal [88]. 44
Figure 2-37: Position of cobalt in the European Commission criticality list in 2017, where blue represents critical raw material on the basis of economic importance and high supply risk and green represents non-critical raw material [89]. 45
Figure 2-38: Mine production and price of Co [89] [92], [93]. 45
Figure 2-39: Rupture strength vs hardness [108]. 49
Figure 2-40: Influence of Ni content in a Fe-Ni binder on the transverse rupture strength [108]. 51
Figure 2-41: Phase diagram of the W-C system [130]. 59
Figure 2-42: Fe-C equilibrium phase diagram [110]. 60
Figure 2-43: The calculated Fe-W phase diagram [131]. 61
Figure 2-44: Vertical section of the Fe-Cr-C system at 13 % Cr [133]. 62

Figure 2-45: W-Fe-C isothermal section at 1000 °C [135]. 63
Figure 3-1: LENS 850-R system [140]. 68
Figure 3-2: Powder flow from the nozzles. 69
Figure 3-3: Relationship between RPM and g/min. 69
Figure 3-4: Hatch spacing [143]. 76
Figure 3-5: Scanning pattern of the LENS® deposition process. 77
Figure 3-6: Ceramic heating stage. 78
Figure 3-7: Conventionally manufactured cylindrical rotary burr. 79
Figure 3-8: Example of a crystal lattice where the black circles represents lattice points, the purple arrows are the incoming and scattered x-ray [10]. 86
Figure 3-9: Palmqvist indentation characteristics.....87
Figure 3-10: (a) Three-dimensional heat flow, (b) Two-dimensional heat flow [61]. 89
Figure 3-11: Schematic representation of the single wall sample. 90
Figure 4-1: PSD (a) WC powder, (b) FeCr powder, (c) WC-10wt% FeCr powder. 93
Figure 4-2: SEM-SEI image of the feedstock WC powder. 94
Figure 4-3: SEM-SEI image of the feedstock FeCr powder......95
Figure 4-4: SEM-BEI image of the WC-10wt% FeCr......95
Figure 4-5: EDS analysis area and results of the WC particle......96
Figure 4-6: EDS analysis area and results of the FeCr particle. 96
Figure 4-7: EDX mapping of the WC-10w.t% FeCr powder. 97
Figure 4-8: XRD spectrum of the WC/W_2C powder......98
Figure 4-9: XRD spectrum of the FeCr powder......99
Figure 4-10: XRD spectrum of the WC-10wt% FeCr. 99
Figure 4-11: OM images of the WC powder. 100
Figure 4-12: OM images of the FeCr powder......100
Figure 5-1: DOE single wall samples. 102
Figure 5-2: Sample profile of the thin walls. 102
Figure 5-3: Effect of traverse speed and powder feed rate on sample height. 104
Figure 5-4: Effect of traverse speed and powder feed rate on sample height. 104
Figure 5-5: Effect of traverse speed and powder feed rate on sample height. 105
Figure 5-6: Effect of laser power and powder feed rate on sample height......105
Figure 5-7: Effect of laser power and powder feed rate on sample height......106
Figure 5-8: Effect of laser power and powder feed rate on sample height......106
Figure 5-9: Normal probability plot for the exponential model. 108

Figure 5-10: Normal probability plot for the quadratic model. 108
Figure 5-11: Residual plot for the exponential model. 109
Figure 5-12: Residual plot for the quadratic model. 109
Figure 5-13: Effect of laser power on % porosity at a traverse speed of 8.5 mm/s and powder feed rate of 12.2 g/min. 111
Figure 5-14: Effect of laser power on % porosity at a traverse speed of 6.4 mm/s and powder feed rate of 12.2 g/min. 112
Figure 5-15: (a) Binary micrograph, (b) aspect ratio of pores at different circularity ranges at 400 W, 8.5 mm/s, 12.2 g/min. 112
Figure 5-16: (a) Binary micrograph, (b) aspect ratio of pores at different circularity ranges at 300 W, 8.5 mm/s, 12.2 g/min. 113
Figure 5-17: Effect of traverse speed on % porosity at a laser power of 200 W and powder feed rate of 12.2 g/min. 113
Figure 5-18: Effect of traverse speed on % porosity at a laser power of 300 W and powder feed rate of 12.2 g/min. 114
Figure 5-19: Porosity area of samples deposited at 300 W, 10 g/min at traverse speed of (a) 3.2 mm/s, (b) 6.4 mm/s, (c) 8.5 mm/s. 114
Figure 5-20: Porosity of samples fabricated @ 200 W, with powder feed rate of (a) 7.3 g/min and (b)12.2 g/min; @ 300 W, with powder feed rate of (c) 7.3 g/min and (d)12.2 g/min. 115
Figure 5-21: Effect of powder feed rate on porosity at a laser power of 200 W and traverse of 3.2 mm/s. 115
Figure 5-22: Effect of powder feed rate on porosity at a laser power of 300 W and traverse of 3.2 mm/s. 116
Figure 5-23: Main effects of parameters on % porosity. 116
Figure 5-24: Influence of z-increment on sample height. 120
Figure 5-25: Effect of z-increment on the % porosity at a laser power of 200 W, traverse speed 3.2 mm/s and powder feed rate of 7.3 g/min. 121
Figure 5-26: Effect of z-increment on the % porosity at a laser power of 200 W, traverse speed of 6.4 mm/s and powder feed rate of 10 g/min. 121
Figure 5-27: Effect of z-increment on the % porosity at a laser power of 300 W, traverse speed of 6.4 mm/s and powder feed rate of 12.2 g/min. 122
Figure 5-28: Sample deposited at 200W, 3.2 mm/s, 7.3 g/min and z-increment; (a) 0.167 mm, (b) 0.2 mm. 122

Figure 5-29: Samples deposited at 200W, 6.4 mm/s, 10 g/min and z-increment; (a) 0.167 mm, (b) 0.2 mm. 123
Figure 5-30: Porosity morphology, (a) sample area close to substrate, (b) sample area on the top layer, at 200 W, 3.2 mm/s, 7.3 g/min and z-increment of 0.167 mm. 123
Figure 5-31: Effect of z-increment on porosity. 123
Figure 5-32: Cube samples deposited at 200 W, 3.2 mm/s, 12.2 g/min and a hatch spacing of, (a) 0.7 mm, (b) 0.53 mm. 124
Figure 5-33: Lack of attainment of height in sample B and fusion cracks in sample I... 124
Figure 5-34: Optimum cube samples,(D) 200 W, 3.2 mm/s, 12.2 g/min, (G) 300 W, 3.2 mm/s, 10 g/min and (K) 400 W, 6.4 mm/s, 12.2 g/min. 125
Figure 5-35: Influence of heat input on the densification of cube samples. 126
Figure 6-1: Microstructure at 400 W, 6.4 mm/s, 10 g/min. 128
Figure 6-2 :(a) Microstructure and EDS analysis of;(a) bright surface zone, (b) bottom area at 400W, 8.5 mm/s, 12.2 g/min. 129
Figure 6-3: EDS mapping of the bright surface zone at 200 W, 3.2 mm/s, 12.2 g/min. .130
Figure 6-4: EDS mapping of the centre of the single wall build at 200 W, 3.2 mm/s, 12.2 g/min. 131
Figure 6-5: Effect of laser power on the bright surface zone at a traverse speed of 8.5 mm/s and powder feed rate of 12.2 g/min. 133
Figure 6-6: Effect of laser power on the bright surface zone at a traverse speed of 6.4 mm/s and powder feed rate of 12.2 g/min. 133
Figure 6-7: Influence of laser power on the thickness of the bright surface zone. 134
Figure 6-8: Dissolution of spherical WC in the bright surface zone. 135
Figure 6-9: Reaction zone at 200 W, 8.5 mm/s, 12.2 g/min. 136
Figure 6-10: Reaction zone at 300 W, 8.5 mm/s, 12.2 g/min. 136
Figure 6-11: Reaction zone at 400 W, 8.5 mm/s, 12.2 g/min 137
Figure 6-12: Influence of laser power on the thickness of the reaction zone. 137
Figure 6-13: Influence of heat input on the thickness of the bright surface zone. 138
Figure 6-14: Effect of heat input on the reaction zone at a powder feed rate of 12.2 g/min. 138
Figure 6-15: Effect of powder feed rate on the thickness of the reaction zone at 400 W. 139
Figure 6-16: Bright surface zone at 200W, 6.4mm/s, 10g/min and z-increment of; (a) 0.167 mm, (b) 0.2 mm. 140

Figure 6-17: Banding structure at 200 W, 6.4 mm/s, 10 g/min, z-increment: 0.167 mm. 140
Figure 6-18: Schaeffler prediction of FeCr phase field [153]. 141
Figure 6-19: Microstructure of FeCr showing the deposition beads. 142
Figure 6-20: Micrograph of FeCr with arrows showing retained austenite. 142
Figure 6-21: Microstructure showing lathe martensite. 143
Figure 6-22: Decarburisation on the top layers of the FeCr alloy. 143
Figure 6-23: SEM BSE image of the fusion line. 144
Figure 6-24: SEM BSE image of columnar grain on the edges of the spherical WC indicated by arrows. 145
Figure 6-25: Herringbone structure indicated with the dashed regions. 146
Figure 6-26: Columnar grains forming a herringbone structure within the dashed regions. 146
Figure 6-27: Trapezoidal phase at the top of the sample indicated by the arrows. 147
Figure 6-28: Columnar grains and the trapezoid phase at the top of the deposit. 147
Figure 6-29: WDS elemental point analysis on different phases of the cube sample. 148
Figure 6-30: WDS elemental mapping at the bottom of the sample. 149
Figure 6-31: WDS elemental mapping on sample top. 150
Figure 6-32: WDS elemental mapping at the centre of the sample. 151
Figure 6-33: WDS elemental mapping around WC grains. 152
Figure 6-34: XRD spectrum of the single wall samples at 8.4 mm/s, 12.2 g/min; (a) 200 W, (b) 300 W, (c) 400 W. 154
Figure 6-35: XRD spectrum of the thin wall samples at 3.2 mm/s; (a) 200 W, (b) 300 W. 155
Figure 6-36: XRD spectrum of single wall samples at 200 W, 3.2 mm/s, 7.3 g/min; (a) z-increment of 0.2 mm, (b) z-increment of 0.167 mm. 156
Figure 6-37: XRD spectrum for FeCr cube sample. 157
Figure 6-38: XRD spectrum of cube sample deposited at 200 W, 3.2 mm/s, 12.2 g/min. 158
Figure 6-39: Influence of laser power on the micro-hardness of thin wall samples. 159
Figure 6-40: Influence of laser power on sample macro-hardness. 159
Figure 6-41: Micro-Vickers hardness profile at 300 W, 3.2 mm/s, 12.2 g/min. 160
Figure 6-42: Micro-Vickers hardness profile at 200 W, 3.2 mm/s, 12.2 g/min. 161
Figure 6-43: Phases for hardness measurements. 161

Figure 6-44: Palmaqvist indent showing multiple cracks originating away from the corners. 163
Figure 6-45: Influence of heat input on surface roughness. 164
Figure 6-46: Temperature profile away from the heat source. 165
Figure 7-1: Sample A, LENS deposited sample at 200 W, 3.2 mm/s, 12.2 g/min without crack mitigation. 166
Figure 7-2: Cracks on cube sample (a) Dye penetrant tested sample, (b) As-sectioned cross section, (c) As-polished cross section. 167
Figure 7-3: Sample A deposited with a FeCr buffer layer. 168
Figure 7-4: Ni buffer layer shown by the arrows. 168
Figure 7-5: Ni-alloy buffer; (a) dye penetrant sample, (b) macro-image showing cracks. 169
Figure 7-6: Micrograph of the FeCr buffer layer. 169
Figure 7-7: Sample A deposited with a Ni-alloy buffer layer. 170
Figure 7-8: Ni-alloy buffer; (a) dye penetrant sample, (b) macro-image showing cracks. 170
Figure 7-9: Micrograph of the Ni-alloy buffer layer with arrows showing inclusions... 170
Figure 7-10: Effect of laser re-melting, (a) and (c) 1 layer re-melting; (b) and (d) 3 layers re-melting. 171
Figure 7-11: Effect of laser re-melting, (a) and (b) 1 layer re-melting; (c) and (d) 3 layers re-melting. 172
Figure 7-12: Preheat at 250 °C; (a) dye penetrant sample, (b) macro-image. 172
Figure 7-13: Influence of crack restraining methods on hardness. 174
Figure 7-14: XRD spectra of the different crack restraining methods. 175
Figure 8-1: LENS® process flow for the manufacture of the prototype burr. 176
Figure 8-2: Process flow in the conventional manufacturing of hardmetal burrs [158]. 177
Figure 8-3: Side view of the cylindrical rotary burr. 177
Figure 8-4: Offset front view of the burr on the shank. 178
Figure 8-5: Shank view of the cylindrical rotary burr. 178
Figure 8-6: LENS fabricated cylindrical rotary burr. 179
Figure 8-7: LENS® fabricated cylindrical rotary burr without preheat. 179
Figure 8-8: LENS® fabrication of a cylindrical rotary burr with preheat of 250°C. 180
Figure 8-9: Finite element model of the cylindrical rotary burr. 181

Figure 8-10: Applied operational loads and boundary conditions. 182
Figure 8-11: Von Mises stress due to imposed load. 182
Figure 8-12: (a) Pre-existing weld area for machining, (b) measurement of the amount of material removed by the burr on surface A. 183
Figure 8-13: Machining performance of LENS® fabricated and sintered cylindrical rotary burrs. 183
Figure 8-14: Machined weld surface. 184
Figure 8-15: Fracture of LENS® cylindrical rotary burr. 184
Figure 8-16: Fracture surface of LENS® fabricated rotary burr. 185
Figure 8-17: Fracture surface of the rotary burr 185
Figure 9-1: Solidification structures as a function of temperature gradient and solidification/growth rate [177]. 195

LIST OF TABLES

Table 2-1: Comparison of mechanical properties for alloys produced by the LENS® process with traditional fabrication methods [42]. 17
Table 2-2: Powder characteristics from different manufacturing processes [47]. 19
Table 2-3: Effects of carbon content of 75 WC/25 Fe specimens on transverse rupture strength [108]. 49
Table 2-4: Characteristics of carbides [132]. 62
Table 2-5: Carbide phase in the quaternary W-Fe-Cr-C system [138]. 64
Table 3-1: Chemical composition of the cast WC powder. 66
Table 3-2: Chemical composition of the gas atomized AISI 420. 66
Table 3-3: Chemical composition of the substrate. 67
Table 3-4: DOE parameters. 70
Table 3-5: DOE matrix. 71
Table 3-6: Work control system parameters. 76
Table 3-7: Cylindrical rotary burr dimensions [144]. 80
Table 3-8: Performance requirements of the cylindrical rotary burr [144]. 81
Table 3-9: Experimental conditions for single wall builds. 90
Table 4-1: Powder size distributions. 94
Table 4-2: EDS results of WC-10wt% FeCr compared to calculated results from the material certificates. 98
Table 5-1: Sample height measurements. 103
Table 5-2: R^2 value for the regression models. 107
Table 5-3: F-test of the regression models. 107
Table 5-4: Optimum process parameters according to Solver software package. 110
Table 5-5: Extended DOE. 110
Table 5-6: Average porosity measurements. 117
Table 5-7: Pareto optimal solutions. 117
Table 5-8: Influence of z-increment on sample height. 119
Table 5-9: Height and % porosity of the cube samples at optimum process parameters. 126
Table 5-10: Densification of the optimum cube samples. 126

Table 6-1: Mapping analysis of the bright surface zone and centre of the single wall builds. 132
T*able 6-2: Optimum parameters for cube samples.* 143
Table 6-3: WDS analysis of the different phases. 148
Table 6-4: XRD phase results. 155
Table 6-5: Calculated mass % of the different phases. 158
Table 6-6: Hardness of different phases. 162
Table 6-7: Hardness of the optimum cube sample. 162
Table 7-1: Influence of crack restraining methods on cracks. 173
Table 8-1: Dimensions of the LENS® fabricated and sintered WC burrs. 181
Table A-1: Process parameter mapping of LENS® deposited WC and FeCr alloys. 222
Table A-2: Colour coding for process parameter mapping. 222
Table B-1: Rotary burr applications and material groups [144]. 223
Table B-2: Rotary burr design [144]. 224
Table B-3: Recommended rotational speeds [144]. 224
Table B-4: Rotational speed based on burr diameter [144]. 225
Table C-1: Quadratic regression model for sample height. 226
Table C-2: Multiple linear regression model for sample height. 227
Table C-3: Exponential regression model for sample height. 227

Abbreviations

LENS	Laser Engineered Net Shaping
AM	Additive manufacturing
WC	Tungsten carbide
W_2C	Ditungsten carbide
Wt	Weight
FeCr	Iron-chromium
Ni	Nickel
Co	Cobalt
CTE	Coefficient of thermal expansion
CAD	Computer aided design
3D	Three dimensional
SEM	Scanning electron microscope
BSE	Backscattered electron
SE	Secondary electron
OM	Optical microscope
XRD	X-ray diffraction
EPMA	Electron probe microanalyzer
EDS	Energy dispersive spectroscopy
FEA	Finite element analysis

CHAPTER 1 Introduction

1.1 Background and Motivation for the Research

Additive manufacturing (AM), simply known as 3D printing has become a revolutionary technology that has changed the way products are designed and manufactured. The sudden move from conventional manufacturing processes to AM has been fuelled by the advantages of AM namely, the production of near net-shaped components which require minimal machining or cutting, reduced tooling and fixtures, shorter manufacturing turnaround and the manufacture of intricately shaped components [1].

There are three main types of AM powder-based processes and their difference lies in the feedstock process form: (1) Powder Bed, which includes Selective Laser Sintering (SLS), Selective Laser Melting (SLM) and Electron Beam Melting (EBM), (2) Powder Directed Energy Deposition, which includes Laser Engineered Net Shaping (LENS®), and (3) Wire Directed Energy Deposition which includes Electron Beam Additive Manufacturing (EBAM®) [2]. *Figure 1-1*shows an overview of AM processes.

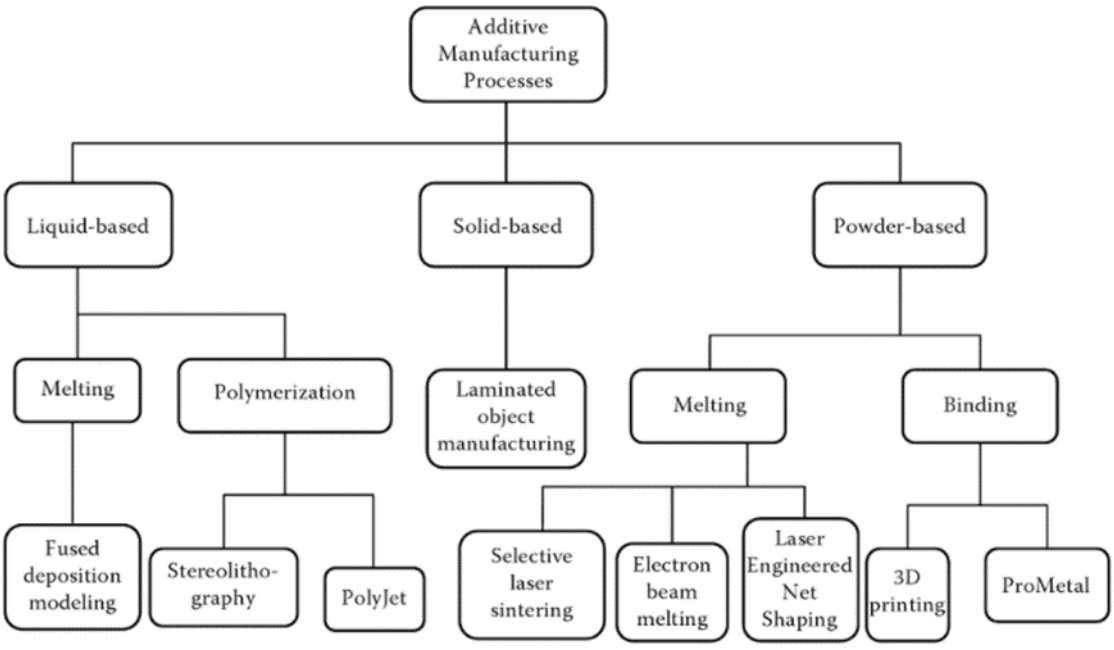

Figure 1-1: Flow diagram overview of various additive manufacturing processes [1]**.**

The main focus of this research project is the LENS® manufacturing of WC-FeCr hardmetals. The LENS® technology was developed at Sandia National Laboratories (U.S) in 1990 and was licensed to Optomec, Inc., Albuquerque N.Mex in 1997 [3]. The LENS® technology was derived from the approach used for rapid prototyping technology into the direct fabrication of alloy parts [4]. The technology has found use in materials such as, stainless steel, tool steels, nickel alloys, cobalt alloys and titanium alloys [3]. The application of the LENS® technology in the fabrication of tungsten carbide (WC) based materials may overcome disadvantages posed by conventional sintering processes, namely longer manufacturing times, grain coarsening of WC crystals, formation of brittle constituents and increased fixtures for complex geometries [5].

The LENS® technology in the manufacture of hardmetals have not been adopted on a commercial level yet as more work is still required on a research level. Challenges in applying the technology include the high melting points and availability of raw materials [6]. In 2004, the University of California, Davis in the United States was awarded funding by the National Science Foundation to conduct a fundamental investigation of the LENS® process for the fabrication of nanostructured hardmetals [7]. Limited experiments were conducted to compare the conventional sintering process to LENS® manufacturing of WC based materials, but application gaps still remain [8].

In the current study an iron-chromium (FeCr, AISI 420) martensitic stainless steel alloy has been selected as the binder for the LENS® manufacturing of hardmetals. WC is usually predominantly embedded in a cobalt (Co) matrix due to its excellent wetting of carbide grains [9], with nickel (Ni) or Fe matrices being employed to a lesser extent [10]. In recent years it has been established that cobalt has a negative effect on human health due to its carcinogenic effects [11]; additionally, in 1978 Co was reported as a scarce mineral, following the Co crisis, thus leading to high Co prices [12]. The disadvantages posed by Co binders have rendered Ni as the more viable binder option due to its good corrosion properties. This has sparked research on Ni as a replacement binder, however it has been reported that Ni has inferior mechanical properties compared to its Co counterparts [13] [14] [15]. In addition Ni is expensive and there have been reports on its toxicity [16]. Fe binders are the most cost

effective binders and were initially mentioned in a patent by K. Schröter which was filed in 1923 [17]. However, to date the application of Fe as a binder in hardmetals is limited. More so, to the best of the author's knowledge, there is currently limited research into the manufacture of WC-FeCr hardmetals using the LENS® technology.

1.2 Research Aim and Objectives

The aim of this study was to investigate the feasibility of using additive manufacturing with particular focus on LENS® technology to manufacture WC-FeCr hardmetals, in order to broaden the scientific knowledge base on the application of rapid manufacturing technologies in the field of hardmetals. This aim was achieved through the following objectives:

- Conducting a full factorial design of experiments to establish the optimal processing parameters for the WC-FeCr hardmetals, with thin walls being deposited.

- Applying statistical regression models to find the mathematical relationships between process parameters, sample profile and sample porosity.

- Using statistical optimization techniques namely generalised reduced gradients (GRG) and multi-objective optimization (MOO) in order to achieve near optimum processing parameters.

- Depositing samples with a cube geometry onto a substrate using near optimum parameters and caring out parameter refinement in order to achieve a single optimum parameter set.

- Studying the effect of process parameters such as laser power, traverse speed and powder feed rate on microstructural evolution, hardness and surface finish.

- Investigating different crack restraining methods and their influence on crack formation using the optimal deposition parameter set.

- Manufacturing a prototype (proof-of-concept) rotary burr using the optimal deposition parameter set and benchmarking against a conventionally manufactured product through field testing.

1.3 Contribution to Knowledge

The use of the LENS® technology in the commercial fabrication of hardmetals is yet to be exploited as there is limited research in this area. To date, research has been confined to the usage of cobalt (Co) or nickel (Ni) binder systems and according to the authors knowledge the current research study is the first to consider the application of LENS® technology to manufacture an iron-chromium (FeCr) martensitic steel binder system. Thus, the study provides new results to advance the scientific knowledge base on the application of rapid manufacturing technologies to produce hardmetals. Relationships between process parameters, microstructure, porosity and hardness have been derived. A proof-of-concept prototype rotary burr was designed, manufactured and benchmarked. Overall this research forms the foundation on which further research on the feasibility of the LENS® technology to produce WC-FeCr hardmetals can be based.

1.4 Structure of the Thesis

The thesis is structured in the following manner: Chapter 1 gives the background into the LENS® manufacture of harmetals and provides the motivation for undertaking the research study. Chapter 2 reviews published literature on the history and conventional production of hardmetals, additive manufacturing with particular focus on the LENS® technology, and finally the different binder systems with the focus drawn to the Fe binder system. Chapter 3 provides a detailed experimental methodology including materials, equipment, and test procedures used for carrying out the work. Chapter 4 presents the results for the feedstock powder analyses. Chapter 5 provides the results for the design of experiments (DoE) and all optimization techniques used to attain optimum process parameters. Chapter 6 presents the material characterization results while Chapter 7 is based on crack restraining test results. Chapter 8 provides the

results for simulations and field tests on the prototype component. A discussion of the results is provided in Chapter 9, while Chapter 10 is the conclusions and recommendations for future work. The thesis ends with a list of references and the appendices.

CHAPTER 2 Literature Review

This review starts by looking into the historical development and commercial application of hardmetals. The properties of hardmetals and the conventional method of production is described. Limitations of the conventional manufacturing process will be highlighted. This is followed by a review into the development, operational principles, and different types of additive manufacturing (AM) processes. The focus is drawn to the LENS® technology, looking at its design, impact of operational principles on the final product, material applications and defect generation. A review of AM as an alternative manufacturing process for hardmetals is then presented. This chapter ends with a description of the different binders used for hardmetals with particular focus on FeCr binders.

2.1 Tungsten Carbide History

Tungsten carbide (WC) was first synthesized by H. Moissan in 1893 in an attempt to produce artificial diamond [18]. It is a chemical compound containing tungsten (W) and carbon (C) atoms and has a melting temperature of ~ 3060 K [19]. Its hardness is stable at 300 K and ranges between 18 – 22 GPa [19] and decreases with an increase in temperature. WC has a Young's modulus of elasticity of ~ 700 GPa, which is twice as large as compared with other carbides and a thermal coefficient of expansion of ~ 5.5 x 10^{-6} K^{-1} [19]. The WC was, however, too brittle for commercial use, and it was only after ~ 20 years that the commercial development of WC was made between 1918 - 1923 in Germany, by K. Schröter [19] [20] from the Osram Study Society for Electrical Lighting. This practical interest was sparked from the replacement of the costly and hard to find diamond wire drawing dies for tungsten carbide filaments [18] [20]. The first experiments by Schröter included a Ni metal binder which was known to be superior to known carbides, however the Ni binder was seen to evaporate at high sintering temperatures, and it was later replaced by Co which yielded a superior carbide [21]. K. Schröter filed a USA patent in 1923 which was granted in 1925 [17]. Through this patent it was established that to successfully use WC in wear applications it needs to be embedded/cemented and metallurgically bonded to a ductile matrix or binder phase with a lower melting point such as Co, Ni or Fe which supports the WC

grains, hence the name cemented tungsten carbides which then also came to be known as hardmetals.

Figure 2-1 shows the historic developments of hardmetals. The initial breakthrough in the production of hardmetals was not complemented with industrial exploitation due to the lack of resources. Hence, the Osram Study Society for Electrical Lighting sold the patent license to Fried, Krupp and it was in 1927 when commercial hardmetals became available under the name Widia (acronym for Wie Diamant = like diamond) [20] [18]. During the 2nd World War, WC was used to manufacture armour-piercing projectiles, which led to a rocketing demand close to the world supply of off-grade tungsten ore [22]. This shortage of WC led to research into replacement of the hard phase which resulted in replacing some of the WC with titanium carbide (TiC) and tantalum carbide (TaC) as shown in *Figure 2-1*. In the years following Schröters 1923 patent, several hardmetal companies were founded, as shown in *Figure 2-2*.

1923 - 25	WC-Co
1929 - 31	WC-TiC-Co
1930 - 31	WC-TaC(VC, NbC)-Co
1938	WC-Cr_3C_2-Co
1948 - 70	Sub-micron WC-Co
1956	WC-TiC-Ta(Nb)C-Cr_3C_2-Co
1959	WC-TiC-HfC-Co
1965- 78	TiC, TiN, Ti(C,N), HfC, HFN and Al_2O_3 CVD coatings on WC-base hardmetal
1968-69	WC-TiC-Ta(Nb)C-HfC-Co
1968 - 69	WC-TiC-Ta(Ta)C-HfC-Co
1969 - 71	Thermochemical surface hardening
1974 - 77	Polycrystalline diamond on WC-base hardmetal
1973 - 78	Multi-carbide, carbonitride/nitride and multiple carbide/carbonitride/nitride/oxide coatings
1981	Many thin coatings with AION (aluminium oxynitride) layers
1983 - 92	Sinter-HIP
1992 - 95	Plasma CVD diamond coating
1993 - 95	Coating complex carbonitrides
1994	Fine-grain WC/Co agglomerates in tougher WC/Co matrix

Figure 2-1: Historical developments of hardmetals [23].

1924 Montanwerke Walter, Germany
1926 Krupp-WIDIA, Germany
1928 Carboloy Corp. by General Electric, USA
From 1929 onwards: Sumitomo, Japan
1930 Plansee Titanit, Austria
1931 WIMET, Great Britain
From 1931 onwards: Mitsubishi, Japan
1938 Kennametal Inc., USA
From 1942 onwards: Sandvik Coromantfabriken, Sweden

Figure 2-2: The foundation of hardmetal companies [24].

Since the first commercial development of hardmetals as wire drawing dies were made using a 6 wt% Co binder [20], the material expanded into the manufacture of cutting tools, wear parts and machine components due to the high hardness, wear resistance and good fracture toughness. *Figure 2-3* shows an example of the relationship between these three properties. Control of the WC grain size and binder content allows tailoring of the hardness and strength of the hardmetal [9]. It has been shown that by decreasing the WC particle size the hardness and wear resistance can be increased [25] [26].

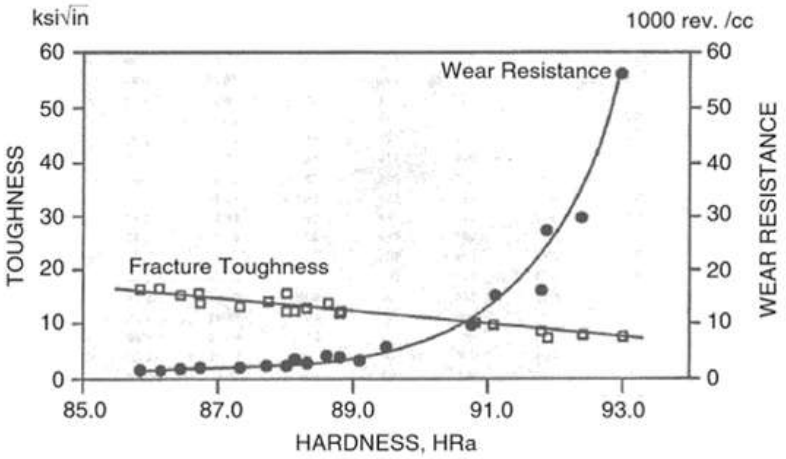

Figure 2-3: Relationship between toughness, hardness and wear resistance of tungsten carbide coatings [27].

Over the past 30 years the conventional method of manufacturing hardmetals has been by powder metallurgy which consists of a sequence of steps whereby each step must be controlled to obtain a final product with the desired mechanical properties,

microstructure and performance [28]. *Figure 2-4* shows the typical sequence of steps which are followed in the production of three different hardmetals.

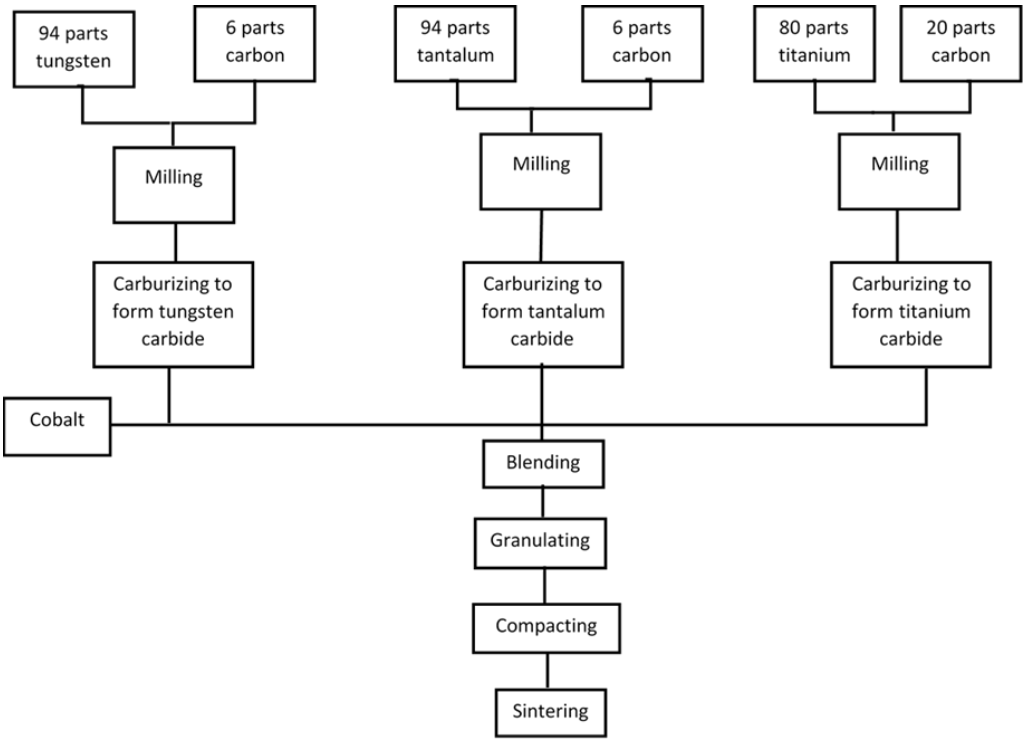

Figure 2-4: Flowchart of hardmetal production [29].

In the powder metallurgy of hardmetals, tungsten metal powder is carburised by adding controlled amounts and a uniform distribution of carbon black [28]. During the carburising stage a deficiency in the carbon content will result in the formation of di-tungsten carbide (W_2C) phase, while an excess carbon results in flakes of free graphite which lowers the resistance to cracking [28] [20]. The carburised powders are then combined with a binder phase such as cobalt for the manufacture of hardmetals. This process requires blending so that every carbide particle may be coated with the binder material [28]. Once a WC powder is formed with the required binding agent, powder consolidation is required to produce a coherent metal structure and to develop materials with controlled microstructure [29].

Following compaction of the hardmetal powders, sintering takes place to ensure cohesion of the powder particles. In as much as sintering is a densification process, grain and pore growth takes place due to the high temperatures [30]. The degree of densification is dependent on the particle size and temperature. According to a study

conducted by Fang *et al*. [31] to evaluate the degree of densification of WC-10 wt.% Co with temperature, it was shown that densification of nano-sized powders exceeded those of coarser powders and densification increased with an increase in temperature. *Figure 2-5* shows a plot of degree of densification against temperature for different size particles.

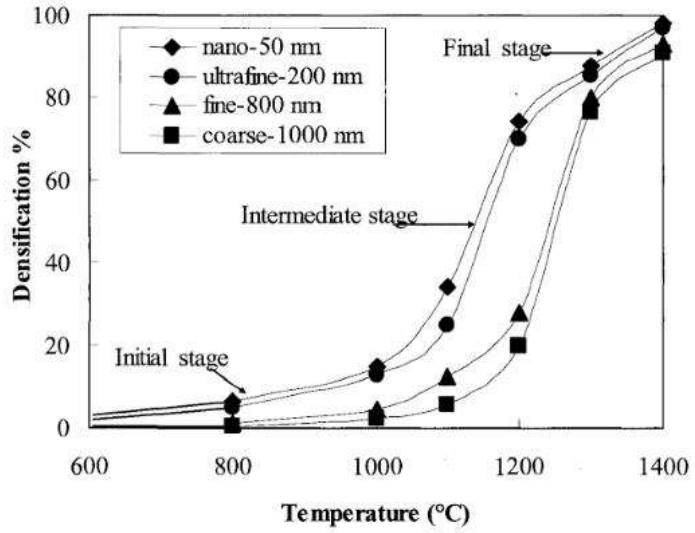

Figure 2-5: Plot of % densification vs. temperature for the four grades of WC-Co samples, i.e., 50nm, 200nm, 800nm, 1000nm [31].

There are disadvantages with the sintering of hardmetals as the process cannot be carried out within short periods of time. Sintering cycles take ~ 15 - 20 hours, thus leading to longer production times [5]. Grain coarsening therefore seems to be a major problem as this is due to solution re-precipitation of WC crystals [32]. In order to control grain size, inhibitors such as vanadium may be added, which also results in an increase in hardness [32]. Good densification during sintering requires the use of nano-crystalline powders [31], which also require more time during the milling process.

Due to the disadvantages posed by sintering and powder metallurgy processes in the production of hardmetals, AM with particular focus on the LENS® technology provides a motivation to apply this method in the fabrication of WC-FeCr hardmetals. A review of additive manufacturing and its application to hardmetals is given in Section 2.2.

2.2 Additive Manufacturing

2.2.1 General additive manufacturing

The manufacturing industry is accelerating towards additive manufacturing (AM) simply known as 3D printing. AM has now been referred to as a revolutionary disruptive process. The sudden move has been fuelled by the advantages posed by AM namely, the production of net-shaped components which require no additional machining or cutting, reduced tooling and fixtures, shorter manufacturing turnaround and intricate shapes can be manufactured. [1]. AM is a process of manufacturing components from a 3D CAD model using the layer-by-layer principle.

AM is a formalised term of what used to be called rapid prototyping (RP) and was developed in the 1980s through the development of the first form of 3D printing named stereolithograhy (SLA) following the use of lasers in AM [33]. SLA is based on the concept of focusing an ultraviolet (UV) light source onto a liquid polymer bath, which induces polymerization of the liquid in that region and transformation into a polymerized solid. Patterns could be formed using the UV light, whereby after a layer of printing is done, the hardened polymer layer moves down on the build plate and the next layer is built until the part is finished based on the CAD design. In 1986 the first company to develop and manufacture 3D printers was established by Chuck Hull and named 3D Systems. This was the first development of allowing a CAD file to communicate with a rapid prototyping system. In 1986 the first patent of a RP system was approved [33]. The first use of AM was in polymers, however, this process expanded to different types of materials inclusive of metals. The roadmap of AM is shown in *Figure 2-6*.

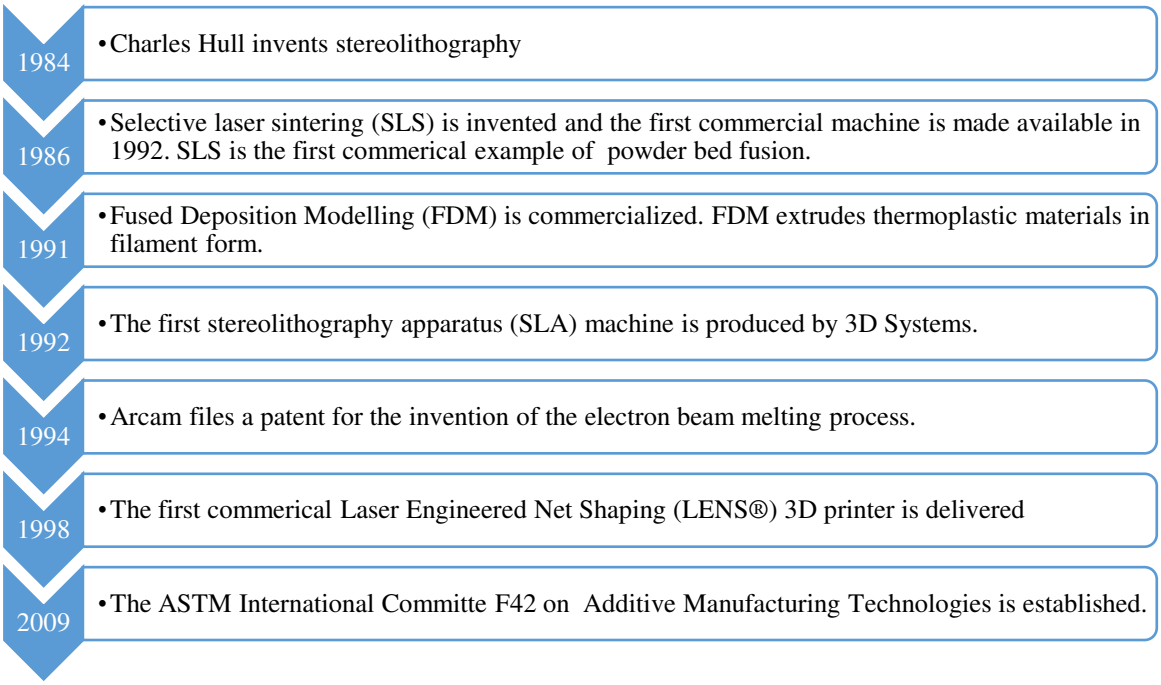

Figure 2-6: Roadmap of AM [34].

The basic principal of AM is that a part is manufactured directly from a three-dimensional Computer-Aided Design (3D CAD) model and it is based on an additive process rather than subtractive process such as machining. CAD models can be established by use of reverse engineering techniques, such as 3D laser [35]. Once the CAD model has been established it needs to be converted into an STL file so that it can be read by the AM machine [35]. An STL file format is a simple way of describing a CAD model in terms of geometry alone by outlining the external closed surfaces of the original CAD model in a form of unordered collection of triangular facets [35]. The AM machine reads the STL solid model and divides it into thin layers orthogonal to the z-axis, the data for each thin layer is translated into laser scanning paths to fabricate a single layer. Materials are then added layer by layer where each layer is a cross section from the CAD model. The fabrication process is automated with little supervision required, *Figure 2-7* shows the AM process chain. Following the AM fabrication of a component, post processing in the form of heat treatment and surface finishing processes may be required depending on the application.

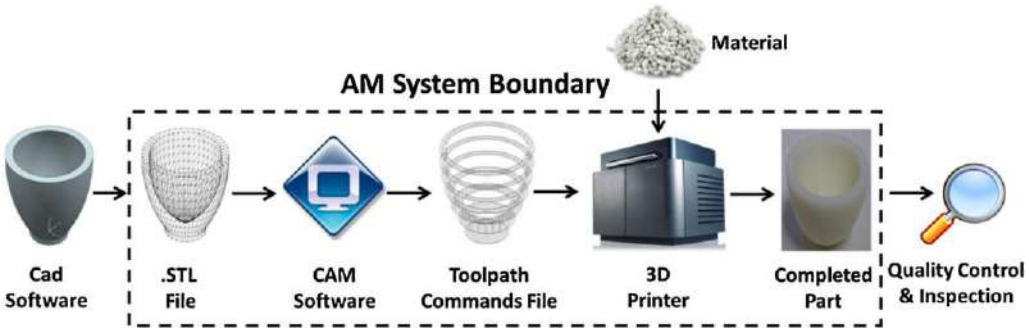

Figure 2-7: Additive manufacturing process chain [36].

There are different AM processes and the difference lies in the feedstock material, layer pattern and heat source [2]. AM processes are classified into 7 main categories in accordance with ASTM F2792-12a [37], namely: Vat photo-polymerization, Powder bed fusion, Material extrusion, Material jetting, Binder jetting, Directed energy deposition and Sheet lamination.

2.2.2 Laser Engineered Net Shaping (LENS®)

Directed energy deposition (DED) processes directs the energy required from a laser or electron beam heat source for fabrication into a narrow, focused region to heat the substrate and to melt the feedstock material as it is deposited onto the substrate from a nozzle which is mounted on a multi-axis arm [35] [38]. Laser-based systems can either use wire or powder as the feedstock material, these systems can operate in a fully inert chamber when using reactive materials or shielding gas for less reactive materials [38]. The difference between DED and powder bed fusion is that for the latter a laser selectively melts the feedstock material that is pre-laid in a powder bed. In a powder based DED system the flow of powder from the nozzle is controlled amongst other properties by a carrier gas such as helium or argon. During fabrication a CAD solid model is divided into thin layers orthogonal to the Z-axis [39]. The data for each thin layer is translated into laser scanning paths to fabricate a single layer. The layers are fabricated by first generating an outline of each feature and filling it up on a repetitive basis [39]. Once the first layer is deposited the nozzle moves up by a z-increment in order to deposit more layers until fabrication is complete. In a 4 or 5 axis DED system the nozzle and substrate can move at the same time but independent of each other, due to this a flat surface is not a prerequisite for fabrication meaning, component repair

would be possible [35]. DED is sometimes referred to by using other technological terms such as laser engineered net shaping (LENS®), direct metal deposition, and laser cladding depending on the application method [35] [38].

Advantages of DED [38] [40]:

- In the 4 and 5 axis system the technique does not require a flat surface and can be used in the repair of components in addition to fabrication of new parts.
- DED is a relatively fast process in comparison to other AM technologies.
- Fabrication of dense parts.
- Increased material utilization.
- Production of refined microstructures.
- Accurate part fabrication.

Disadvantages of DED [38]:

- If a fully inert chamber is required, a large volume of argon or nitrogen is required and it can take a long time to reach low oxygen levels.
- Final machining step is required to attain the finish required.
- Not all the powder which is blown from the nozzle is fused hence unless powder can be recycled, the process efficiency is reduced.

The LENS® technology is a process that directly fabricates alloy parts. This process was developed at Sandia National Laboratories in the United States in 1990 [8], however in 1997 the process was licensed to Optomec, Inc., Albuquerque N.Mex [3]. Optomec has since been the sole manufacturer and distributor of LENS® systems [3]. Follow-up development work was done on the LENS® process in order to promote the advancement of the technology and speed up its commercialization through the sponsorship of a Cooperative Research and Development Agreement (CRADA), with members including but not limited to Ford Motor Co, Optomec Design Co and the National Aeronautics and Space Administration (NASA) to name a few [3]. There are currently more than 20 LENS® systems with an energy source of 1 kW Nd:YAG laser, with the modern systems coupled to the new IPG fiber lasers ranging from 1 to 3 kW [3]. The known features of the LENS® technology are high cooling rates, rapid process, and accurate shape control [8].

The LENS® process uses a controlled atmosphere glove box, a 5-axis computer-controlled positioning system, and a powder feed unit [39]. The atmosphere glove box is backfilled with argon gas which is responsible for achieving a controlled atmosphere by purging the system of oxygen and moisture [41]. The first LENS® system comprised of a laser beam directed to the deposition region through a window which is mounted on the top of the glove box [39]. The LENS 850-R System operates with a high-powered IPG fiber laser and optical delivery system. The laser consists of a power distribution unit, power supply, cooling system, and delivery fiber. The laser beam is delivered to the laser deposition head through a laser fiber, after which a series of laser optics are used to direct and focus the beam on the work piece [41]. The powder delivery nozzle is designed to deliver the powder streams directly into the focused laser beam. Deposition is carried out on a flat solid substrate usually made of the metal to be deposited. The laser beam is then focused onto the substrate to form a molten pool into which powder particles are fed. All LENS® deposits are metallurgically bonded and have a heat affected zone (HAZ) and a dilution zone [3]. Laser deposition processes are characterized by a low heat input and minimum distortion and this is mainly because of the high traverse speeds and thus high cooling rates. *Figure 2-8* shows the layout of the LENS® system.

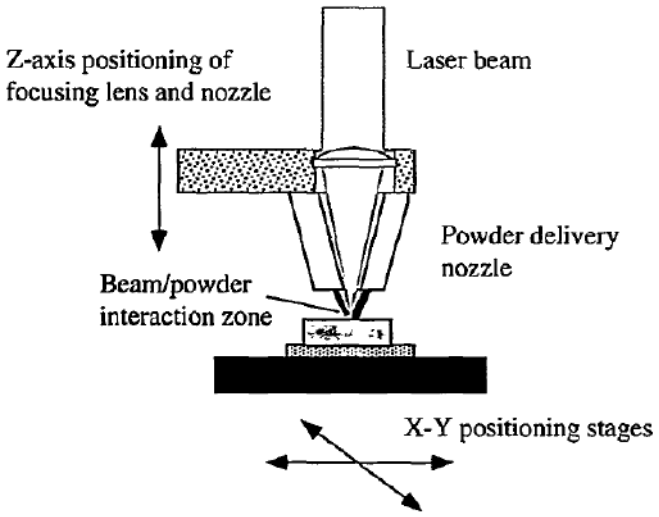

Figure 2-8: Schematic representation of the LENS® process [42].

2.2.2.1 LENS® process parameters

LENS® process parameters have a strong influence on the quality of the final product hence, it is required that optimum parameters are established. The main process parameters in the LENS® process are laser power, powder feed rate and traverse speed for a specific laser spot size [40]. The powder feed rate is the speed at which the inert gas transports the metallic powders to the delivery head. Popoola *et al*. [40], investigated these parameters and established that a comparatively low feed rate may lead to poor deposition rate, while a high feed rate leads to thick layer formation and hence poor adhesion. An increase in the laser power yields an increase in the injected energy. Surface roughness decreases linearly with an increase in the laser power. However, a high laser power results in the formation of a larger heat affected zone (HAZ) which may cause alteration in the mechanical properties. The traverse speed is the speed at which the laser beam carries out its deposition along a track path during fabrication of the component. An increase in the traverse speed may lead to a reduction in the time for completion.

2.2.2.2 Application of the LENS® system

The LENS® process is used to manufacture products of low volume and high value. The LENS® system has successfully deposited a range of materials namely stainless steels (grade AISI 304, AISI 316, AISI 410, AISI 420, 17-4PH), tool steels (H13), nickel alloys (617, 625, 718), cobalt alloys (#6 stellite, #21 stellite), titanium alloys (Ti-6-4, Ti-6-2-4-2), composites and graded materials [3] [43]. The deposition of graded materials allows the designer to tailor the physical and mechanical properties. The properties of materials which have been successfully deposited using the LENS® process are in most cases better than the traditionally fabricated materials with an improvement in the yield strength while retaining ductility [42]. This is attributed to the Hall–Petch grain size refinement, where finer grain sizes result in high yield strengths [44]. It has been established that it is difficult to deposit aluminium and copper alloys due to their reflective properties. *Table 2-1* shows the room temperature mechanical properties of LENS® deposited materials in comparison to traditionally fabricated materials

Table 2-1: Comparison of mechanical properties for alloys produced by the LENS® process with traditional fabrication methods [42].

Material Type	Yield Strength (MPa)	Ultimate Tensile Strength (MPa)	Elongation (%)
LENS® Ti-6Al-4V	932	1004	13
Ti-6Al-4V Annealed bar	883	952	14
LENS® 316 stainless steel	434	758	46
Wrought 316 stainless steel	228	586	50
LENS® 304 L stainless steel	324	655	70
Wrought 304L stainless steel	276	-	55
LENS® Inconel 625	614	931	38
Wrought Inconel 625	400	834	37
LENS® tool steel H-13	1462	1703	1-3
Wrought tool steel H-13	1448	1724	12

The LENS® process has found extensive use in component repair such as the repair of gas bottles. Other uses include components which were previously non-repairable due to the avoidance of high heat inputs and a large HAZ, which is characteristic of conventional welding processes. Low-wattage repair of titanium components in the aerospace industry namely gas turbine compressor seals, drive shafts and drive couplers can be done using the LENS® process [3]. Previously side/contact surfaces of jet engine turbines were cladded using the tungsten inert gas (TIG) welding process, however, final grinding was required in order to meet the final geometrical tolerances, the LENS® process has thus been used for the cladding of side surfaces of jet engine turbines. This has led to fast machining times as the process leads to near-net shaped clads, lower manufacturing costs and process automations [45]. *Figure 2-9* shows a titanium (Ti) aerofoil repair and *Figure 2-10* shows Inconel 625 freeforms manufactured by the LENS® process.

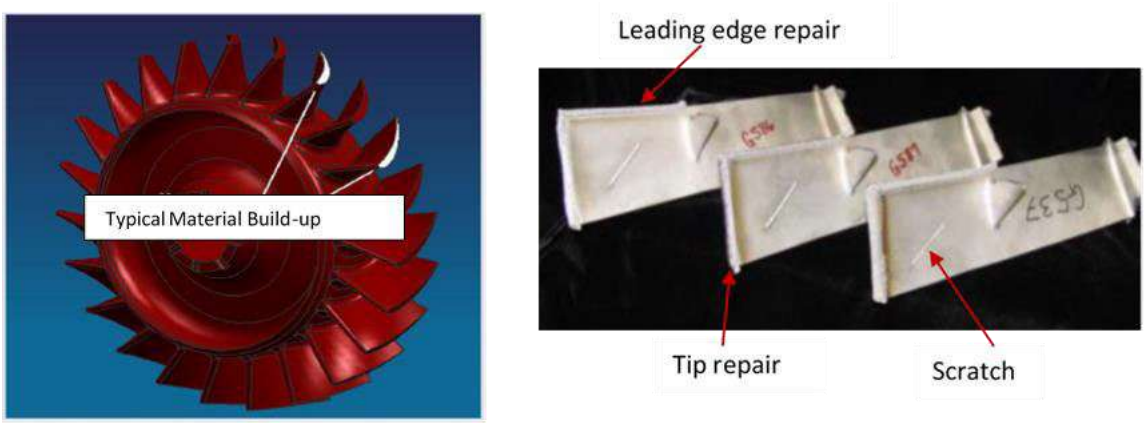

Figure 2-9: LENS® repair of motor blower fan blade (left) and Ti airfoils [43].

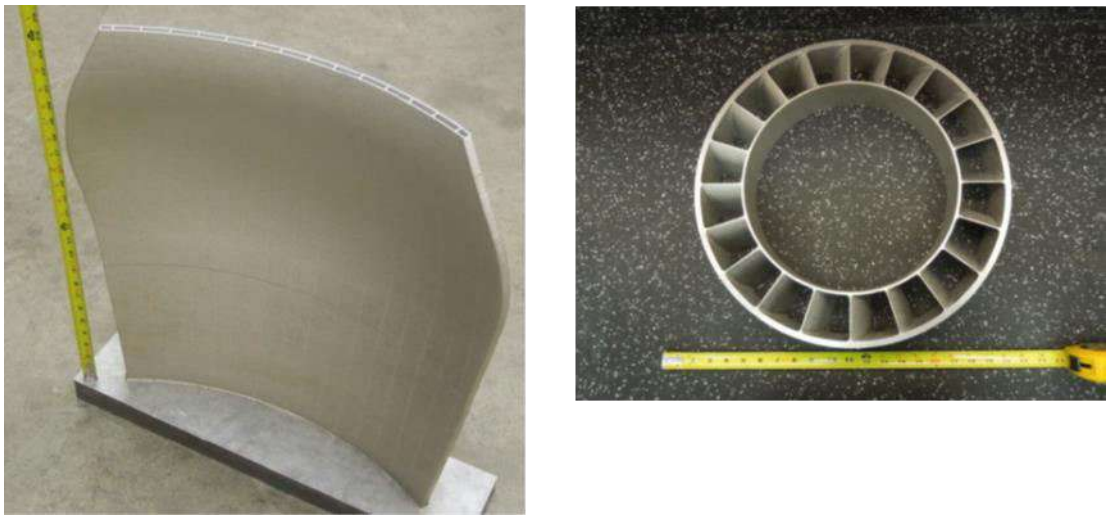

Figure 2-10: LENS® manufactured Inconel 625 free-forms [38].

2.2.2.3 Powder feed system

The feedstock powders used for the LENS® system and other AM processes need to be spherical in shape because this yields less internal friction in the powder allowing it to easily flow, prevent blockage of the powder feed system and to attain higher layer densities [41] [46] [47]. The quality of the feedstock powder determines the quality of the deposited material. The parameters that determine powder quality are the powder shape, internal porosity, size and composition [48]. The particle size requirements of different AM processes are shown in *Figure 2-11* and the different powder characteristics according to manufacturing process are shown in *Table 2-2*.

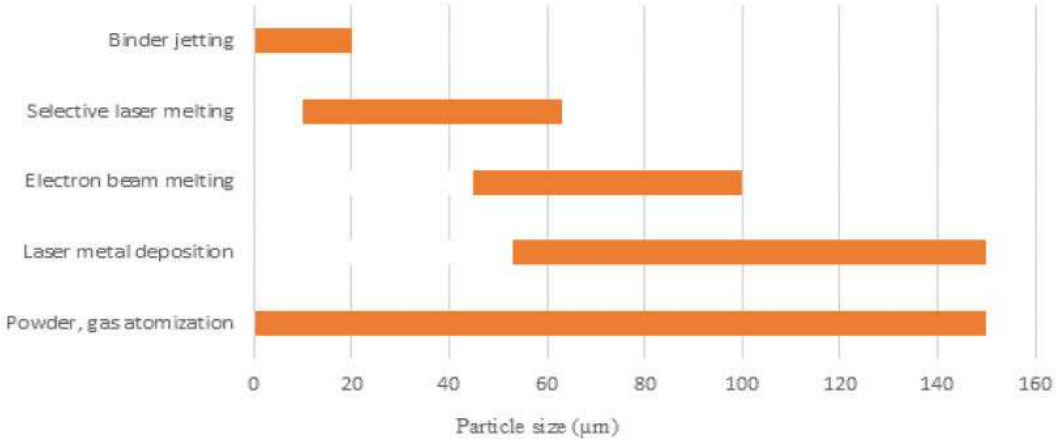

Figure 2-11: Comparison of gas atomized powder size requirements for different AM processes [49].

Table 2-2: Powder characteristics from different manufacturing processes [47].

Manufacturing process	**Particle size range (µm)**	**Advantages**	**Disadvantages**
Water atomization	0 – 500	High production rate, large particle size range, feedstock in ingot form	Post-processing for water removal, irregular particle shape, satellites present, wide particle size distribution
Gas atomization	1 – 500	Wide range of alloys available, suitable for reactive alloys, feedstock in ingot form, high throughput, large particle size range, spherical particles	Satellites present, wide particle size distribution
Plasma atomization	0 – 200	Highly spherical particles	Feedstock must be in a wire or powder form, high cost
Plasma rotating electrode process	0 – 100	High purity powders, highly spherical particles	Low productivity, high cost
Centrifugal atomization	0 – 600	Narrow particle size	Difficulty in making extremely fine powder
Hydride-dehydride process	45 – 500 m	Low cost	Irregular particle shape, limited to metals which form a brittle hydride.

The layer height of the deposited material is dependent on the powder flow rate amongst other process parameters. If the powder flow rate decreases from the set point, the deposition head will "run away" from the part and if the powder flow rate increases from the set point, the part will crash into the head [50]. The powder delivery system consists of powder hoppers, motorized feed mechanisms, powder delivery lines and powder delivery nozzles which are situated on the deposition head [41]. The different powder injection systems in DED processes are shown in *Figure 2-12* and include [51]:

- Off-axis configuration (lateral) – A single powder flow laterally passes through the laser beam.
- Continuous coaxial configuration – Conical powder flow surrounds and interacts with the laser beam.
- Discontinuous coaxial configuration – powders are ejected from different injection nozzles which are distributed around the laser beam and feeds the powder in the path of the laser beam.

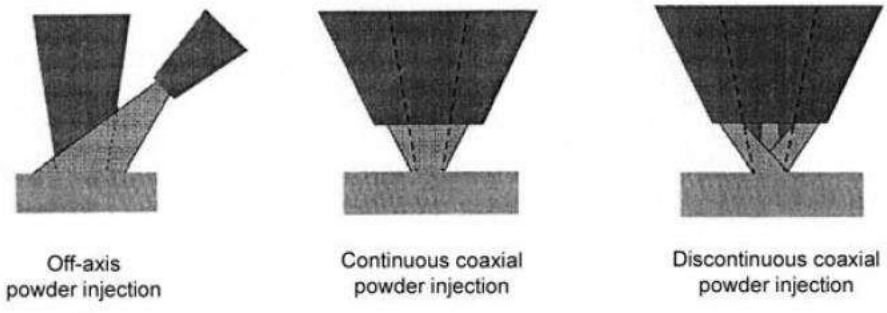

Figure 2-12: Powder injection configurations [52].

The LENS® process uses a discontinuous coaxial powder injection configuration which allows for the fabrication of intricately shaped parts. Both the continuous and discontinuous coaxial powder injection system results in a better powder catchment efficiency than the off-axis powder injection system [53]. The disadvantages of a discontinuous coaxial powder injection system includes a non-uniform powder flow [51], melted powder sticking on to the powder delivery nozzles, powder oxidation prior to deposition and poor laser energy utilization [53]. The powder injection system of the LENS® process is made up of four powder delivery nozzles and a centre purge

nozzle [41] [52] . The function of a centre purge nozzle is to ensure a flow of gas out of the path of the laser beam to prevent the powder from damaging the laser optics [41] [52].

2.2.2.4 Laser and powder interaction

An omnidirectional (from all directions) continuous coaxial powder injection leads to lower powder efficiency as it becomes difficult to achieve a powder focus from behind the melt pool [54]. Omnidirectional powder feed leads to an increase in the interaction between the powder and laser beam above the substrate, which affects powder temperatures, laser beam attenuation and beam intensity distribution at the substrate surface [54]. Pinkerton *et al.* [55] modelled the powder stream from a coaxial nozzle and observed that the powder concentration along the beam axis reached a maximum at the point that the converging annular powder stream from the nozzle merged into a consolidated flow. Beam attenuation increases with distance from the nozzle and on or close to the axis below the plane at which the powder converges into a single stream. In addition beam attenuation also increases with increase in mass feed rate, smaller particles and high laser power [54] [56] [57]. At the consolidation plane where the annular stream merges into a single stream, the average particle temperature is a maximum at the centre of the beam. In a study done by Xiong *et al*. [58] it was observed that the highest laser intensity was achieved at the focal plane. At a working plane below and above the focal plane a decrease in the laser intensity was observed. The spot with high laser intensity was described as the working plane or focal plane of the laser. The spot size of the laser correlates to the laser intensity with a smaller spot size and large spot size relating to both high and low laser intensity respectively.

When looking into the beam-powder interaction it is important to understand the phenomena through which powder is lost in the system and not deposited into the molten pool. Spatter is the reason why not all the powder deposited forms the molten pool, spatter is molten powder droplets which are ejected away from the deposition melt pool. This phenomenon is mostly observed in welding processes due to an erratic arc which could be caused by fast welding speeds or contaminated substrate surfaces. In DED processes spatter is caused by a high energy beam which creates localised heating, the energy in the molten droplet then overcomes the surface tension forces

and becomes ejected away from the molten pool [59]. *Figure 2-13* shows the powder interaction in a coaxial nozzle.

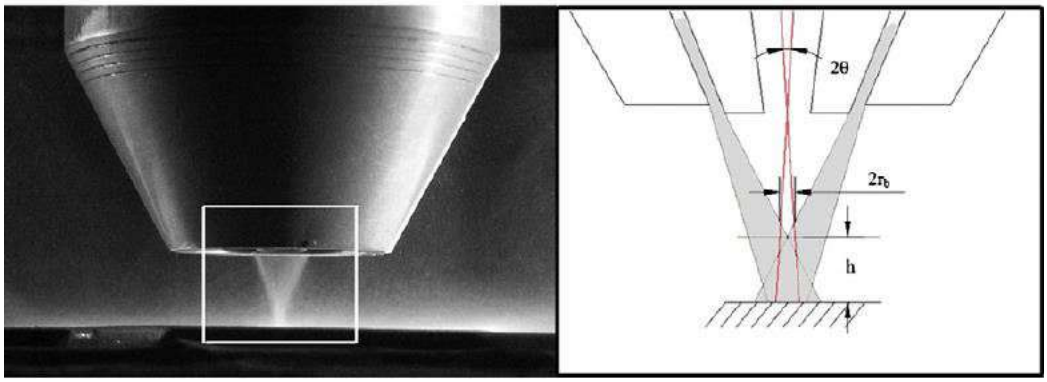

Figure 2-13: Powder flow from a coaxial nozzle [60].

2.2.2.5 Thermal profile in directed energy deposition processes

Similar to welding processes, DED processes are subjected to thermal cycles due to rapid heating and cooling during deposition. In welding, microstructural variation occurs in the weld due to the variation in the heat flow patterns such as heterogeneous solidification which starts from the substrate into the weld. The substrate material is not heated to melting temperature, however, the temperatures reached during welding are sufficient to induce microstructural phase transformation such as grain growth and recrystallisation. *Figure 2-14* shows the metallurgical regions in a weld. The weld zone comprises completely of the molten metal and heat transfer within this region is through convection. The fusion line is the boundary between the un-melted substrate and the solidified weld metal. The HAZ is the most important zone second to the weld metal as most failures occur in this region. This region experiences high temperatures which are capable of causing microstructural changes, but low enough not to cause any melting.

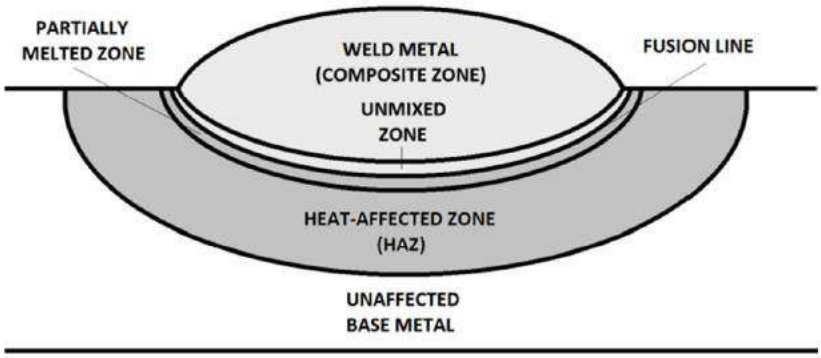

Figure 2-14: Metallurgical zones developed in a weld [61].

The LENS® process uses a laser as the source of energy for melting and the same metallurgical zones are experienced. However, lasers have a low heat input as compared to arc welding processes. *Figure 2-15* shows the energy intensity of lasers compared to other welding processes. The laser's coherent beam allows it to be focused to a small spot, leading to high energy densities [62]. Laser welding has a high energy density compared to other welding processes except for electron beam, but a low heat input, hence leading to faster processing times, narrow HAZ and lower risk of distortion.

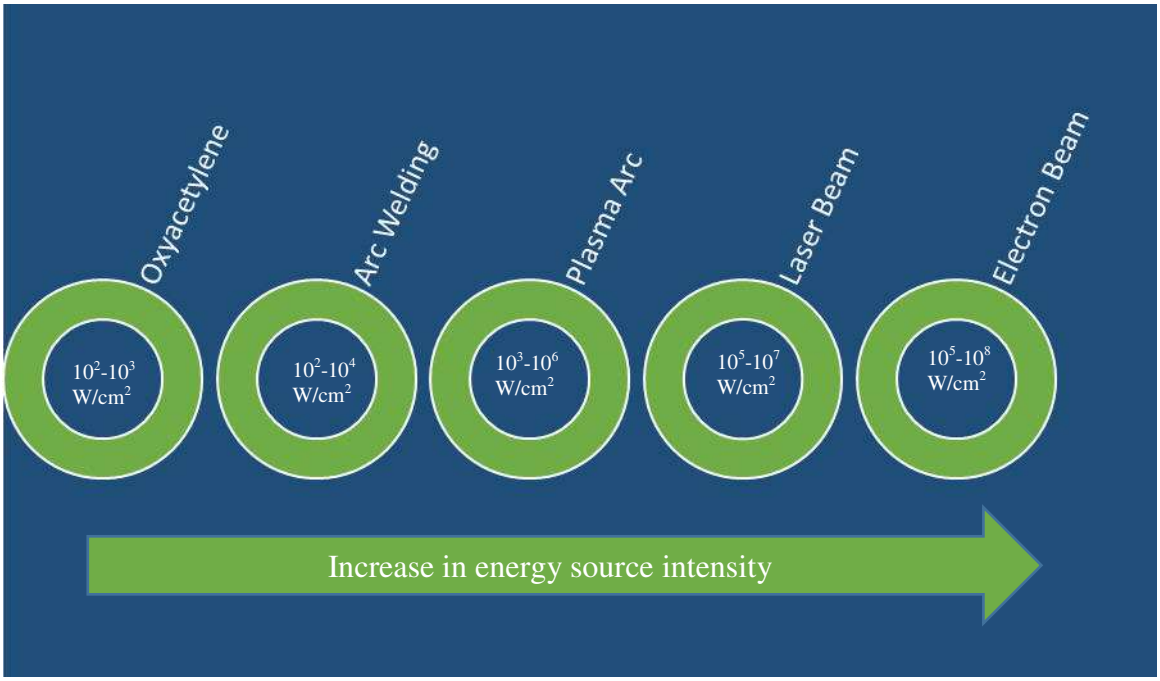

Figure 2-15: Energy intensity of different welding processes [62].

Heat transfer in welding is by conduction of heat from the surface down into the material to produce the molten/weld pool, but heat transport within the weld pool is by convection which dominates other mechanisms [61] [63]. Convective heat loss is directional and changes the shape of the weld pool which was produced by a conduction heat transfer. The heat transfer during laser welding is similar to that of other welding processes and it is mainly divided into two modes namely conduction and the keyhole mode. In the conduction mode the power density is smaller and no vaporisation of the workpiece takes place, whereas the keyhole mode involves the use of high power densities creating a vapour field cavity into the workpiece. It thus becomes clear that the conduction mode is used for laser cladding and hard-facing techniques and the keyhole mode is used for welding thicker materials.

The temperature differences that occur in an arc welding process also occur in the laser welding process and hence the importance of investigating the heat and fluid flow of molten material during deposition is because these dynamics control the solidification of the material. Temperature differences within the molten/weld metal leads to surface tension driven thermo-capillary flow known as Marangoni flow which leads to heat transfer through thermal convection within the molten/weld pool. Convection affects the molten pool shape, aspect ratio, surface ripples and can lead to defects such as lack of penetration, porosity and lack of fusion in both conventional arc welding and laser welding [62]. In addition convection is responsible for molten pool mixing and therefore affects the composition of the molten pool.

If surface tension exists on a surface of a liquid, fluid will be drawn along the surface from regions of low surface tension to those of high surface tension. Surface tension is temperature dependent and decreases with an increase in temperature so the centre of the molten pool experiences the high temperatures and hence the lowest surface tension. The temperature away from the centre of the molten pool is the lowest hence this region has high surface tension [61]. Hence, fluid flow will be from the centre of the molten pool outwards, this is called a divergent flow as seen in *Figure 2-16*.

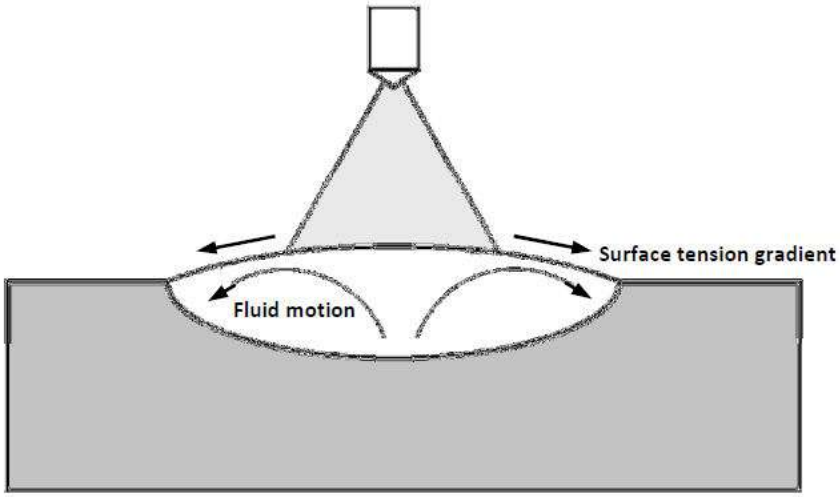

Figure 2-16: Divergent Marangoni flow [61].

Elements such as sulphur and oxygen segregate to the surface of the liquid metal and lower the surface tension. Thus the surface tension of the liquid-metal surface will be lower than the molten pool centre thus leading to a convergent Marangoni flow as shown in *Figure 2-17*. Convergent Marangoni flow leads to deeper penetrations in comparison to divergent flows.

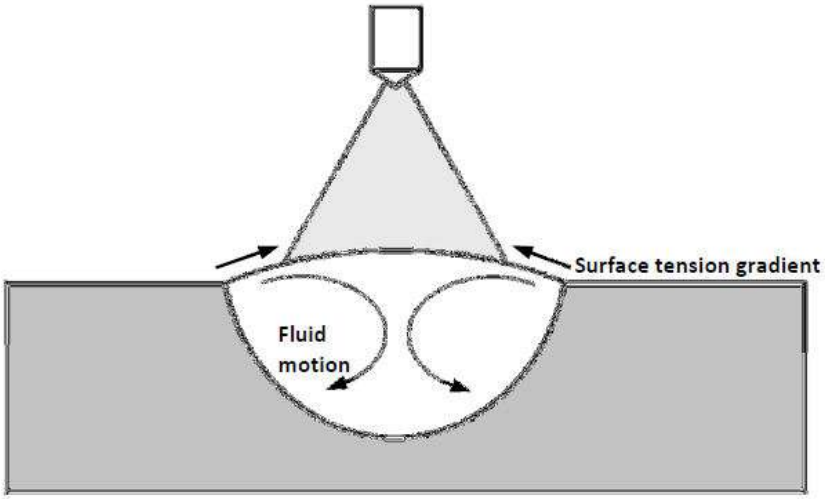

Figure 2-17: Convergent Marangoni flow [61].

2.2.2.6 Porosity and cracks

The disadvantage of the LENS® and other DED processes include microstructural defects in the form of pores between the deposition layers, giving rise to non-fused layers during fabrication thus reducing mechanical properties [43]. In addition

components produced by the LENS® process display a rough surface finish (5-7.6 micrometres) and hence post processing is required in order to achieve the desired net shape and surface finish since a material envelope remains after the deposition [43]. The porosity in AM parts can result from the process itself or from the inherent porosity in the feedstock powders [48]. The LENS® process uses an inert gas to transport the feedstock powder to the deposition area, in a gas assisted powder transfer, the gas jet delivers the powder while minimising oxidation of the molten metal at the same time. The LENS® machine consists of an argon gas circulator which maintains an inert atmosphere, preventing oxidation of reactive materials and porosity. Porosity can be categorised as gas and lack of fusion porosity [64], *Figure 2-18* shows the different types of porosities in AM. Gas porosity in AM parts can result from porosity present in the feedstock powder or from the manufacturing process itself. Inherent porosity in the feedstock powder is normally caused by entrapped atomization gases [48], however it has been seen that baking the feedstock powder before deposition reduces the formation of spherical pores on the final deposited product [65]. It has been observed that the method of controlling porosity through AM process parameters is by increasing the heat input which reduces the solidification rate and hence allowing the gas bubbles to escape into the environment before the molten pool solidifies.

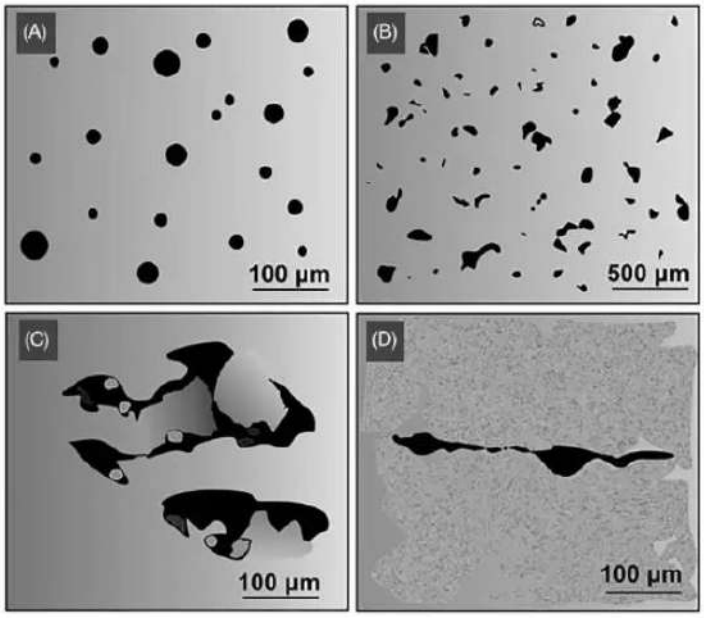

Figure 2-18: Characteristic pores in laser-based powder bed fusion parts: (A) entrapped gas porosity; (B) incomplete melting-induced porosity, (C) lack of fusion with un-melted particles inside large irregular pores and (D) cracks [64].

Ng *et al.* [66], investigated porosity in the DED laser deposition of gas atomized nickel-based Inconel 718. In this study lack of fusion porosity was defined as angular porosity that is found in the intersection between the deposited tracks. Gas porosity was defined as spherical porosity caused by gas entrapment and confined in any location of the deposited material. It was established in this study that the factors affecting lack of fusion porosity were traverse speed, powder feed rate and deposition track overlap. Lack of fusion porosity was seen to reduce with an increase in traverse speed. This was not expected as increased traverse speed leads to a decrease in the heat input into the molten pool and the reduction in heat input would lead to an increase in the lack of fusion, however this is contrary to what is expected. An increase in the traverse speed also leads to less powder delivered into the molten pool. This study clearly showed that porosity is more dependent on the amount of powder delivered into the molten pool than the reduction of heat input. The increase in the powder feed rate significantly increased the lack of fusion porosity and an increase in the deposition track overlap also resulted in an increase in the lack of fusion porosity but was less significant than the powder feed rate and traverse speed.

Ng *et al.* [66], further observed that the gas porosity present in the deposited material had a diameter bigger than the largest particle in the feedstock powder blend, which suggest that entrapped gas bubbles in the deposited material agglomerated and coalesced in the melt pool hence it was concluded that the gas porosity in the powder could not fully account for the gas porosity found in the deposited material. Gas porosity was seen to increase with the powder feed rate and shielding gas. During powder deposition when the powder interacts with the molten pool, shielding gas can become entrapped in the process. An increase in laser power was also seen to increase the gas porosity and this was due to the molten pool fluid flow dynamics known as the Marangoni flow which has an influence not only on the molten pool geometry but also on the formation of defects such as lack of fusion and gas porosity. The convective Marangoni flow was seen to be responsible for depositing gas bubbles at the bottom of the melt pool and cause agglomeration of gas bubbles resulting in coalescence and the

creation of large gas pores. *Figure 2-19* shows the influence of parameters on lack of fusion and gas porosity.

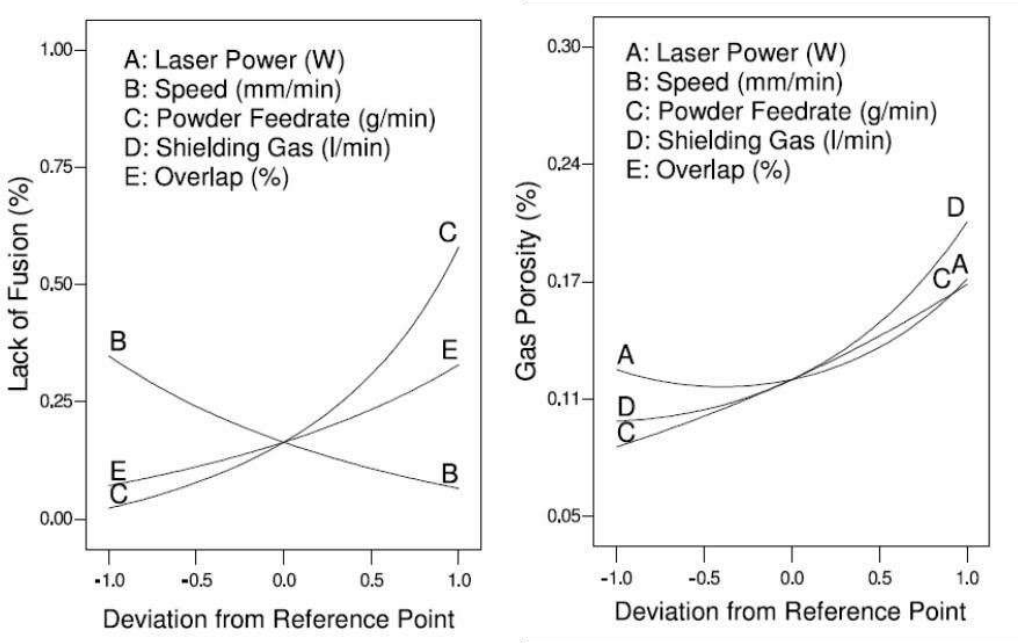

Figure 2-19: Influence of process parameters on lack of fusion and gas porosity [66].

Ferguson *et al.* [67], investigated the influence of process parameters namely traverse speed and powder flow rate on the gas and lack of fusion porosity of AISI 420 and AISI 4140 steels deposited by the LENS® process. It was established from this investigation that the vast majority of the observed porosity was from lack of fusion as this type was irregular in shape, however, gas porosity was also found. There was a maximum powder feed rate that allowed for the deposition of fully dense samples above which porosity was seen to increase with an increase in powder feed rate. *Figure 2-20* shows the influence of powder feed rate and linear mass density (which is powder feed rate divided by the traverse speed) on the porosity in the deposited material.

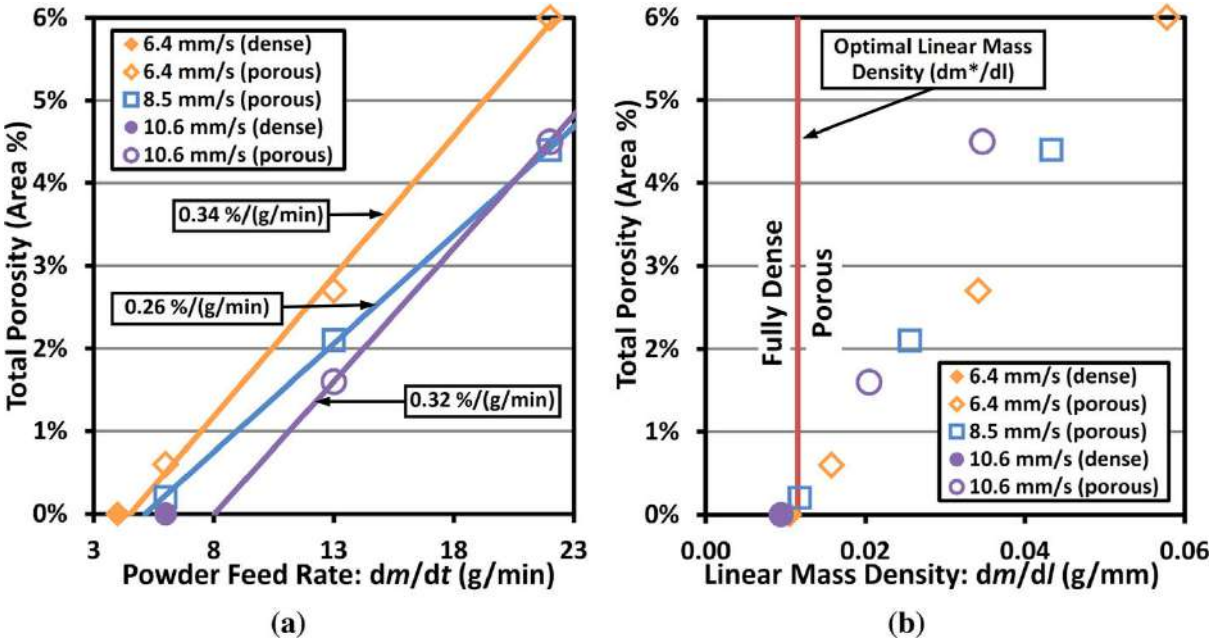

Figure 2-20: Changes in porosity with: (a) powder feed rate, (b) linear mass density for various velocities in AISI 420 stainless steel [67].

Gong *et al.* [68], carried out experiments on the deposition of Ti-6Al-4V parts using the SLM and electron beam melting (EBM) process in order to analyse the defect characteristics at different process parameters and system conditions. It was observed that gas porosity increased with a decrease in the scan speed, hence an increase in the heat input. In contrast it was also observed that an increase in the scan speed resulted in an increase in the lack-of-fusion porosity due to insufficient heat input. These results from Gong *et al.* [68] were graphically represented by Tang *et al.* [69], in *Figure 2-21*. It was established that for porosity creation there are process windows divided into melting zones, namely; fully dense (zone I), over melting (zone II), incomplete melting (zone III) and over-heating (zone OH), *Figure 2-22*. Hence porosity is not linearly related to energy density. Porosity free samples could only be fabricated in zone I. Zone II and zone III parameters were capable of building Ti-6Al-4V samples, but the samples contained measurable porosity. Zone OH led to the formation of unusable parts.

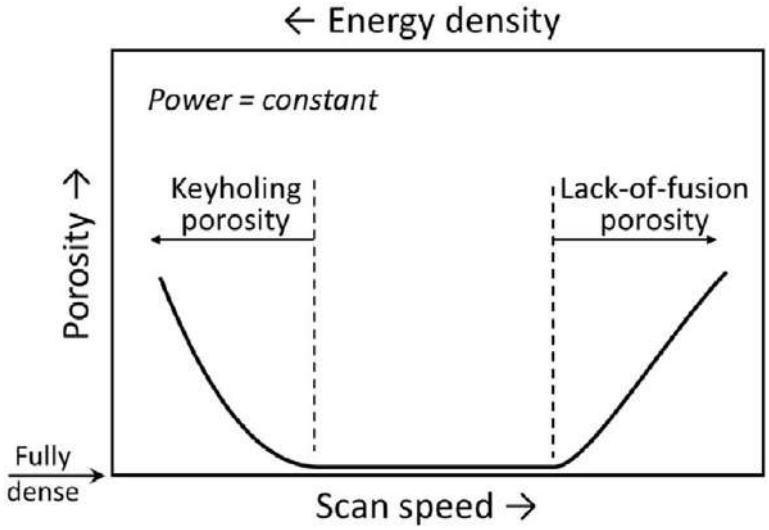

Figure 2-21: Influence of scan speed and energy density on porosity [69].

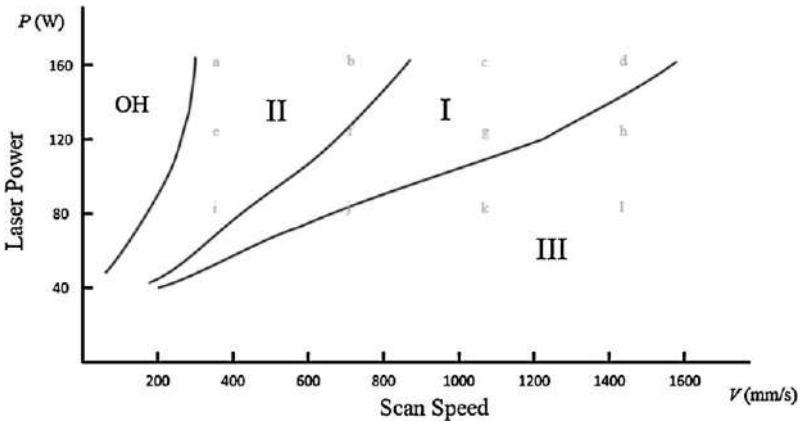

Figure 2-22: Process window for SLM of Ti-6Al-4V [68].

Delamination is a cracking phenomenon whereby there is a separation of adjacent layers due to incomplete melting between layers, (*Figure 2-23*) [48]. Delamination is macroscopic and no post-processing or repair can mitigate it. Substrate preheating has been seen to reduce macroscopic cracking.

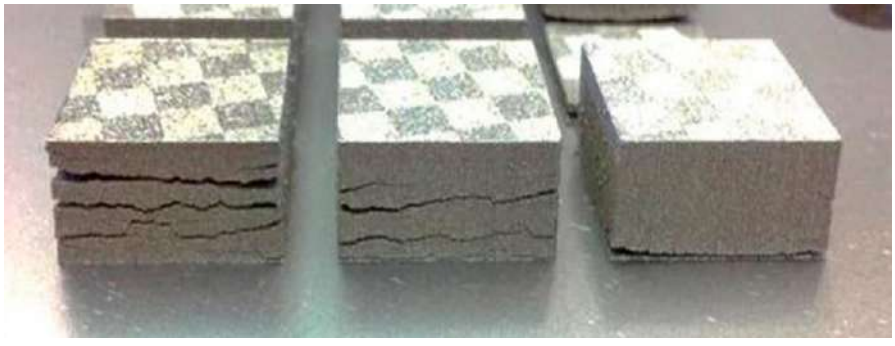

Figure 2-23: Layer delamination and cracking [48].

2.2.3 Additive manufacturing of hardmetals

There has been a few studies on the applicability of AM of hardmetals. Xiong, *et al*. [8] [58] [70] [71] [72], studied the microstructure, hardness, effect of process parameters, influence of working distance, thermal behaviour and comparison between sintering and LENS® deposition of hardmetals by the LENS® 750 system (OPTOMEC, Albuquerque, NM, USA). It was established that the microstructure of hardmetals deposited by the LENS® process were denser than those manufactured using the sintering process [71], as shown in *Figure 2-24*. The microstructure was composed of alternating layers composed of fine and coarse grains, and this was attributed to layer re-melting during subsequent deposition [8].

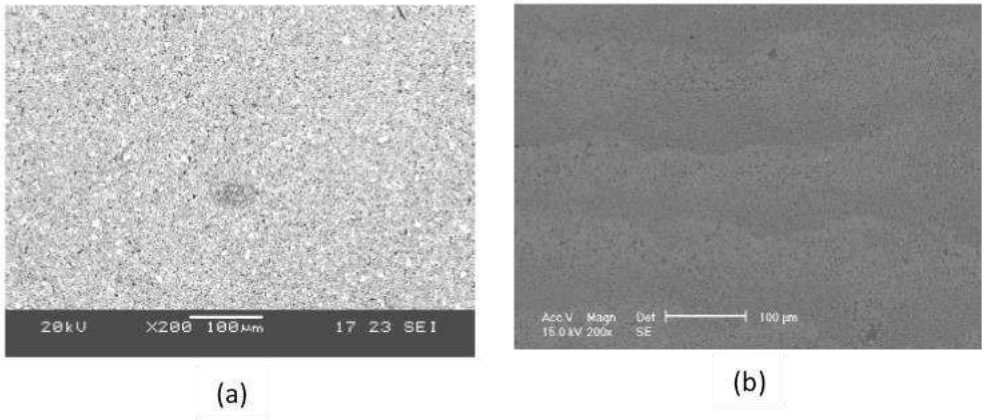

Figure 2-24: SEM images of: (a) sample sintered at 1450 °C for 1 hour with a few pores; (b) Laser deposited sample at 200W showing a dense microstructure [71].

The hardness profile was seen to increase from the top to the bottom of the sample, with the last to be deposited layer displaying the lowest hardness (*Figure 2-25*). This was attributed to the change in cooling rate along the sample height, whereby cooling rate decreases with the height of the sample being deposited. In addition LENS® deposited hardmetals had a hardness and fracture toughness superior to that of sintered hardmetals [71].

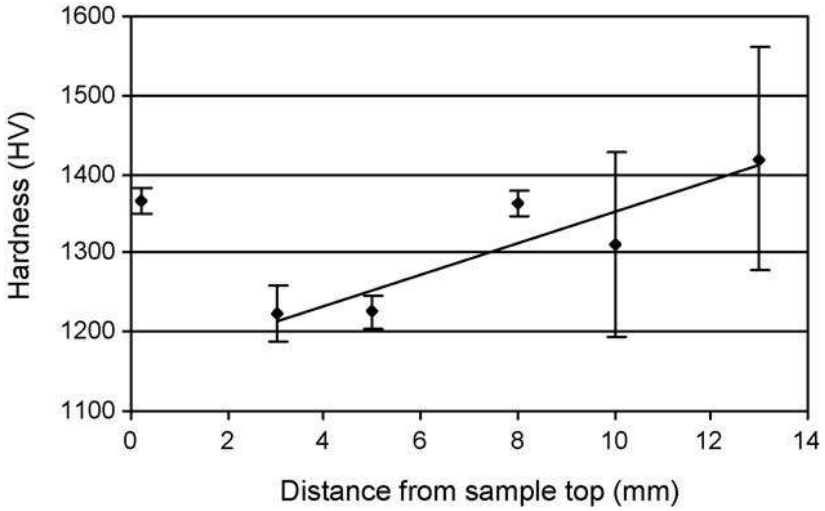

Figure 2-25: Hardness profile of a LENS® deposited hardmetals [8].

Process parameters such as laser power, powder feed rate, traverse speed and working distance were found to have an impact on the profiles and microstructures of the LENS® deposited hardmetals. Sample height (deposition height from the first layer deposited on the substrate to the last layer) increased with an increase in laser power and powder feed rate, however sample height decreased with traverse speed [70]. A shorter work distance and hence lower laser intensity resulted in improved specimen density and microstructure. *Figure 2-26* and *Figure 2-27* show the deposited sample height as a function of process parameters.

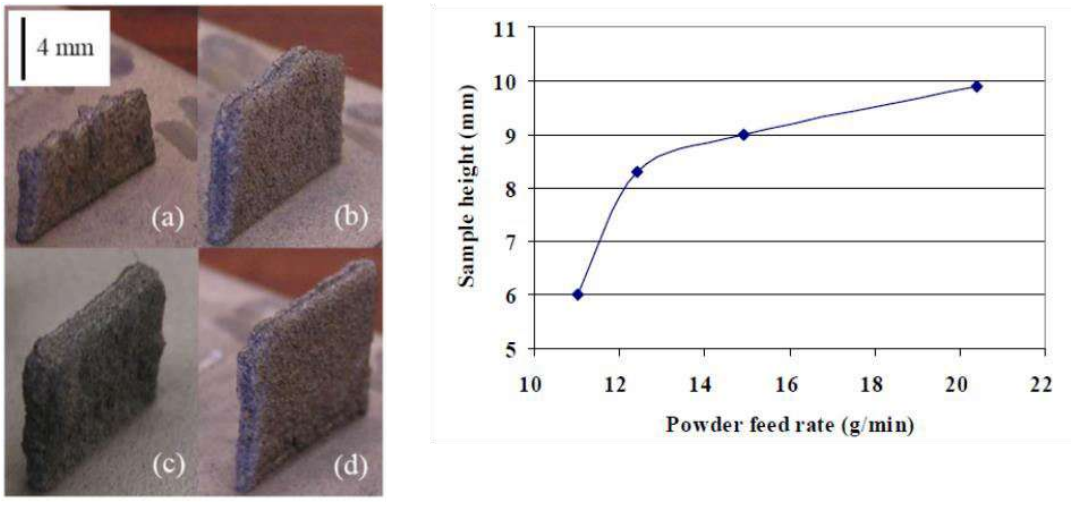

Figure 2-26: Influence of powder feed rate on sample height: (a) 11 g/min, (b) 12.4 g/min, (c) 14.9 g/min, (d) 20.4 g/min [70].

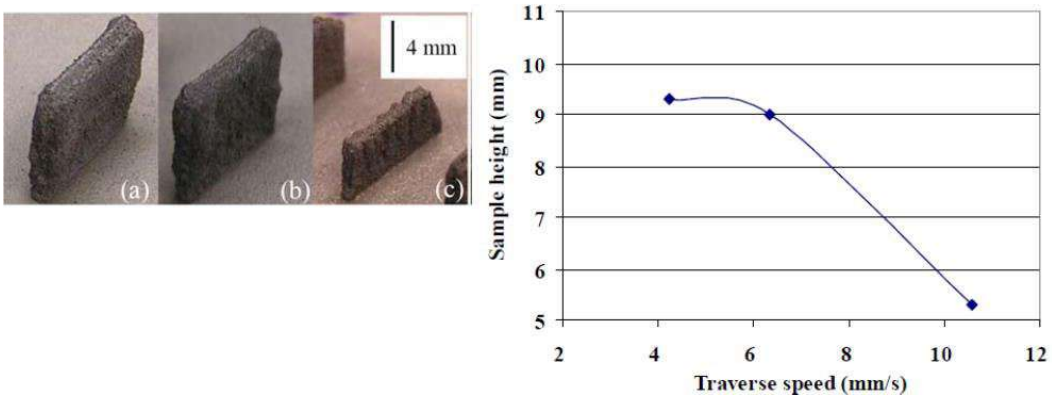

Figure 2-27: Influence of traverse speed on sample height: (a) 4.2 mm/s, (b) 6.4 mm/s, (c) 10.6 mm/s [70].

The influence of working distance on LENS® deposited hardmetals was investigated and it was established that a working distance longer than the focal plane leads to a defocused laser beam which has low laser intensity and less powder-laser interaction resulting in the deposition of materials with low height measurements. The same applies to a working distance shorter than the focal plane. In order to achieve the greatest laser-powder interaction the working distance should be at the focal plane, however a homogeneous microstructure was observed at a short working distance and particle coarsening was not significant [58]. *Figure 2-28* shows the relationship between working distance, laser spot size, laser intensity and laser powder interaction.

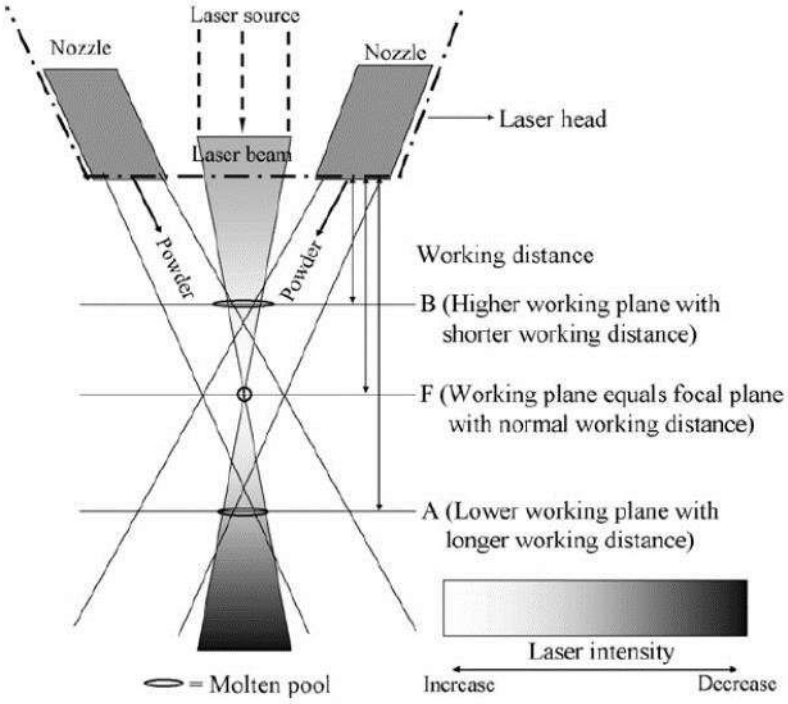

Figure 2-28: Relationship between laser intensity, laser spot size and working distance [58].

The thermal behaviour within hardmetals during LENS® deposition was studied using a high-speed digital camera system and a 3-dimensional Finite Element Method (FEM) [72]. Thermal imaging was used to observe the area and length of the molten pool together with the highest temperatures reached in the molten pool. *Figure 2-29* shows the thermal measurement layout. It was established that the area and length of the molten pool, together with the highest temperature increased with sample height. A swirling phenomenon was observed in the molten pool and this was associated with movement of solid WC particles. The highest cooling rate was observed near the solid-liquid interface (this is at the substrate and deposition layer interface). This study further established the re-melting phenomenon. When one layer is deposited, re-melting occurs in the top portion of the previous layer, which results in coarsening of the WC particles. The bottom portion of the previous layer is only reheated which does not result in grain growth. *Figure 2-30* shows the thermal image of LENS® deposited hardmetals from the 5th layer deposited, it is clear that the highest temperatures are experienced in the centre of the molten pool. However, when the 30th layer was deposited, the highest temperatures were not experienced in the centre of the molten pool as expected due to the swirling effect.

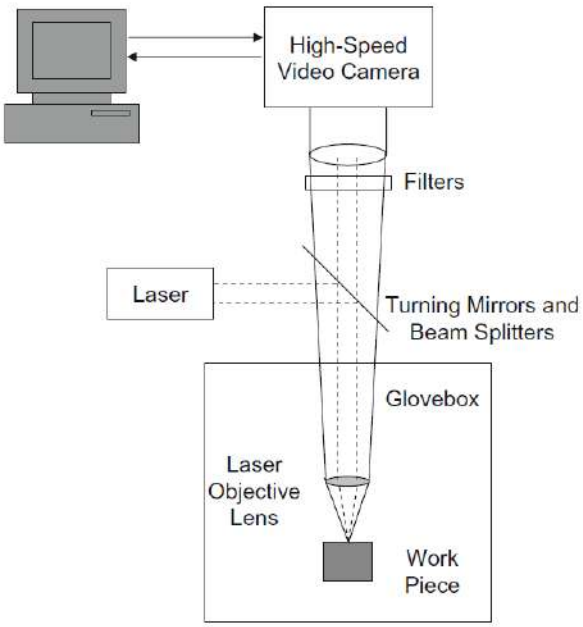

Figure 2-29: Experimental setup showing the thermal measurement system [72].

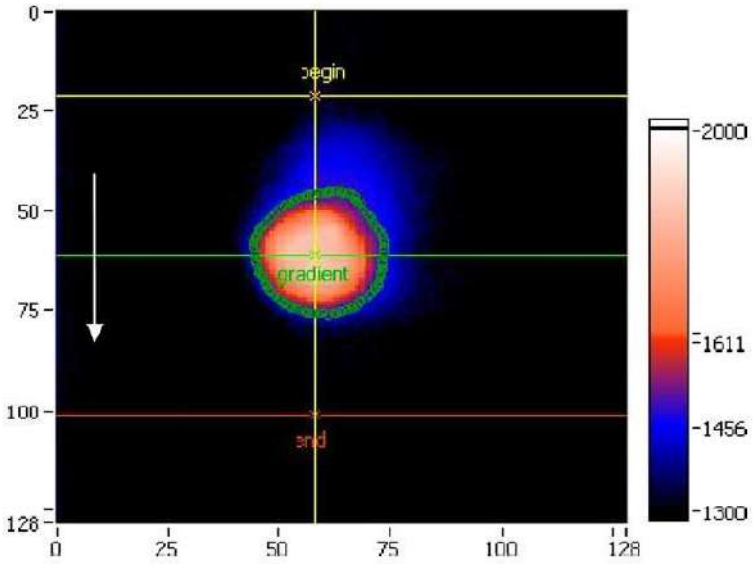

Figure 2-30: A thermal image of a WC-Co thick wall sample [72].

Li *et al.* [73] studied the microstructural evolution of WC-Ni hardmetals fabricated by selective laser melting (SLM) process. The microstructure was composed of a few round-shaped spheres which were un-melted WC. A dendritic microstructure was also observed which was formed after solidification of molten carbides and binder phase, in addition to that faceted carbides were observed around the un-melted spherical WC and throughout the matrix.

During selective laser melting (SLM), high power laser scanning melts both the WC and the binder phase, however un-melted spherical WC also exists. During solidification M_2C dendrites form with face centred cubic (FCC) metal in the inter-dendritic regions, prismatic MC carbide precipitates not only in the dendritic regions but also around the un-melted WC/W_2C particles [73]. Li *et al.* [73] also reported the presence of the eta (η) phase within the repeated heating zone and this was attributed to laser scanning overlaps. A rapid cooling rate was seen to limit the formation of the η phase. *Figure 2-31* shows the different microstructural phases in a WC-Ni-alloy sample deposited by SLM.

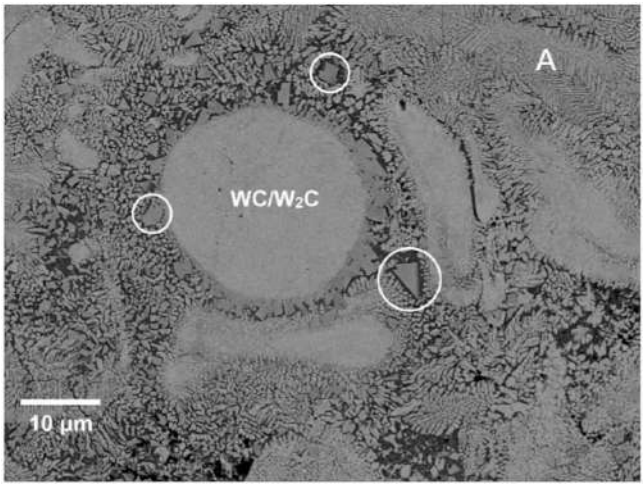

Figure 2-31 : BSE image of the as-built sample showing round shape un-melted WC/W2C particle, prismatic carbide (circled), dendritic carbide (site A), and Ni binder (dark grey regions) [73].

In an additional study done by Li *et al.* [74] on the microstructural characteristics of WC-NiAlCuCrCuFe fabricated by the SLM process, it was established that the microstructure of the hardmetal was heterogeneous from the substrate to the top surface of the built (along the height of the build). The top surface which is the last to solidify was composed of W_2C/metal binder dendritic colonies within the molten pools, un-melted carbide powders were hardly seen (*Figure 2-32*). This is evidence that the high power laser could fully melt WC/W_2C powders within the molten pool. The microstructure analysis from the top surface of the build towards the substrate showed a different layer of coarse W_2C/metal binder dendritic structure and this region was identified as the HAZ, no η phases were present in this region. The heterogeneity in

the microstructure along the SLM build correlated with the variation in composition along the sample build from the substrate/sample interface to the top surface. Evaporation and dilution were seen to be the main mechanisms controlling composition variations. Binder phases namely Ni, Fe, Co and Cr, were seen to decrease along the build direction due to evaporation hence W was seen to increase along the build direction. The presence of W_2C dendrites in the molten pool shows that during SLM the melting point of W_2C (3003 K) is reached, hence the vaporization of the binder metal is possible.

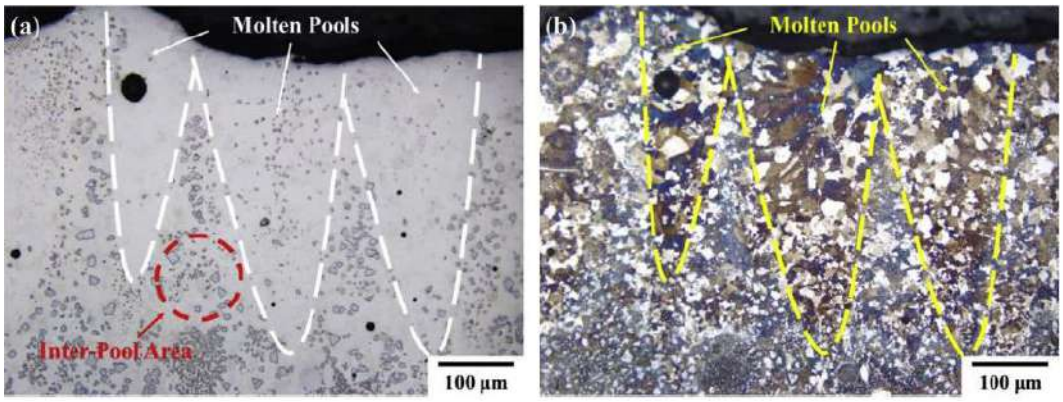

Figure 2-32: (a) As polished, (b) etched, optical micrograph of the hardmetal top surface [74].

Uhlmann *et al.* [75], studied the process behaviour of WC-Co material fabricated using the SLM process, it was observed that a reduction in the energy input when depositing WC-Co using the SLM process resulted in an increase in porosity. An increase in the laser power was seen to result in a decrease in porosity due to the closing of cavities from the continuity in the melt pool but also resulted in the evaporation of Co. A reduction in the traverse speed was seen to expand the melt pool through the increase in the energy input and thus resulted in an increase in the density of the material. The increase in the degree of overlap between individual deposited tracks led to the reduction in porosity. All fabricated samples showed a tendency of cracking regardless of the process parameter combinations. Uhlmann *et al.* [75], did not qualify the porosity in terms of lack of fusion and gas porosity and the findings of their study contradicted that of Ng *et al.* [66] in terms of the relationship between porosity and laser power.

Picas *et al.* [76], investigated the wear behaviour of WC-Co coatings using three consolidation methods, namely, high velocity oxy-fuel (HVOF) spray, spark plasma sintering (SPS) and the LENS® process. The HVOF coating displayed the highest density, while the SPS displayed higher porosity than the HVOF and LENS® coating. The microstructure of the LENS® coating showed a bimodal structure consisting of both fine and coarse grains. The HVOF and SPS coatings had a better wear resistance than the LENS® coating and this was due to the limited melting and heating time during the LENS® process resulting in lower cohesion of the WC particles within the coating.

High temperature deposition processes such as AM and welding easily generate cracks due to the large temperature gradient from the rapid heating/cooling cycle, the difference in properties of the materials to be deposited and the substrate and the different coefficient of thermal expansion of the composites to be deposited. The initiation sites for some cracks are macro-pores which are present within the deposited materials, these cracks are due to thermal stresses generated in the material during cooling [77]. WC is known to be brittle due to its high hardness and hence has a high cracking susceptibility. Susceptibility to cracking is seen to decrease with the application of preheating, addition of alloying elements and laser re-melting which involves shutting down the powder supply while the laser is still on. Laser re-melting leads to melting of the top layer to form a molten pool, and un-melted particles can be melted into the molten pool. In this way the surface quality and properties of cladding coatings are improved.

Dai *et al.* [78], studied the effects of re-melting, heat treatment and the additions of alloying elements namely Co on the cracking susceptibility, microstructure and mechanical properties of WC/Fe laser cladding coatings. Laser re-melting was seen to reduce cracks on the surface, reduce porosity and remove non-melted surface particles. In addition laser re-melting gave rise to a smooth coating. During laser re-melting the temperature of the laser coating and substrate is higher than the laser cladding process, this thus results in lower cooling rates thus reducing the thermal stress which lowers the cracking susceptibility. *Figure 2-33* shows the benefits of laser re-melting.

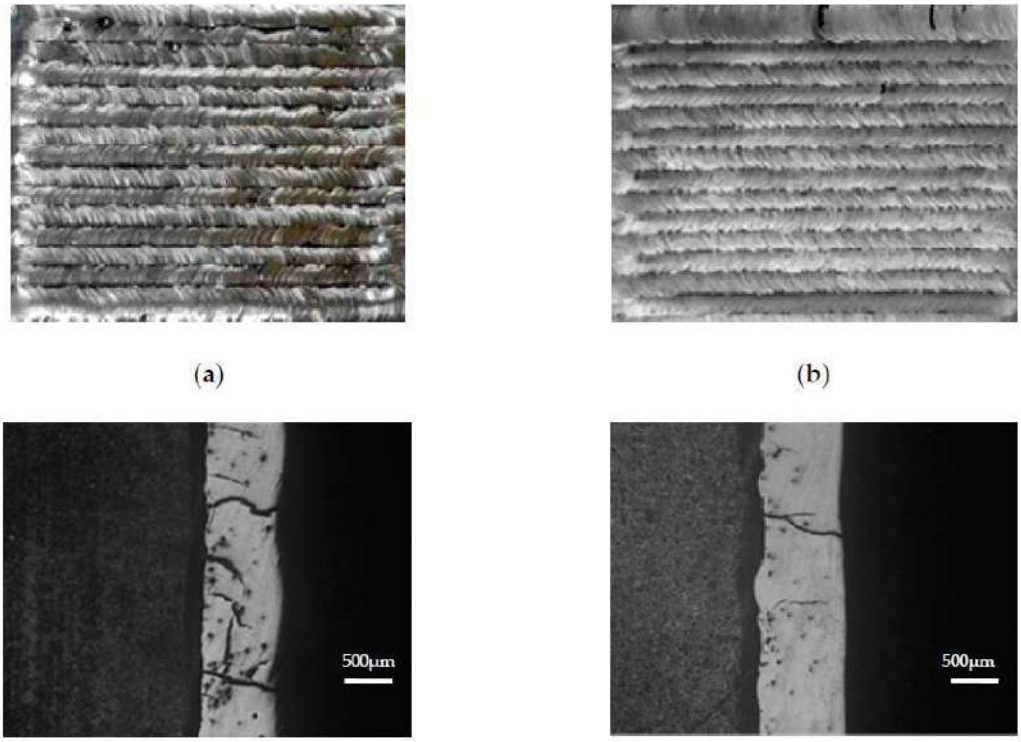

Figure 2-33: Morphology of the coatings; (a) before laser re-melting, (b) after laser re-melting [78].

Grain growth was observed at the surface where laser re-melting was carried out as expected, because at high temperatures and lower cooling rates grain growth is expected. Laser re-melting was however seen to reduce the surface hardness, but the hardness was more uniform in comparison to the coating which did not undergo laser re-melting. Preheating was seen to reduce the number of cracks on the coating, with an increase in temperature leading to a reduced number of cracks. The initial cracks present were wide and perpendicular to the coating-substrate interface and propagated throughout the entire coating, by preheating, the temperature gradient is reduced and cooling rate is reduced and thermal stresses are relieved. Annealing of the coating had no obvious impact on the formation of cracks because annealing is applied after the cladding when the cracks have already formed.

Dai *et al.* [78], also showed that even though laser re-melting and preheating reduced the amount of cracks, these methods could not completely eliminate the cracks. The addition of 8 wt% Co was seen to give rise to a crack free WC/Fe coating. An increase in the Co addition was also seen to increase the transverse rupture strength of the coating. Luenda *et al.* [79] applied a maximum preheating temperature of 350 °C in

the laser cladding of WC reinforced Ni because at high preheat temperatures (700 – 800 °C) it was observed that the laser head could not withstand the heat from preheating and the cladding process itself. However, a preheat temperature of 350 °C was not high enough to produce crack-free coatings. The use of a buffer layer was carried out using a Ni alloy, the buffer layer was deposited between the base metal and hard coating, however, the Ni buffer did not yield crack free coatings. Even though preheating and the use of a buffer layer did not avoid cracks individually, the combination of both produced crack free coatings.

The crack formation in WC particles reinforced Fe-based (316 L stainless steel) metal matrix composites deposited using the laser melting deposition was studied by Wang *et al.* [80]. It was established that the micro-cracks and macro-cracks all crossed through the WC particles and these cracks were perpendicular to the laser scanning direction. The investigation showed that the cracks initiated inside the WC particle, this can be explained by the induced volume contraction of the composite when cooling to room temperature. Thermal stresses are induced by the high temperature gradients during laser melting deposition and the different coefficients of thermal expansion between WC and the matrix. The cracks did not initiate at the 316L stainless steel, because of its high toughness and ductility, however, thermal stresses were generated in the WC particles because the coefficient of thermal expansion of WC particles is lower than that of 316L stainless steel. When the thermal stresses were larger than the yield strength of WC, micro-cracks formed and propagated through the WC particles. High traverse speeds were also seen to induce high thermal shock which caused crack initiation and propagation. *Figure 2-34* shows the crack initiation sites and propagation path.

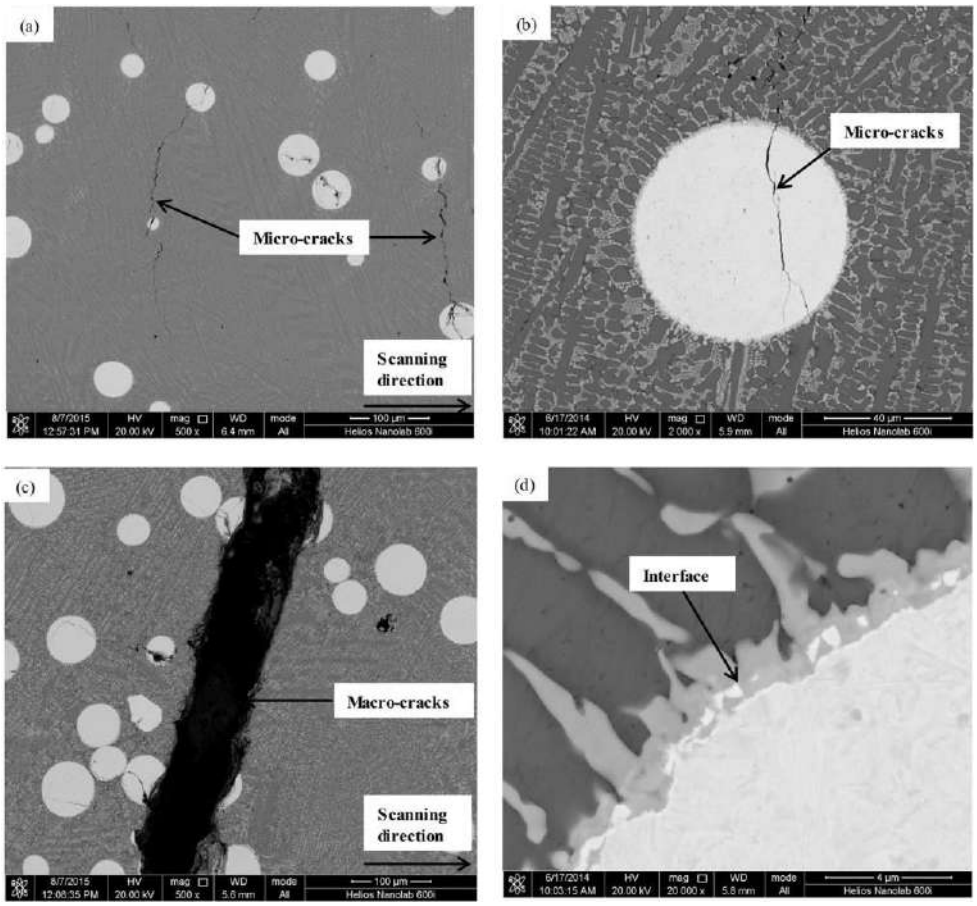

Figure 2-34: (a) Micro-cracks cross through WC particles, (b) micro-cracks inside the WC particle, (c) macro-cracks cross through WC particles, (d) high magnification of (b) [80].

Fracture toughness is the resistance to crack propagation. Unlike hardness, fracture toughness of hardmetals is difficult to evaluate because of their brittle nature. The methods used for the evaluation of the toughness of hardmetals include the Palmqvist indentation method or the impact strength test on plane or notched bars [81]. The Palmqvist method is a non-destructive indentation method which measures the toughness by calculating the total length of cracks emanating from the corners of a Vickers hardness indentation [82]. The fracture toughness value of hardmetals is within the range of 6 – 25 MPa.m$^{1/2}$ [24]. The fracture toughness of WC-12 w.t% Co is ~ 14.3 MPa.m$^{1/2}$ [83], that of WC-10 w.t% AISI304 was found to be in the range of 8 – 10 MPa.m$^{1/2}$ [84] and WC-30 w.t% FeCr (2% additional carbon) was found to be between 11 and 12 MPa.m$^{1/2}$ [85]. The fracture toughness is normally inversely proportional to the hardness [86]. *Figure 2-35* shows the Palmqvist cracks on the corners of WC-Co materials.

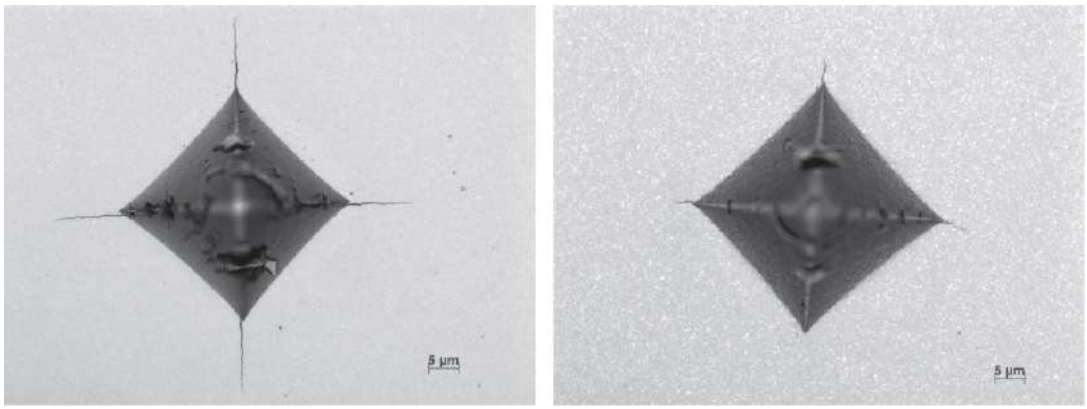

Figure 2-35: Vickers indentation and Palmqvist cracks on hardmetal [81].

2.3 Binder Systems for Hardmetals

It is well-known that the binder system in hardmetals plays a significant role in the microstructure, properties and performance. Although Co is the most commonly used binder for WC, both Ni and Fe have found increasing application as a binder for hardmetals. In the current study a martensitic stainless steel binder was selected and hence the Fe-based binder system is reviewed in this section. However, a brief overview of both the Co and Ni binder systems is first provided.

The binder phase in hardmetals is ductile and offer the toughness required in load bearing circumstances. The binder phase absorbs the plastic deformation avoiding fracture of the reinforcement material. The reinforcement material is normally a refractory metal which is hard and has low ductility. In hardmetals, binders such as Co, Fe, and Ni have been investigated with Co displaying the best wear resistance, fracture toughness and hardness.

2.3.1 Cobalt binders

Following the commercial inception of hardmetals in 1927 [18], cobalt (Co) has been the dominant binder metal due to its good wetting and adhesion characteristics with WC. There are two allotropic forms of Co, namely, a low-temperature hexagonal closed-packed (HCP) phase and a high-temperature metastable face centred-cubic (FCC) phase with a phase transition at ~ 415 °C [28]. This phase transition of Co in

hardmetals, however, relies on the WC content with the transition temperature increasing with the WC content. The grain size affects the stability of these two allotropes, with fine grained Co favouring a metastable FCC structure, Co powders could hence maintain a FCC structure at normal temperatures in combination with a HCP structure [20]. This phase transition of Co with temperature is responsible for the work-hardening capabilities. It has been observed that although Co comprises of the same amounts of the HCP and metastable FCC phases, during milling the amount of the HCP phase increases to 100%, which is evidence of work hardening.

The physical and mechanical properties namely density, compressive strength, relative adhesion resistance, modulus of elasticity and density decreases with an increase in the Co content of the hardmetal [28]. Contrary to that, the transverse rupture strength and coefficient of thermal expansion increases with an increase in the Co content [28]. The properties of Co as a hardmetal binder are:

a) Co has a high melting point of 1493 °C.
b) Co has excellent strength at high temperatures.
c) Co is capable of forming a liquid phase with WC at temperatures of ~ 1275 °C
d) Co is capable of dissolving WC and forms a eutectic mixture with WC at 1275-1350 °C.
e) During cooling WC re-precipitates in the Co matrix rendering high hardness and toughness.

WC-Co for machining applications generally contains 3-12% Co and the carbide grain size ranges from 0.5 to more than 5 µm [87]. *Figure* 2-36 shows a micrograph of a WC-Co hardmetal where the white areas display the Co matrix.

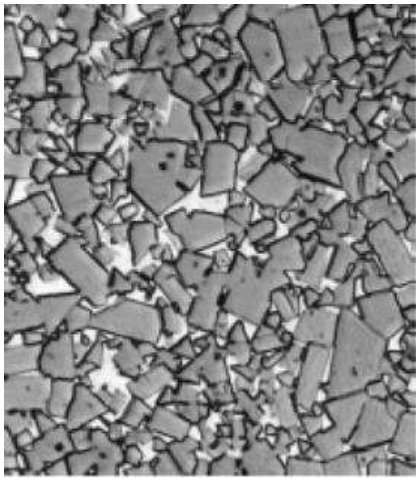

Figure 2-36: WC-Co hardmetal [88].

2.3.1.1 Co global supply and price

The Democratic Republic of the Congo (DRC) is the largest worldwide producer of Co, accounting for over 55% of global Co production in 2016 [89]. The political unrest in the DRC has affected mineral reserves which are now inaccessible [90] and following the 1978 Co crisis which was due to civil wars, unethical mining relating to human rights and infrastructure issues to name a few, this resulted in an increase in Co prices [12] [89]. According to the 2011, 2014 and 2017 study conducted by the European Commission, Co has been identified as a critical raw material in terms of supply and economic importance [91]. *Figure 2-37* shows Co position in the European Commission criticality list conducted in 2017, and *Figure 2-38* shows historical mine production and cost of Co.

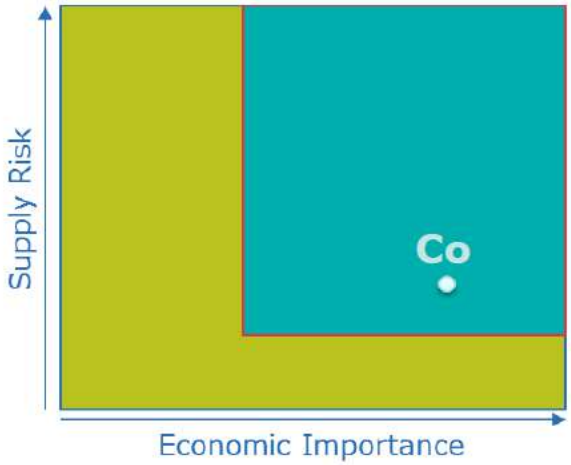

Figure 2-37: Position of cobalt in the European Commission criticality list in 2017, where blue represents critical raw material on the basis of economic importance and high supply risk and green represents non-critical raw material [89].

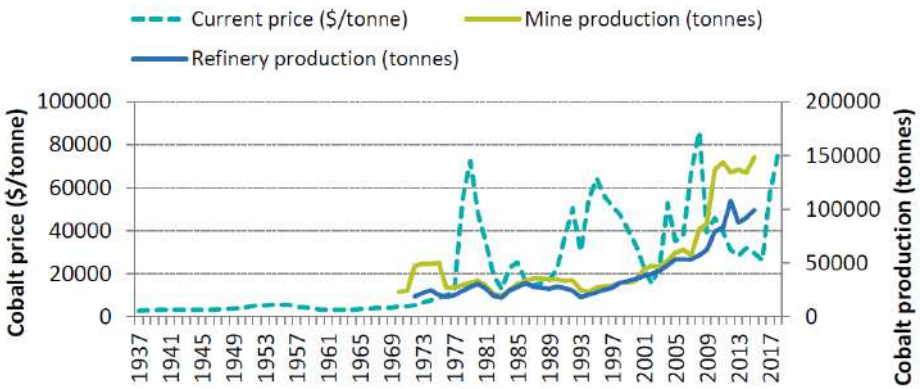

Figure 2-38: Mine production and price of Co [89] [92], [93].

2.3.1.2 Carcinogenicity of Co

There have been issues raised around occupational diseases associated with exposure to Co such as hardmetal diseases. Due to limited data on the toxicity and carcinogenicity of Co, in 2014, the Cobalt Development Institute and the United Auto Workers conducted research into the toxicity of inhaled Co since this is the most common route of exposure to Co metal dust in occupational setting in humans [11]. For the purpose of the research, male and female rats were used in inhalation tests of various Co concentrations. It was established from these tests that all groups of male and female rats exposed to Co metal had incidence of lung neoplasms, inflammation,

fibrosis and hyperplasia of the nose and lung. In addition there was also increased incidence of pheochromocytomas of the adrenal medulla in both male and female rats [11]. It can thus be seen that inhalation exposure of Co causes respiratory, cardiovascular, hematopoietic and immune system deficiency in animals. There have been reports on the cause of pulmonary fibrosis related to hardmetal lung disease which is mainly caused by inhalation of dust formed during hardmetal processing [94]. However, it was established that the toxicity results were attributed to the effects of Co on respiratory tissues and not W. The effect of hardmetals on the possible cause of dermatitis was attributed to the presence of Co. The toxicity of Co is intensified by the presence of W [95].

Due to all disadvantages related to the carcinogenic effects and supply of Co, it becomes imperative to find replacement binder metals especially in the hardmetal industries, as all commercial hardmetals use Co as the binder. Possible replacements include the use of Ni and Fe as the binder phase.

2.3.2 Nickel binders

Nickel (Ni) was the first experimentally tested binder for hardmetals by K. Schröter, however, the nickel evaporated during the high sintering temperatures [24]. Ni has a melting temperature and vapour pressure below that of Co, and is hence susceptible to evaporation during high temperature manufacturing processes. However, there has been a surging interest in the use of Ni binders in hardmetals, especially in corrosive environments such as those experienced during cutting and milling operations where hardmetals are in contact with aqueous cooling mediums, sealing rings of pumps and wear parts in chemical components. In addition to this, the rising interest in the use of Ni binders is due to the high and fluctuating costs and toxicity concerns relating to Co. The reason why Ni is used as a binder for hardmetals is as follows [96]:

a) Ni has a high melting point of 1453 °C.
b) Ni is capable of forming a liquid phase with WC at temperatures of 1310 °C, this liquid phase pulls sintered parts together by surface tension.
c) On cooling, Ni can re-precipitate WC rendering a tough matrix with dispersed -carbide particles.

d) Ni has a high resistance to corrosion and oxidation.

Nickel has the characteristics of imparting good corrosion resistance. In addition WC is a BCC (body centred cubic) structure and less ductile; the addition of a nickel binder which is FCC (face centred cubic) enhances ductility and deformability [97]. The microstructure of a WC-Ni system exhibits only two phases, namely angular WC (α-phase) grains and the nickel binder (γ-phase) [96]. The nickel present is not in its pure form but as a solid solution with tungsten and carbon based on its ability to dissolve considerable amounts of WC at sintering temperatures of 1310 °C [96]. The matrix structure of a WC-Ni composite comprises of soft primary nickel dendrites with a hardness of ~ 350 HV, with inter-dendritic regions of WC [98].

Although the use of Ni as a binder for WC has the advantage of imparting corrosion resistance as compared to Co binders, the mechanical properties (hardness and toughness) are inferior to those of Co binders of similar composition [99]. In a study done by Wentzel, *et al.* [15], to understand the erosion corrosion behaviour of WC with 6wt% Co, Ni, Ni-Cr and Ni-Cr-Co binders, it was established that hardmetals exhibit decreasing slurry erosion rate with an increase in hardness. It was also established that the difference in binder composition influences the hardness and corrosion behaviour of the hardmetal, with WC- 6w.t% Ni having the highest erosion rate and lowest hardness in comparison to WC – 6w.t% Co. This is evident that WC-Ni hardmetals have inferior mechanical properties to WC-Co hardmetals. Ni and Co are both FCC metals, with Co having an FCC structure at high temperatures and Ni having an FCC structure at all temperatures. However, Ni has a higher stacking-fault energy thus resulting in lower hardening rates [100]. The mechanical properties of Ni binders can be enhanced by solid-solution strengthening and dispersion hardening [101]. The main differences between Ni and Co binders are as follows [100]:

a) FCC Co is metastable and can transform to hexagonal close packed (HCP).
b) Co is a stronger ferromagnetic metal than Ni, hence making it easier for binder phase determination through non-destructive testing such as magnetic saturation measurements [102].
c) Ni has a vapor pressure 10 times that of Co, therefore high temperatures cause losses of Ni.

d) At ambient pressure for temperatures below 695 K, Co has a stable HCP phase, however the transformation from HCP to FCC is slow and both phases coexist from room temperature up to 723 K [103]. The FCC structure of Ni is known to be more ductile with a lower work-hardening coefficient to absorb less energy in the powder milling process than does 40-60% HCP Co [104] which coexist with the FCC phase at room temperature.

2.3.2.1 Carcinogenicity of Ni

According to the National Cancer Institute, Ni exposure is through inhalation of dust particles, fumes and through skin contact. The various Ni compounds increase the risk of lung and nasal cancer [105]. According to the European Union Classification, Labelling and Packaging (CLP), Ni compounds are classified as category 1A carcinogens while Ni metal and alloys as category 1B carcinogens. Category 1A means that Ni compounds are known to have carcinogenic potential for humans and classification is largely based on human evidence and category 1B is based on animal evidence [106].

2.3.3 Iron binders

The first mention of iron (Fe) binders for hardmetals was in a patent by K. Schröter in 1923 [17]. The use of Fe binders in hardmetals was patented by K. Schorter in 1926 [107]. In 1968 another patent was granted to Humenik, Jnr, *et al*. [108] with Ford Motor Co as the assignors, for the production of Fe-bonded WC using the sintering process. However, it was identified that the rupture strength of Fe-bonded WC was half of that obtained from a WC-Co composite, and this was due to the formation of brittle double carbide as a result of the high solid solubility Fe has for WC [108]. The addition of extra carbon above the stoichiometry amount of 6.13 wt% was seen to eliminate the formation of brittle double carbides [108]. It was outlined that Fe can be a possible replacement of Co binders provided that the carbon content of the hardmetal is tailored to avoid the formation of harmful double carbides of tungsten and iron W_3Fe_3C (eta phase) and ensuring that no precipitation of graphite takes place [108] [109]. *Table 2-3* shows the effects of carbon addition on the rupture strength and eta

phase formation and *Figure 2-39* shows the effect of hardness on rupture strength and the transverse rupture strength of WC/Fe materials with different Fe compositions, compared with commercially available WC/Co. In addition, Humenik *et al.* [108] specified that the carbide grain size in the final product should be less than 5 µm.

Table 2-3: Effects of carbon content of 75 WC/25 Fe specimens on transverse rupture strength [108].

% C in Fe	Average Transverse Rupture Strength, p.s.i	Phase observed
0	247,900	η + Fe +WC
1.4	415,200	Fe + WC
3.9	248,800	Graphite + Fe + WC

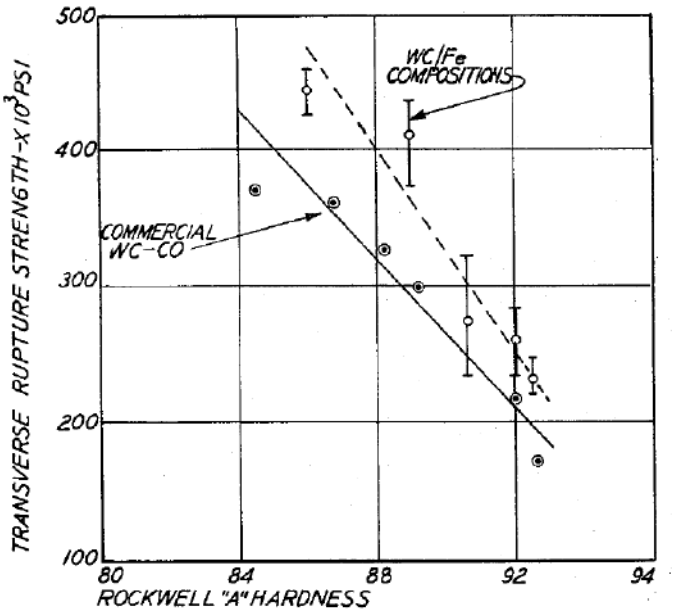

Figure 2-39: Rupture strength vs hardness [108].

WC is unstable in low carbon austenite at elevated temperatures, so in order for the austenite to be carbon saturated, carbon will be obtained from the dissociation of WC to W_2C + C, subsequently producing Fe_3W_3C on cooling [109]. It can be seen from *Table 2-3* that the eta phase and graphite does not form at carbon additions of 1.4%. The maximum solubility of carbon in austenite according to the Fe-Fe_3C phase

diagram is 2% [110]. However, the presence of residual W in solid solution will reduce the solubility of carbon in the austenitic phase [109].

Fe matrix composites have found extensive use in the mechanical, mining, chemical and process industries. Inexpensive techniques such as laser cladding have been applied to fabricate Fe matrix composites [111]. The use of Fe binders has recently been investigated and it was established that they are inexpensive compared to Co and Ni, and possess excellent wear and corrosion resistance with the use of alloying elements [85] [112]. Fe based binders are used in niche applications such as woodworking [24], and hence have not found commercial usage due to the low rupture strength resulting from the difficulty of controlling the carbon content. Due to the low rupture strength of WC-Fe hardmetals, Fe-alloys have been studied in an attempt to improve the mechanical and corrosion properties. Fe bonded hardmetals do not pose a negative impact on the environment and hence the drive for commercial adoption.

An investigation was conducted by Wang *et al.* [113], into the effects of Fe-based alloy powder to WC coatings by high velocity oxyfuel (HVOF) spray methods. Microstructure analysis showed that the composite coatings displayed an amorphous phase and a dense layered structure with low porosity. The composite coating displayed higher corrosion resistance in simulated seawater. The excellent corrosion resistance was an attribute to the alloying elements such as chromium and molybdenum in the matrix. WC-Fe coatings consist of primary WC, fine secondary WC as the reinforcing phase and pearlite accompanied by negligible graphite flakes as the matrix [114].

2.3.3.1 FeNi binders

In an attempt to improve the rupture strength of WC-Fe hardmetals, the addition of Ni was incorporated. Humenik, Jr, *et al.* [108], established that the effect of Ni on the rupture strength depends on its concentration, with the optimum rupture strength attained at 80 wt% Fe/ 20 wt% Ni. *Figure 2-40* shows the effects of different Ni contents in Fe-Ni on the hardmetal rupture strength.

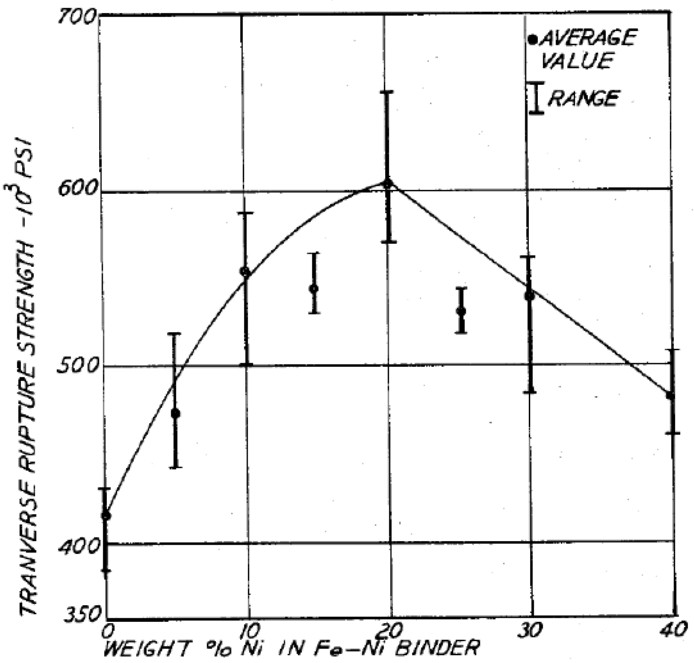

Figure 2-40: Influence of Ni content in a Fe-Ni binder on the transverse rupture strength [108].

Moskowitz, *et al.* [109], demonstrated that Fe-Ni bonded hardmetals are superior over the commercially available Co bonded WC due to the hardening capability of Fe-Ni binders. Fe-Ni binders are hardenable in the sintered condition due to martensitic transformation when cooled below the martensitic start (Ms) temperature. This martensitic transformation was only observed in Fe-Ni binders with Ni contents of 10-25 wt%, resulting in a Rockwell A hardness increase with a subsequent increase in strength. Additions of Co showed further increase in hardness because Co increases the Ms temperature of Fe-Ni alloys and hence increases hardening effect resulting in part of the binder transforming to martensite [108] [109]. The optimum strength was achieved as a result of the optimum amount of martensite and austenite.

An investigation was conducted by Schubert *et al.* [83], into the mechanical properties of sintered hardmetals with Fe-based binders. The FeNi binder system was studied at different Fe/Ni ratios, namely 90/10, 85/15 and 80/20, with the binder phase comprising of 10 and 20% of the hardmetal. Different carbon additions were made in order to achieve eta and graphite free microstructures. The fracture toughness and hardness results showed that a Fe bonded hardmetal without the addition of Ni possessed the highest hardness and lowest fracture toughness. The optimum fracture

toughness/hardness was obtained in a WC-10 wt% (FeNi), with an Fe to Ni ratio of 8.5/1.5. It was observed that controlling the carbon content to optimum level was rather tedious on a lab scale due to the narrow carbon window at which no eta or graphite phase forms. As much as WC-FeNi hardmetals possess a good combination of hardness and fracture toughness, it does not guarantee for a good metal cutting performance due to low high temperature properties such as creep.

2.3.3.2 FeCoNi binders

The first mention of FeNiCo binders was in a 1980 PhD thesis by Prakash [115]. It was established in this work that the structure of Fe-Co-Ni bonded WC is similar to that of WC-Co hardmetals. Similarly to WC-Fe and WC-FeNi hardmetals the carbon content of WC-FeCoNi has to be above the stoichiometric value in order to attain optimum mechanical properties. It was concluded in this thesis that WC-FeCoNi hardmetals have similar transverse rupture strength and hot hardness as WC-Co hardmetals. In addition WC-FeCoNi displayed better fracture toughness and abrasion resistance than WC-Co.

In a study done by Schubert, *et al.* [83], the mechanical properties of a FeNiCo(70/20/10) and FeNiCo (40/40/20) binder was investigated by varying the binder content at 10, 15 and 20 mass %. According to Schubert *et al.* the additions of Co to FeNi bonded WC results in an increase in the hardness through the enhancement of martensite. As with the FeNi binders, the FeNiCo binders displayed a narrow carbon window which exhibits two phases and at which neither the eta phase or graphite is formed. Within the two-phase region, alloys can be fully austenitic, partially austenitic/martensitic or fully martensitic. High strength was observed in martensitic two phase alloys due to grain growth inhibition, and the partial transformation to martensite required a cryogenic treatment. It was observed that WC-FeNiCo (70/20/10) hardmetals displayed excellent hardness and toughness combination when compared to industrial WC-Co hardmetals. However, a binder content of $\leq$ 10 mass % resulted in a very narrow carbon window (40% of the respective window for Co binders), hence the probability of forming the eta or graphite phase is high, it was thus concluded that WC-FeNiCO hardmetals can only be restricted to higher binder concentrations. In addition hot hardness and creep strength

inferior to that of Co was observed due to limited tungsten solid solution strengthening. As much as WC-FeNiCo hardmetals displayed good combination of hardness and toughness, these properties do not translate into good cutting performance.
WC-FeNiCo hardmetals with a ratio of 40/40/20 have a stable austenitic binder and the carbon window for the two phase region is much broader than the FeNi and FeNiCo (70/20/10) binder system. However, the FeNiCo (40/40/20) binder system was observed to have lower hardness, a lower hardness to toughness relationship and a lower bending strength as compared with Co binders.

Fe/Ni/Co(70/20/10) binders for WC were commercialized in 1994 [83], and examples include AMPERSINT® grades by HC Stark [116]

2.3.3.3 FeMn binders

Since it could be observed that FeNiCo binders for WC displayed higher strength and hardness comparable to Co binders when in the martensitic phase, the use of Hadfield steel (Fe-13-14 wt% Mn) as a binder became lucrative as these steels exhibit martensitic transformation on cooling [10]. In addition Fe 13-14 wt% Mn alloys are used in wear resistant applications, hence creep should not be a problem due to work hardening. FeMn alloys also known as manganese steel or Hadfield steel contains 11-14% Manganese (Mn) [117]. FeMn is used as a wear resistant alloy with good work-hardening characteristics [118]. FeMn alloys has found usage in heavy industries such as earth moving, mining, oil and gas drilling to name a few [119].

A study was done by Hanyaloglu. S.C *et al.* [10], in order to investigate the indentation and stress analysis of WC-FeMn hardmetals. The indentation method gives an indication of resistance of brittle materials to crack propagation and hence fracture toughness. In this study a WC-Fe 15 wt% Mn hardmetal with a binder content of 15 wt% and 25 wt% and extra carbon additions of 0.5 wt % and 0.75 wt% were used. It was however, observed that the 15 wt% Mn was reduced to 13.5 wt% Mn and was attributed to evaporation during sintering. In order to avoid the eta and graphite phase it was observed that an addition of 0.75 wt% carbon was required, however higher hardness and fracture toughness were observed at a carbon addition of 0.5 wt%

and this was seen to be attributed to the absence of the eta phase, since the eta phase is brittle, but also imparts hardness. It was concluded in this investigation that even though the WC-FeMn hardmetal possessed higher hardness in comparison with WC-Co hardmetals, the fracture toughness was a bit lower when compared to that of Co binders.

Schubert *et al.* [83], investigated the mechanical properties of WC-10 wt% FeMn with different manganese concentrations. It was established that during sintering of WC-FeMn harmetals, manganese vapour forms, leading to a loss of the initial manganese in the material. In this study up to 16 mass% Mn remained in the Fe binder and the binder remained austenitic during cooling. It was observed that WC-FeMn hardmetals exhibit significantly lower fracture toughness and reduced wear resistance as compared to WC-Co hardmetals at the same low hardness level. The oxidation behaviour of manganese makes it difficult to sinter without forming the eta phase or graphite precipitates, in addition the carbon window is very narrow making it difficult to attain a two phase field.

2.3.3.4 FeNiCr binders

The use of FeNiCr binders for WC has been studied in order to establish a binder system with corrosion resistance in addition to find a cheaper and non-toxic replacement for Co binders. Fernandes *et al.* [112], studied the mechanical properties of WC – 10 wt% AISI 304 with and without added 0.3 wt% carbon, the properties were compared to those of WC-Co hardmetals. AISI 304 is an austenitic stainless steel with Fe, Cr and Ni as the main alloying elements. Austenitic stainless steels are known to have good toughness because Ni is an austenite former and stabiliser limiting the transformation of austenite to ferrite upon cooling, hence austenite is stable at low temperatures. Austenite does not have a ductile to brittle transition temperature and hence can maintain good toughness even at low temperatures. One thing to note about austenitic stainless steels is that they do not harden through heat treatment, however due to the presence of austenite at room temperature these steels tend to work-harden due to austenite transforming to martensite during deformation [120].

According to Fernandes *et al.* [112], it was established that there is less than 1% loss in binder due to volatilization. It was further observed that the hardness of the hardmetal with additional carbon was less than that without extra carbon and this is due to the minimization of the eta phase which is hard and brittle. The hardness and fracture toughness of WC-10 wt% AISI 304 with and without 0.3 wt% carbon was comparable to WC-Co hardmetals, however, the transverse rupture strength for the hardmetal with extra carbon was double that of the hardmetal without additional carbon. It was thus concluded that the presence of the eta phase has an embrittling effect and by adding extra carbon transverse rupture strength can be increased, at this point the transverse rupture strength was below that of WC-Co hardmetals but a potential to replace these hardmetals arises.

In another investigation done by Trung *et al.* [84], it was observed that powder metallurgically produced WC-10 wt% AISI 304 required additional carbon of up to 2 wt% to eliminate the formation of the eta phase during sintering. Contrary to the study done by Fernandes *et al.* [112], the hardness was seen to increase with an increase in additional carbon until a carbon addition of 2 wt%, after which the hardness decreased. In conjunction, the impact toughness increased with carbon addition up to 2 wt% excess carbon.

2.3.3.5 FeCr binders

There is currently limited research on the use of FeCr binders. The nuclear fusion reactor technology industry has shown interest in the use of Fe-Cr as binders for hardmetals, due to their low transmission of hazardous compounds under neutron irradiation [121]. In addition, FeCr alloys are used in the oil and gas industries due to their toughness and strength [122]. FeCr binders are less costly as compared to FeCrNi binders and this is mainly due to the addition of Ni which is costly and hence austenitic stainless steels are more costly than ferritic and martensitic stainless steels. It has been established that FeNiCo binders lack high temperature properties namely creep and hot hardness, conversely FeCr binders are used where creep resistance is a requirement, because Cr acts as a grain growth inhibitor even at high temperatures.

Sakaguchi *et al.* [123] used a high Cr cast iron (Fe-27Cr-3.1C) as a binder for the sintering of WC-(10-40) wt% (Fe-27Cr-3.1C). The phases that were observed were WC, α-Fe and $(Fe,Cr)_7C_3$, the hardness of the hardmetal was higher than that of WC-Co hardmetals with a Vickers hardness of 2000 HV at 10 wt% binder. The wear resistance and high temperature oxidation resistance was superior to that of WC-Co hardmetals. The improved properties were attributed to the dispersion of the $(Fe,Cr)_7C_3$ in the binder phase.

Humphry-Baker *et al.* [124], investigated the thermophysical properties of WC-10 wt% FeCr (Fe- 8 wt% Cr) in order to predict the high temperature performance for plausible use in the nuclear fusion reactor technology. The density of sintered WC-FeCr was less than that of conventional WC-Co hardmetals, this could be attributed to the fact that Fe-8 wt% Cr has a lower density than Co. A Fe_3W_3C phase, which is the double carbide eta phase, was also observed. The room temperature thermal conductivity of WC-FeCr hardmetals was similar to WC-Co hardmetals. However, the thermal expansion results showed the presence of internal stresses which could affect the application of WC-FeCr hardmetals in high temperature applications.

Tarraste *et al.* [125], studied the microstructural and mechanical properties of sintered WC-15 wt% FeCr with extra carbon additions of 0, 1 and 2 wt% C. The binder compositions used were Fe-18 wt% Cr and Fe-28wt% Cr based on commercial ferritic stainless steel grades (AISI 430 and AISI 446, respectively). It could be observed that extra addition of carbon led to the restriction of the eta phase in the Fe-18 wt% Cr alloy. The Fe-28wt% Cr binder showed inhomogeneous distribution of the Cr rich phase with a 1 wt% C addition, which showed to be uniform and homogenous with an increase in sintering temperature. It was seen that FeCr binders exhibit higher hardness and lower toughness as compared with Fe binders. A carbon addition of 1 wt% provided an increase in the fracture toughness, since the addition of carbon retards the formation of the eta phase. Despite the progress in replacing Co binders, FeCr binders remain brittle when compared to conventional WC-Co hardmetals.

In another study by Tarraste *et al.* [85], a higher binder content of 30 wt% of AISI 430L with and without carbon additions was sintered. It was again observed that the microstructure was inhomogeneous with a scatter of the Cr-Fe rich phases. Carbon

additions were seen to retard the formation of the eta phase hence the improvement in the fracture toughness in comparison to WC-15 wt% FeCr. However, considerable work is still required in order to attain a homogeneous microstructure.

Flores *et al.* [126], studied the behavior of WC reinforced Fe-base matrices alloyed with different concentrations of Cr, Mo, Si and with and without carbon additions. The microstructure of WC-FeCr with carbon addition of 2.8% consisted of WC reinforcing particles and W-rich secondary phase embedded in a Fe-rich phase. The secondary phases were composed of primary Cr carbides, herringbone carbides and Fe-W carbides, the secondary phases thus led to Cr-depleted zones and inhomogeneity in the microstructure. The microstructure of WC-FeCr without the addition of carbon displayed an increase in the W-rich secondary phases which could be due to the presence of the eta phase.

In a recent study it was seen that the presence of Cr above the solubility limit in hardmetals leads to the formation of Cr-containing carbides at all carbon contents and lead to an inhomogeneous microstructure [127]. Due to this no classical two phase area containing WC and the binder exists and the amount of the metallic binder can decrease leading to properties that do not meet expectations.

Martensitic stainless steels are Fe-based steels with a chromium content of 11-15%, hence making it stainless [128]. Martensitic stainless steels are used in wear resistant application where moderate corrosion is required. Martensitic stainless steels display good toughness, strength and hardness following tempering [128] and have found applications in steam/water valves, surgical instruments, pumps, shafts, bearings and nozzles to name a few [129]. Martensitic stainless steels are however not desirable in welding conditions as they are prone to hydrogen embrittlement and the formation of a brittle heat affected zone (HAZ) [129]. Welding operations conducted under an inert atmosphere and post-weld heat treatment will prevent both hydrogen embrittlement and a brittle HAZ.

2.4 Phase Equilibria of the W-Fe-Cr-C Hardmetals

In this study a martensitic stainless steel binder was used with WC, and it was important to understand the different phases which could be generated during the LENS® production of WC-FeCr hardmetal. Therefore a review of the W-Fe-Cr-C hardmetal system is provided here. The W-Fe-Cr-C system is complicated, hence in order to understand the phase equilibria it is important to understand the binary W-C, Fe-C, and W-Fe systems and the ternary W-Fe-C and the Fe-Cr-C systems.

2.4.1 W-C system

The WC binary phase equilibria consist mainly of two carbides namely WC and W_2C and the maximum solubility of C in W at the eutectic temperature of 2710 °C (2983.15 K) is 0.7 at% [20]. The two main phases namely WC and W_2C each have structural modifications, which are stable in certain temperature ranges and concentrations [19]. The major phase in the W-C system is the higher WC termed δ-WC, it is hexagonal in structure and stable between 300 and 3030-3050 K and it undergoes no phase transformation [130]. δ-WC is a line compound with insignificant deviation from the stoichiometric composition [100]. The second phase in the W-C system is the lower W_2C termed β-W_2C which originates from the eutectoid reaction between elemental W and δ-WC at 1523 K [100] , this phase exists in three polymorphs namely [130]:

- β”-W_2C – low temperature (1523 – 2370 K) hexagonal structure.
- β’-W_2C – Intermediate temperature (2370 – 2750 K) orthorhombic structure.
- β-W_2C – high temperature (stable above 2750 K).

Figure 2-41 shows the phase equilibria of the W-C system, it can be seen that the W_2C phase forms at lower carbon concentrations, and above temperatures of 1523 K and graphite forms at carbon contents with concentration higher than the stoichiometric values.

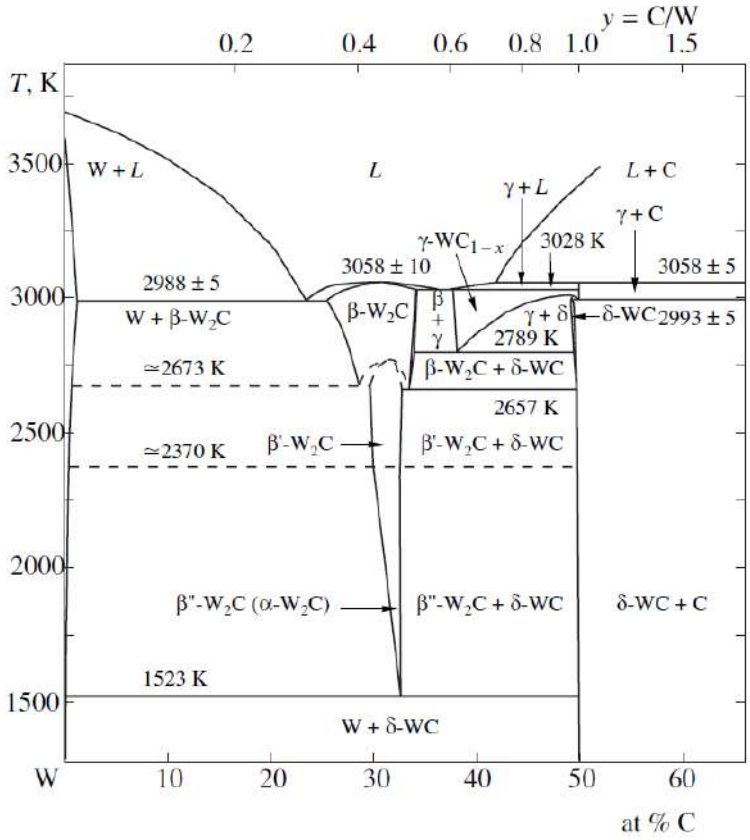

Figure 2-41: Phase diagram of the W-C system [130].

2.4.2 Fe-C system

The Fe-C system is the most studied phase equilibria system with 4 solid phases formed. When Fe first solidifies at 1813 K (1540 °C) it forms δ ferrite which is stable at temperature ranges of 1668 – 1813 K (1395 – 1540 °C). δ ferrite has a BCC crystal structure and has a maximum carbon solid solubility of 0.1 wt% at 1768 K (1495 °C). δ ferrite is only stable at high temperatures and with the decrease in temperature below 1768 K (1495 °C) leads to a peritectic reaction which gives rise to the formation of γ-austenite. γ Austenite has a FCC crystal structure and has higher solubility of carbon reaching to a maximum of 2 wt% at 1421 K (1148 °C), like δ ferrite γ austenite is not stable at room temperature. As temperatures drop towards room temperature, α ferrite forms at temperatures below 1173 K (900 °C). α ferrite is an interstitial solid solution of carbon in the BCC iron crystal having a maximum carbon solubility of 0.025 wt% at 1000 K (727 °C) and decreases to 0.008 wt% at 0 °C. The eutectoid reaction not only leads to the formation of α ferrite but to the formation of cementite (Fe_3C) as well. Fe_3C is an intermetallic phase of iron carbide and has a carbon solid solubility of

6.7 wt% carbon. Fe_3C is hard and brittle and has an orthorhombic crystal structure. *Figure 2-42* shows the Fe-C equilibrium phase diagram and it is clear that Fe has an affinity for carbon and is hence a carbide former.

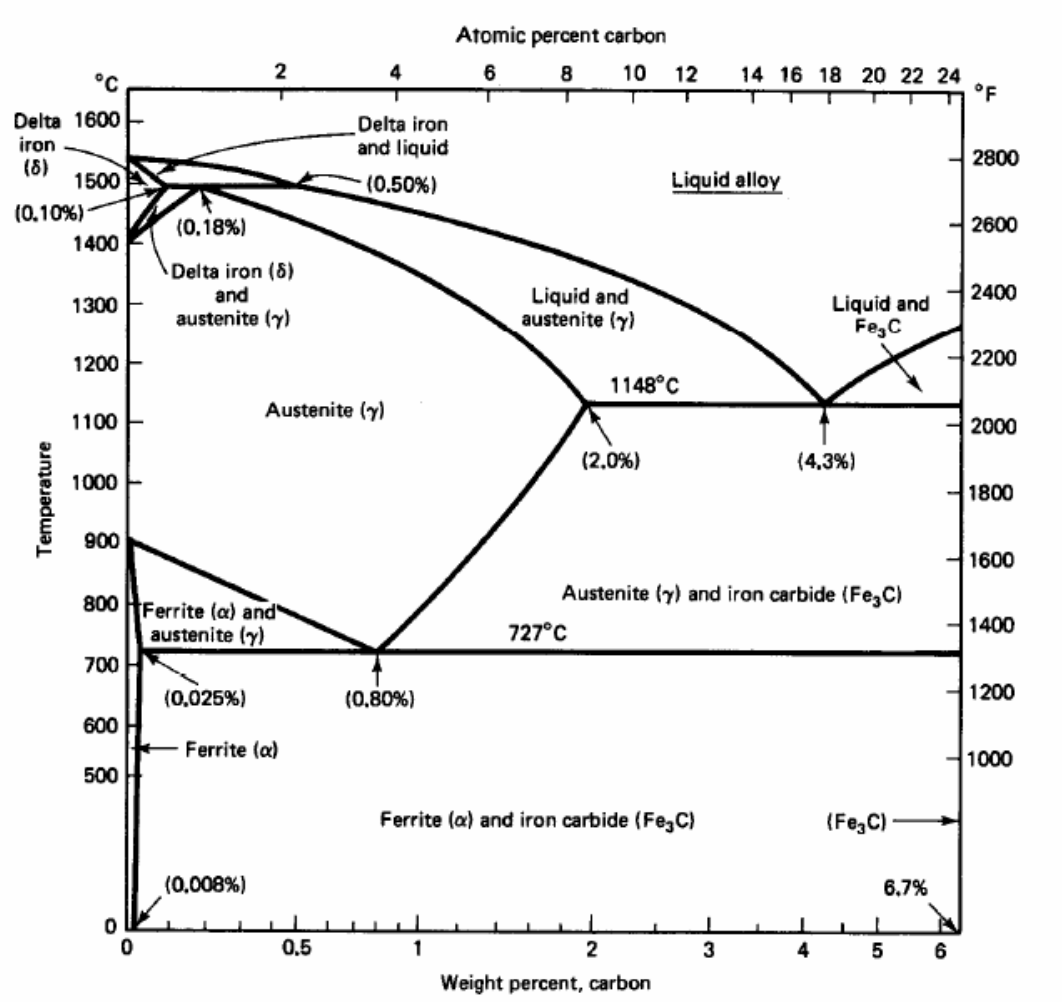

Figure 2-42: Fe-C equilibrium phase diagram [110].

2.4.3 Fe-W system

In order to fully understand the phase equilibria of the Fe-W system Uhrenius [131], incorporated the W-C and Fe-W-C system and made it part of Fe-W system. The equilibria phases that are formed are austenite (γ), ferrite (α) and a line intermetallic phase Fe_3W_2 (μ) which is stable from 1000 – 1910 K and at room temperature. In this system there are two peritectic equilibria between the BCC α-ferrite, Fe_3W_2 (μ) and the liquid phase.

Figure 2-43 shows the binary Fe-W system.

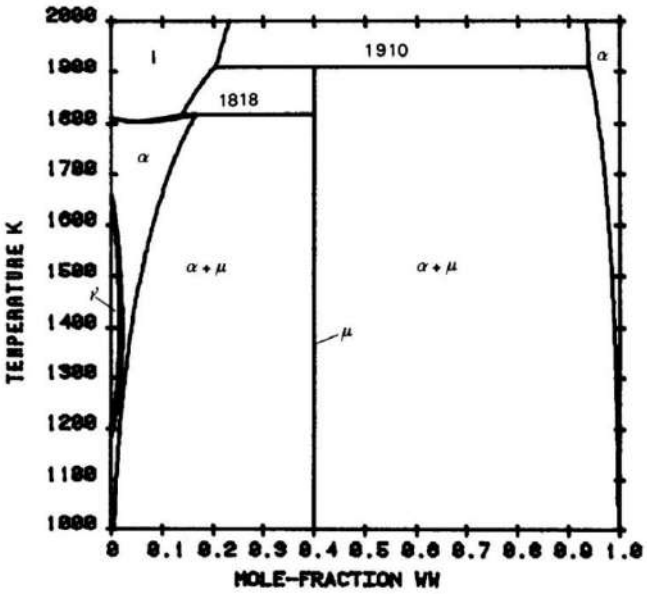

Figure 2-43: The calculated Fe-W phase diagram [131].

2.4.4 Fe-Cr-C system

The ternary Fe-Cr-C system is important as it is applicable to both stainless steel and tool steel. Cr is the major alloying element in stainless steels with a minimum Cr content of 12 wt%, it imparts corrosion resistance and hence makes steel stainless. Tool steels such as medium alloy, high Cr and Cr hot work tool steels to name a few, have high Cr content with a range of 5 – 12 wt% Cr. The main carbides in the Fe-Cr-C system are $M_{23}C_6$ [$(Cr, Fe)_{23}C_6$], M_7C_3 [$(Cr, Fe)_7C_3$] and M_3C [$(Fe, Cr)_3C$] which is cementite [132]. *Table 2-4* shows the lattice type and characteristics of the different carbides. *Figure 2-44* shows a vertical section of an Fe-Cr-C system at a 13 wt% Cr content which meets the requirement of stainless steels.

Table 2-4: Characteristics of carbides [132].

Type of carbides	Lattice type	Characteristics
M_3C	Orthorhombic	Carbide of the cementite (Fe_3C) type. M may be Fe, Cr, with a little bit of W
M_7C_3	Hexagonal	Hard and abrasion resistant
$M_{23}C_6$	Face-centered cubic	Cr can be replaced with Fe to form carbides with W

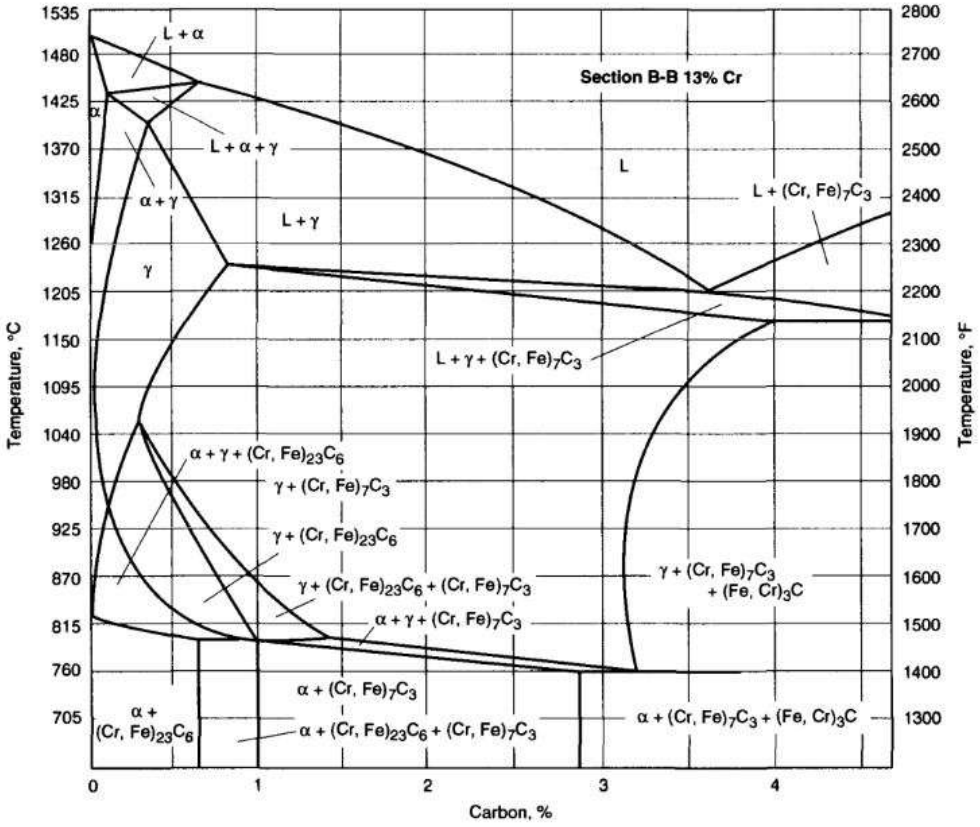

Figure 2-44: Vertical section of the Fe-Cr-C system at 13 % Cr [133].

2.4.5 W-Fe-C system

In order to understand the thermodynamics of the W-Fe-C system, Uhrenius [131] used the binary W-C, W-Fe and Fe-C phase diagrams and thermochemical data in combination with the equilibria information of the W-Fe-C system at 1000 °C.

To understand the phases that are formed in sintered WC-Fe hardmetals, it becomes imperative to understand the phases that are formed at different temperatures and concentration in the W-Fe-C system. Four ternary carbide phases namely M_4C, M_6C, $M_{12}C$ and $M_{23}C_6$ are formed [20]. $M_{12}C$ is known as carbon poor M_6C, with a crystal structure which is different from M_6C due to the absence of carbon atoms from half the carbon sites, it is a low temperature modification of M_6C [134]. From the isothermal section of the W-Fe-C system at 1000 °C constructed by Pollock *et al.* [135], three ternary phases made up of two cubic η-carbides (Fe_3W_3C, Fe_6W_6C) and a hexagonal phase (FeW_3C) were observed. Fe provides the lowest temperature for liquid phase formation at the highest solubility for WC in the liquid phase when compared to the W-Co-C and W-Ni-C systems [136]. It was also concluded that carbon has to be added to avoid the formation of M_6C during liquid phase sintering. *Figure 2-45* shows the isothermal section of W-Fe-C phase diagram.

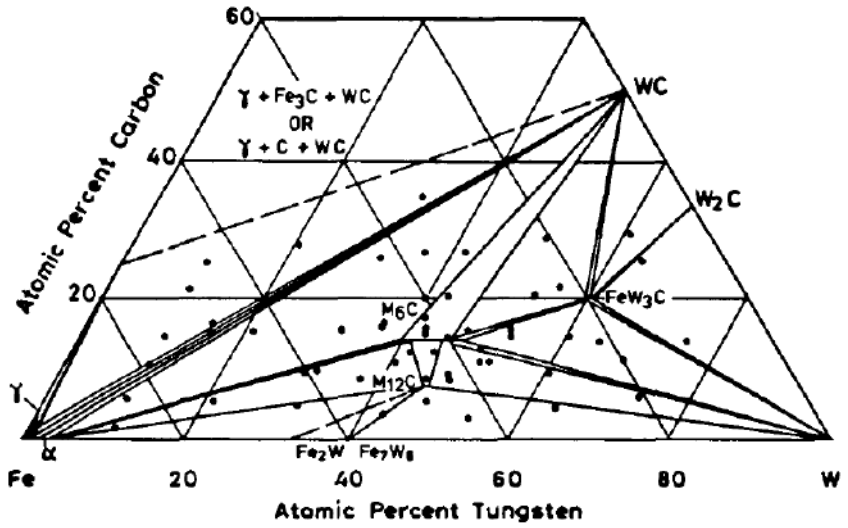

Figure 2-45: W-Fe-C isothermal section at 1000 °C [135].

2.4.6 W-Fe-Cr-C system

The W-Fe-Cr-C system consists of three carbide formers namely W, Fe and Cr which all have a high affinity for carbon, in comparison with the W-Co-C and W-Ni-C system which consists of one carbide former. Uhrenius *et al.* [137] studied the carbide/austenite equilibria at 900 °C, 1000°C and 1100 °C in the W-Fe-Cr-C quaternary system and it was observed that an increase in the W/Cr ratio destabilized the $M_{23}C_6$ in comparison to M_6C. The carbide phases present in the W-Fe-Cr-C system are similar to the ones established in the W-Fe-C system by numerous researchers [131] [134] [135] [137]. In addition it has been established that M_4C, $M_{12}C$, M_7C_3 and M_2C were also observed in the W-Fe-Cr-C quaternary system, with M_2C being stable in the binary W-C system and dissolving large amounts of Cr [138]. However, the range of stability of M_4C and $M_{12}C$ phases is sparse and information regarding these phases is quite meagre. Gustafson [138], showed that M_6C which is stable in the W-Fe-C system had limited solid solubility for Cr and that $Cr_{23}C_6$ can be replaced by Fe and W to attain $Fe_{21}W_2C_6$. However, $Fe_{21}W_2C_6$ is metastable and decomposes during annealing. The W-Fe-Cr-C system comprised of additional phases which were not covered in the W-Fe-C ternary systems such as $Fe_{10}Cr_9W_2C$, this was only found to be stable at temperatures above 1623 K and decomposes upon cooling into Fe and the chi phase [139]. The stable carbides in the W-Fe-Cr-C quaternary system are shown in *Table 2-5*.

Table 2-5: Carbide phase in the quaternary W-Fe-Cr-C system [138].

Phase	**Elemental constituents**
$M_{23}C_6$	W, Fe, Cr, C
M_6C	W, Fe, Cr, C
M_7C_3	W, Fe, Cr, C
M_2C	W, Fe, Cr, C
M_3C	W, Fe, Cr, C
M_3C_2	W, Cr, C
MC	W, C
MC_{1-x}	W, Fe, Cr, C

2.5 Summary

Hardmetals have found extensive usage in wear applications due to their high hardness and good fracture toughness. Challenges exist in the manufacture of hardmetals, namely, long manufacturing times and the need for secondary processes for the fabrication of complex geometries. In addition the conventional Co binder in hardmetals has challenges with the carcinogenicity, high prices and possible shortage; this has led to research into alternative binders such as Ni and Fe. Investigations into the use of Ni as a binder for hardmetals has shown inferior hardness and rising concerns regarding its carcinogenicity. This has led to the possible substitution of the Co binder with Fe. However, it has been shown that WC-Fe hardmetals have low rupture strength due to the formation of the eta phase caused by long sintering times, thus allowing dissolution of WC. Research has shown that the formation of the eta phase could be suppressed by additions of extra carbon, however this too has made it difficult to avoid the eta and graphite phases. Different Fe-alloy binders have been investigated but a martensitic stainless steel binder which may have high hardness, toughness and does not contain the carcinogenic Co and Ni has not been investigated. The challenges that exist in manufacturing hardmetals may be overcome by using AM. Additive manufacturing is a disruptive process which has the potential to manufacture intricately shaped hardmetals at the shortest turn-around time. The LENS® technology is an AM process that could be used to manufacture these materials as it allows a large amount of design freedom and high geometric accuracy. Investigations into AM of hardmetals have focused on WC-Co and WC-Ni hardmetals. The current literature does not examine the LENS® fabrication of WC in a Fe-based binder and specifically not a FeCr martensitic steel binder. Crack restraining methods in LENS® deposited hardmetals also do not appear to have been investigated. Thus it is clear that there are scientific gaps relating to the LENS® fabrication of Fe-based WC and this study aims to address some of these gaps.

CHAPTER 3 Experimental Procedures

3.1 Introduction

This chapter describes the materials, testing equipment and test processes used for the experimental work for this research project. It begins with a description of the feedstock powders and substrate used during deposition. Next the LENS® machine is described followed by the research approach taken to produce WC-FeCr hardmetal. The chapter concludes with descriptions of the materials characterization tests conducted during the various deposition stages.

3.2 Feedstock Powders

Two feedstock powders were used during the LENS® deposition process. The powders were spherical cast WC powder with a particle size of -90+45 µm produced by Zhuzhou Jiangwe Boda Hard-facing Materials Co., Ltd, and a gas atomized AISI 420 martensitic stainless steel powder with a particle size of -125+53 µm produced by Sandvik Osprey Ltd. The chemical compositions of the powders, as listed on the suppliers material datasheets are shown in *Table 3-1* and *Table 3-2*. The steel powder will be referred to as FeCr powder in this thesis, Fe and Cr are the dominant elements.

Table 3-1: Chemical composition of the cast WC powder.

Element	**C**	**Cf**	**Fe**	**W**
wt%	3.88	0.055	0.20	balance

Table 3-2: Chemical composition of the gas atomized AISI 420.

Element	**C**	**Cr**	**Mn**	**Si**	**Fe**
wt%	0.30	13.20	0.90	0.90	balance

The two powders, with a weight ratio of WC to FeCr equal to 9:1, were blended in a rotary mill for 4 hours at a rotational speed of 68.75 rpm. The blending process was

carried out to ensure a homogenous mixture of the two powders. The particle size distribution of the powders was characterized using a Malvern Mastersizer-S, to verify the particle sizes given by the suppliers, to ensure that no agglomeration or fragmentation occurred during the blending process, and to verify that the powders were suitable for the LENS® machine. The LENS® machine manual specifies the usage of spherical powders with a diameter range of 36 – 150 µm in order to avoid powder delivery system damage [41].

3.3 Substrate

The substrate used during the LENS® deposition of the WC-FeCr hardmetals was ground mild steel plates with the dimensions 121 x 121 x 8 mm. The plates were sand blasted with a silicon oxide (SiO) and cleaned with acetone to remove any oils and impurities from the surface of the plate. The chemical composition of the substrate is shown in *Table 3-3*.

Table 3-3: Chemical composition of the substrate.

Element	**C**	**Mn**	**Cr**	**S**	**P**	**Fe**
wt%	0.10	0.44	0.025	0.02	0.04	99.30

3.4 LENS® Equipment

A LENS® 850-R system (Optomec, Albuquerque, NM, USA), with a 1kW IPG fiber laser and a wavelength of 1064 nm was used to deposit the WC-10wt % FeCr samples. The laser consists of a power distribution unit, power supply, cooling system and a delivery fiber. During laser emission a series of laser optics are used to direct the beam and focus it on the work piece. The laser beam having a circular shape was focused to a spot size of 1.4 mm. The powder delivery system comprised of two powder hoppers, motorized feed mechanisms, powder delivery lines and powder delivery nozzles on the deposition head. Within the deposition head a purge nozzle was present in the center of the powder delivery nozzles. The center purge nozzle is responsible for providing a constant flow of gas out of the open path for the laser beam in order to prevent

powdered metal from contaminating and damaging the laser optics. *Figure 3-1* shows the LENS® machine.

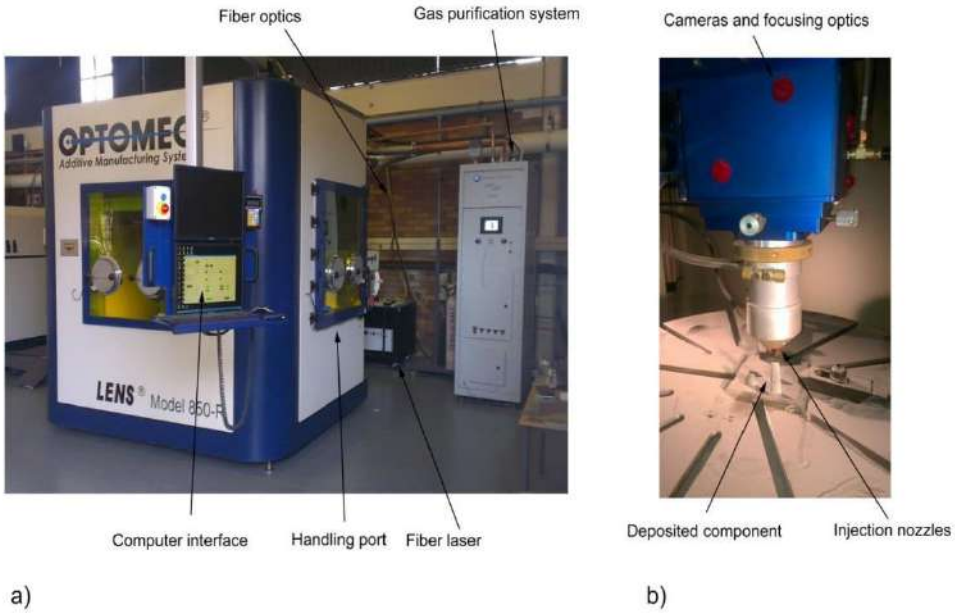

Figure 3-1: LENS 850-R system [140].

During deposition the powders were delivered into the path of the laser beam by an argon gas stream set at 2 l/min, through powder delivery nozzles and the rate of flow for the powder is specified in revolution per minute (RPM). In order to convert this to g/min a container was used to collect the powders from the deposition nozzles, the mass of powder collected in 1 minute was recorded and extrapolated in order to establish the graphical and mathematical relationship between rpm and g/min. *Figure 3-2* shows the powder flow from the four powder nozzles, while *Figure 3-3* and Eq. 3-1 shows the relationship between powder flow rate in rpm and g/min. The interaction of the laser beam and feedstock powder led to the formation of a molten pool which formed a solid deposit upon solidification.

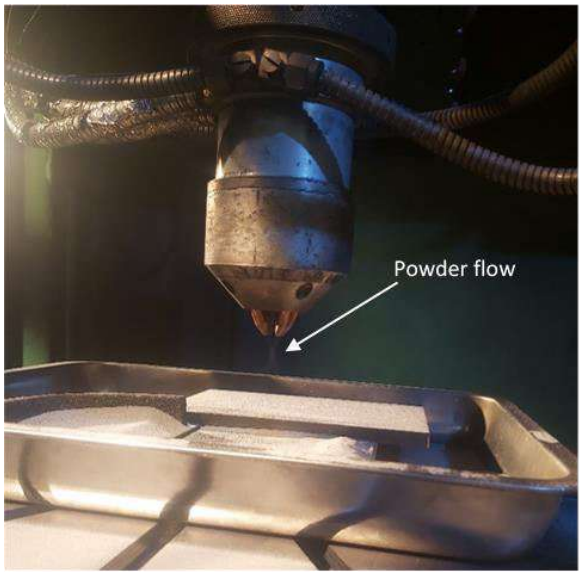

Figure 3-2: Powder flow from the nozzles.

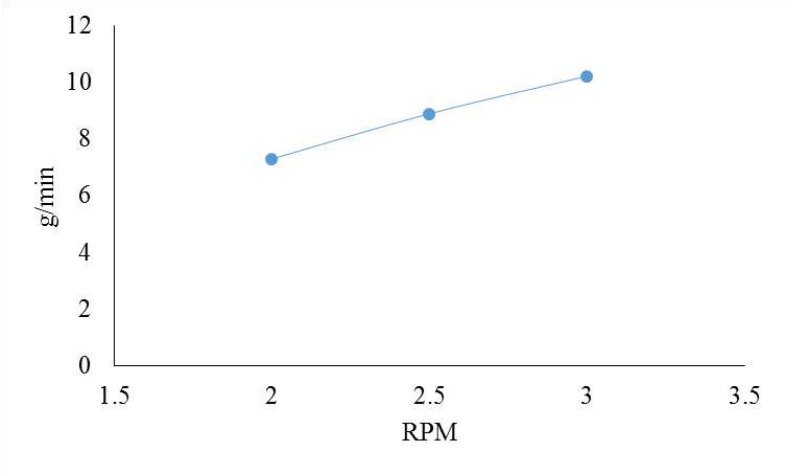

Figure 3-3: Relationship between RPM and g/min.

$$M\ (g\ /\ min) = (2.70 \times Mi(rpm)) + 1.40 \qquad \text{Eq. 3-1}$$

Where M is the powder flow rate in g/min and Mi is the powder flow rate in rpm.

The software used in the LENS® 850-R is PartPrep which converts the engineering drawings in the stl. file format into commands for the LENS® workstation control software. PartPrep slices the stl. file format into multiple layers, and once the output file has been sliced it is converted into a job file format using the workstation control software. The LENS® 850-R workstation control system allows for manual positioning of the motion axes, control of system components and on-screen process monitoring.

3.5 LENS® Production of WC-FeCr Hardmetals

3.5.1 Design of Experiments Matrix and Optimization

A Design of Experiments (DoE) approach was used to investigate the influence of process parameters (input variables) on measured responses. In order to relate process parameters to experimental responses, experiments are conducted in a series of trials or tests which yields quantifiable outcomes, so that the process behavior, variability and overall impact on the process can be understood [141]. To establish the influence of process parameters on experimental responses, deliberate changes are often made to the input variables so that the variations in the measured responses can be determined. This methodology is termed Design of Experiments (DoE) and was developed in the early 1920s by Sir Ronald Fisher [141].

A full factorial DoE with three factors (K= 3) also known as process parameters, namely laser power, traverse speed and powder feed rate, and three factor levels (L = 3), meaning the variable parameters chosen were varied across 3 values, was considered. The process parameters used were based on previous work done on hardmetals. No work has currently been done on the LENS® deposition of WC-FeCr hardmetals therefore a process parameter map of LENS® deposited WC-Co and FeCr alloys was prepared. The overlap in the process parameters of the two materials were used in this investigation. APPENDIX A shows the process parameter window according to literature and *Table 3-4* lists the process parameters used.

Table 3-4: DOE parameters.

Parameters	**Level 1**	**Level 2**	**Level 3**
Power (W)	200	300	400
Traverse Speed (mm/s)	6.4	8.5	12.7
Powder Feed rate (g/min)	7.3	10	12.2

The sample size of the DoE without replication was calculated using Eq. 3-2. The DoE matrix with the combination of input parameters for the optimization process is shown in *Table 3-5*.

$$N = L^K \quad = 3^3 = 27\ experiments \qquad \text{Eq. 3-2}$$

where: N = sample size

K = number of factors

L = factor levels

Table 3-5: DOE matrix.

Experimental runs	Power (W)	Speed (mm/s)	Feedrate (g/min)
1	200	12.7	7.3
2	200	12.7	10
3	200	12.7	12.2
4	200	8.5	7.3
5	200	8.5	10
6	200	8.5	12.2
7	200	6.4	7.3
8	200	6.4	10
9	200	6.4	12.2
10	300	12.7	7.3
11	300	12.7	10
12	300	12.7	12.2
13	300	8.5	7.3
14	300	8.5	10
15	300	8.5	12.2
16	300	6.4	7.3
17	300	6.4	10
18	300	6.4	12.2
19	400	12.7	7.3
20	400	12.7	10
21	400	12.7	12.2
22	400	8.5	7.3
23	400	8.5	10
24	400	8.6	12.2
25	400	6.4	7.3
26	400	6.4	10
27	400	6.4	12.2

The sample height and porosity were used as the experimental responses because the feasibility of using LENS® to deposit WC-FeCr hardmetals was the aim. The optimization technique was carried out in three steps as follows:

- Single wall sample height optimization
- Single wall sample height and porosity optimization
- Influence of z-increment on single wall samples
- Verifying the near optimum parameters by manufacturing cube samples and the selection of the optimum parameters for the LENS® deposition of WC-FeCr hardmetals.

3.5.1.1 Singe wall sample height optimization

Linear, quadratic and exponential regression models were used to achieve a statistical model for establishing a functional relationship between process parameters and sample height by graphical representation and analysis of the coefficient of variability/determination (R^2). The higher R^2 is the more the variability in data is accounted for by the model. R^2 may have a value between 0 and 1 as shown in Eq. 3-3.

$$0 \leq R^2 \leq 1 \qquad \text{Eq. 3-3}$$

There are limitations with R^2, as the value does not necessarily mean that the model accounts for the data behavior, as it can be close to 1 due to the additions of more variables, hence R^2 cannot be the only measure for the appropriateness of the model. In order to see the statistical significance of the regression model an analysis of variance using the F-test was conducted. A P-value was calculated from an F-statistical value (Eq. 3-4) which gave the probability of the null hypothesis being true. The P-value ranges from 0 - 1 where 1 signifies that the null hypothesis (H_0) is true, which means that the coefficients of the independent variables are equal to 0, and 0 signifies that the null hypothesis may not be true depending on the significance level of the model.

$$Fvalue = \frac{Mean\ regression\ sum\ of\ squares\ (MS)}{Mean\ error\ sum\ of\ squares} \quad \text{Eq. 3-4}$$

The hypothesis: $H_0: \beta_1 = \beta_2 = \beta_3 = 0$ $H_1: at\ least\ on\ of\ the\ variables\ \beta \neq 0$

where H_0 is the hypothesis test

β_1, β_2 and β_3 represents the coefficients of the independent variables.

Residual analysis was carried out to compare the adequacy of the regression models through graphical representation where the residuals are defined in Eq. 3-5.

$$Residuals\ (e) = y - \hat{y} \quad \text{Eq. 3-5}$$

where y is actual observations and $\hat{y}$ is the predicted observations.

An Excel Software Data Analysis package was used for all the least-of squares statistical analysis. Once a statistical model was established, height optimization was carried out by using a generalized reduced gradients (GRG) non-linear optimization in order to achieve the required sample height as calculated in Eq. 3-6. The GRG optimization technique is used in non-linear programming problems with non-linear constraints, whereby the main aim during optimization entails linearizing the non-linear objective and constraint functions through iteration steps. This method was used using the Microsoft Excel Solver statistical package. Solver adjusts the input variables (laser power, powder feed rate and traverse speed) to satisfy the experimental response (sample height)

$$Height\ (mm) = zincrement\ (mm)\ \text{x}\ nr\ layers \quad \text{Eq. 3-6}$$

3.5.1.2 Single wall sample height and porosity optimization

Attaining the required sample height is important to ensure a constant working distance, however, sample porosity plays a major role in the integrity and hence the mechanical properties. In order to achieve samples with the required height and minimum porosity, a multi-objective optimization (MOO) process was carried out on samples with close to optimum height measurements, whereby the height was maximized and porosity minimized. The MOO process is used when a problem

involves two or more objectives, whereby these objectives may be conflicting [142]. A Pareto non-dominated optimization process was used to establish the Pareto optimal solutions.

3.5.1.3 Influence of z-increment on sample height and porosity

An attempt to refine the Pareto optimal solutions was carried out by investigating the influence of the z-increment on sample height and porosity. The z-increment was obtained by depositing one layer and measuring the layer thickness. The experimental responses were compared to those with a z-increment of 0.2 mm in accordance with literature (*Table A-1* and *Table A-2*) and an optimum z-increment was selected.

3.5.1.4 Cube sample parameter verification

Cube samples were deposited using the optimum parameters to compare the porosity with the thin wall samples. The process parameters which resulted in the lowest porosity were used as the optimum solution for this study.

3.5.2 Thin wall and cube depositions

The mild steel substrate was sandblasted using silicon carbide (SiC) grits and cleaned with acetone to improve adhesion and remove grease and impurities respectively.

3.5.2.1 Thin wall samples

The LENS® system was used to deposit WC-10wt% FeCr thin walls using the DoE matrix described in Section 3.5.1, with the input variables namely laser power, traverse speed and powder feed rate listed in Table 3-4 and Table 3-5. Initially the z-increment (layer thickness) was kept constant at 0.2 mm, the laser spot size and working distance were set at 1.4 mm and 8 mm respectively. Single walls with a length of 25 mm comprising of 40 layers were deposited under atmospheric conditions. Once the Pareto optimal solutions were established samples with a z-increment equal to the layer thickness were deposited. These samples also had a length of 25 mm, comprising of 40 layers and the same laser spot size and working distance were used.

The height of the all single wall samples were measured at 5 positions and the effect of process parameters on sample height was plotted. A relationship between the process parameters and sample height was defined in terms of the regression models specified in Section 3.5.1. The relationship of the heat input with laser power and traverse speed was represented by Eq. 3-7 and the influence of the heat input on sample height and porosity could be determined.

$$HI\ (J/mm) = \frac{Power\ (W) \times 60}{Traverse\ speed\ (\frac{mm}{\min})} \qquad \text{Eq. 3-7}$$

Longitudinal sections of the thin wall samples that yielded close to optimum height measurements were prepared for porosity analysis as specified in Section 3.6.6. The effects of process parameters on porosity were plotted and the optimum parameters based on both height and porosity were established by using a MOO technique as explained in Section 3.5.1. The samples with the z-increment equal to the layer thickness were also prepared for height and porosity quantification.

The thin wall samples were also subjected to material characterization tests explained in Section 3.6 to understand the effects of process parameters on sample microstructure, phase characteristics, hardness and thermal properties'.

3.5.2.2 Cube samples

Once optimum parameters were established these were used to deposit cube samples with dimensions of 11 mm x 16 mm and 15 layers. A laser spot size of 1.4 mm and working distance of 8 mm was used in the deposition of samples The LENS® control system parameters which were used for the cube samples are namely the hatch and contour parameters. These parameters define how the overall slicing process will work. The contour is the outline of the build and the hatch spacing defines the distance between the centers of two neighboring scanning paths (*Figure 3-4*). The hatch shrink allows the hatch fill lines to be shortened within a contour, in cases were more material is deposited on the contour edge.

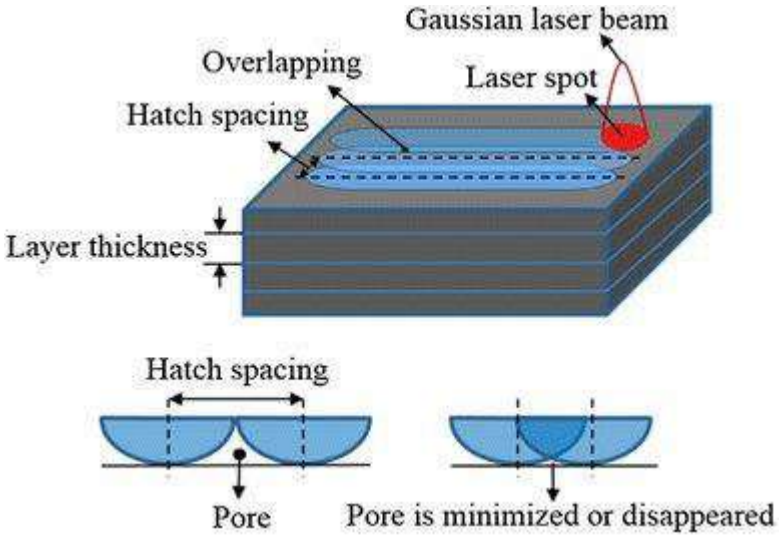

Figure 3-4: Hatch spacing [143].

The hatch spacing was calculated using equation Eq. 3-8. A high laser pass overlap may lead to excessive re-melting resulting in shrinkage defects, and a low laser pass overlap may lead to lack of fusion defects. A large hatch spacing results in a small overlap and a small hatch spacing results in a larger overlap. In this present work the hatch spacing was determined by depositing cube samples using optimum parameters, the hatch spacing was varied between of 0.7 and 0.5 mm. The laser pass overlap and hence hatch spacing which displayed minimum porosity was used for the rest of the work. *Table 3-6* shows the contour parameters used.

$$Laser\ pass\ overlap\ (\%) = D - X/D \times 100 \qquad \text{Eq. 3-8}$$

where X (mm) is the hatch spacing and D (mm) is the laser spot size.

Table 3-6: Work control system parameters.

	Number of contours	**Hatch spacing (mm)**	**Hatch shrink (mm)**
Cube samples	1	0.5/0.7	0.191

The scanning pattern used for the deposition of cube samples is important as it determines the quality and precision of the parts manufactured. The scanning pattern used during the deposition of cube samples is shown in *Figure 3-5*.

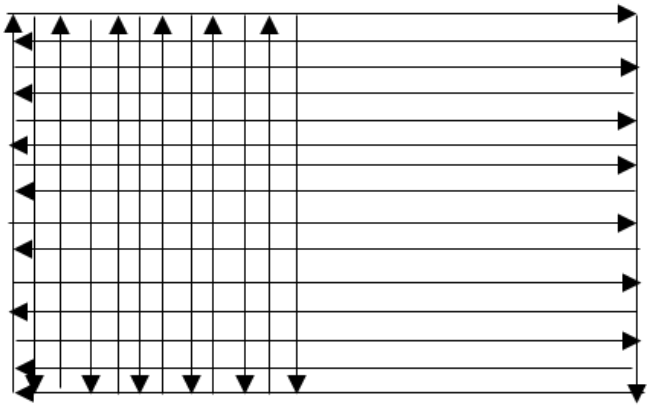

Figure 3-5: Scanning pattern of the LENS® deposition process.

The deposited cube sample was subjected to material characterization tests explained in Section 3.6. The microstructure, phase analysis, hardness and the density were measured. The material properties were compared with conventionally manufactured WC-Co and WC-FeCr hardmetals as reported from literature.

The same methods and parameters were used to deposit a FeCr cube sample. The cube sample was transversely sectioned and prepared in accordance with Section 3.6.5 for phase analysis and microstructural analysis.

3.5.3 Crack restraining methods

To eliminate, or at least reduce the cracks observed during LENS® deposition and to ensure adhesion of the WC-FeCr hardmetal to the substrate material, cube samples were deposited using the optimal processing parameters determined according to Section 3.5.1 in conjunction with the following residual stress relieving methods:

a) Depositing a buffer layer of 0.6 mm Monel 400 onto the mild steel substrate using the optimum parameters determined in Section 3.5.1, and depositing the

WC- FeCr hardmetal on top of the buffer layer. The buffer layer was used for absorption of the thermal residual stresses.

b) Depositing a buffer of 0.6 mm AISI 420 (the martensitic stainless steel binder metal) onto the mild steel substrate using the optimum process parameters, and depositing the WC-FeCr hardmetal on top of the buffer layer. The buffer layer was used to match the WC binder and limit the use of different coefficients of thermal expansion (CTE) and hence reducing the thermal residual stresses.

c) Laser re-melting the finally deposited surface layers. One to three layers of laser re-melting without a powder feed was carried out on the top layer. The optimum process parameters were used with the powder feed rate set to zero.

d) Preheating the mild steel substrate to a temperature of 250 °C in order to relieve the thermal residual stresses. This was achieved by using a ceramic heating stage shown in *Figure 3-6*. Once the substrate reached the desired temperature the cube alloy was deposited.

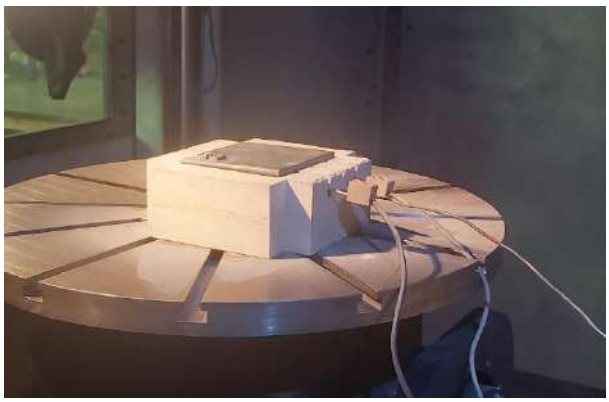

Figure 3-6: Ceramic heating stage.

All the cube samples were sectioned transversely (cross section) and a dye penetrant test method was carried out for crack identification and counting as specified in Section 3.6.15. Phase characterization and hardness measurements were done on the samples to assess the influence of the crack restraining methods on the material properties. The crack restraining method which reduced the number of cracks was selected and included in the component prototyping stage.

3.5.4 Cylindrical rotary burr prototype

The viability of using the LENS® process to manufacture a prototype using the optimal cube processing parameters was investigated. A rotary burr was chosen and designed to have a shank diameter of 6 mm, burr diameter x length of 12 x 25 mm and a total length of 65 mm. It was designed without a rotary end cut and all designs were based on DIN 8033 and the PFERD burr catalogue [144]. CAD models were made on Creo Parametrics, which uses a history based parametric modelling which entails building a 3D geometry, piece by piece by using 2D sketches. Once the CAD model was established it was saved as a stl, format for the LENS® machine software. The stl file was sliced in layers perpendicular to the z-axis which were translated into laser scanning paths. The chosen design for the rotary burr is shown in APPENDIX B. The conventionally manufactured burr is shown in *Figure 3-7* and the burr dimensions in *Table 3-7*. During LENS® deposition, the component is fabricated on to a substrate and requires mechanical cutting for removal from the substrate. The burr length was increased by 5 mm to accommodate component removal.



Figure 3-7: Conventionally manufactured cylindrical rotary burr.

Table 3-7: Cylindrical rotary burr dimensions [144].

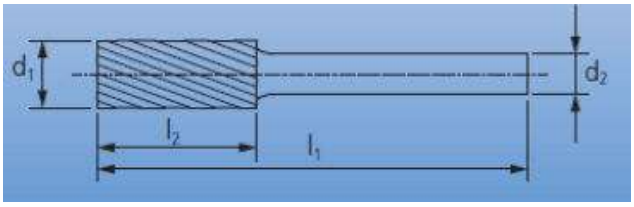

Shank diameter d_2 (mm)	Burr diameter d_1 (mm)	Burr length l_2 (mm)	Total length l_1 (mm)	Flute angle
6	12	25+5(to accommodate removal from substrate	65	50 flutes at a helix angle of 39° and 1mm depth

3.5.4.1 LENS® deposition of the cylindrical rotary burr

Two WC-FeCr hardmetal cylindrical rotary burrs were manufactured by the LENS® process using the optimum process parameters selected in Section 3.5.1. One burr was manufactured without any crack restraining technique and the other burr was manufactured using the crack restraining technique which was effective in reducing

the number of cracks as based on the testing methods shown in Section 3.5.3. The burr was sectioned from the substrate using the method described in Section 3.6.2, the dimensions of the rotary burrs were measured using a Vernier caliper and compared with the dimensions of the conventionally manufactured burr to verify part accuracy

3.5.4.2 Finite element analysis (FEA) of the cylindrical rotary burr

To understand the stress concentrations on the rotary burr at static conditions, a FEA analysis was done using MSC Patran® and Nastran® software to verify where the largest von Mises stresses were experienced. A structural analysis using first principle approach and FEA linear static assessment was done. The performance matrix used for the analysis was derived based on the burr functionality shown in APPENDIX B and is shown in *Table 3-8*.

.

Table 3-8: Performance requirements of the cylindrical rotary burr [144].

Component	Rotational speed (rpm)	Cutting speed (m/min)
Cylindrical rotary 6 mm burr without end cut	32000	600

The torque acting on the burr was calculated as shown in Eq. 3-9.

$$P = \frac{T\pi n_{rpm}}{30} \qquad \text{Eq. 3-9}$$

where: P = Power of the rotary tool (W)

η = Rotational speed (rpm)

T = torque (Nm)

Once the torque (T) was established the stress concentration was calculated by using the maximum shear stress acting on the burr as shown in Eq. 3-10 to Eq. 3-13. Stress concentration is caused by stress raisers within the material surface such as scratches, notches and other surface imperfections.

$$\tau_{max} = k_{ts}\frac{Tr}{J} \quad \text{Eq. 3-10}$$

$$J = {\pi d^4}/{32} \quad \text{Eq. 3-11}$$

$$r = {d}/{2} \quad \text{Eq. 3-12}$$

$$\tau_{max} = \frac{16T}{\pi d^3} \quad \text{Eq. 3-13}$$

Where: τ_{max} = Maximum shear stress (MPa)

k_{ts} = Stress concentration factor which is 1 for brittle materials

J = Polar second moment of area

d = Diameter of the shank (m)

r = Radius of the shank (m)

A four nodes tetrahedral (tet4) element type mesh was used for the finite element analysis. The analysis boundary conditions was a fixed end at the burr shank. The properties of the WC-FeCr hardmetal used for the analysis is as follows:

- Elastic Modulus(E):513 MPa [112]
- Poisson Ratio(ν): 0.30 [145]
- The density of the optimum cube sample in Section 3.5.2 was used.

3.5.4.3 Benchmarking tests

The LENS® manufactured WC-FeCr hardmetal burr was benchmarked to conventionally manufactured burrs in terms of removal of previously deposited weld material as shown in Appendix. B weld deposit made from AWS A5.1 E7018-1 having a tensile strength of 490 – 5550 MPa was used for the test. The weld deposit was machined at one minute intervals for a total time of five minutes. The thickness of the weld deposit and substrate were measured using the Vernier caliper after each interval to record the amount of material removed by the two burrs. The burr which removed more material in the allocated time was selected as the better performing burr.

3.6 Material Characterization Tests

3.6.1 Powder particle size characterization

The powder size distribution of the WC, FeCr and WC-10wt% FeCr powders was obtained by the use of the Malvern Mastersizer-S. During particle size analysis through the laser diffraction method, the powders are dispersed and circulated by water through the machine. An angular distribution of light passes through the optically dilute dispersion of suspended particles [146]. Larger particles scatter light at small angles and small particles at large angles relative to the laser beam. The Mastersizers' optical unit (comprises annular detectors) captures the actual scattering pattern from a field of particles and the Malvern software analyzes the angular scattering intensity data to calculate the sizes of the particles responsible for creating the scattering pattern. The particle size is then reported as the volume equivalent sphere diameter.

3.6.2 Sample cutting

The thin wall and cube samples were removed from the substrate by using a Struers Secotom-10 precision cutting machine, with a 12 cm diameter Struers diamond coated wheel. The wheel cutting speed was set at 3500 rpm with a feed rate of 0.015 mm/s. Water was used as a coolant during the cutting process.

3.6.3 Sample height measurements

The deposited thin wall and cube sample height measurements were carried out using a digital Vernier caliper precise to two decimal places. Measurements were done at five different positions and averaged to attain a representative height measurement.

3.6.4 Surface roughness

Surface roughness of the thin wall samples was measured using a Surtronic S128 Duo Surface Roughness Tester. The principles of this instrument involve placing the instrument pickup on the surface to be analysed and then tracing the surface profile at a constant rate. The distance that the machine should trace the sample is set by the user, here the distance was set to 2.5 mm. The pickup acquires the sample roughness by a sharp stylus located in the pickup. The surface roughness causes displacement of the pickup which results in a change in the inductive value of the induction coils within the pickup. This creates an analogue signal which is in proportion to the surface roughness.

3.6.5 WC-FeCr hardmetal sample preparation

Longitudinal sections from the thin wall samples and cross sections from the cube samples were prepared and hot mounted using Struers bakelite resin. Metallographic sample preparation was carried out in accordance with the requirements of ASTM B665 [147]. These were ground using Struers diamond grinding discs grit 220 and 1200 respectively and polished with a 6 µm, 3µm and 1 µm finish using a Struers diamond suspension in preparation for metallographic analysis.

The samples were analyzed in both the as-polished and etched state. As-polished samples were used to analyze the porosity within the samples. Etching was done with a Murakami's etchant (potassium ferricyanide, $K_3Fe(CN)_6$, sodium hydroxide, NaOH; and water with a mass ratio of 1:1:10) in order to reveal the microstructure, scanning pattern, binder evaporation and intermediate phases formed during deposition.

3.6.6 Powder morphology

The morphology of the WC, FeCr and WC-10wt% FeCr powders was analyzed using a Camscan Maxim 2000 scanning electron microscope (SEM). Both the secondary electron (SE) and backscattered electron (BSE) mode were used for SEM analysis. BSE signals are dependent on the mean atomic number which allows phases with different atomic numbers to be recognised, as a result heavier element which backscatter more efficiently will appear brighter than lighter elements in the electron image [148].

3.6.7 Porosity

The level of porosity of the feedstock WC, FeCr powders and the deposited single wall and cube samples was analyzed using an Olympus GX51 optical microscope. Optical microscopy analysis was carried out at a magnification of 100x (magnification of the eyepiece x magnification of the objective lens). A total of 4 images per sample were used. An imageJ software was used to quantify the porosity. This software is a computer image analysis tool which separates the image into different shades of gray in order to visually magnify the porosity and allow for binarization. A binary image is divided into a background and objects and allows for these objects to be counted and morphology analysis to be done. ImageJ binarization is done using the threshold option, which separates the porosity from the background. The image analysis software measured the level of porosity by counting the pixels for the porosity to give the percentage area. The porosity of the thin wall and cube samples were measured in terms of circularity in terms of the circularity range namely 0 – 0.3, 0.31 – 0.5, 0.51 – 0.8, 0.81 – 1, and a circularity range of 0 – 1 so as to distinguish between lack of fusion and gas porosity whereby gas porosity was given a circularity range of 0.8 – 1 and lack of fusion porosity was less than 0.8.

3.6.8 WC-FeCr hardmetal microstructure

The microstructure, and deposition pattern of the single wall samples in the etched condition were revealed by an optical microscope with an objective lens of 5, 10, 20, 50 and 100 X. The digital camera of the microscope was connected to computer acquisition software in order to view, capture, record and store the micrographs of samples in digital format.

3.6.9 Elemental chemical analysis

The elemental chemical analysis of the substrate was carried out by mass spectroscopy. The elemental chemical analysis of the WC, FeCr, WC-10wt% FeCr powder and thin wall samples were carried out by means of energy dispersive spectroscopy (EDS) which is attached to the SEM. The EDS results from the

feedstock powders were compared with the chemical composition certificates from the suppliers. EDS analysis cannot quantify carbon, because light elements are difficult to analyse due to their low photon energies, carbon was therefore excluded from the analysis. A Cameca SX5-FE electron probe micro-analyzer (EPMA) was used for the chemical analysis of the optimized cube sample using wavelength-dispersive spectroscopy (WDS. In comparison to the SEM, the EPMA is capable of acquiring precise, quantitative elemental analysis at small spot sizes (1 -2 µm) by WDS and the quantification of carbon could be carried out.

3.6.10 Phase analysis

Phase analysis and the crystal structure of the phases in the WC- FeCr hardmetal, single wall and optimum cube samples were carried out by means of a Bruker D2 X-ray diffraction (XRD) spectroscopy machine with a copper (Cu) radiation (wavelength of 1.54060 Å) and a traverse speed of 2 degree/min. The principles of XRD involve the production of X-ray radiation by the application of high voltage (30 kV) across a filament to discharge electrons focused at a target. The target material in a Bruker D2 Phaser is made of Cu, which produces X-rays at 1.54 Å. The X-rays that are generated are directed at the sample at an angle of theta (θ). When the X-rays encounter an atom they can either be absorbed, reflected or transmitted. Bragg's law is obeyed if the X-rays are reflected at angle θ, hence ensuring maximum intensity results. *Figure 3-8* shows a diffracted x-ray beam. Metal powders are made of crystal structures which are made of repetitive 3-dimensional unit cells such that when X-rays are diffracted. The intensity and positions of these peaks are used to identity the underlying structure. An EVA software program was used to determine the structure of the sample from the collected diffraction patterns.

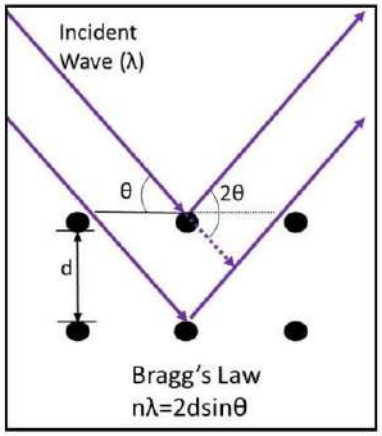

n an integer

λ wavelength

d distance between the crystal lattice planes

θ angle of incidence

Figure 3-8: Example of a crystal lattice where the black circles represents lattice points, the purple arrows are the incoming and scattered x-ray [10].

3.6.11 Hardness

The single wall samples hardness profile from the substrate end to the top layers and hardness of the different phases observed during metallographic examination were measured using an FM-800e micro-Vickers hardness machine with a diamond indenter under a load of 50gf. Vickers macro-hardness measurements were done by means of an Innovatest Nexus 8000 series universal hardness machine where a diamond indenter with a load of 30 kgf was applied. Three indentations were done and averaged for each hardness value. Hardness measurements were done in accordance with the requirements of ISO 3878 [149].

3.6.12 Fracture toughness

The fracture toughness of the deposited samples was evaluated by means of the Palmqvist method in accordance with ISO 28079 [82]. This method involves Vickers hardness indentation of the samples in accordance with ISO 3878 and then measuring the crack lengths emanating from the corners of the indents (*Figure 3-9*). The fracture toughness was then calculated using Eq. 3-14.

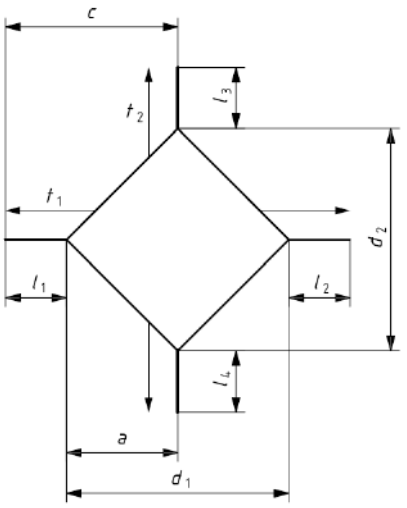

Figure 3-9: Palmqvist indentation characteristics.

$$K_{IC} = 0.15\sqrt{\frac{HV30}{\sum l}} \quad \text{Eq. 3-14}$$

where $\sum l$ is the sum of crack lengths [150], and HV is the Vickers hardness.

3.6.13 Density

The density of the cube sample was measured using Archimedes' principle in accordance with ASTM C373-88 [151]. The cube samples were boiled in distilled water for five hours in order for the water to be absorbed into the pores. Hereafter the samples were weighed in distilled water to attain the suspended mass (W3) and in air to attain the wet mass (W2) using a Sartorius ED224S density measuring machine. The samples were then placed in an oven, set at 80 °C, for 24 hours to dry and following drying the samples and weighed to attain the dry mass (W1). The equations below (Eq. 3-15 to Eq. 3-20) were used to calculate the open porosity and true density of the samples [151].

$$True\ Volume\ of\ Sample = \frac{W1-W3}{\rho w} \quad \text{Eq. 3-15}$$

where: ρw is the density of distilled water at room temperature.

$$True\ Density\ of\ Sample = \frac{W1\rho w}{W1-W3} \quad \text{Eq. 3-16}$$

$$\%\ Densification = \frac{True\ density}{Theoritical\ density} \times 100\% \quad \text{Eq. 3-17}$$

$$Theoritical\ Density\ \left({}^{g}/_{cm^3}\right) = 100\ wt\% \times \left[\frac{90\ wt\%\ WC}{\rho WC} + \frac{10\ wt\%\ FeCr}{\rho FeCr}\right] \quad \text{Eq. 3-18}$$

$$Volume\ of\ Open\ Porosity = \frac{W2 - W1}{\rho w} \quad \text{Eq. 3-19}$$

$$Volume\ \%\ Open\ Porosity = \frac{W2 - W1}{W2 - W3} \times 100\% \quad \text{Eq. 3-20}$$

3.6.14 Thermal profiling

In order to understand the thermal profile from the deposition fusion line to the top layer of the sample, the Rosenthal [152] heat flow equations were used. The Rosenthal equations have been applied to arc welding thermal cycles, however, in this study these equations were applied to the LENS® process. The thermal profile will assist in understanding the hardness profile properties. A number of assumption were made in order to apply Rosenthal's equations [152], and these included:

a) A moving point source represents the laser beam.
b) The thermal conductivity and specific heat are not affected by changes in temperature.
c) Heat transfer is by conduction only and heat loss at the substrate is negligible.
d) Latent heat changes are negligible.

The thick plate three-dimensional heat flow was chosen for the calculations because during laser deposition full heat penetration of the substrate does not occur. *Figure 3-10* shows the different heat flows predicted by Rosenthal [152].

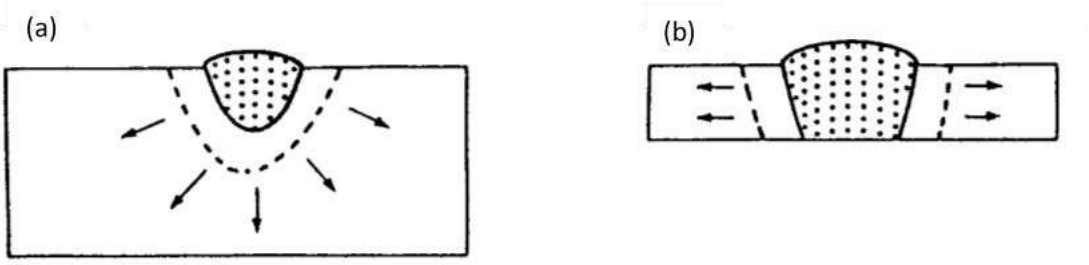

Figure 3-10: (a) Three-dimensional heat flow, (b) Two-dimensional heat flow [61].

The temperature profile across the sample height was calculated using Eq. 3-21 [152].

$$T - T_0 = \left(\frac{2}{\pi e}\right)\frac{q/v}{\rho c r^2} \qquad \text{Eq. 3-21}$$

Where: T = the temperature at a distance r from the heat source (K)

T_0 = the original temperature of the substrate prior to deposition (K)

q = the laser power (W)

v = the traverse speed (m/s)

ρc = the specific heat per unit volume ($Jm^{-3}K^{-1}$)

r = the radial distance from the heat source (m)

r is calculated by using Eq. 3-22.

$$r = \sqrt{(x^2 + y^2 + z^2} \qquad \text{Eq. 3-22}$$

Where: x is the distance from the moving heat source in the x-direction (x > 0 for point in front of the heat source, and x < 0 for points behind the heat source.

y is the distance from the heat source in the y-direction

z is the distance from the heat source in the z-direction

The movement of laser heat source during the deposition of a single layer is shown in *Figure 3-11*. The heat distribution along the deposition length and height was calculated using the Rosenthal equations and parameters shown in *Table 3-9*.

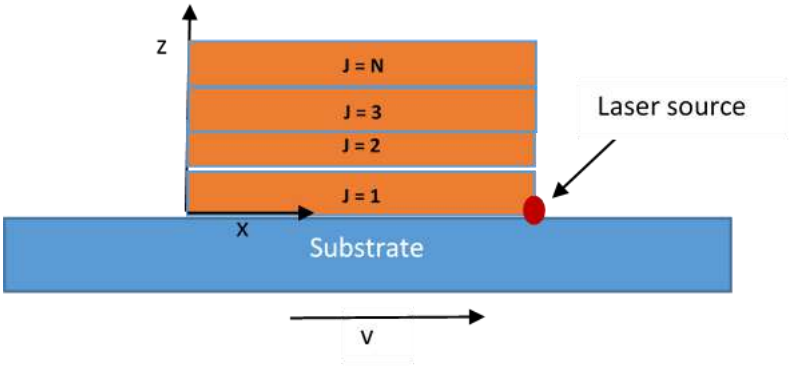

Figure 3-11: Schematic representation of the single wall sample.

During the LENS® process the first layer was deposited for a length of 25.4 mm. The temperature across the length of the sample was established by calculating the temperatures at different distances away from the laser source for a single layer sample.

Table 3-9: Experimental conditions for single wall builds.

Meaning	**Symbol**	**Unit**	**Value**
Temperature of the substrate	T_o	K	298
Laser power	q	W	200
Traverse speed	v	m/s	0.0032
Heat input	(q/v)	J/m	62500
Time (first layer)	t	s	10
Distance from heat source	r	m	0.0014
Thermal diffusivity	a	$m^2.s^{-1}$	0.000039 [124]
Thermal conductivity	λ	$J.m^{-1}.s^{-1}.K^{-1}$	111 [124]
PI	π		3.141592654
e			2.718281828
z-increment		m	0.0002
Specific heat per unit volume	ρc	$Jm^{-3}K^{-1}$	2846153.846
Measured wall length	L	m	0.0254
Sample height	h	m	0.00792

3.6.15 Liquid dye penetrant testing

The samples that underwent crack testing were transversely sectioned and cleaned for contamination; once the surfaces were dry the red penetrant was sprayed on the surfaces for a dwell time of 10 minutes after which it was wiped using a clean lint cloth. A developer was then applied to draw out the red penetrant from the defects. Inspection of the cracks was done after 10 minutes.

CHAPTER 4 Characterization of Feedstock Powders

4.1 Introduction

This chapter presents the properties of the feedstock powders used for the deposition of the WC-FeCr hardmetals. The powder particle size distribution (PSD), chemical composition, powder morphology and porosity of the individual WC and FeCr powders were investigated to ensure that the powders were suitable for the LENS® process and the results were also used to assess possible impact on the material properties.

4.2 Particle Size Distribution (PSD)

Figure 4-1 and *Table 4-1* show the D_{10}, D_{50}, D_{90}, mean sizes and the nominal particle sizes which describes the PSD of the WC, FeCr and WC-10wt% FeCr powders. The particle sizes of all the powders were within the required range of the LENS® machine (36 – 150 μm) [41]. The particle size distribution of the WC-10wt% FeCr was also analyzed in order to verify whether agglomeration or fragmentation occurred during the blending process and from the PSD of the WC-10wt% FeCr no agglomeration was evident as it was similar to the WC feedstock powder. The PSD of both feedstock powders were similar to the specified supplier's material certificates. The powder size distribution of the blended WC-10wt% FeCr powder resembled that of the WC powder because the mixture was predominately WC.

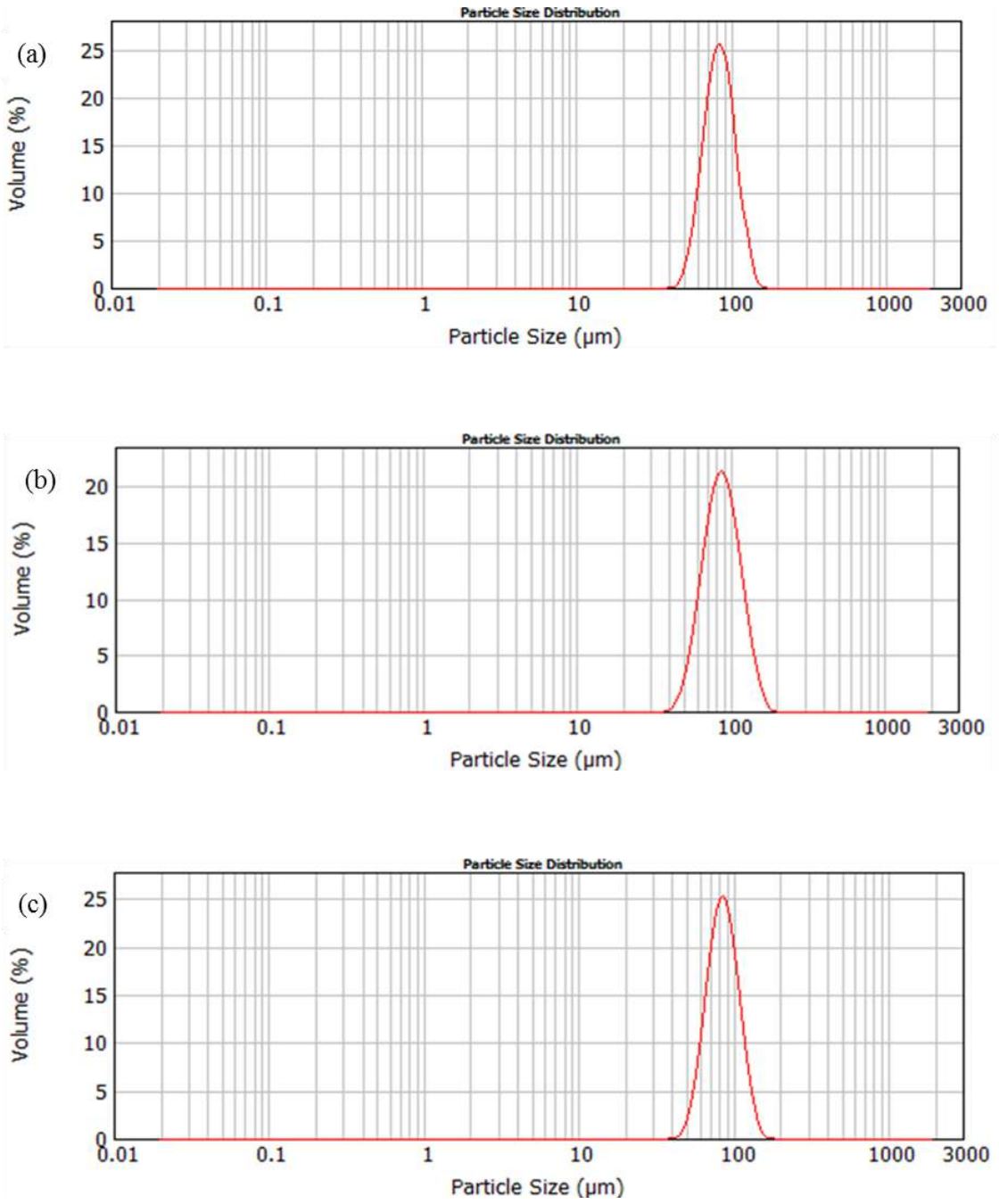

Figure 4-1: PSD (a) WC powder, (b) FeCr powder, (c) WC-10wt% FeCr powder.

Table 4-1: Powder size distributions.

Size/Powder	WC	FeCr	WC- 10 wt.% FeCr
D10 (µm)	62.577	61.413	62.911
D50 (µm)	83.902	87.318	84.775
D90 (µm)	112.031	124.284	114.018
Mean (µm)	85.970	90.581	86.984
Nominal size (µm)	+45 -114	+45 -125.6	+45 -115
Supplier specification (µm)	+45 - 90	+52 - 125	

4.3 Morphology

The WC powder was spherically cast and during SEM analysis it displayed a spherical morphology, the particles displayed darker spots on the particle surface (*Figure 4-2*). The FeCr powder comprised of spheroidal and spherical particles with evidence of smaller satellites attached to the main particles (*Figure 4-3*). The morphology of the WC-10wt% FeCr powder did not display the presence of fragmentation or agglomeration during blending, and showed a close to homogenous mixture. *Figure 4-4* shows the backscattered electron image (BEI) of the powder, the WC powder particles appeared brighter than the FeCr powder particles.

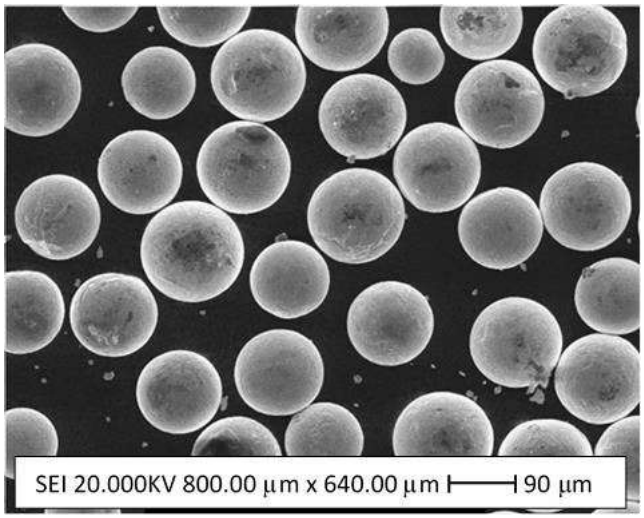

Figure 4-2: SEM-SEI image of the feedstock WC powder.

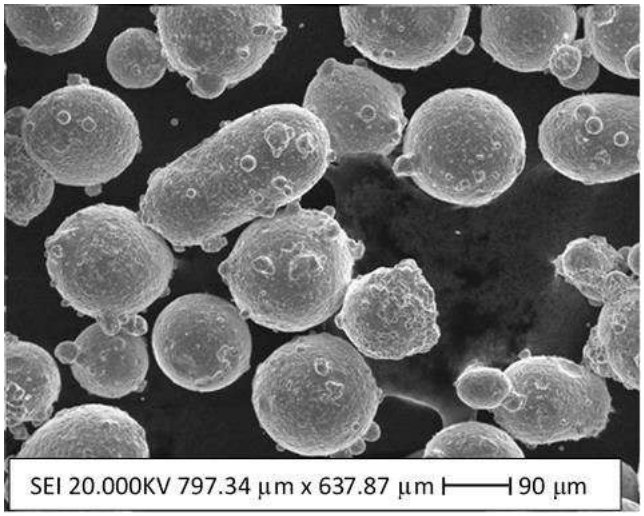

Figure 4-3: SEM-SEI image of the feedstock FeCr powder.

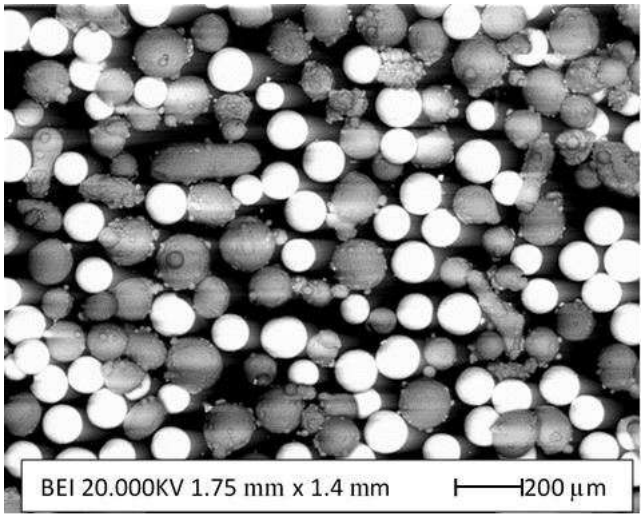

Figure 4-4: SEM-BEI image of the WC-10wt% FeCr.

4.4 Chemical Composition

Figure 4-5 and *Figure 4-6* shows the point elemental analysis positions and results of the WC and FeCr powders. The results were compared to the supplier's material certificate results shown in *Table 3-1* and *Table 3-2* , it can be seen that the dark spots found on the WC particles were elemental contamination of oxides, chlorine, calcium, potassium, and sodium. No contamination was evident in the FeCr powder as the composition was similar to the supplier's material certificate.

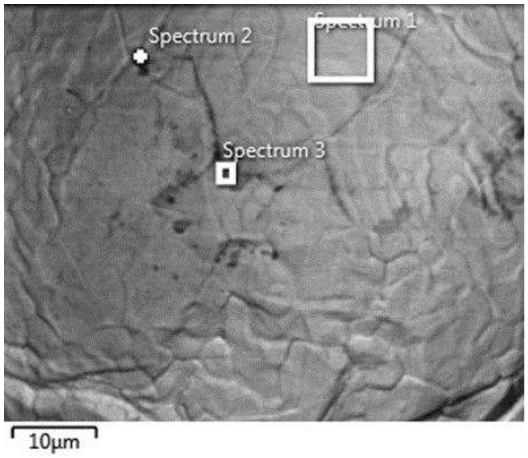

Spectrum Label	Spectrum 1	Spectrum 2	Spectrum 3
O	0.81	9.79	6.67
Na		0.95	0.53
Cl		0.94	0.33
K		0.39	0.25
Ca		0.93	0.38
Fe		0.37	
Co		0.84	0.73
W	99.19	85.8	91.11

Figure 4-5: EDS analysis area and results of the WC particle.

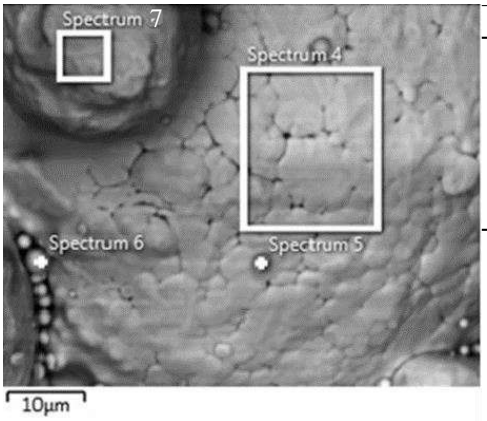

Spectrum Label	Spectrum 4	Spectrum 5	Spectrum 6	Spectrum 7
O	0.43	0.44	0.87	
Al		0.33	0.34	
Si	0.48	0.18	1.02	0.92
Cr	14.15	17.09	13.35	13.47
Mn	1.43	2.55	1.22	1.2
Fe	83.51	79.41	83.2	84.41

Figure 4-6: EDS analysis area and results of the FeCr particle.

Figure 4-7 shows the EDS elemental mapping of the WC-10wt% FeCr powder. The main elements detected were W, Fe, Cr, C and O as expected from the chemical composition of the individual powders. *Table 4-2* shows the EDS chemical results of the WC-10wt% FeCr powder in comparison to the stoichiometric calculations. Carbon was omitted from the analysis as the EDS could not accurately quantify it, as light elements are difficult to analyse because of their low photon energies hence carbon was excluded from the analysis.

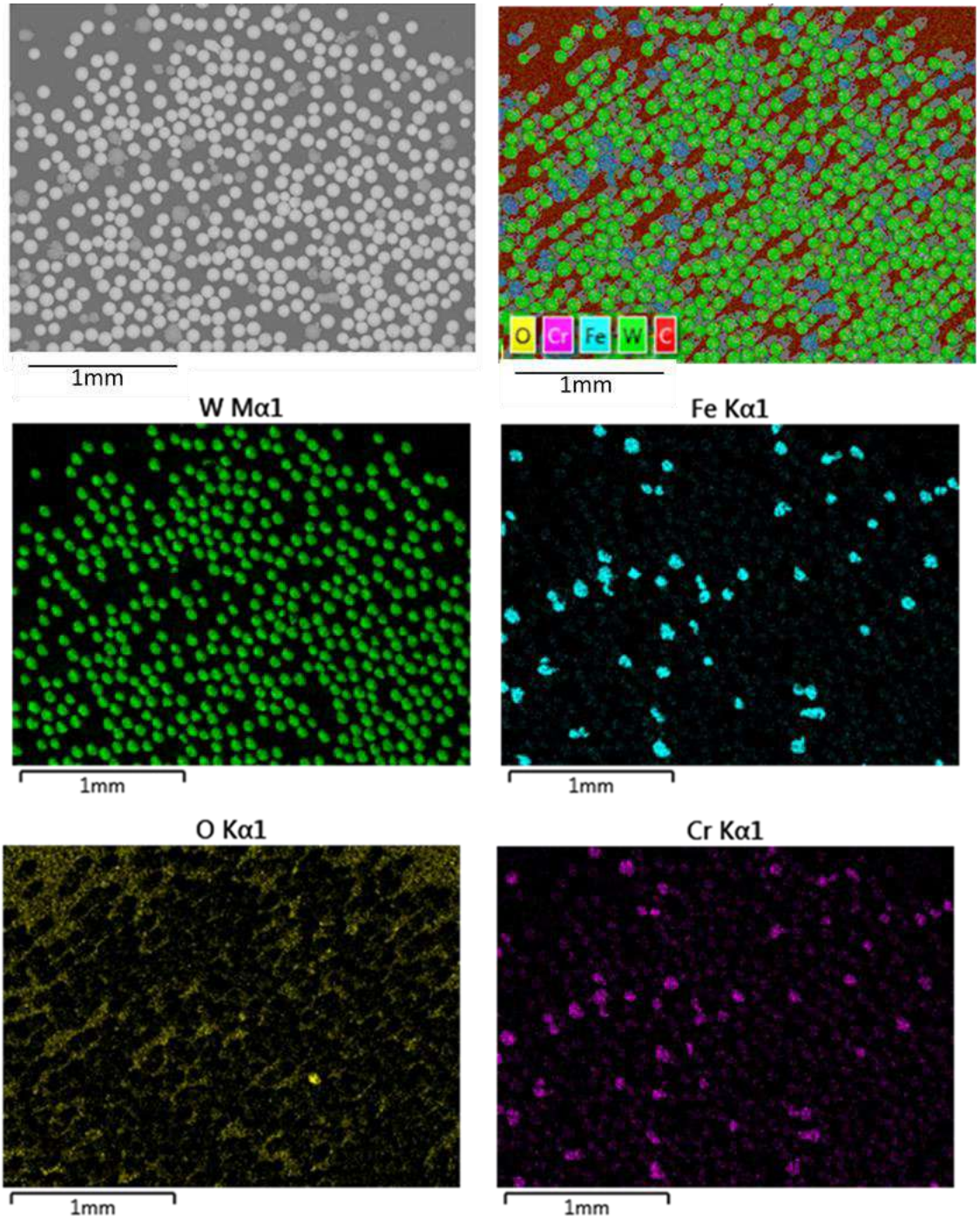

Figure 4-7: EDX mapping of the WC-10w.t% FeCr powder.

Table 4-2: EDS results of WC-10wt% FeCr compared to calculated results from the material certificates.

Composition	**WC**		**FeCr**	
	W	**C**	**Fe**	**Cr**
WC- 10 w.t.% FeCr (calculation)	86.28	3.49	8.47	1.32
EDS results	84.4 ±0.1		7.6 ± 0.1	1.6 ± 0.1

4.5 Phase Analysis

The WC powder had three phases namely; di-tungsten carbide (W_2C), tungsten carbide (WC) and elemental tungsten (W). The peaks for WC were located at 2θ = 31.3, 35.4 and 48.1°. W_2C peaks were located at 2θ = 34.3, 37.8 and 39.3. A weak tungsten (W) peak was observed at 40.1°. Both WC and W_2C were major phases because both had the highest peaks, with WC having two highest peaks at 2θ = 35.4 and 48.1 and W_2C having the highest peak at 2θ = 39.3. The FeCr had one strong α-Fe peak located at 44.5°. The WC-10wt% FeCr powder had cementite (FeCr), WC, W_2C and α-Fe phases. *Figure 4-8* to *Figure 4-10* shows the XRD spectrums for the powders.

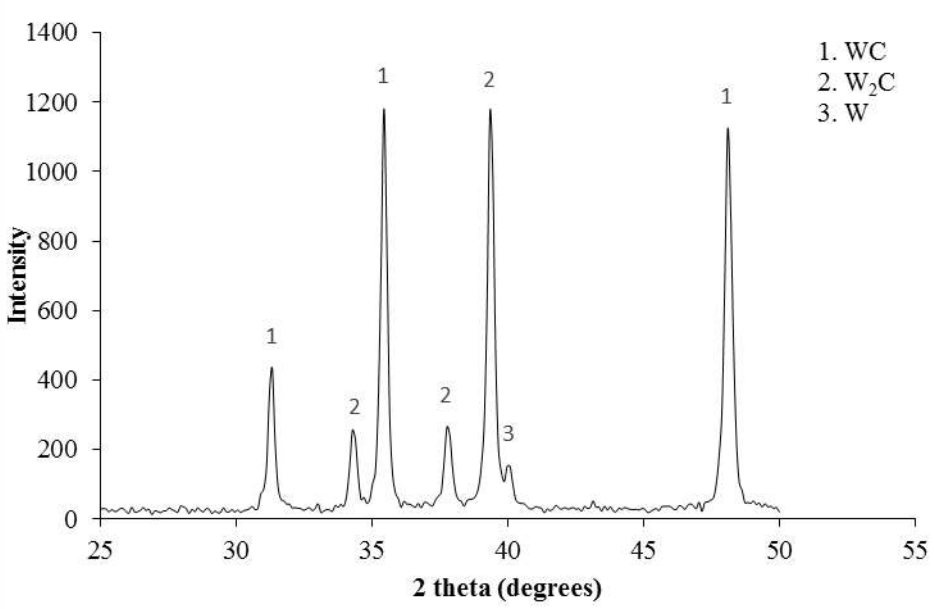

Figure 4-8: XRD spectrum of the WC/W_2C powder.

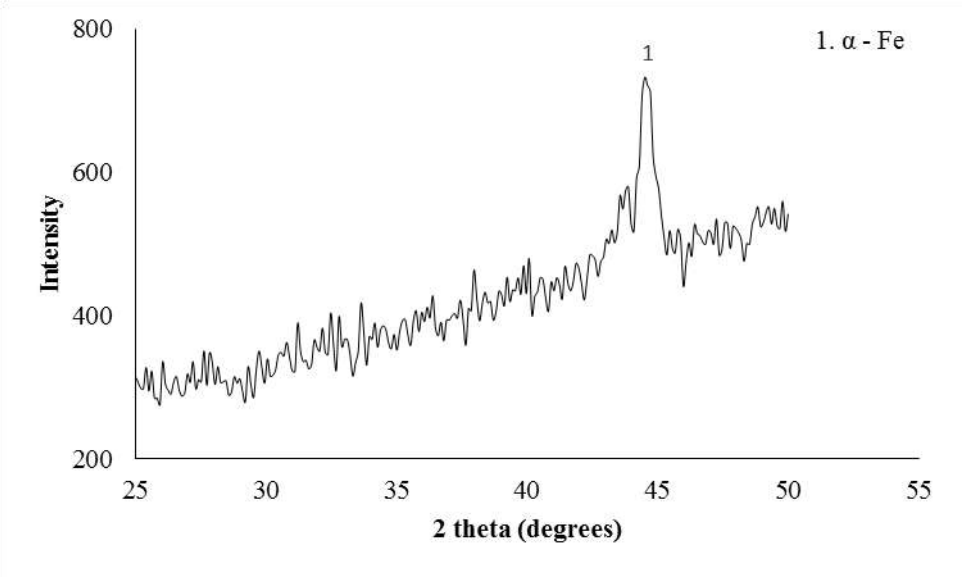

Figure 4-9: XRD spectrum of the FeCr powder.

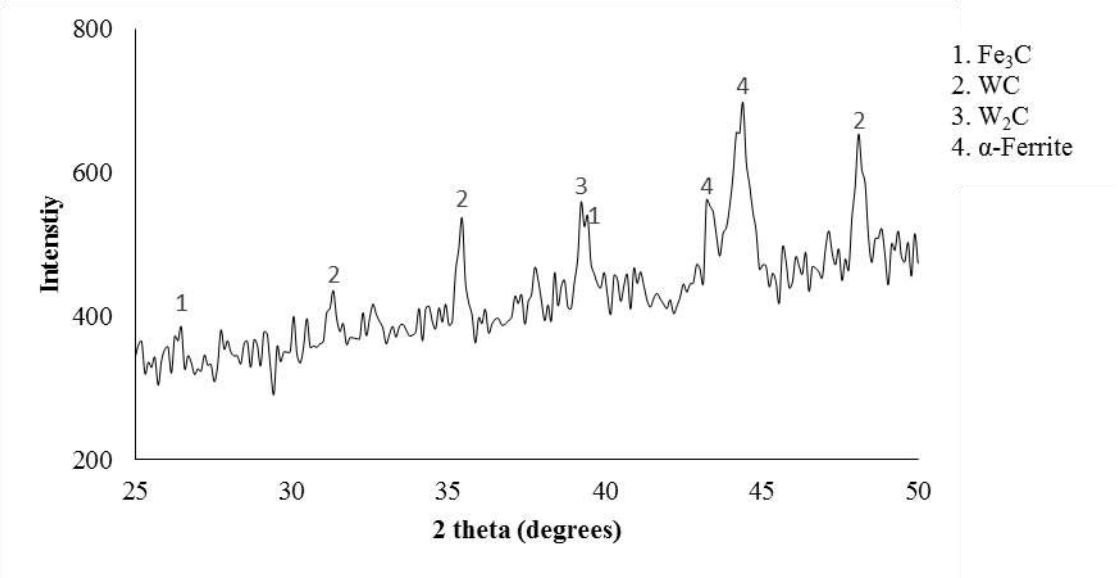

Figure 4-10: XRD spectrum of the WC-10wt% FeCr.

4.6 Porosity Analysis

Figure 4-11 and *Figure 4-12* shows the optical microscopy (OM) used for porosity analysis and the porosity results for the WC and FeCr powder. The porosity observed on the powders had a spherical morphology.

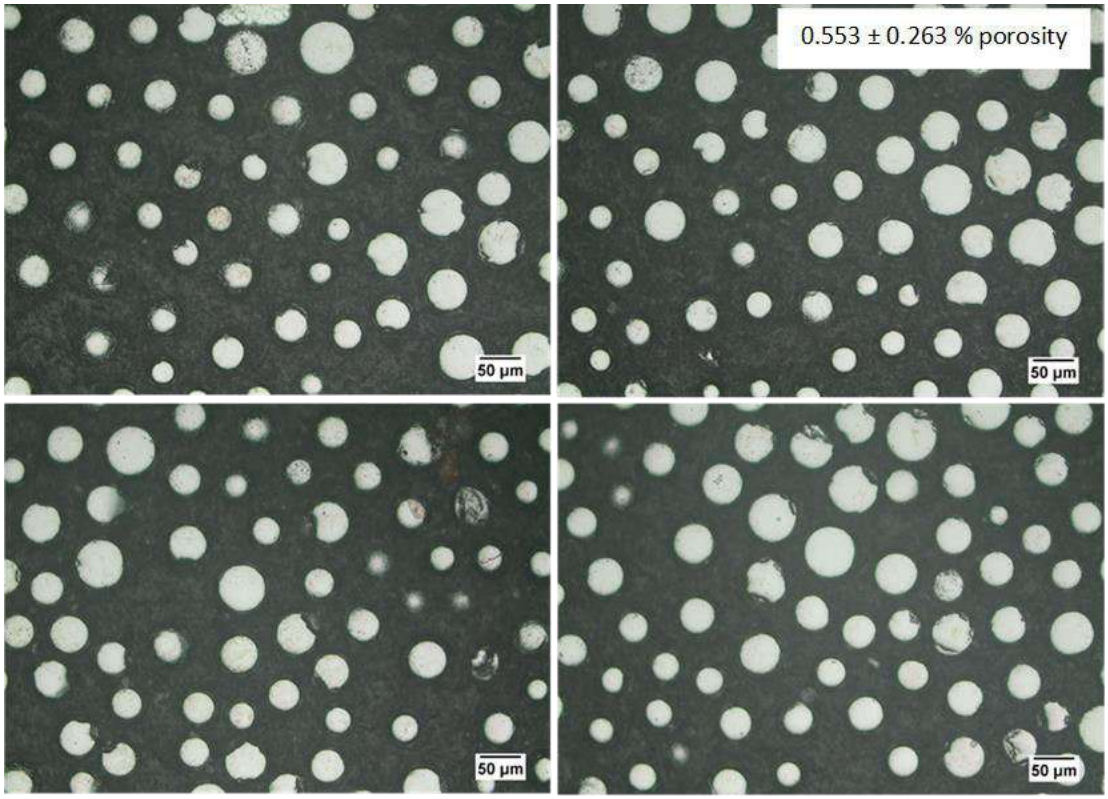

Figure 4-11: OM images of the WC powder.

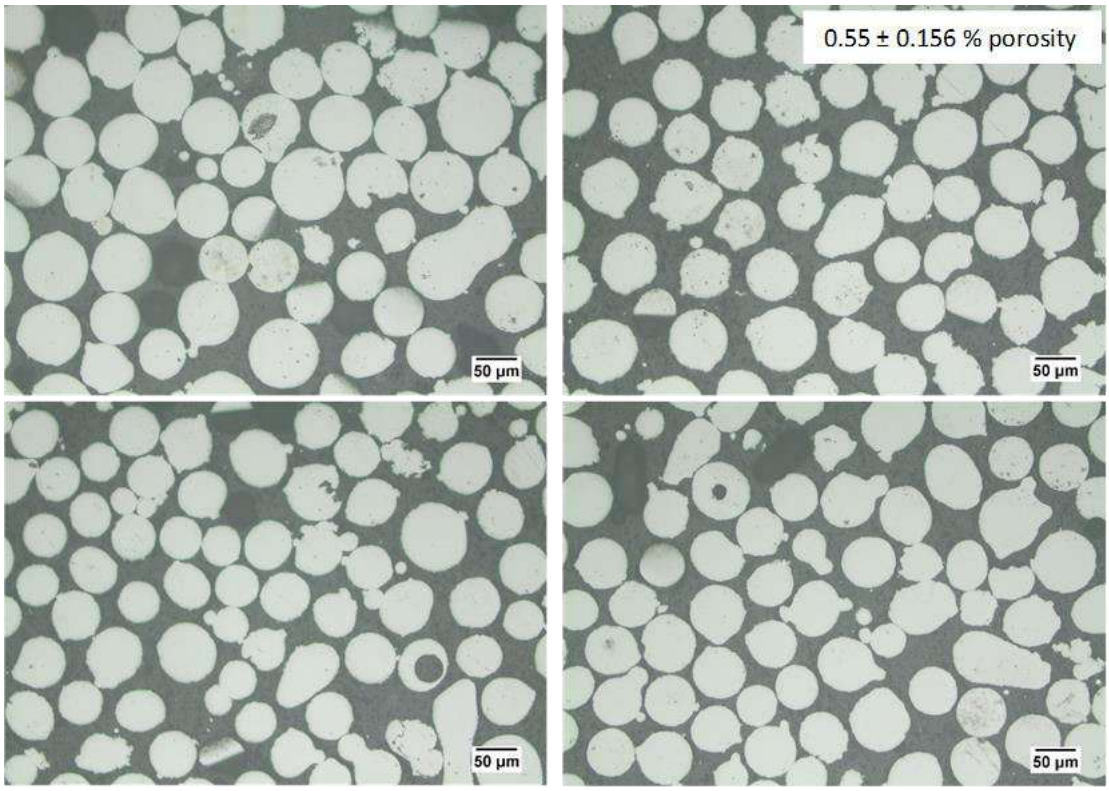

Figure 4-12: OM images of the FeCr powder.

CHAPTER 5 Thin wall and Cube Deposition Results and Analyses

5.1 Introduction

This chapter highlights the results from the full factorial DoE technique used for the optimization of process parameters in the LENS® deposition of WC-FeCr hardmetals. Thin wall samples were deposited and the effects of process parameters namely laser power, powder feed rate and traverse speed on the experimental responses namely, sample height and porosity were investigated. Regression analysis was carried out to establish the mathematical relationship between the process parameters and experimental responses. Optimization was done in a stepwise process, firstly a GRG technique was done to optimize the sample height and reduce the sample size for further analysis, secondly a MOO using the Pareto technique was carried out to optimize both the sample height and porosity, and finally the influence of the z-increment on the experimental responses was investigated and optimum parameters were established. Cube samples using the optimum parameters were deposited for further refinement.

5.2 Optimization of Sample Height

5.2.1 Sample profile

Figure 5-1 shows the deposited thin wall samples based on the DoE matrix presented in Section 3.5.1, *Table 3-5*. Sample 14 (300 W, 8.5mm/s, 7.3 g/min), 24 (400 W 8.5 mm/s, 12.2 g/min) and 25 (400W, 6.4 mm/s, 7.3 g/min) showed cracking and delamination (*Figure 5-2*) which is caused by poor adhesion with the substrate due to different reasons such as, differences in the coefficient of thermal expansion between the substrate and deposited material, a substrate material which was not cleaned from contamination prior to the deposition process, or insufficient heat for powder melting. It was also observed that the shape profile of some of the samples were not uniform on the last to be deposited layers. This is clear that not enough metal powder was captured into the molten pool.

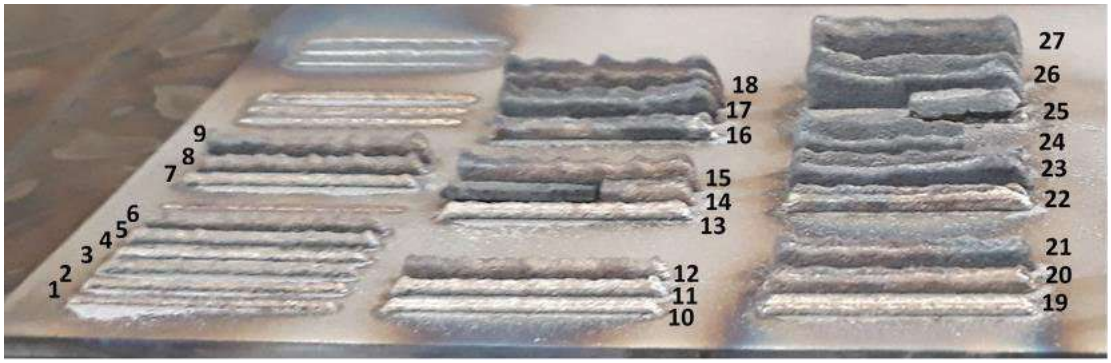

Figure 5-1: DOE single wall samples.



Figure 5-2: Sample profile of the thin walls.

5.2.2 Effect of process parameters on sample height

Table 5-1 shows the height measurements obtained for the thin wall samples and *Figure 5-3* to *Figure 5-5* show the influence of traverse speed and powder feed rate on sample height, an increase in the traverse speed resulted in a decrease in the sample height. At fast traverse speeds there is less contact time for the powder-laser interaction, this results in less heat available to melt the powder and less powder is introduced into the molten pool. The relationship between heat input and traverse speed is presented in Eq. 3-7, where heat input decreases with an increase in the traverse speed. An increase in the powder feed rate led to an increase in sample height.

Table 5-1: Sample height measurements.

Experimental runs	Power (W)	Speed (mm/s)	Feed rate (g/min)	Sample height (mm)
1	200	12.7	7.3	0.50 ± 0.093
2	200	12.7	10	1.20 ± 0.020
3	200	12.7	12.2	2.20 ± 0.059
4	200	8.5	7.3	1.40 ± 0.029
5	200	8.5	10	2.00 ± 0.25
6	200	8.5	12.2	4.00 ± 0.16
7	200	6.4	7.3	2.20 ± 0.12
8	200	6.4	10	3.00 ± 0.062
9	200	6.4	12.2	4.80 ± 0.15
10	300	12.7	7.3	1.10 ± 0.17
11	300	12.7	10	1.40 ± 0.01
12	300	12.7	12.2	2.70 ± 0.14
13	300	8.5	7.3	2.00 ± 0.091
14	300	8.5	10	2.60 ± 0.24
15	300	8.5	12.2	4.80 ± 0.025
16	300	6.4	7.3	2.60 ± 0.053
17	300	6.4	10	4.90 ± 0.036
18	300	6.4	12.2	6.80 ± 0.057
19	400	12.7	7.3	1.80 ± 0.015
20	400	12.7	10	2.30 ± 0.029
21	400	12.7	12.2	3.10 ± 0.084
22	400	8.5	7.3	2.40 ± 0.15
23	400	8.5	10	3.00 ± 0.32
24	400	8.5	12.2	5.00 ± 0.26
25	400	6.4	7.3	3.50 ± 0.15
26	400	6.4	10	6.38 ± 0.37
27	400	6.4	12.2	7.30 ± 0.12

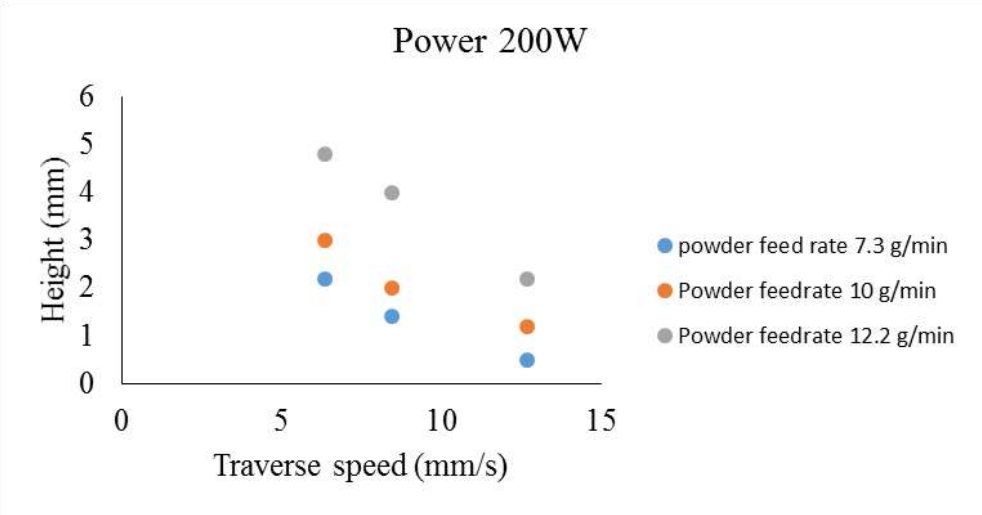

Figure 5-3: Effect of traverse speed and powder feed rate on sample height.

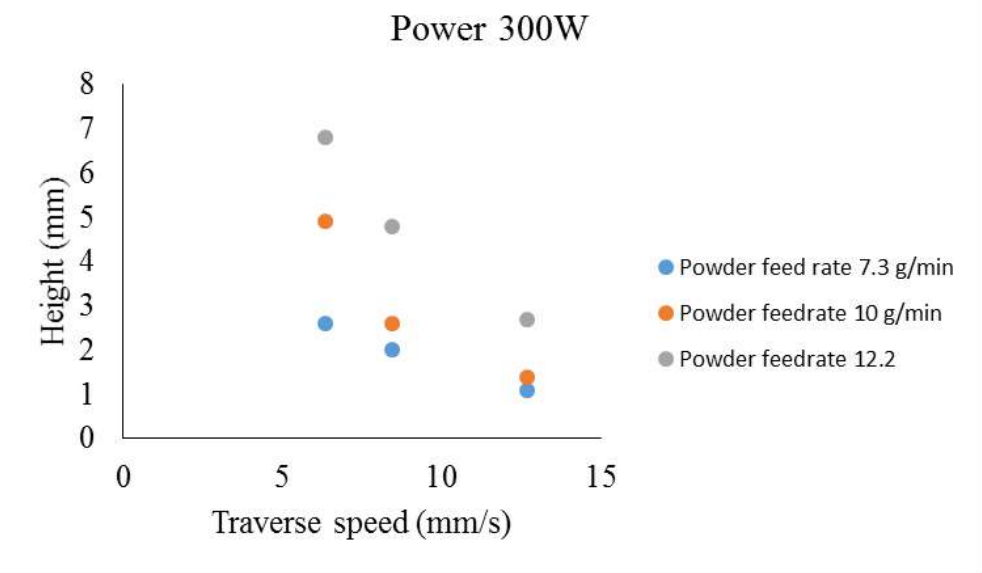

Figure 5-4: Effect of traverse speed and powder feed rate on sample height.

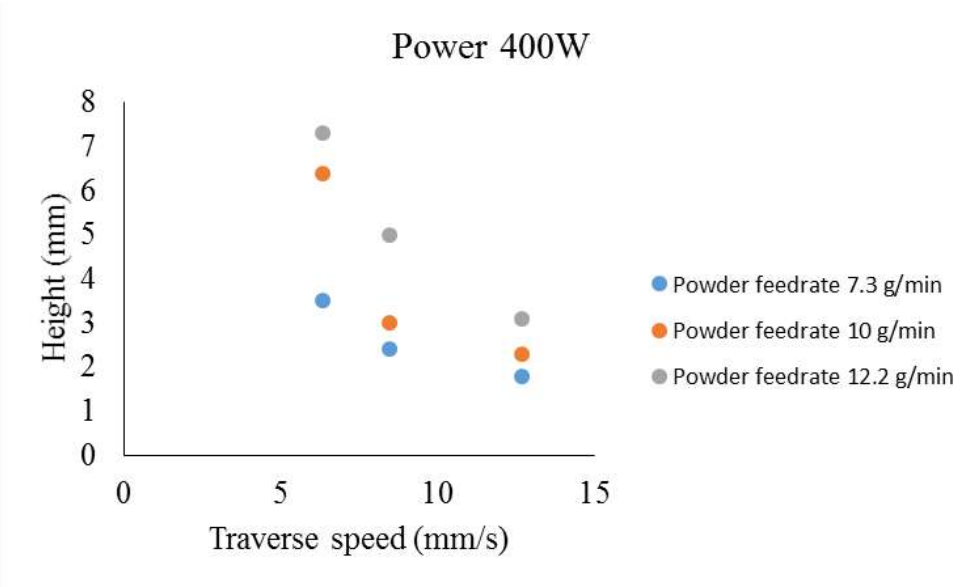

Figure 5-5: Effect of traverse speed and powder feed rate on sample height.

The effect of laser power on sample height is shown in Figure *Figure 5-6* to *Figure 5-8*, an increase in the laser power resulted in an increase in the sample height. An increase in the laser power leads to an increase in the heat input which contributes to an increase in the molten pool and hence sample height.

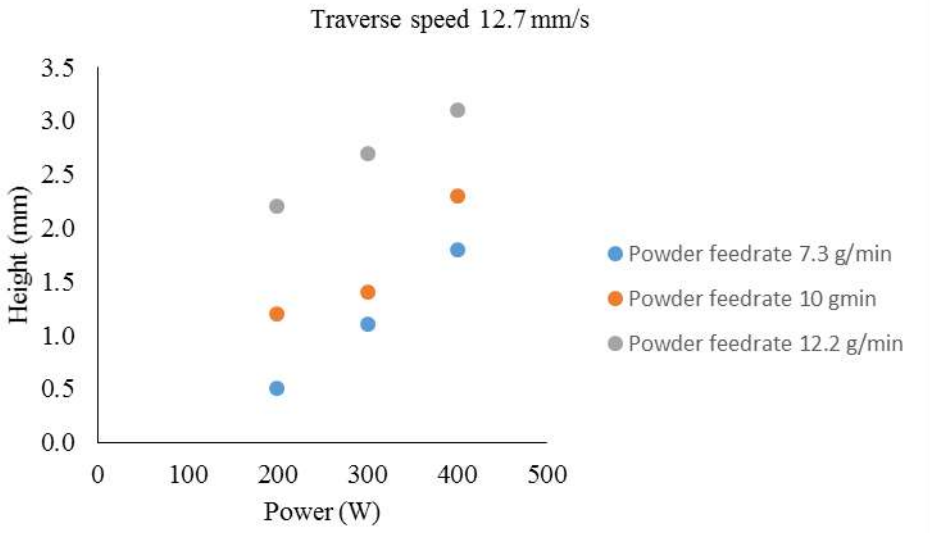

Figure 5-6: Effect of laser power and powder feed rate on sample height.

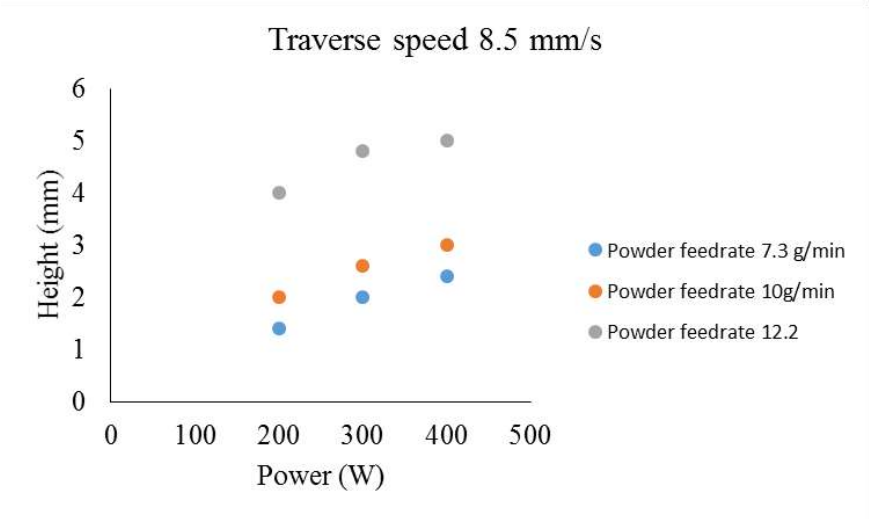

Figure 5-7: Effect of laser power and powder feed rate on sample height.

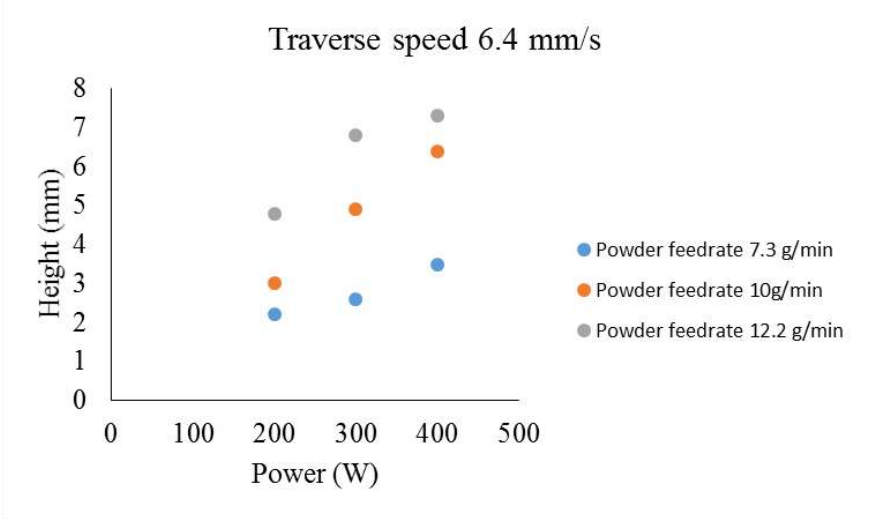

Figure 5-8: Effect of laser power and powder feed rate on sample height.

5.2.3 Regression analysis and parameter optimization

5.2.3.1 Regression analysis

The ANOVA regression analysis of the multiple linear, quadratic and exponential models, with sample height as the output response is shown in APPENDIX B. *Table 5-2* summarizes R^2 of the different models and the quadratic model was found to have the highest value. A R^2 value closer to 1 means that the model chosen represents the variability in the data better. From the analysis it is clear that the quadratic regression

model provides the best fitment, however R^2 can also be artificially inflated by higher order quadratic terms, hence R^2 cannot be the only statistical method used to measure the appropriateness of the model.

Table 5-2: R^2 value for the regression models.

Regression model	Multiple linear	Quadratic	Exponential
R^2	0.870	0.959	0.936

To further verify the adequacy of the models in describing the relationship between process parameters and sample height an F-test using the P-value was done as described in section 3.5.1 and a significance level $\alpha = 0.05$ was used, *Table 5-3* summarizes the results. The null hypothesis was rejected for all the regression models as all the P-values were below the significance level of the models, meaning all models were significant and all process parameters had an influence on the sample height.

Table 5-3: F-test of the regression models.

Model	Model P-value	Significance level (α)	F-test
Linear regression	2.49×10^{-10}	0.05	Reject null hypothesis
Quadratic regression	4.81×10^{-10}	0.05	Reject null hypothesis
Exponential regression	7.724×10^{-14}	0.05	Reject null hypothesis

Residual analysis was carried out to compare the adequacy of the exponential and quadratic regression models, the linear regression model had the lowest R^2 value and the relationship between process parameters and sample height was non-linear (*Figure 5-3* to *Figure 5-8*). The exponential model displayed a normal probability plot with data points falling within a straight line when compared to the quadratic models (*Figure 5-9* and *Figure 5-10*).

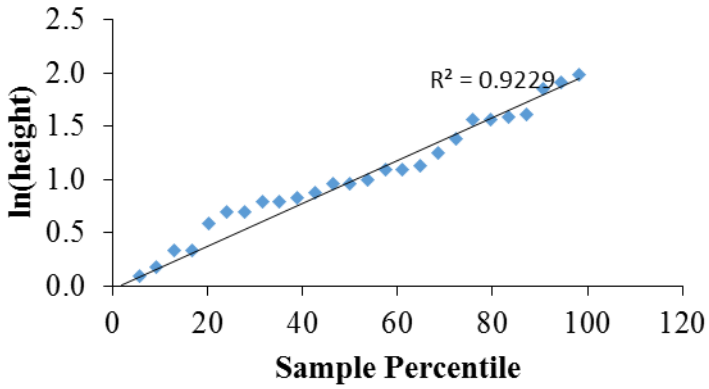

Figure 5-9: Normal probability plot for the exponential model.

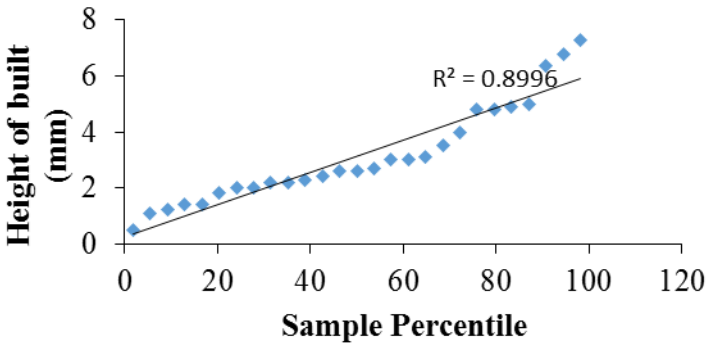

Figure 5-10: Normal probability plot for the quadratic model.

To further establish the adequacy of the regression models the residual plots were visually analyzed to verify whether the errors (residuals) were normally distributed with a constant variance. The random dispersion of points around the horizontal axis of a residual plot shows that the regression model is appropriate for the data. According to *Figure 5-11* and *Figure 5-12* the residual plot showed more randomness with less variability in the data for the exponential model as compared to the quadratic model. It can be concluded from the normal probability plot and residual plot that the exponential regression model showed the best fit for the experimental data. The influence of process parameters namely laser power, powder feed rate and traverse speed on sample height can therefore be best described by Eq. 5-1.

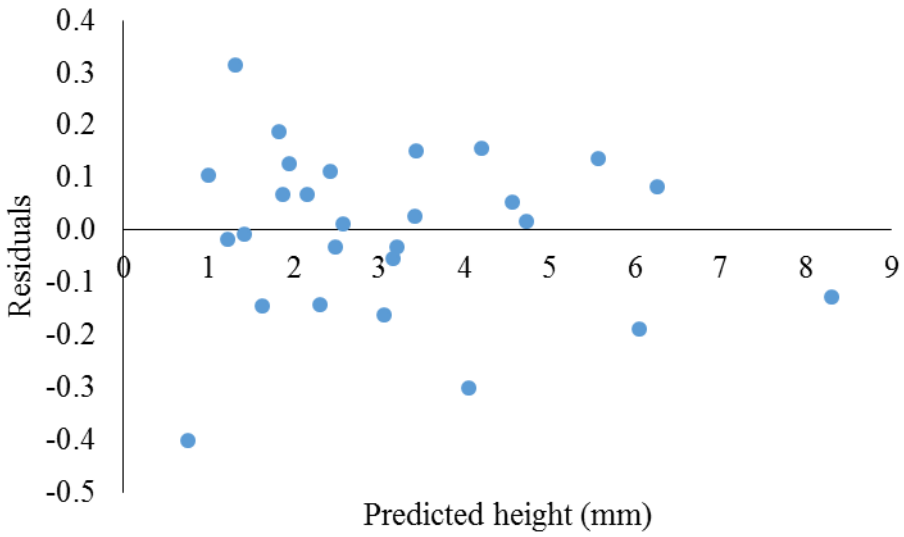

Figure 5-11: Residual plot for the exponential model.

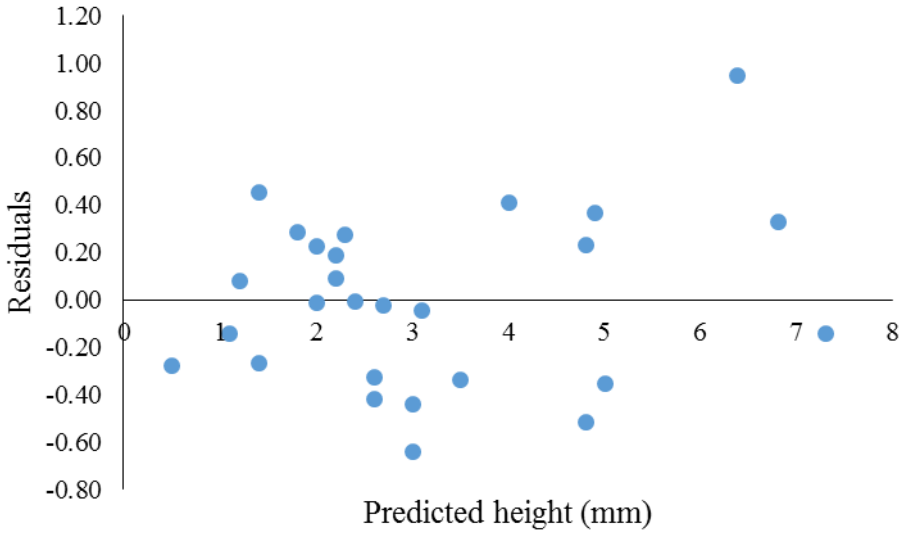

Figure 5-12: Residual plot for the quadratic model.

$$H = \exp(-0.28 + (0.0028P) - (0.15v) + (0.18F)) \qquad \text{Eq. 5-1}$$

where P (W) is the laser power, v (mm/s) is the traverse speed and F (g/min) is the powder feed rate.

5.2.3.2 Parameter optimization

Optimization was based on obtaining a sample height of 8 mm as described in Eq. 3-6. *Table 5-4* shows the optimum parameter results obtained from the GRG non-linear optimization technique using Solver, however these parameters were not part of the DoE (Table 3-5).

Table 5-4: Optimum process parameters according to Solver software package.

Parameter	Value
Laser Power (W)	200
Traverse Speed (mm/s)	3.2
Powder feed rate (g/min)	12.2
Sample height (mm)	8

The DoE parameters were extended to include a traverse speed of 3.2 mm/s, however it was observed that fumes accumulated in the LENS® machine chamber at a traverse speed of 3.2 mm/s and laser power of 400 W, hence this combination was not included in the experimental trials. Single wall samples were deposited in accordance with the extended DoE in *Table 5-5* and sample height measurements were carried out. The process parameters which yielded a sample height close to 8 mm was the same as the optimum parameters simulated using the GRG optimization technique. The measured height of the optimum parameter set was 7.92 mm.

Table 5-5: Extended DOE.

Power (W)	Traverse speed (mm/s)	Feed rate (g/min)	Height of built (mm)
200	3.2	7.3	4.3
200	3.2	10	5.4
200	3.2	12.2	7.92
300	3.2	7.3	6.57
300	3.2	10	7
300	3.2	12.2	8.5

5.3 Optimization of Sample Height and Porosity Simultaneously

5.3.1 Effect of process parameters on sample porosity

Porosity measurements were only done on samples which attained 50 % of the required height. *Figure 5-13* and *Figure 5-14* show the influence of laser power on porosity at different circularity ranges. The porosity with a circularity range of 0 – 0.5 decreased with an increase in laser power and the porosity with a circularity range of 0.51 – 1 increased with an increase in the laser power. Gas pores are spherical and have a circularity close to 1 and lack of fusion are irregularly shaped and have a circularity close to 0. In further defining the morphology of the pores, *Figure 5-15* and *Figure 5-16* show the aspect ratio of the pores at different circularity ranges, the aspect ratio decreased with an increase in circularity. Aspect ratio is the depth to width ratio and gives the morphology of the pores.

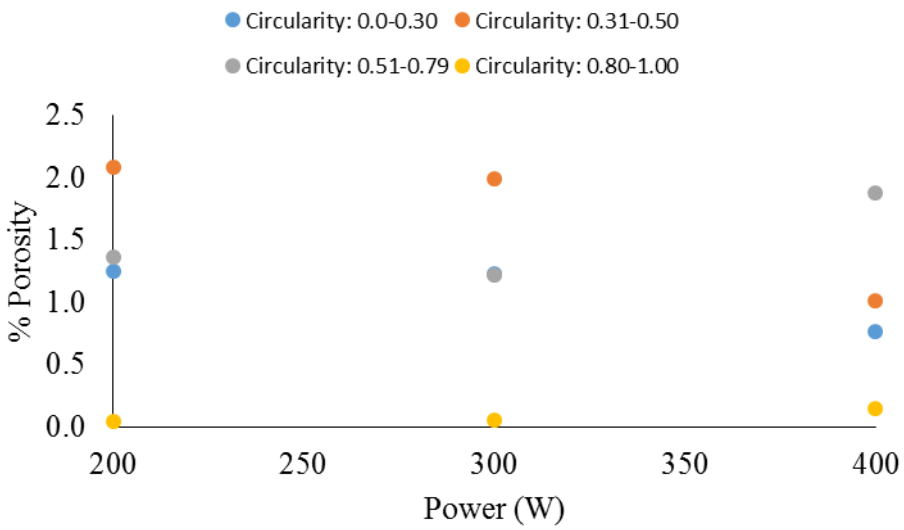

Figure 5-13: Effect of laser power on % porosity at a traverse speed of 8.5 mm/s and powder feed rate of 12.2 g/min.

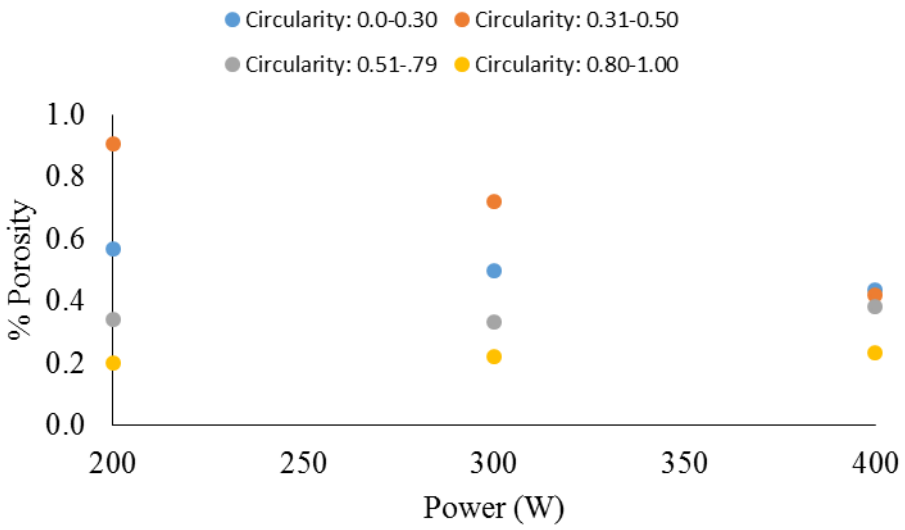

Figure 5-14: Effect of laser power on % porosity at a traverse speed of 6.4 mm/s and powder feed rate of 12.2 g/min.

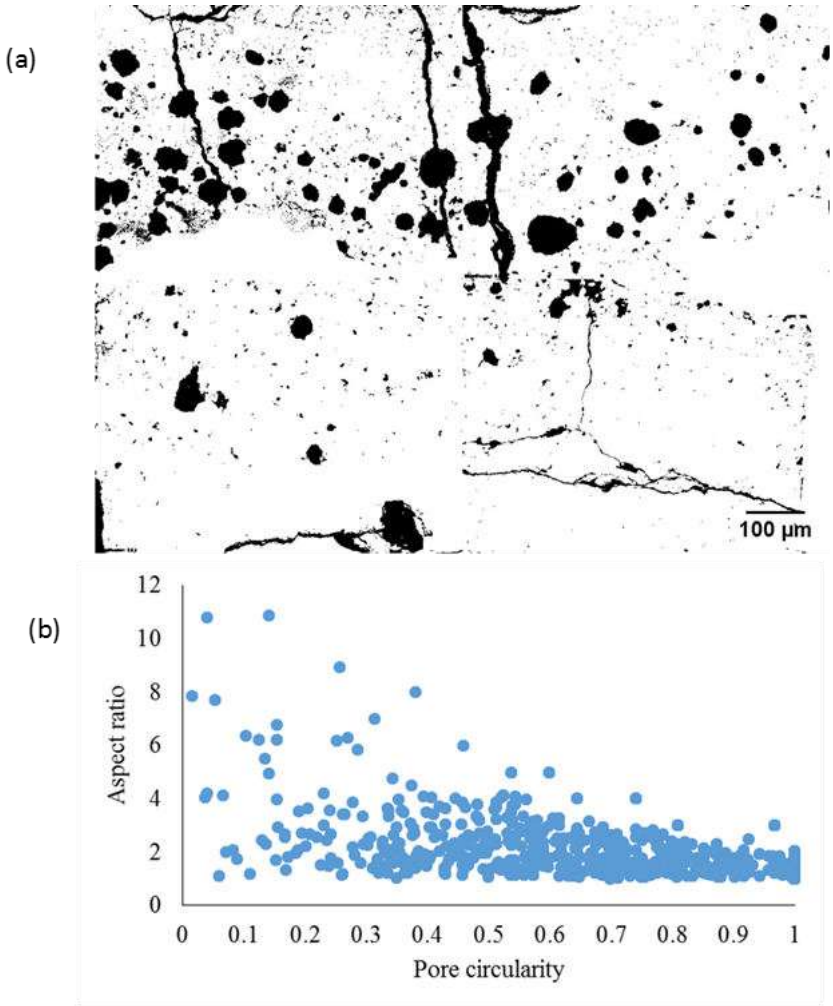

Figure 5-15: (a) Binary micrograph, (b) aspect ratio of pores at different circularity ranges at 400 W, 8.5 mm/s, 12.2 g/min.

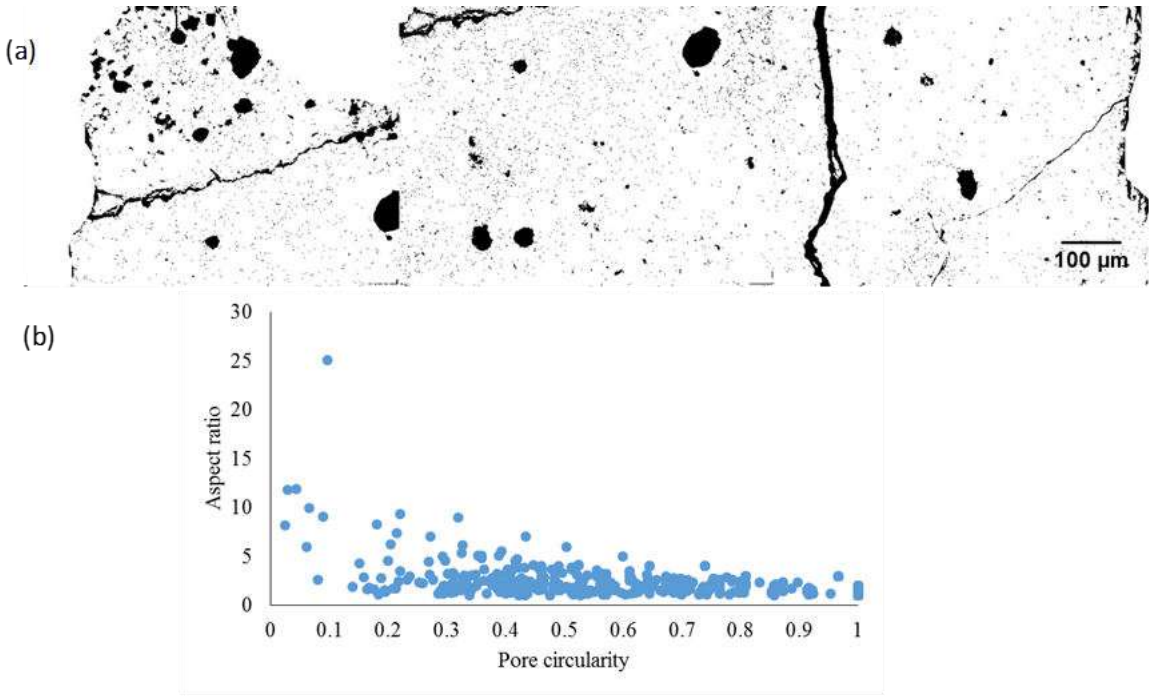

Figure 5-16: (a) Binary micrograph, (b) aspect ratio of pores at different circularity ranges at 300 W, 8.5 mm/s, 12.2 g/min.

Figure 5-17 and *Figure 5-18* show the influence of traverse speed on porosity, an increase in the traverse speed led to a decrease in porosity with circularity of 0.0-0.30. 0.31-0.50 and 0.51-0.79 at a traverse speed of 6.4 mm/s and a further increase at a traverse speed of 8.5 mm/s. However, a noticeable decrease in the % porosity with circularity of 0.80-1.00 was observed

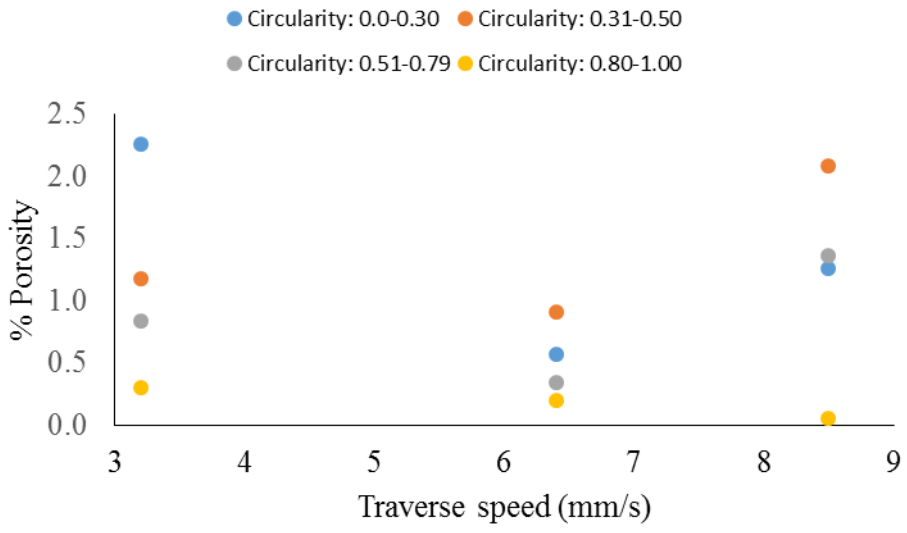

Figure 5-17: Effect of traverse speed on % porosity at a laser power of 200 W and powder feed rate of 12.2 g/min.

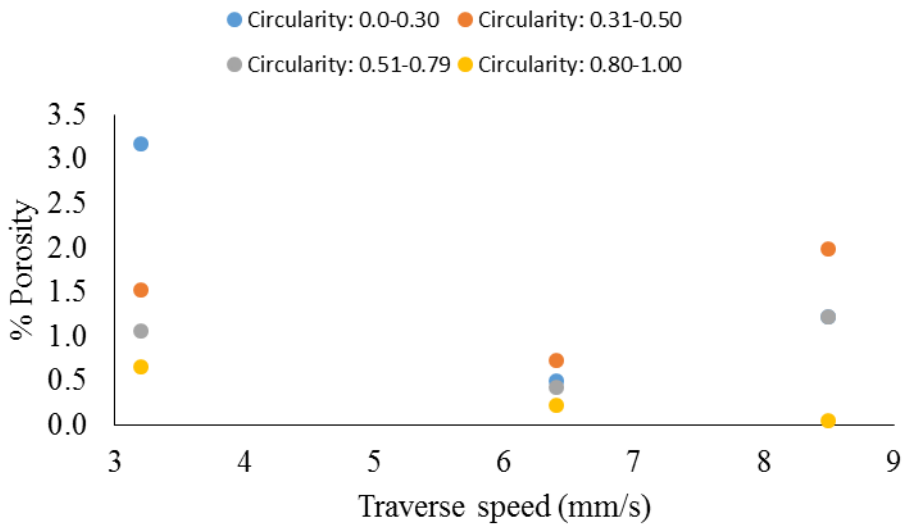

Figure 5-18: Effect of traverse speed on % porosity at a laser power of 300 W and powder feed rate of 12.2 g/min.

The average area occupied by the porosity at different circularity ranges on random areas on the samples is shown in *Figure 5-19*, it can be seen that at a traverse speed of 6.4 mm/s both the lack of fusion and gas porosity decreased.

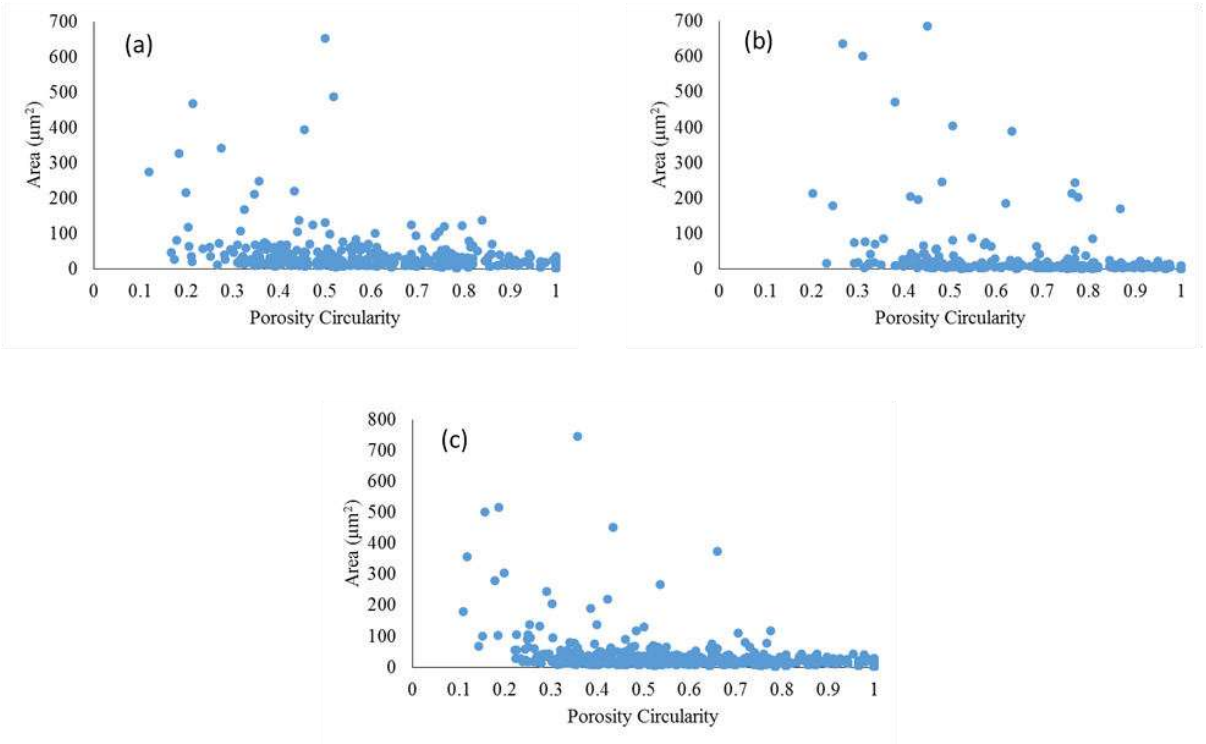

Figure 5-19: Porosity area of samples deposited at 300 W, 10 g/min at traverse speed of (a) 3.2 mm/s, (b) 6.4 mm/s, (c) 8.5 mm/s.

Figure 5-20 to *Figure 5-22* show the influence of powder feed rate on porosity, an increase in the powder feed rate led to an increase in the porosity.

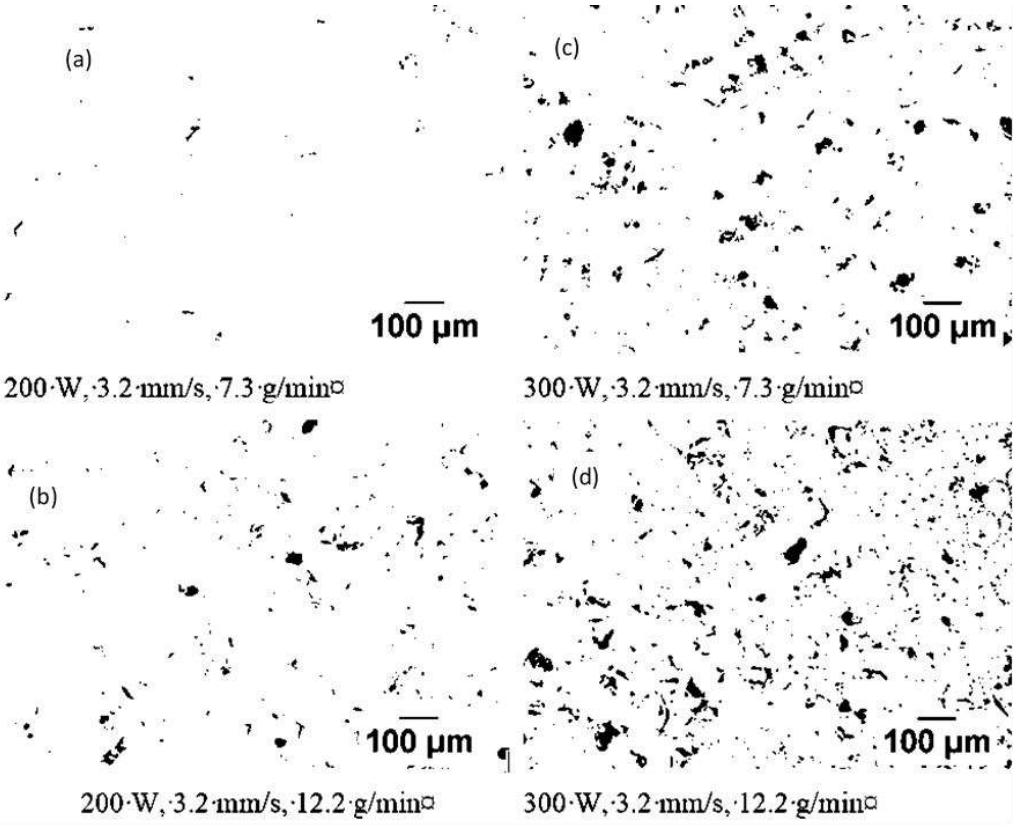

Figure 5-20: Porosity of samples fabricated @ 200 W, with powder feed rate of (a) 7.3 g/min and (b)12.2 g/min; @ 300 W, with powder feed rate of (c) 7.3 g/min and (d)12.2 g/min.

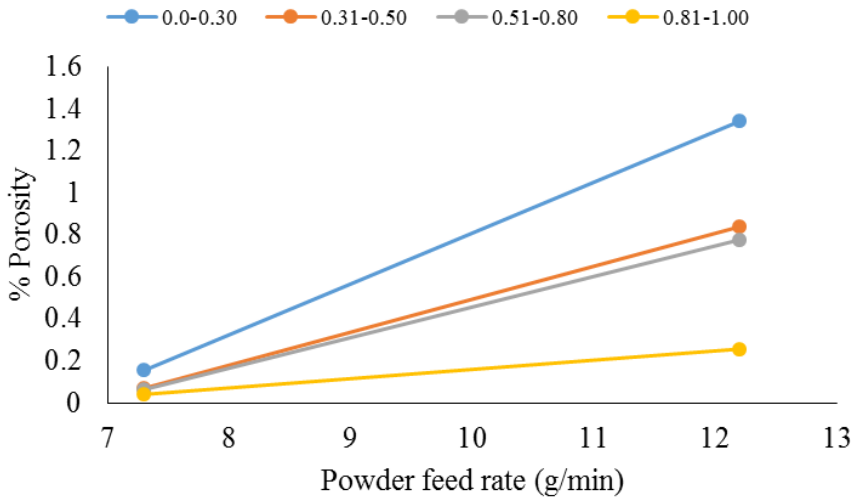

Figure 5-21: Effect of powder feed rate on porosity at a laser power of 200 W and traverse of 3.2 mm/s.

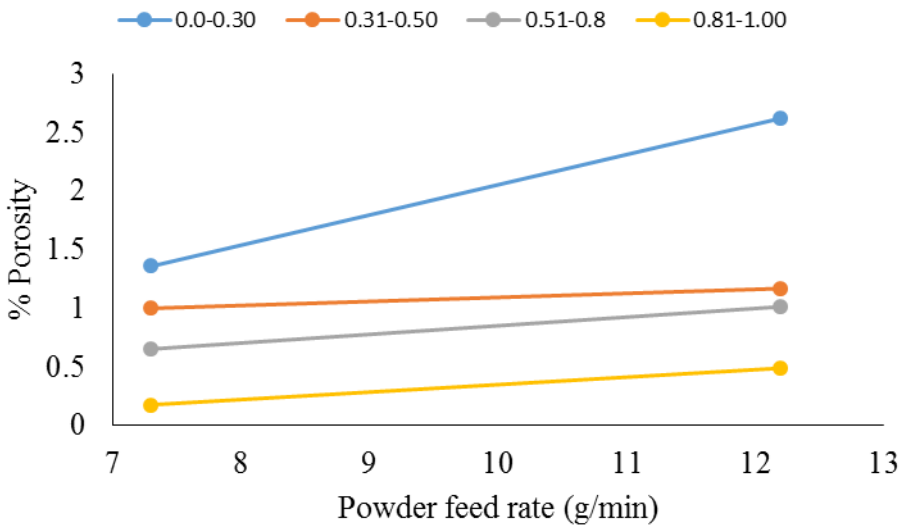

Figure 5-22: Effect of powder feed rate on porosity at a laser power of 300 W and traverse of 3.2 mm/s.

The mean % porosity analysis (*Figure 5-23*) showed that porosity increased with an increase in laser power, powder feed rate and a decrease in the traverse speed. It is clear that the mean porosity follows the trend of the porosity with high circularity.

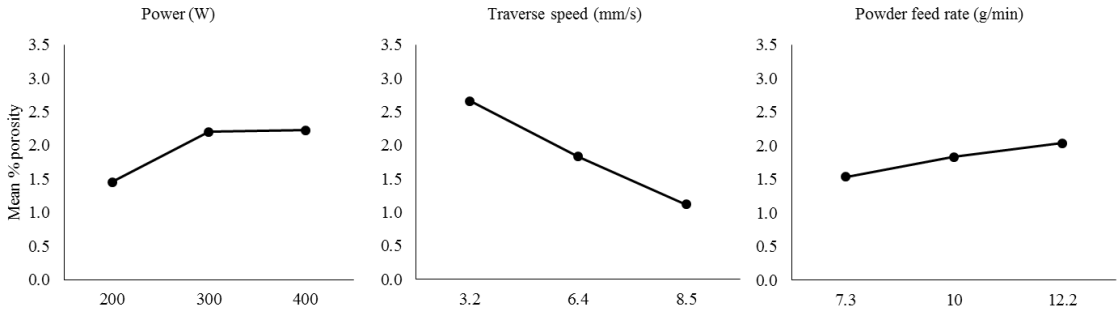

Figure 5-23: Main effects of parameters on % porosity.

5.3.2 Parameter optimization

A regression analysis could not be used to model the porosity due to the scattering of data. An MOO optimization technique was used to optimize both height and porosity by maximizing the height and minimizing the porosity. *Table 5-6* shows the parameters used for the optimization process and from the porosity results it can be seen that a minimum porosity of 0.57% was attained at a laser power of 200 W, traverse speed of

6.4 mm/s and a powder feed rate of 12.2 g/min. However, the goal was to optimize both porosity and height simultaneously by minimizing the % porosity while maximizing the sample height. *Table 5-7* shows the Pareto optimal solution by using the domination concept to differentiate the dominated and non-dominated solution. The optimum process parameters for height shown in *Table 5-4* also form part of the Pareto MOO optimum solutions, it can thus be seen that the optimum process parameters for both height and porosity is 200W, 3.2 mm/s and 12.2 g/min

Table 5-6: Average porosity measurements.

Sample identification	Power (W)	Speed (mm/s)	Feed rate (g/min)	Height of built (mm)	% Porosity
A	200	8.5	12.2	4	0.91
B	200	6.4	12.2	4.8	0.57
C	200	3.2	7.3	4.3	1.54
D	200	3.2	12.2	7.92	2.8
E	300	8.5	12.2	4.8	1.31
F	300	6.4	10	4.9	1.21
G	300	3.2	10	7	1.5
H	300	3.2	12.2	8.5	4.8
I	400	8.5	12.2	5	1.14
J	400	6.4	10	6.38	2.80
K	400	6.4	12.2	7.3	2.75

Table 5-7: Pareto optimal solutions.

Pareto domination analysis	Pareto set/non dominated set
A dominates J	
B dominates A, C and E	
D dominates J	
F dominates C and E	B, D, G, I, K
G dominates C and J	
I dominates C, E, F	
K dominates J	

5.4 Optimization of the Z-increment

5.4.1 Effect of the z-increment on sample height

The optimum parameters in Section 5.2.3 and 5.3.2 were established by using a constant z-increment of 0.2 mm. This section looks into the effect of z-increment on both the sample height and porosity and aims to establish whether the attained optimum parameters can be refined by changing the z-increment. In order to investigate influence of the z-increment the traverse speed was kept between 3.2 and 6.4 mm/s as these two speeds ensured a balance between sample height and porosity in the Pareto optimal solution analysis (section 5.3.2). The laser power was varied between 200, 300 and 400 W and the powder feed rate was varied between, 7.3, 10 and 12.2 g/min. *Table 5-8* and *Figure 5-24* show that a z-increment equal to the layer thickness resulted in an increase in sample height. An increase in sample height shows that there was enough heat to melt the powder, hence more powder was introduced into the molten pool. It can be seen that the z-increment is critical in preventing a defocused laser and if an incorrect z-increment is set not all the powder will be captured in the molten pool. It could also be observed that the near optimum parameters (200 W, 3.2 mm/s, 12.2 g/min) had a layer thickness of 0.2 mm.

Table 5-8: Influence of z-increment on sample height.

Z-increment	Power (W)	Speed (mm/s)	Feed rate	Expected	Height(mm)

			(g/min)	height(mm)	
0.2	200	3.2	7.3	8	4.30
0.167				6.68	7.22
0.2	200	3.2	10	8	5.40
0.18				7.2	5.45
0.2	200	3.2	12.2	8	7.92
0.2				8	7.93
0.2	200	6.348	7.3	8	2.2
0.067				2.68	Fracture
0.2	200	6.348	10	8	3
0.167				6.68	6.22
0.2	200	6.348	12.2	8	4.8
0.167				6.68	7.91
0.2	300	3.2	7.3	8	6.57
0.21				8.8	9.2
0.2	300	3.2	10	8	7.00
0.22				8.8	10
0.2	300	3.2	12.2	8	8.5
0.22				8.8	11.09
0.2	300	6.348	7.3	8	2.6
0.067				2.68	Fracture
0.2	300	6.348	10	8	4.9
0.167				6.68	8.07
0.2	300	6.348	12.2	8	6.8
0.167				6.68	8.5
0.2	400	6.348	7.3	8	3.5
0.067				2.68	Fracture
0.2	400	6.348	10	8	6.38
0.167				6.68	8.49
0.2	400	6.348	12.2	8	7.30
0.17				6.8	10.51

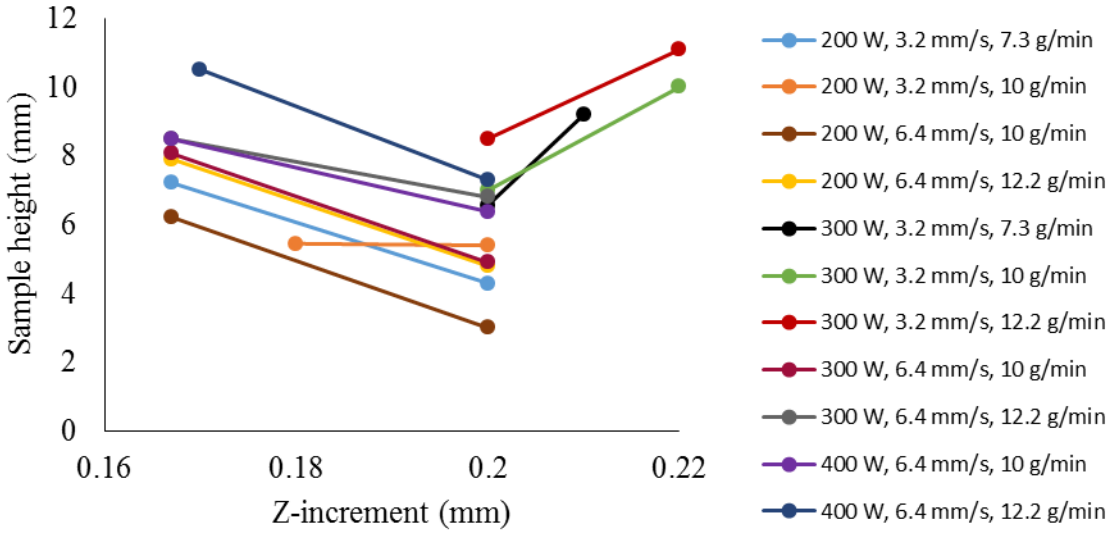

Figure 5-24: Influence of z-increment on sample height.

5.4.2 Effect of the z-increment on porosity

Figure 5-25 to *Figure 5-27* show the effect of the z-increment on porosity as a function of pore circularity, the porosity increased when the z-increment was set equal to the layer thickness, however a slight decrease in the % porosity with a circularity of 0.8-1.0 was observed. *Figure 5-28* and *Figure 5-29* shows the OM micrograph comparison of porosity at different z-increment levels. As much as a z-increment equal to the layer thickness leads to an increase in sample height it also leads to an increase in porosity (*Figure 5-25* to *Figure 5-29*), hence a z-increment of 0.2 mm was seen to be the optimum in all cases. *Figure 5-30* shows the porosity at different position on the sample and *Figure 5-31* shows the influence of the z-increment on the mean porosity.

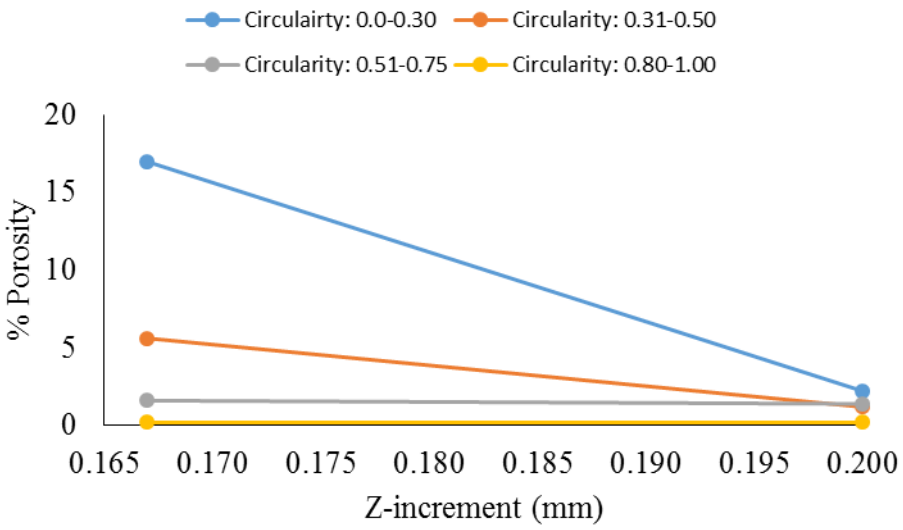

Figure 5-25: Effect of z-increment on the % porosity at a laser power of 200 W, traverse speed 3.2 mm/s and powder feed rate of 7.3 g/min.

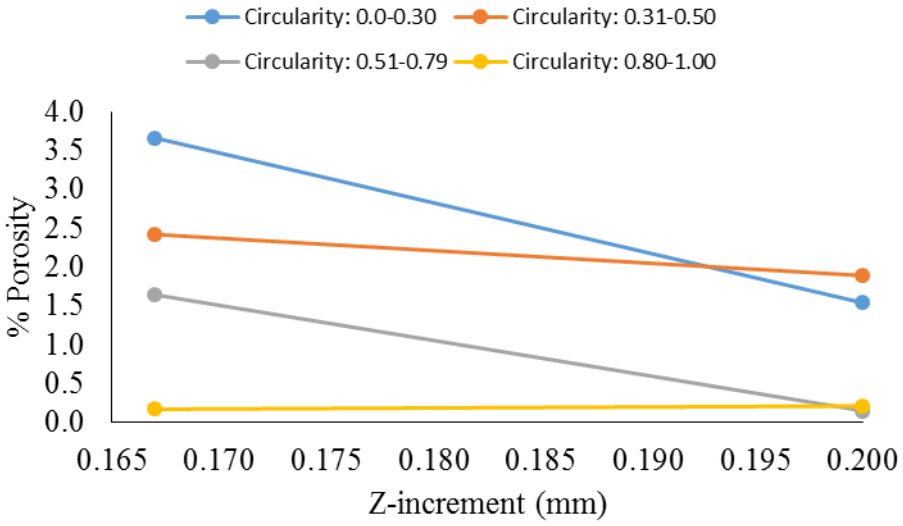

Figure 5-26: Effect of z-increment on the % porosity at a laser power of 200 W, traverse speed of 6.4 mm/s and powder feed rate of 10 g/min.

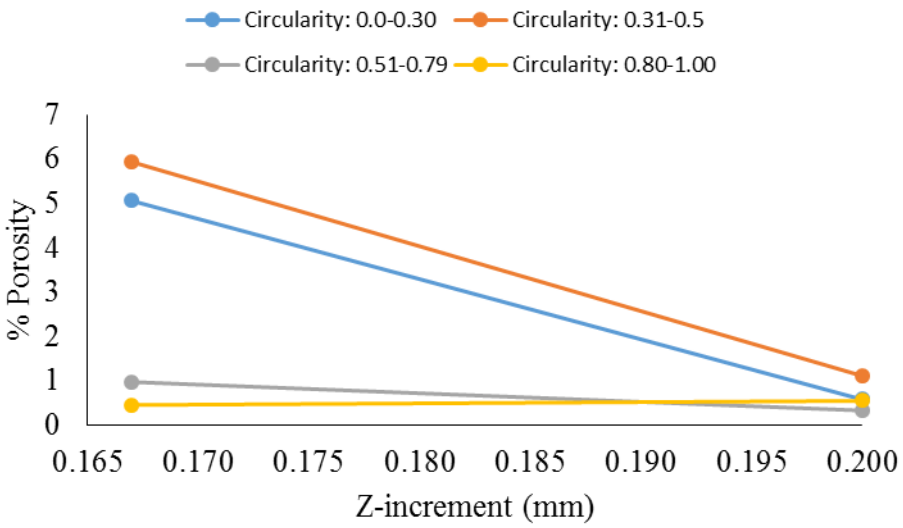

Figure 5-27: Effect of z-increment on the % porosity at a laser power of 300 W, traverse speed of 6.4 mm/s and powder feed rate of 12.2 g/min.

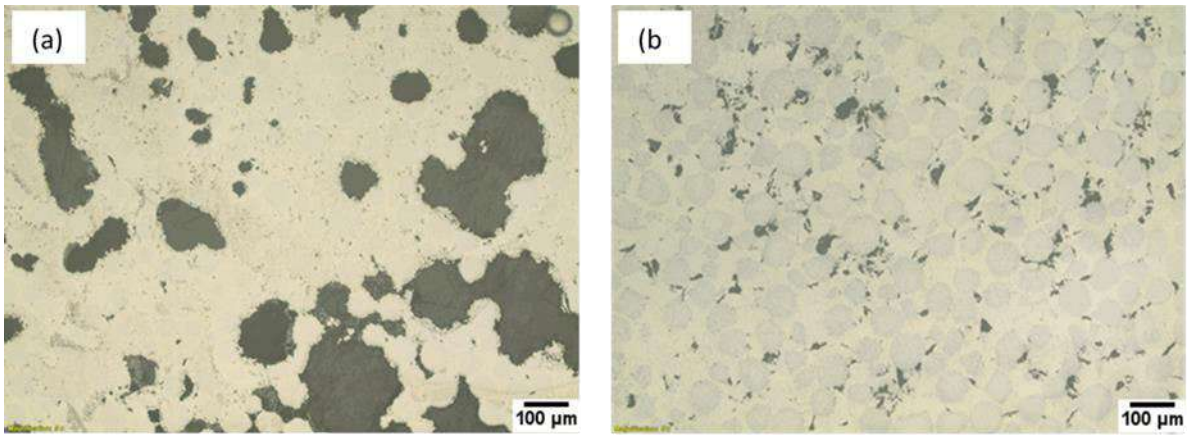

Figure 5-28: Sample deposited at 200W, 3.2 mm/s, 7.3 g/min and z-increment; (a) 0.167 mm, (b) 0.2 mm.

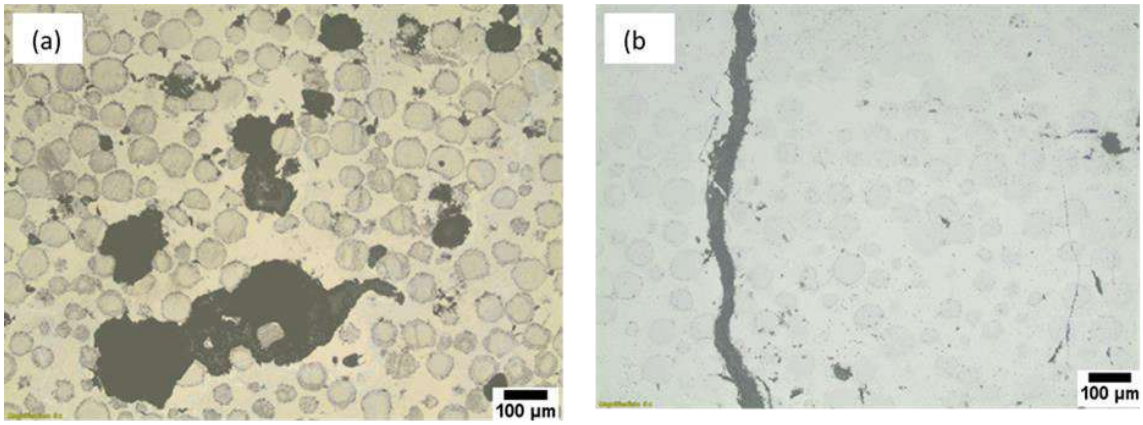

Figure 5-29: Samples deposited at 200W, 6.4 mm/s, 10 g/min and z-increment; (a) 0.167 mm, (b) 0.2 mm.

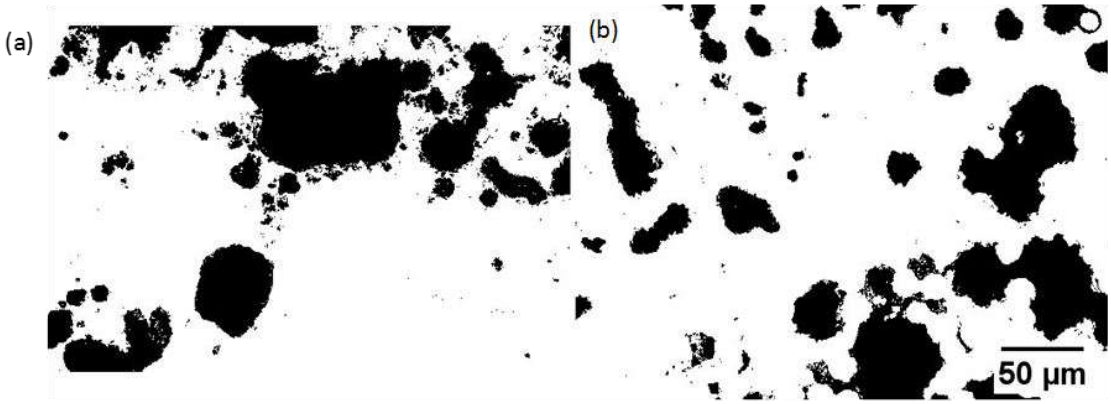

Figure 5-30: Porosity morphology, (a) sample area close to substrate, (b) sample area on the top layer, at 200 W, 3.2 mm/s, 7.3 g/min and z-increment of 0.167 mm.

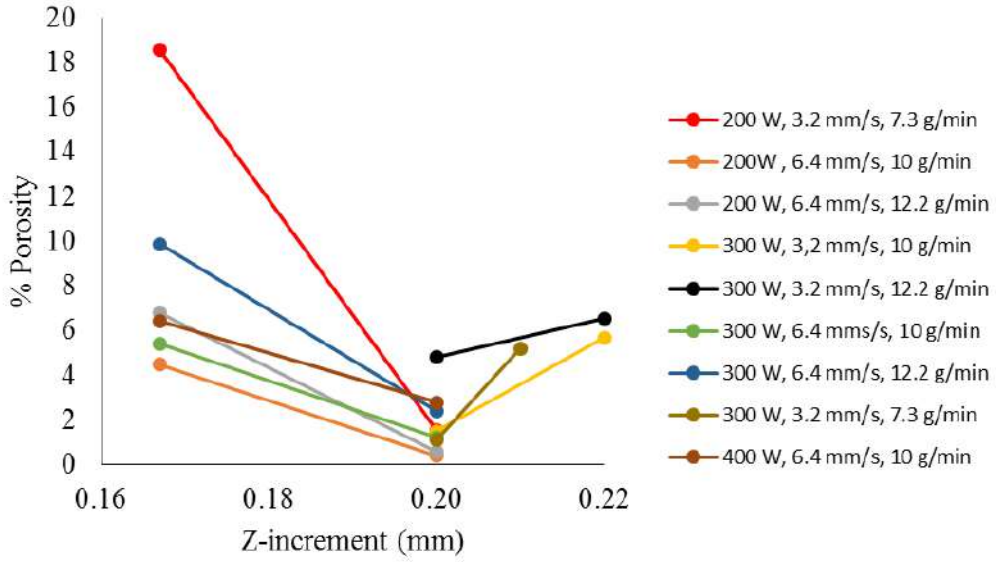

Figure 5-31: Effect of z-increment on porosity.

5.5 Optimization of Cube Samples

The Pareto MOO optimum solutions in *Table 5-7* were used to manufacture cube samples to see whether there was a difference in sample % porosity between cube and single wall samples. *Figure 5-32* shows the porosity at two hatch spacing levels, a hatch spacing of 0.53 mm led to less porosity and was chosen for the deposition of cube samples.

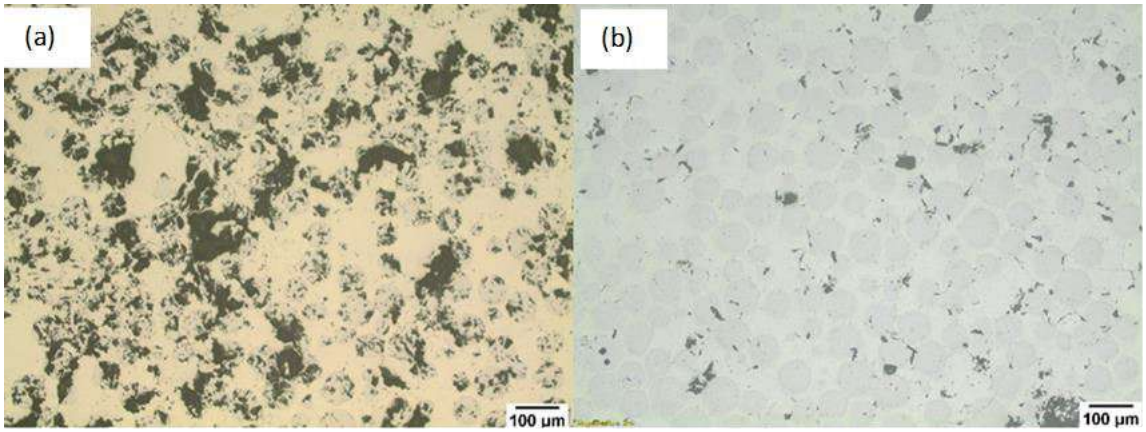

Figure 5-32: Cube samples deposited at 200 W, 3.2 mm/s, 12.2 g/min and a hatch spacing of, (a) 0.7 mm, (b) 0.53 mm.

Parameter set B did not attain any height and led to a defocused laser beam, hence the deposited powders did not land in the focal point of the laser and were not melted. Parameter I had cracks originating from the fusion line (*Figure 5-33*), hence parameter B and I were eliminated from the optimum parameters.

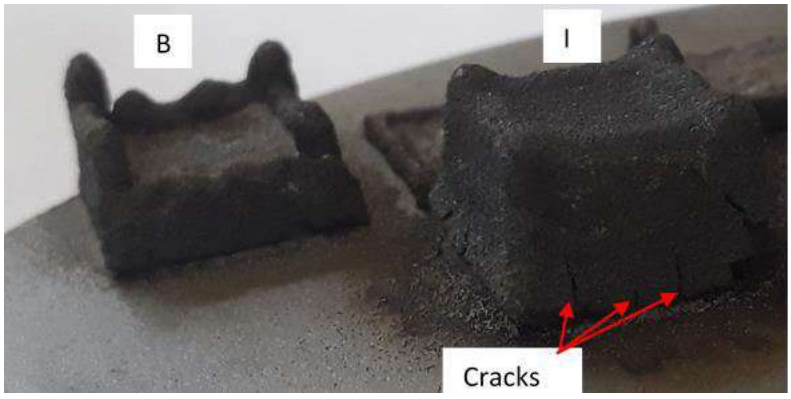

Figure 5-33: Lack of attainment of height in sample B and fusion cracks in sample I.

Sample D, G and K were deposited successfully with no visually observable defects such as lack of fusion, cracking, or lack of height attainment (*Figure 5-34*) and the expected height at 15 layers was 3 mm in accordance with Eq. 3-6. *Table 5-9* shows the sample height and % porosity of the cube samples. A minimum % porosity of 2.87% was obtained for the parameters 200 W, 3.2 mm/s and 12.2 g/min, this was similar to that of the single wall sample (2.80%) in *Table 5-6*. The effect of heat input on the % densification calculated from the Archimedes principal (Eq. 3-17) is shown in *Figure 5-35*, an increase in the heat input led to a decrease in the % densification. *Table 5-10* shows the density of the cube samples in comparison to the density of WC-FeCr hardmetals and the reference WC-Co hardmetals manufactured using the sintering process. It was concluded from the porosity and density measurements (*Table 5-9* and *Figure 5-35* respectively) that a power of 200 W, traverse speed of 3.2 mm/s and a powder feed rate of 12.2 g/min were the optimum process parameters for the deposition of WC-FeCr bulk samples using the LENS® process. The densification obtained on LENS® deposited WC- 10wt% FeCr cubes was higher than that obtained from sintered WC-10wt.% FeCr but lower than the traditional WC–12wt% Co (*Table 5-10*) mainly because Co has a density of 8.9 g/cm^3, while FeCr has a density of 7.8 g/cm^3.

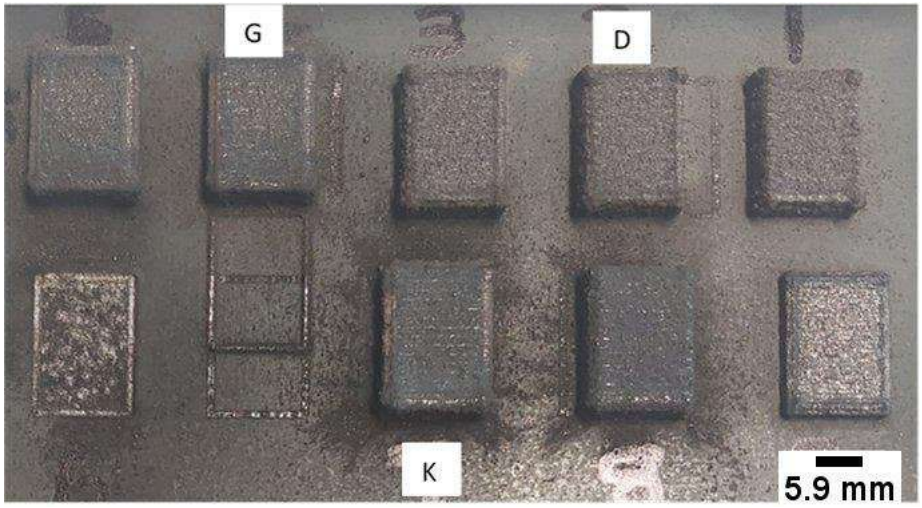

Figure 5-34: Optimum cube samples,(D) 200 W, 3.2 mm/s, 12.2 g/min, (G) 300 W, 3.2 mm/s, 10 g/min and (K) 400 W, 6.4 mm/s, 12.2 g/min.

Table 5-9: Height and % porosity of the cube samples at optimum process parameters.

Sample	Power (W)	Speed (mm/s)	Feed rate (g/min)	Height of build (mm)	% Porosity
D	200	3.2	12.2	4.33 ± 0.012	2.87 ± 0.42
G	300	3.2	10	5.04 ± 0.057	7.75 ± 2.00
K	400	6.35	12.2	4.31 ± 0.057	14.13 ± 1.10

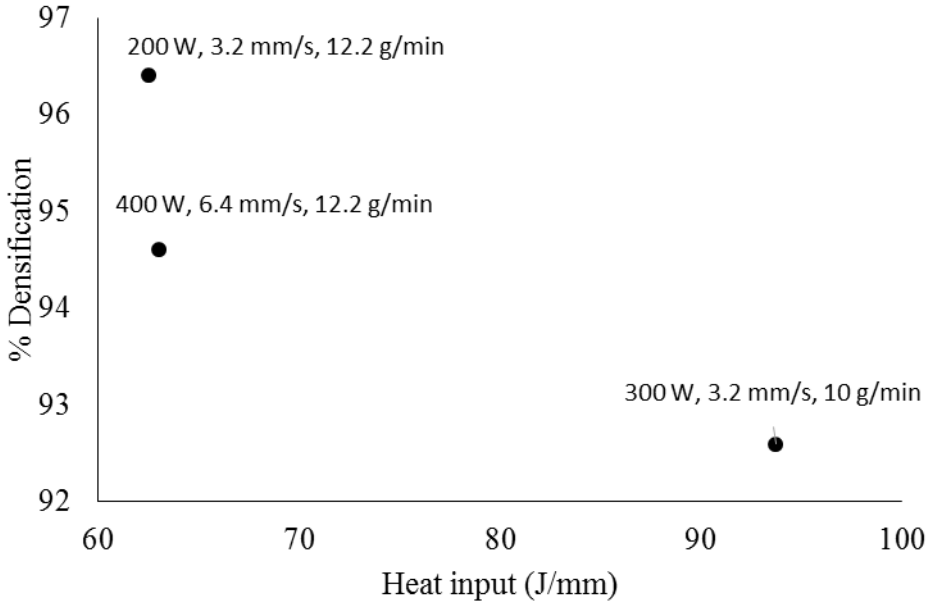

Figure 5-35: Influence of heat input on the densification of cube samples.

Table 5-10: Densification of the optimum cube samples.

	Samples		
Power (W)	**200**	**300**	**400**
Traverse speed (mm/s)	3.2	3.2	6.4
Powder feed rate (g/min)	12.2	10	12.2
True density	14.467	13.874	14.177
Bulk density	13.797	13.247	13.511
% Densification	96.5	92.6	94.6
% open porosity	4.63	4.52	4.702
Density of sintered WC-10w.t% FeCr (WC grain size 8+ µm) [124]	13.55 g/cm^3/ 94 % densification		
Density of sintered WC-12w.t% Co (reference grade) [83]	14.31 g/cm^3		

CHAPTER 6 Material Characterization Results and Analysis

6.1 Introduction

This chapter presents the microstructural and mechanical property results for the thin wall samples and optimum cube samples. The characterization of the microstructure and the effects of process parameters on the different microstructural phases formed were carried out. A microstructural and phase analysis of the optimum cube sample was done. The influence of process parameters on the hardness and hardness profile of the thin wall samples was analyzed and a hardness comparison was made between the optimum cube sample and hardmetals fabricated by conventional methods. A thermal profile analysis was carried out on the thin wall samples to understand microstructural and hardness results and fracture toughness tests of the single wall samples were evaluated.

6.2 Microstructure

6.2.1 Microstructure of the thin wall samples

The microstructures of all the thin wall samples comprised of spherical WC embedded in a FeCr matrix. The spherical WC comprised of a reaction zone around the grain edges resembling a halo effect which had a lighter color. The reaction phases were composed of equiaxed white grains, light grey trapezoid shaped and strip shaped phases. The equiaxed white grains formed throughout the build and transformed into columnar grains from the coalescence with other equiaxed grains throughout the builds. The columnar grains detached from the spherical WC and coalesced with other similar grains to form a herringbone structure within the FeCr matrix. *Figure 6-1* shows the microstructure at different positions along the build directions.

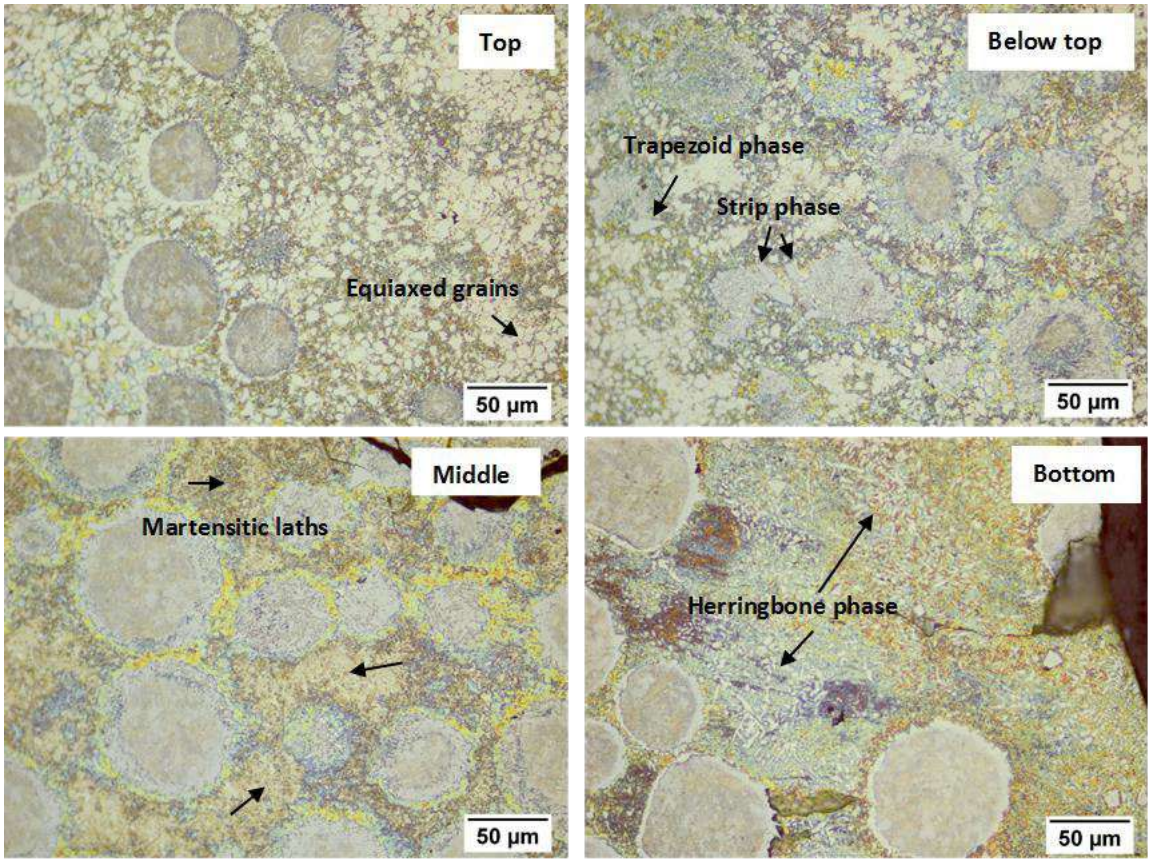

Figure 6-1: Microstructure at 400 W, 6.4 mm/s, 10 g/min.

The herringbone structure was only present at the first layers deposited, close to the substrate (bottom of sample). The center and top of the samples comprised of light grey trapezoid and strip shaped phases which detached from the spherical grain and dispersed into the matrix, this detachment occurred mostly on the top layers until full decomposition of the WC spherical grain occurred. The top layers consisted of detached white columnar grains and light grey trapezoid and strip shaped phases. The last layers to be deposited had a white phase comprising of partially melting equiaxed and columnar grains, and was referred to as a bright surface zone. The FeCr matrix displayed a dark brown zone which comprised of martensitic laths with retained austenite.

Figure 6-2 shows the EDS analysis of the different phases observed during microstructural analysis. The equiaxed/columnar grain reaction zone was directional to the build height. *Figure 6-3* shows the elemental mapping of the bright surface zone, and it is evident that this zone mainly comprised of WC and the spectrum shows that partial melting of WC occurred as the spherical WC was not as discernable in comparison to the other areas. The bright surface zone seemed to have a reduction in

the Fe content as compared to the centre of the builds. It can be seen that the bright surface zone comprised of partially dissolved WC and a reduction in Fe. The elemental mapping of Fe in the bright surface zone showed a faded color in comparison to the rest of the deposit, this shows that a lower Fe concentration was detected in the bright surface zone which can be attributed to evaporation. In order to verify whether Fe evaporated the chemical composition of this zone was compared to the centre of the single wall builds. *Table 6-1* makes a comparison between the chemical composition of the bright surface zone and the centre of the single wall builds. The wt% W in the bright surface zone was similar to that of the center of the single wall builds, this means that the same concentration of W was present the only difference was that WC dissolution occurred. Porosity was also observed on the last deposited layers.

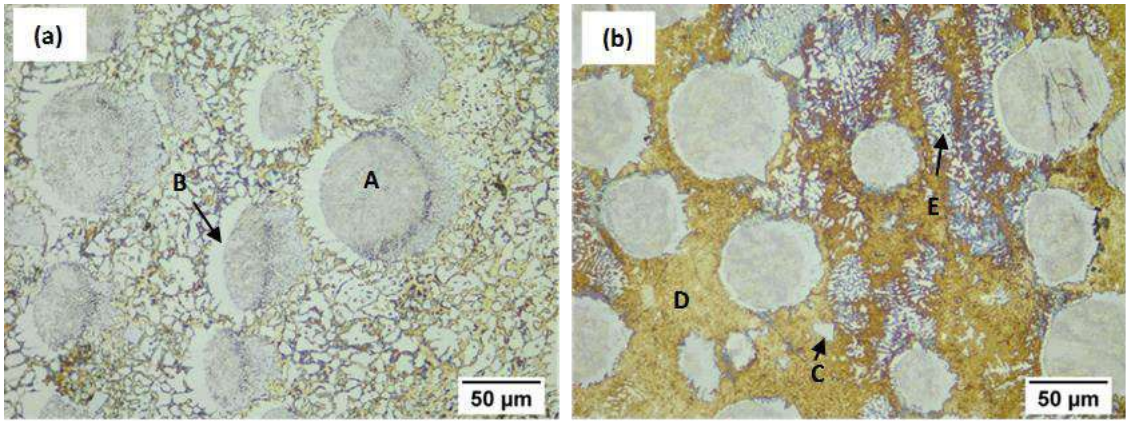

Label	Morphology	Chemical composition by EDS (wt.%)		
		W	Fe	Cr
A	Spherical WC	89.84	-	-
B	Columnar (halo effect)	95.2	3.49	-
C	Trapezoidal phase	77.6	19.2	3.1
D	Matrix	13.3	71.8	14.9
E	Columnar (dendritic)	81.98	15.29	2.73

Figure 6-2 :(a) Microstructure and EDS analysis of;(a) bright surface zone, (b) bottom area at 400W, 8.5 mm/s, 12.2 g/min.

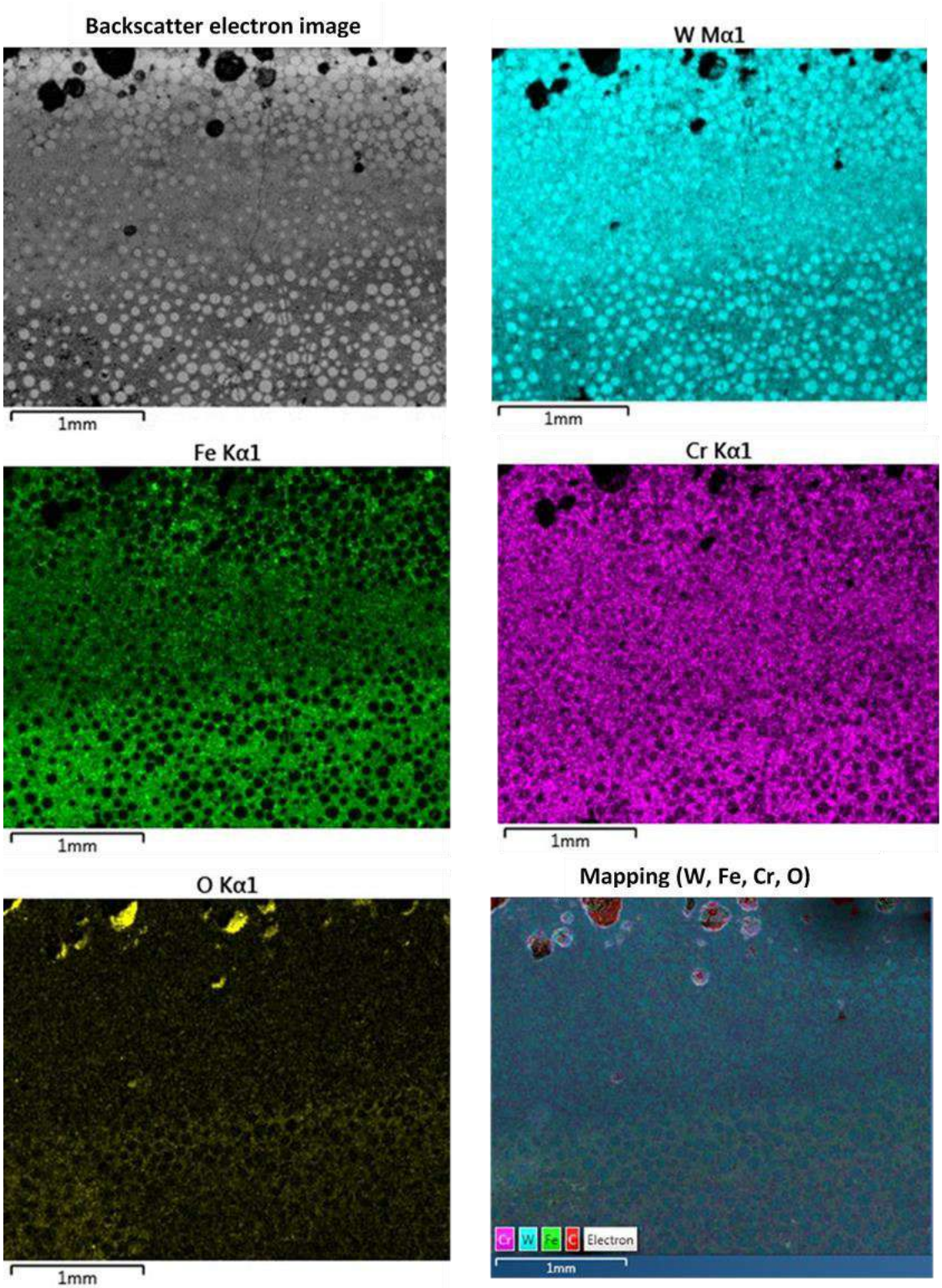

Figure 6-3: EDS mapping of the bright surface zone at 200 W, 3.2 mm/s, 12.2 g/min.

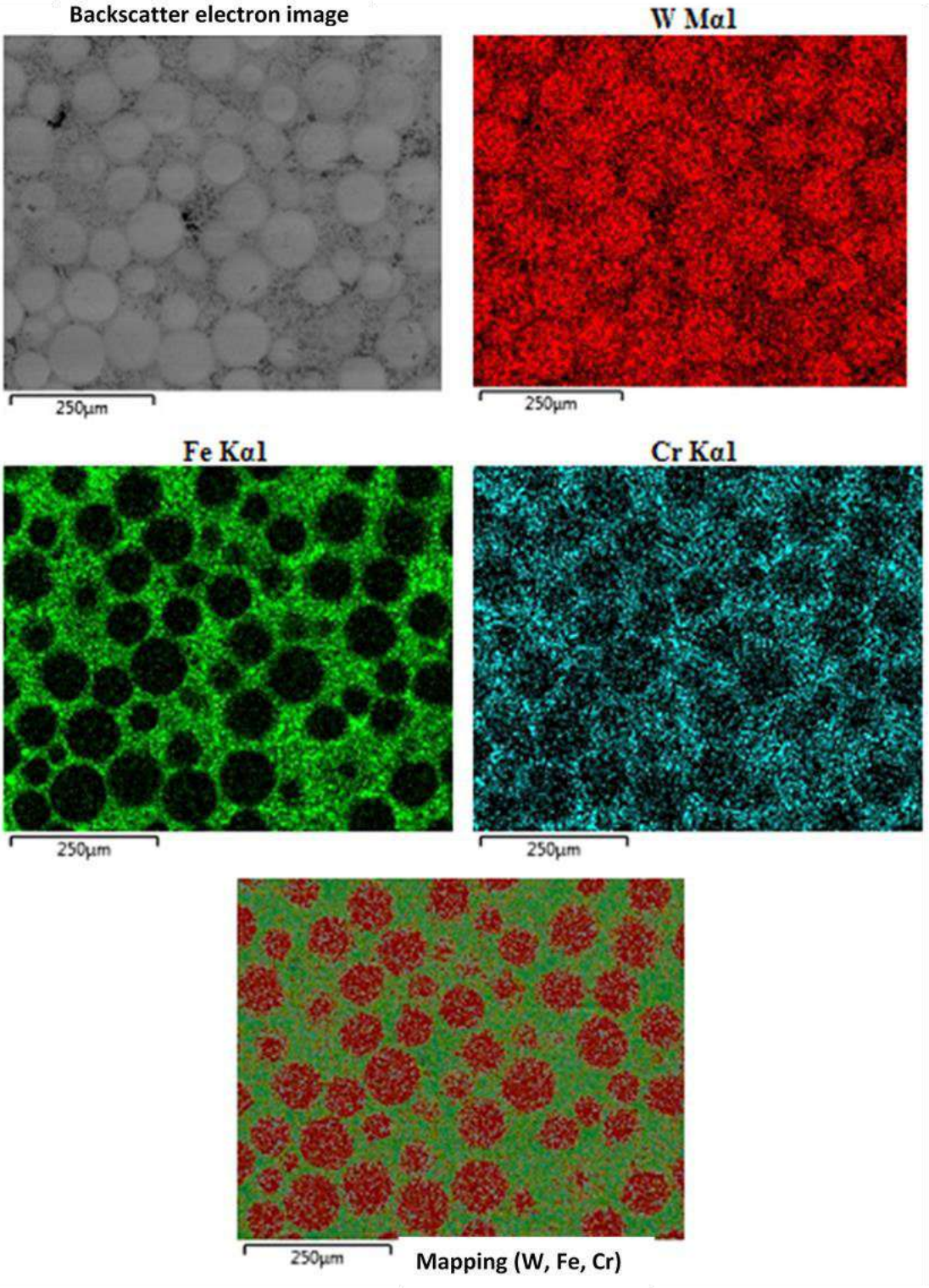

Figure 6-4: EDS mapping of the centre of the single wall build at 200 W, 3.2 mm/s, 12.2 g/min.

Table 6-1: Mapping analysis of the bright surface zone and centre of the single wall builds.

Parameters/Elements	**200 W, 3.2 mm/s, 12.2 g/min**	
Wt.%	**Bright surface zone**	**Centre of build**
W	76 ±0.1	75±0.2
Fe	7 ±0.0	13±0.1
Cr	2±0.0	2.2±0.0

6.2.2 Effects of process parameters on microstructure

6.2.2.1 Effect of laser power on microstructure

Figure 6-5 and *Figure 6-6* shows the microstructures of the top layers at constant powder feed rate and traverse speed. The thickness of the bright surface zone increased with an increase in the laser power. The thickness of the bright surface zone was measured using Image J analysis software at 5 points and the influence of laser power on the bright surface zone thickness is shown in *Figure 6-7*.

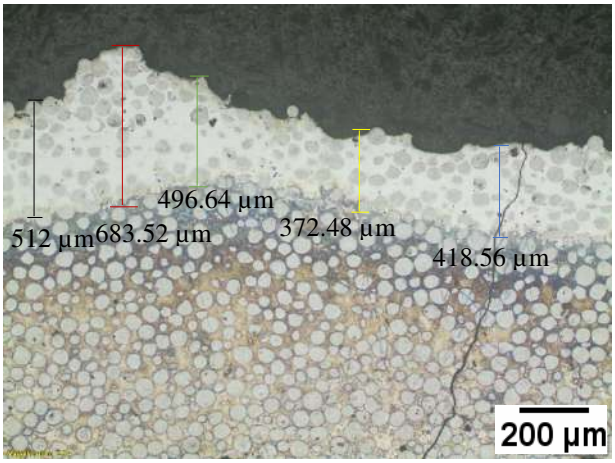

200 W, 8.5 mm/s, 12.2 g/min

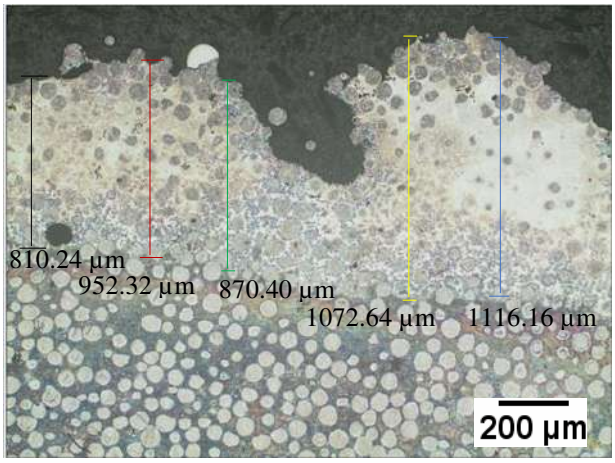

300 W, 8.5 mm/s, 12.2 g/min

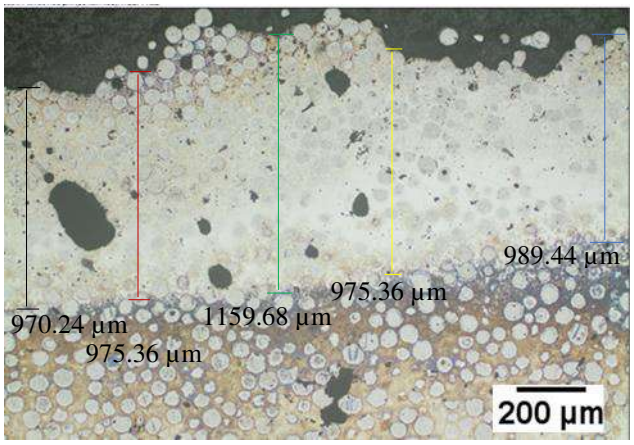

400 W, 8.5 mm/s, 12.2 g/min

Figure 6-5: Effect of laser power on the bright surface zone at a traverse speed of 8.5 mm/s and powder feed rate of 12.2 g/min.

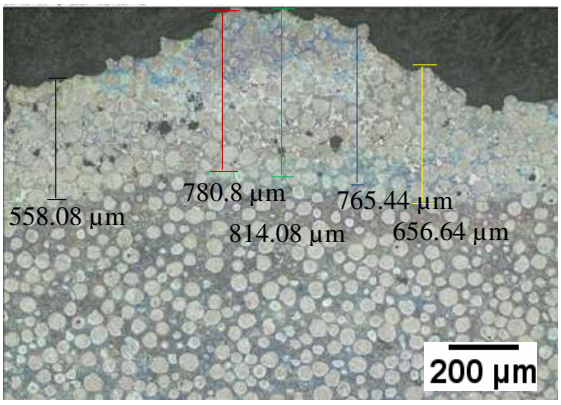

200 W, 6.4 mm/s, 12.2 g/min

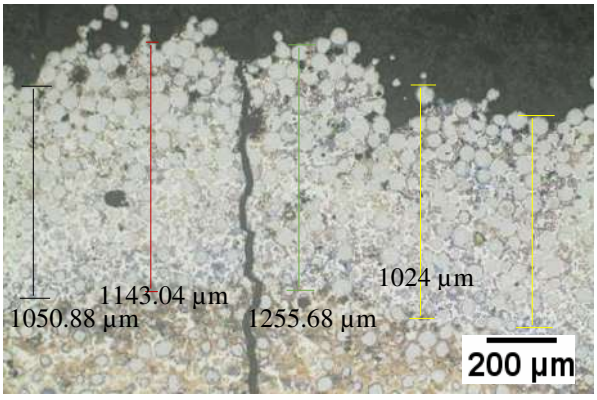

400 W, 6.4 mm/s, 12.2 g/min

Figure 6-6: Effect of laser power on the bright surface zone at a traverse speed of 6.4 mm/s and powder feed rate of 12.2 g/min.

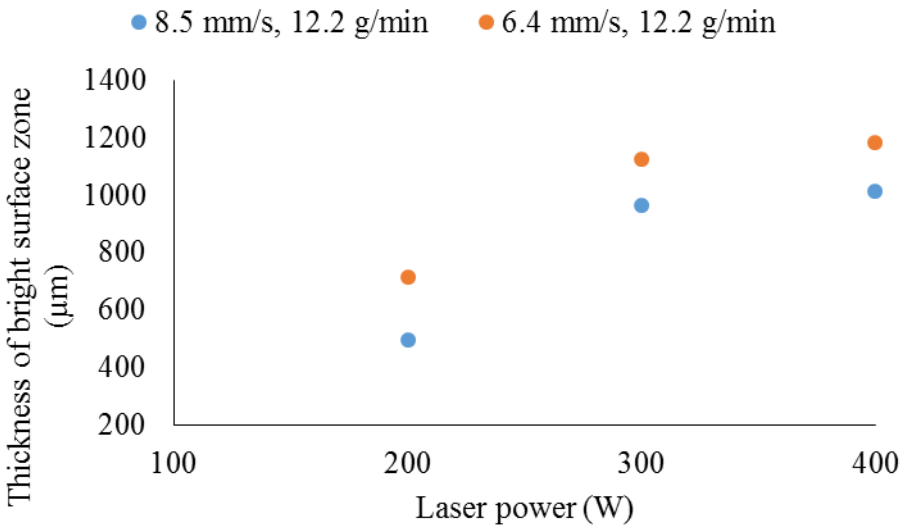

Figure 6-7: Influence of laser power on the thickness of the bright surface zone.

The bright surface zone showed dissolution and decomposition of the spherical WC particles, which increased with an increase in laser power (*Figure 6-8*). Complete dissolution and disintegration of the WC particles occurred at a laser power of 400 W and resulted in the formation of grey trapezoidal and strip phase constituents.

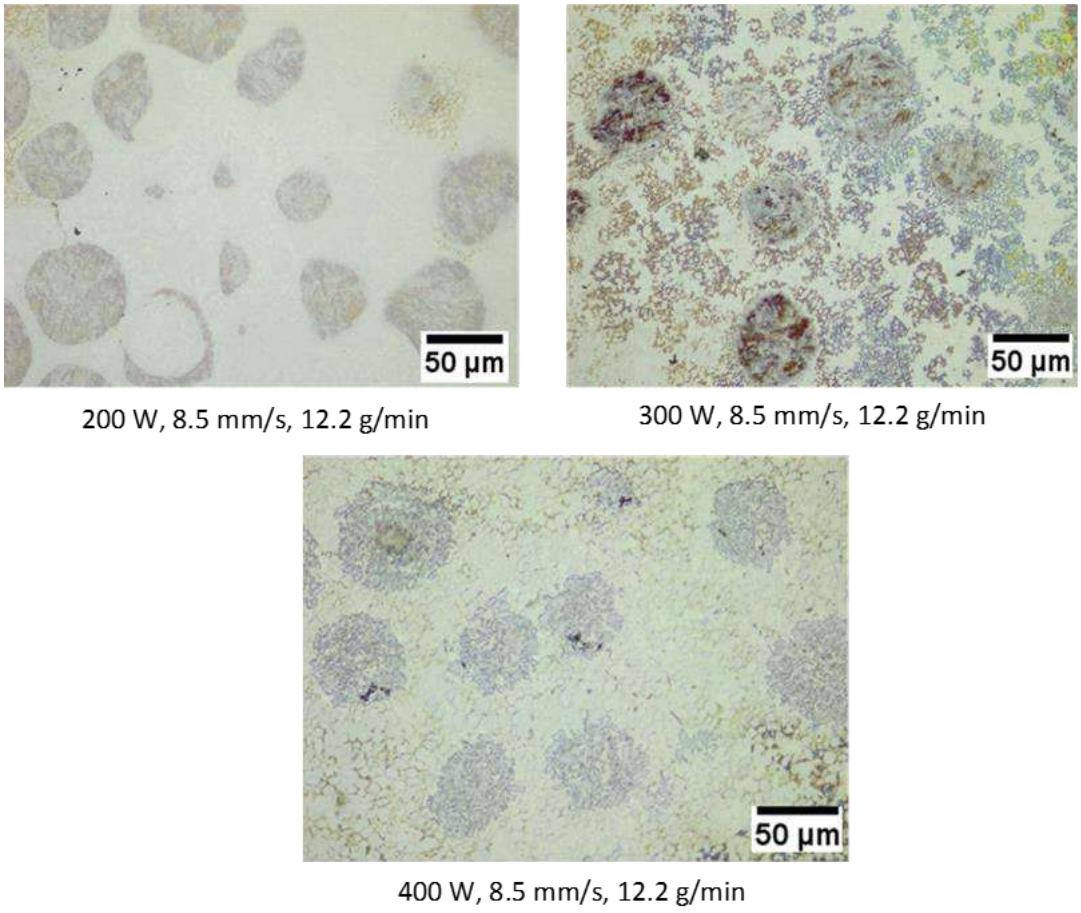

Figure 6-8: Dissolution of spherical WC in the bright surface zone.

The centre of the single wall builds comprised of spherical WC particles, with equiaxed and columnar grains embedded in a darker coloured phase. The spherical WC also comprised of a reaction zone (halo effect) on the edges of the sphere, resembling a rim and core structure. The core comprised of undissolved WC and maintained the original morphology, while the rim/reaction zone comprised of dissolved phases. *Figure 6-9* to *Figure 6-11* show the thickness of the reaction zone measured using an Image J analysis software at different laser powers, with higher dissolution of spherical WC occurring at a laser power of 400 W, and *Figure 6-12* shows that an increase in the laser power resulted in an increase in the thickness of the reaction zone.

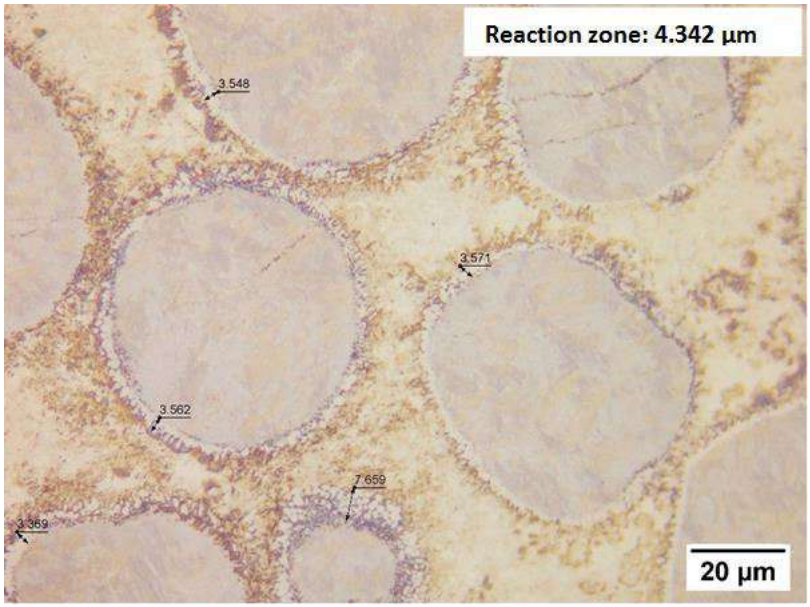

Figure 6-9: Reaction zone at 200 W, 8.5 mm/s, 12.2 g/min.

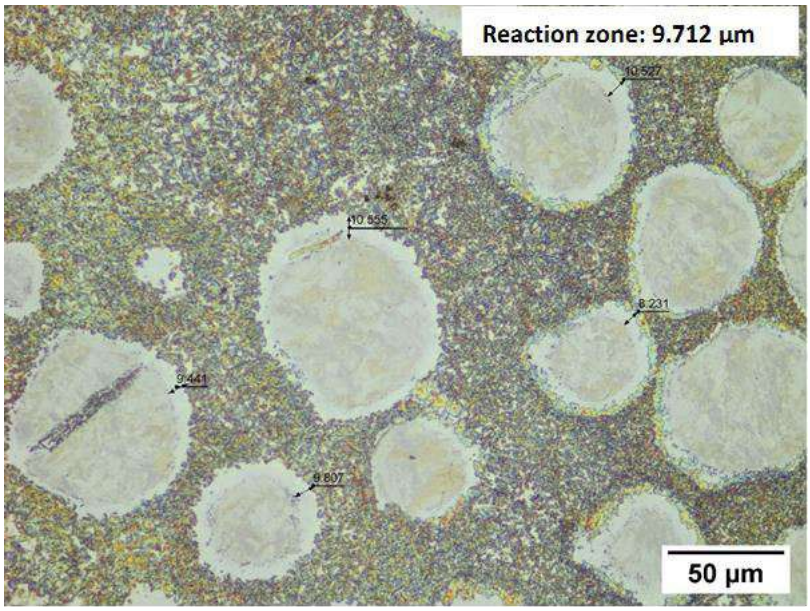

Figure 6-10: Reaction zone at 300 W, 8.5 mm/s, 12.2 g/min.

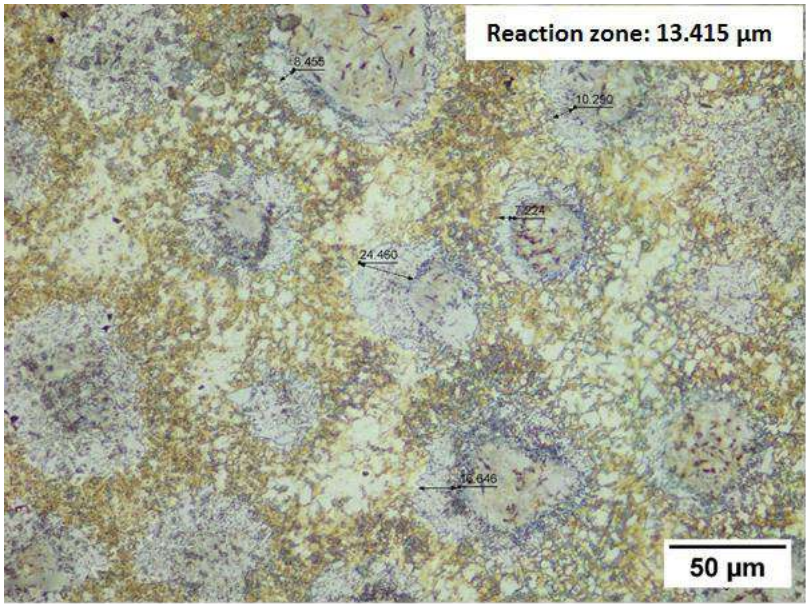

Figure 6-11: Reaction zone at 400 W, 8.5 mm/s, 12.2 g/min

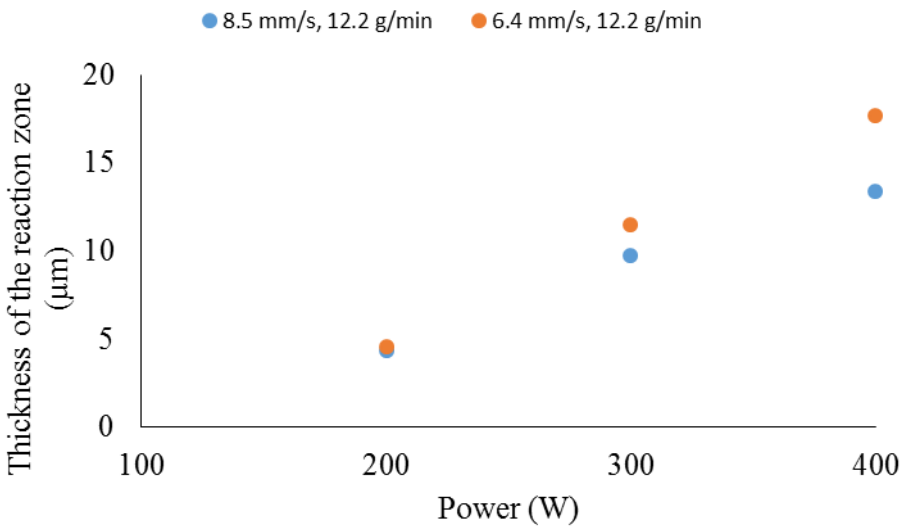

Figure 6-12: Influence of laser power on the thickness of the reaction zone.

6.2.2.2 Influence of traverse speed on microstructure

Figure 6-7 and *Figure 6-12* show a decrease in the traverse speed led to an increase in thickness of the bright surface zone and reaction zone. This is because at slow traverse speeds, there is enough time for the laser to interact with the powder particles and hence more heat is available for melting. The heat input increases with an increase in the laser power and a decrease in the traverse speed, and hence an increase in the

deposition temperature. This then results in more of the WC spherical particles being melted. Thus an increase in the heat input results in an increase in thickness of the bright surface zone and reaction zone (*Figure 6-13* and *Figure 6-14*). The graphical representation shows that an increase in the heat input results in the dissolution and melting of WC.

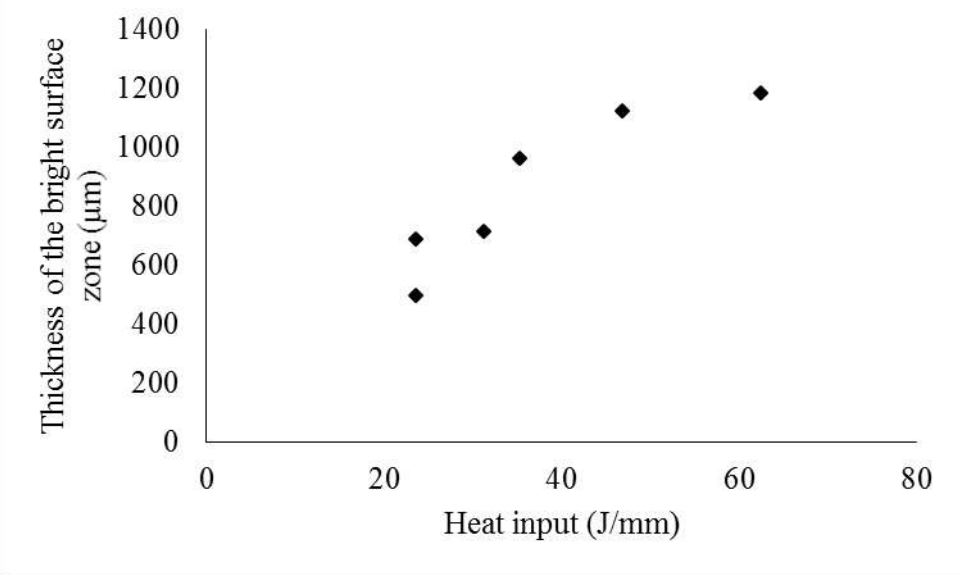

Figure 6-13: Influence of heat input on the thickness of the bright surface zone.

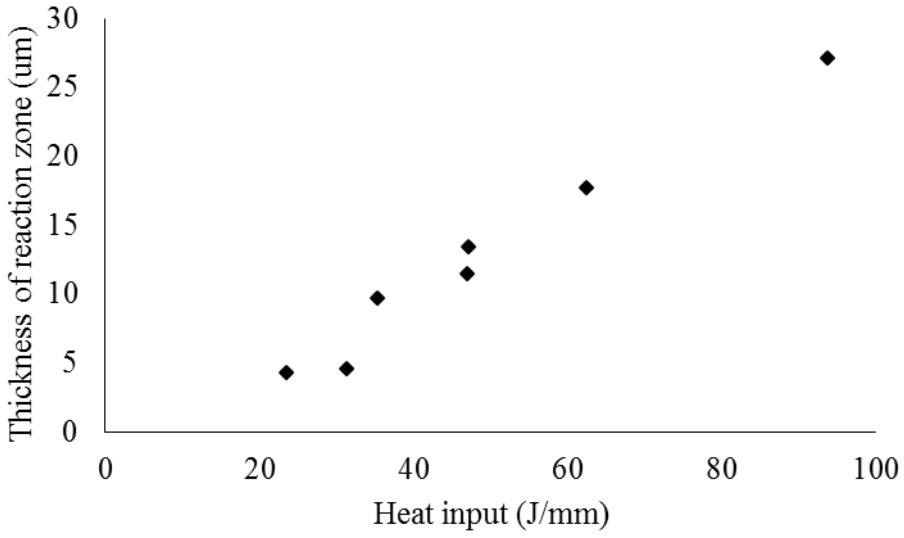

Figure 6-14: Effect of heat input on the reaction zone at a powder feed rate of 12.2 g/min.

6.2.2.3 *Influence of powder feed rate on the microstructure*

The effect of powder feed rate on the reaction zone in the centre of the deposited single wall samples was also investigated. The laser power and traverse speed were kept constant, while the powder feed rate was varied between 7.3, 10 and 12.2 g/min. *Figure 6-15* shows that the reaction zone slightly decreased with an increase in the powder feed rate.

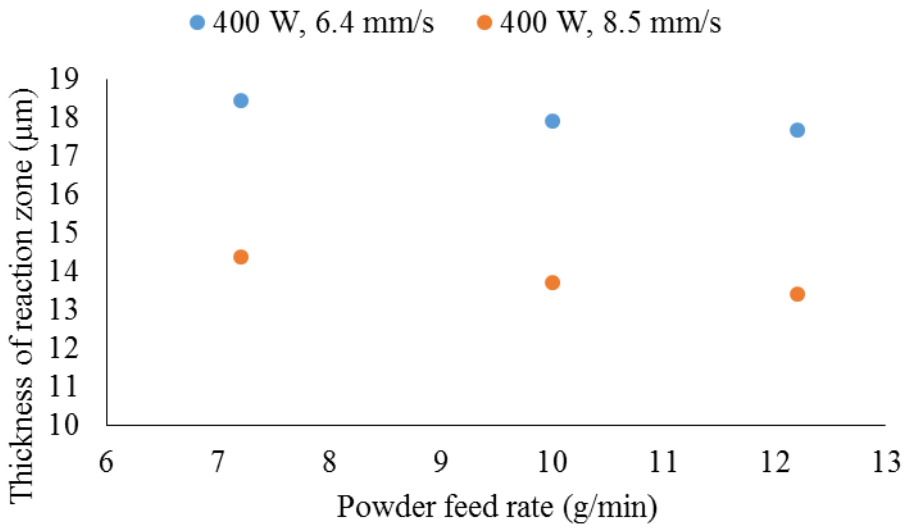

Figure 6-15: Effect of powder feed rate on the thickness of the reaction zone at 400 W.

6.2.2.4 *Effect of the z-increment on the microstructure*

Figure 6-16 shows that the bright surface zone increased when the z-increment was set equal to the layer thickness. A z-increment equal to the layer thickness resulted in a banded structure with two different alternating layers. These layers consisted of a light and a dark layer, the dark layers consisted of grey, strip-shaped phases resulting from the dissolution of WC. The light layers consisted of trapezoid shaped grey phases. A banded structure was not evident when a z-increment of 0.2 mm was used. Microstructural banding occurs as a result of subsequent layer melting or reheating following deposition. During deposition the first layer is deposited on to a substrate and will experience higher cooling rates due to a thermal gradient, provided that the substrate is not preheated. The second layer is then deposited on to the first layer

which is still at high temperatures, so as subsequent layers are deposited the cooling rate decreases due to a decrease in the temperature gradient. In addition the deposition of a layer causes re-melting or reheating of the layer below it, re-melting will lead to further dissolution of WC. Layer reheating will lead to grain growth of the preceding layers. This in-situ heat treatment during deposition will result in a banded microstructure. *Figure 6-17* shows microstructural banding in a sample deposited at 200 W, 6.4 mm/s, 10 g/min and z-increment of 0.167 mm.

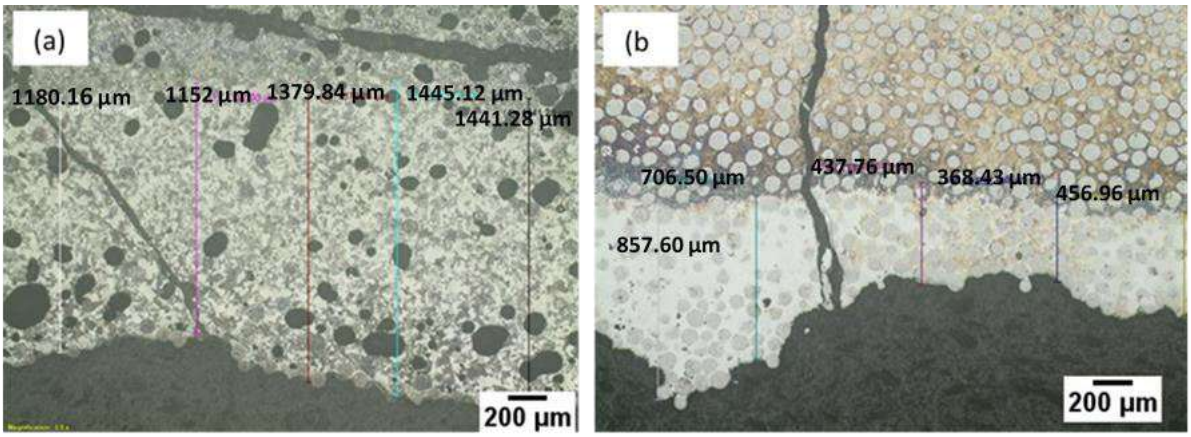

Figure 6-16: Bright surface zone at 200W, 6.4mm/s, 10g/min and z-increment of; (a) 0.167 mm, (b) 0.2 mm.

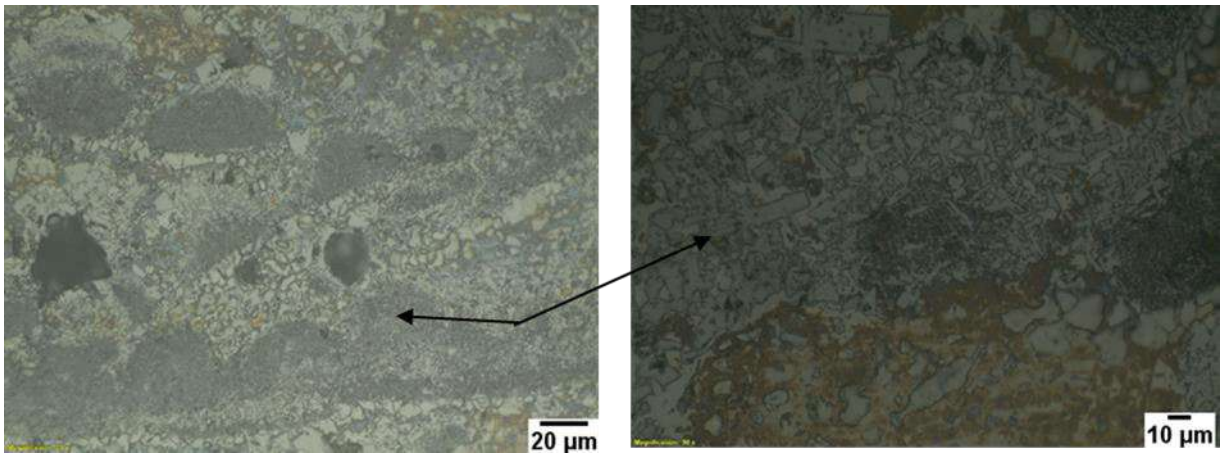

Figure 6-17: Banding structure at 200 W, 6.4 mm/s, 10 g/min, z-increment: 0.167 mm.

6.2.3 Microstructure of the FeCr Cube Sample

The microstructure of the cube FeCr sample was predicted by means of the Schaeffler diagram which uses the alloy's chemical composition to predict the microstructure. The elemental constituents in steel are either austenitic formers/ stabilisers, i.e. Ni, or ferritic formers/stabilisers, i.e. Cr. The Schaeffler diagram plots austenitic and ferritic promoting elements in terms of Ni and Cr equivalent and the two intersects in the phase field. The Ni and Cr equivalents were calculated using Eq. 6-1 and Eq. 6-2, the chemical composition used was that specified on the supplier material datasheet. The Schaeffler diagram and predicted phase field of the FeCr binder is shown in *Figure 6-18*. The predicted phase field was within the austenite and martensite phase

$$Ni_{eq} = (\%\, Ni) + 0.5 \times (\%\, Mn) + 30 \times (\%\, C) \qquad \text{Eq. 6-1}$$

$$Cr_{eq} = (\%\, Cr) + (\%\, Mo) + 1.5 \times (\%\, Si) + 0.5 \times (\%\, Nb) \qquad \text{Eq. 6-2}$$

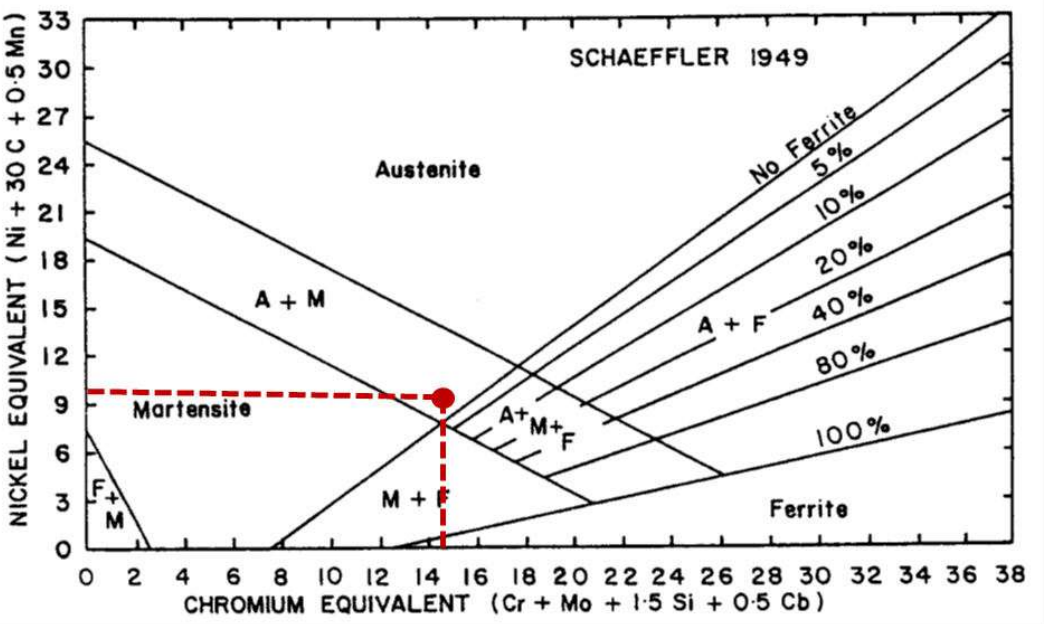

Figure 6-18: Schaeffler prediction of FeCr phase field [153].

Figure 6-19 shows the microstructure of the FeCr alloy which showed deposition beads. The microstructure was inhomogeneous displaying a banded structure consisting of darker band pattern across each deposition bead (*Figure 6-20*). The darker

band was evidence of a reheating thermal cycle resulting in a carbide spherodised zone which is characteristic of the tempering process. So it can be seen that during laser deposition in-situ tempering of subsequent layers occurs. The microstructure comprised of martensitic lathes and inter-dendritic retained austenite *Figure 6-21*. The last layer to be deposited was composed of a decarburised layer (*Figure 6-22*). This was due to the heat build-up as subsequent layers were deposited



Figure 6-19: Microstructure of FeCr showing the deposition beads.



Figure 6-20: Micrograph of FeCr with arrows showing retained austenite.

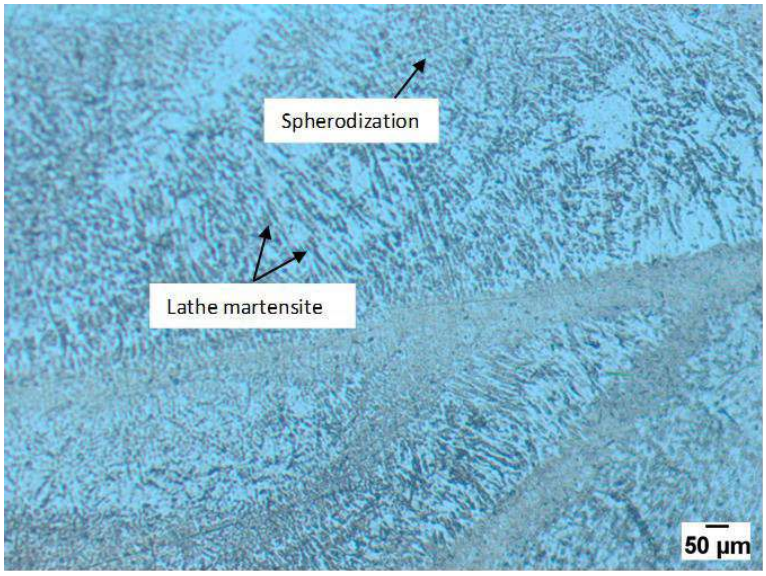

Figure 6-21: Microstructure showing lathe martensite.

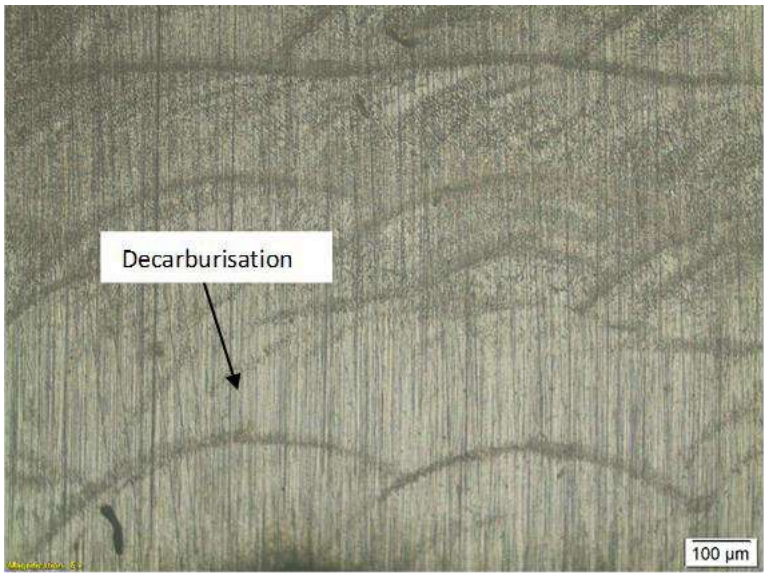

Figure 6-22: Decarburisation on the top layers of the FeCr alloy.

6.2.4 Microstructure of the cube sample

T*able 6-2* shows the optimum parameters for the cube sample.

T*able 6-2: Optimum parameters for cube samples.*

Power (W)	Speed (mm/s)	Feed rate (g/min)
200	3.2	12.2

The fusion zone between the substrate and cube sample did not show any lack of fusion defects, which indicates suitable processing parameters. However, cracks originating from lack of fusion porosity were seen propagating through the spherical WC grains. *Figure 6-23* shows the fusion zone and crack propagation.

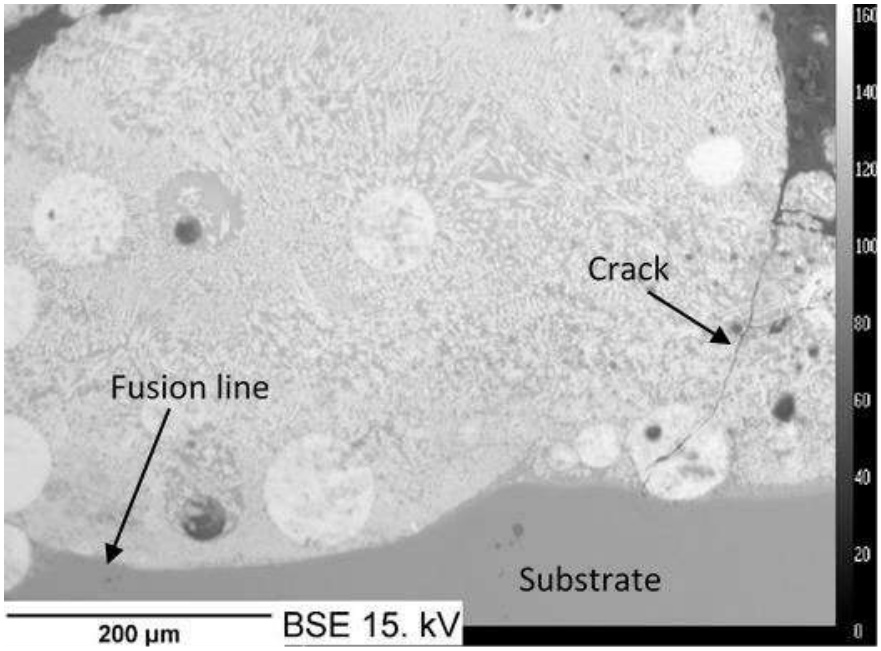

Figure 6-23: SEM BSE image of the fusion line.

The BSE image in *Figure 6-24* indicates partial dissolution of the spherical WC grain leading to different reaction products. The first reaction product observed, formed around the spherical WC grain in a halo-form effect. The grains within the halo region were equiaxed as well as columnar shaped, where the latter is evident of a steep temperature gradient. Columnar grains are heterogeneous solidification structures and have an elongated shape. They grow from a region of high temperature in the direction of a positive temperature gradient.

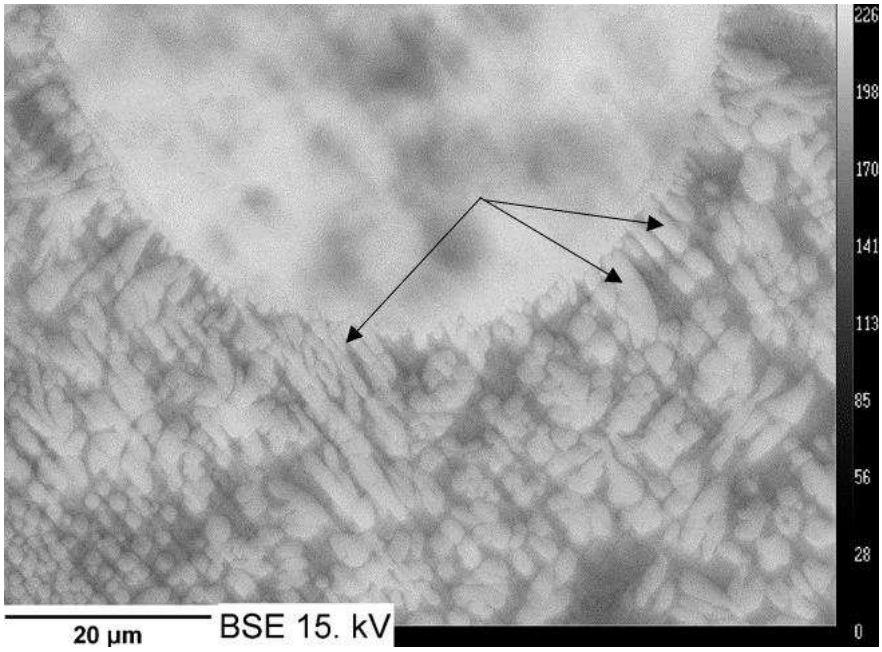

Figure 6-24: SEM BSE image of columnar grain on the edges of the spherical WC indicated by arrows.

The columnar grains detached from the spherical WC and dispersed throughout the microstructure within the matrix. The matrix consisted of a herringbone structure which formed from the columnar grains. This structure formed at the bottom of the sample, close to the substrate. *Figure 6-25* and *Figure 6-26* show the herringbone structure displaced from the spherical WC grains and together with the close up view of the herringbone structure. Since the herringbone structure was composed of columnar grains it was termed columnar herringbone growth.

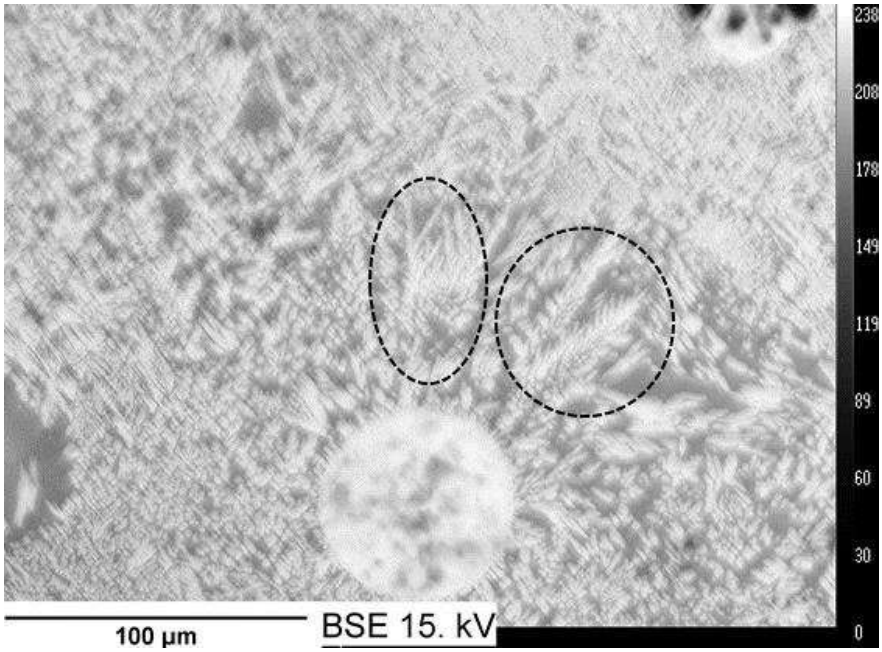

Figure 6-25: Herringbone structure indicated with the dashed regions.

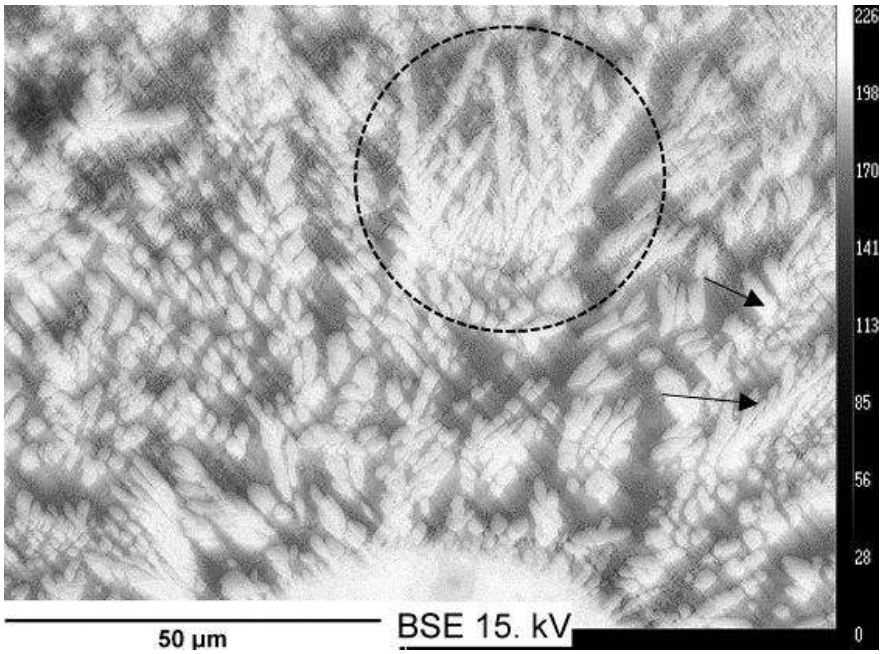

Figure 6-26: Columnar grains forming a herringbone structure within the dashed regions.

The top and middle of the cube sample revealed a trapezoidal and strip phase which formed from the edges of the spherical WC grain and detached from the spherical grain. The grain structure at the top of the sample was also predominately columnar. *Figure 6-27* shows the trapezoidal and strip phase at the top of the sample and *Figure 6-28* shows both the trapezoidal phase and columnar grains.

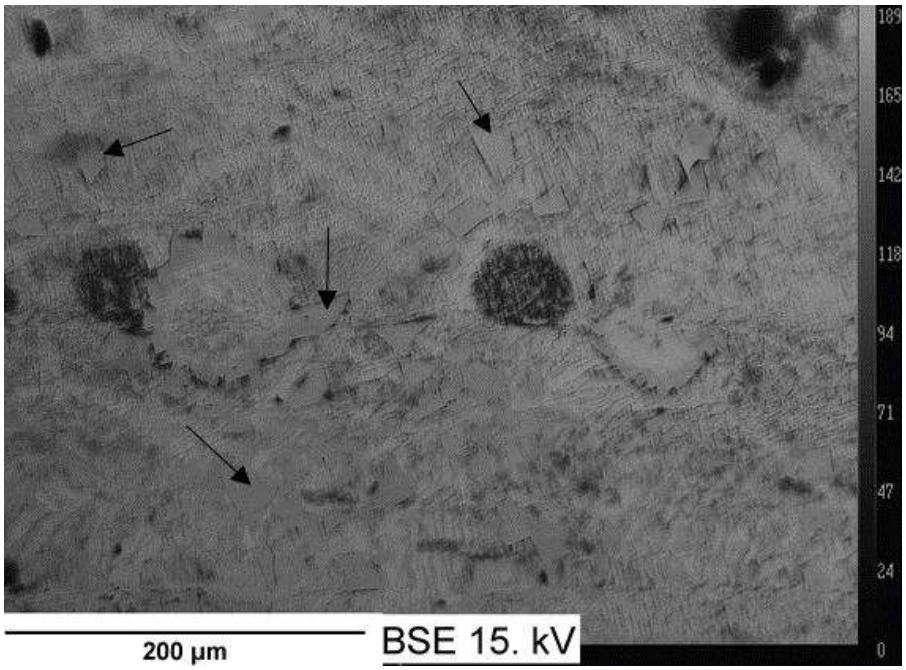

Figure 6-27: Trapezoidal phase at the top of the sample indicated by the arrows.

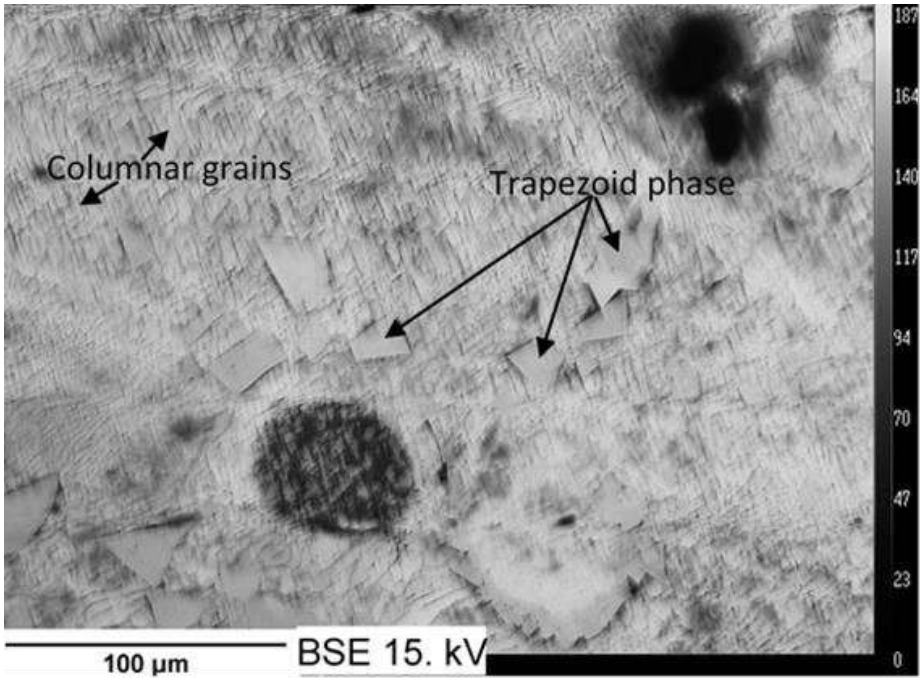

Figure 6-28: Columnar grains and the trapezoid phase at the top of the deposit.

Figure 6-29 and

Table 6-3 shows the WDS positions and elemental compositions respectively. From. *Table 6-3* it is clear that un-melted spherical WC grains have a W content of ~86 wt%.

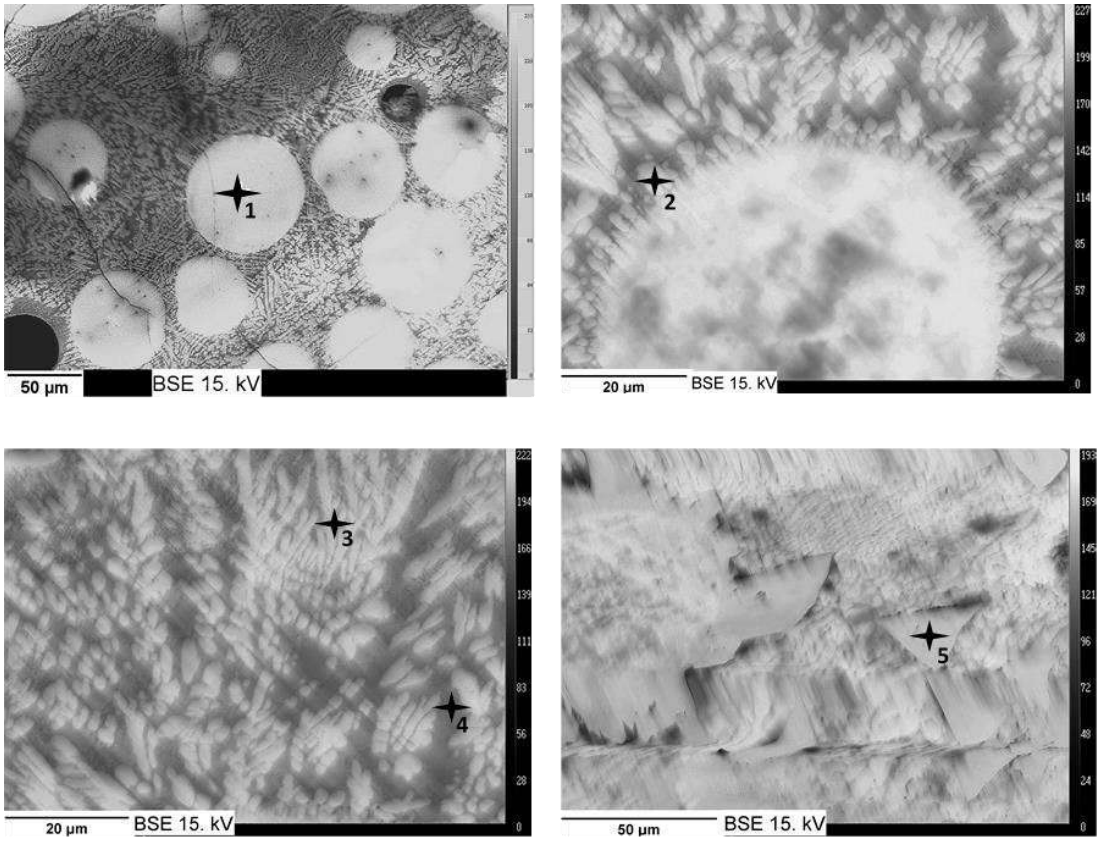

Figure 6-29: WDS elemental point analysis on different phases of the cube sample.

Table 6-3: WDS analysis of the different phases.

Composition (wt%)	**1**	**2**	**3**	**4**	**5**
C	3.74	3.96	3.25	1.06	4.50
W	85.76	93.70	79.06	47.13	77.49
Fe	4.83	1.11	15.48	48.72	15.52
Cr	0.35	1.23	0.68	1.70	0.72
Mn	0.015	<0.01	0.13	0.28	<0.01
O	5.31	<0.01	1.40	1.10	1.77
Morphology	Spherical	Columnar	Herringbone	Dark phase	Trapezoidal

Figure 6-30 to *Figure 6-32* shows the WDS mapping analysis for the top, bottom and middle of the cube sample. A high concentration of carbon was observed in the crack in *Figure 6-30*.

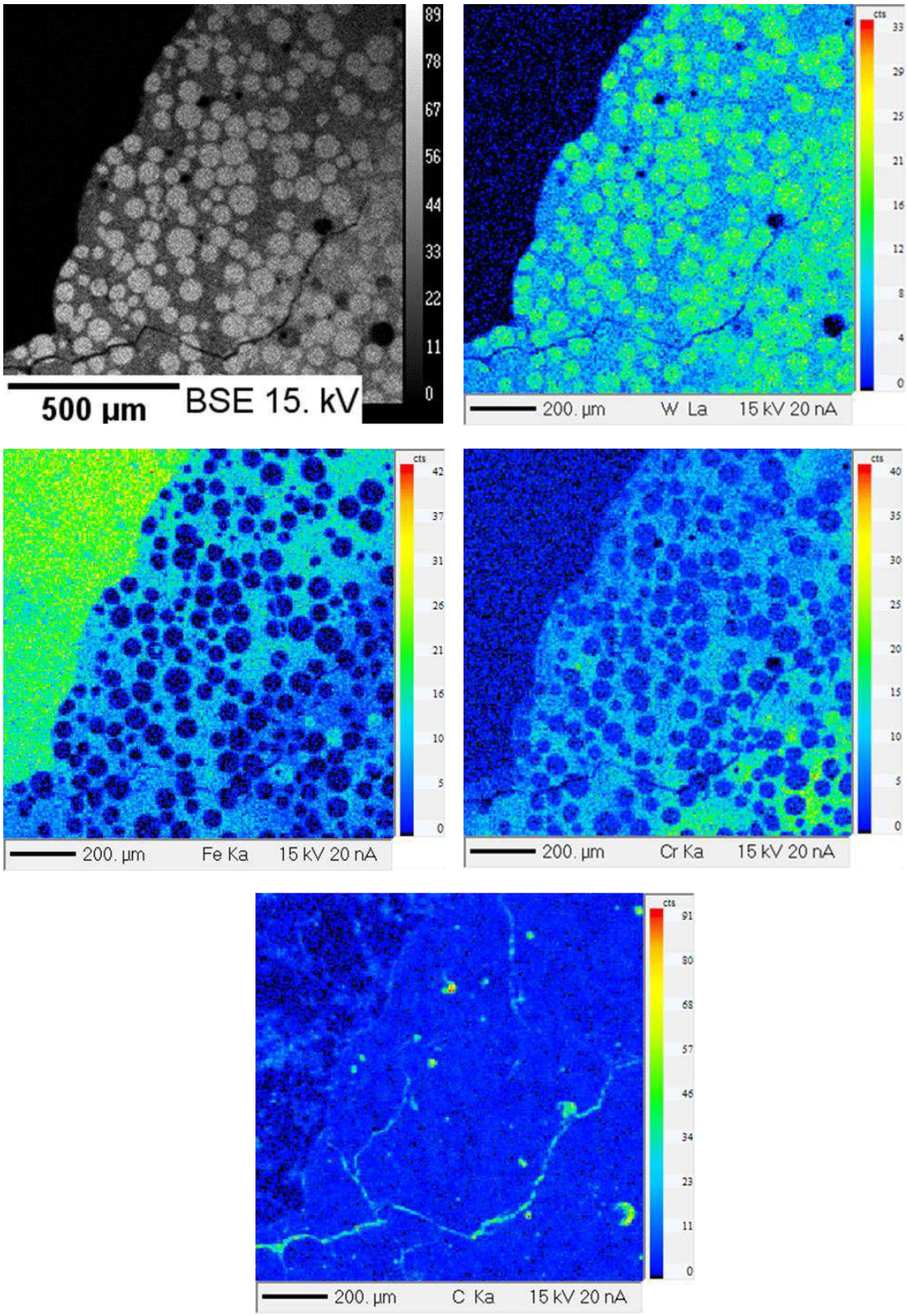

Figure 6-30: WDS elemental mapping at the bottom of the sample.

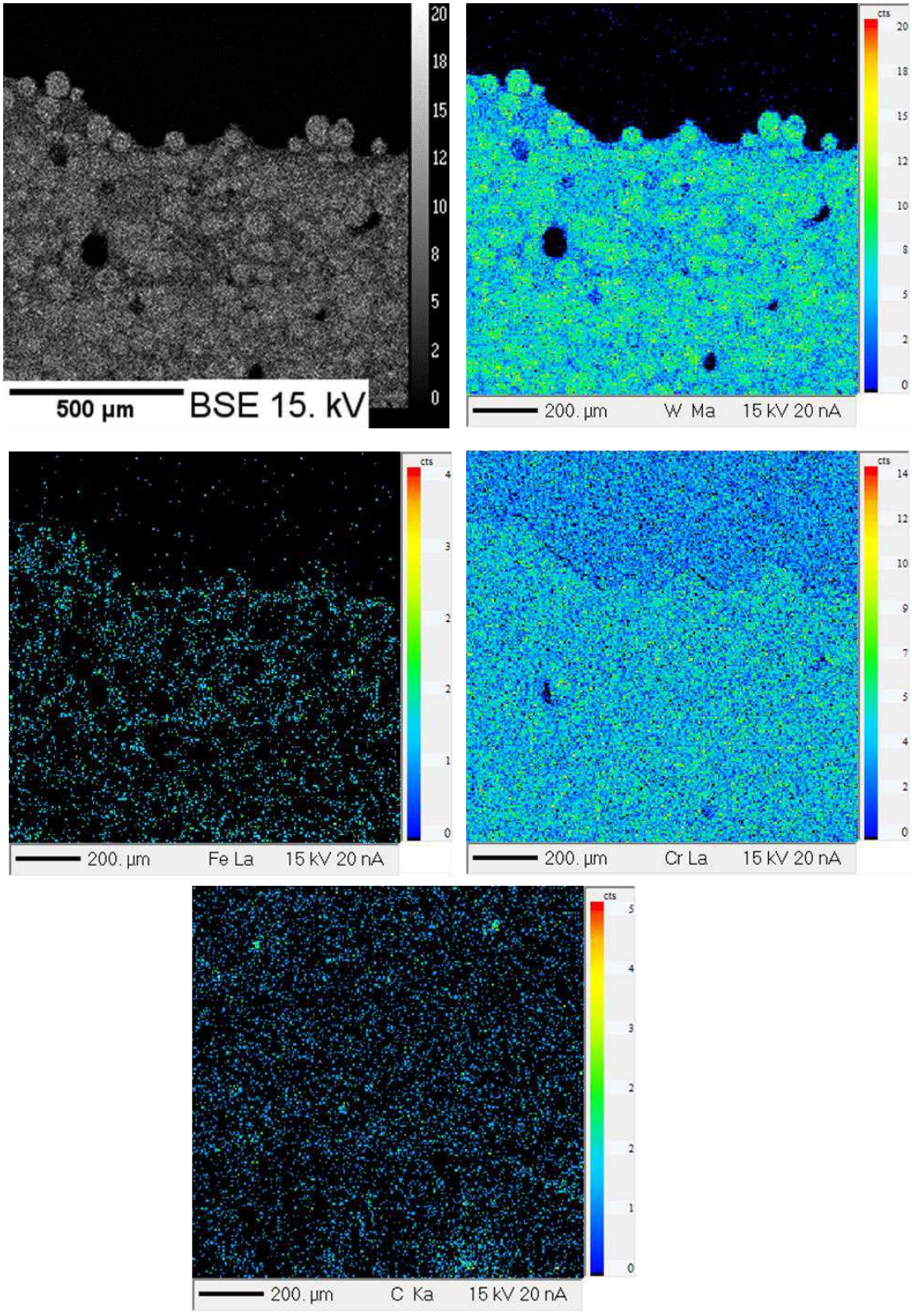

Figure 6-31: WDS elemental mapping on sample top.

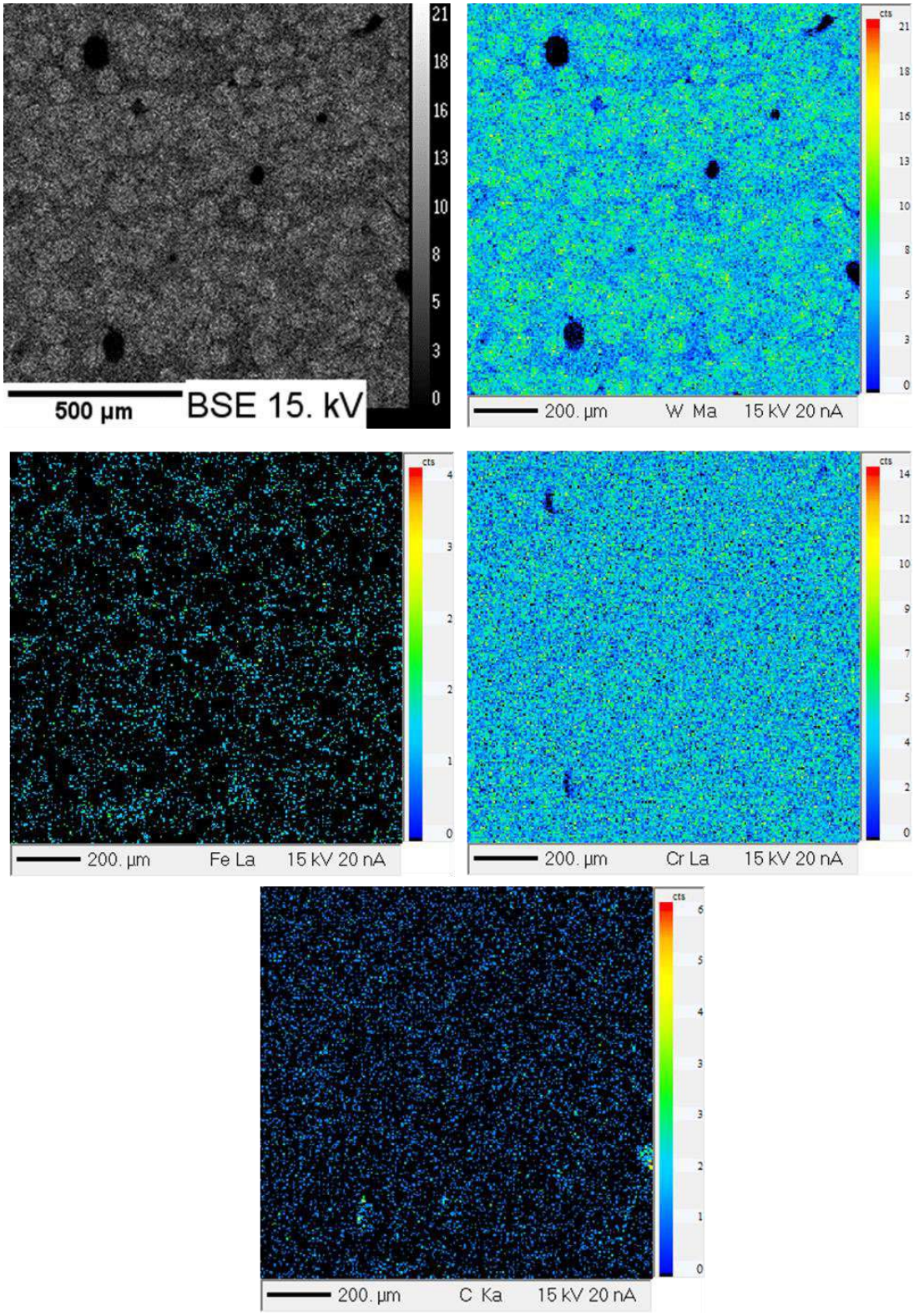

Figure 6-32: WDS elemental mapping at the centre of the sample.

The elemental distribution at the region of the herringbone structure and spherical WC was also studied by WDS mapping analysis. It is clear from *Figure 6-33* that the herringbone structure is within the FeCr matrix, hence it has a higher concentration of Fe in comparison to

the columnar W carbides. The dissolution of W into the FeCr matrix resulted in a decreased concentration of W within the herringbone structure.

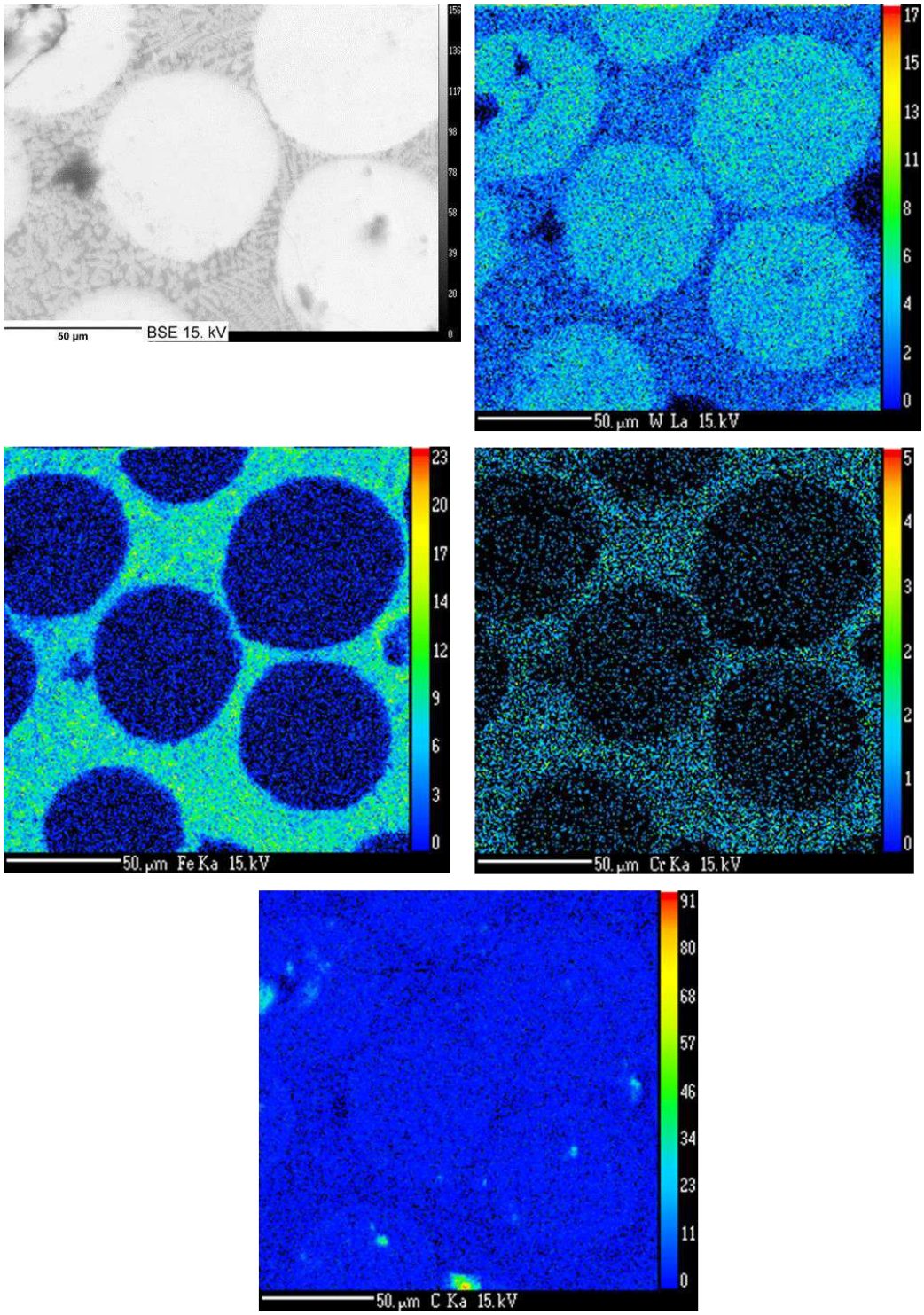

Figure 6-33: WDS elemental mapping around WC grains.

6.3 Constituent Phases

6.3.1 Phases present in thin wall samples

Figure 6-34 and *Figure 6-35* shows the XRD spectrums of the thin wall samples deposited at different process parameters. The XRD spectrums of the single wall sample showed partial dissolution of WC. The dissolution products occurred as precipitates of M_3C and $M_6C/M_{12}C$ carbides namely Fe_3W_3C (22.660°, 42.083° peaks) and Fe_6W_6C (35.626° peak). A dissolution phase namely Fe_7W_6 was present at the 43° peak. It was observed from the XRD patterns that the intensity of the Fe_3W_3C peak at 42.083° mainly increased with laser power. A graphite peak was present at 29.143°, however this was due to the bakelite mounting resin which was used. Ignoring the graphite peak, W_2C was observed as the major phase from the XRD patterns. *Table 6-4* shows the process parameters and the phases present in the thin wall samples.

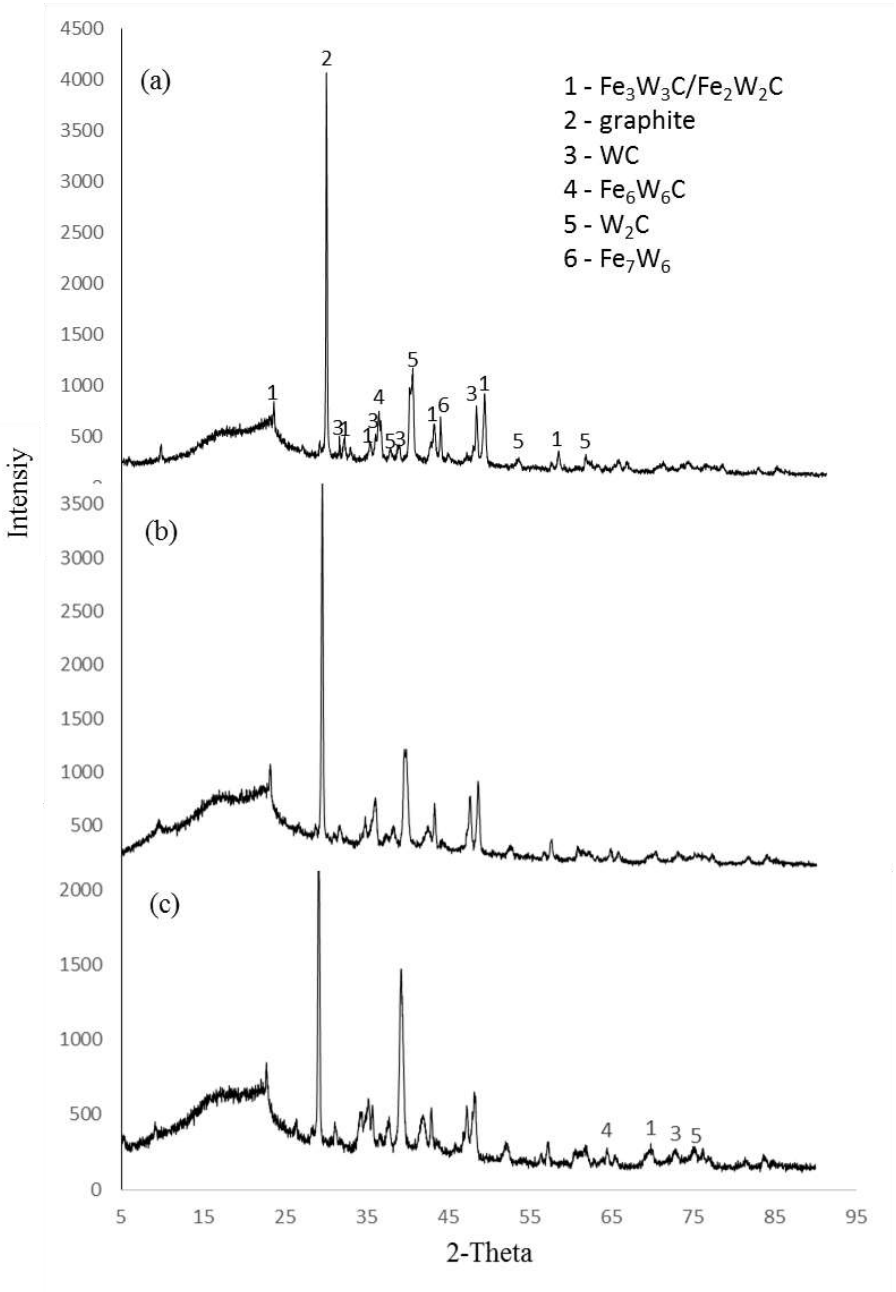

Figure 6-34: XRD spectrum of the single wall samples at 8.4 mm/s, 12.2 g/min; (a) 200 W, (b) 300 W, (c) 400 W.

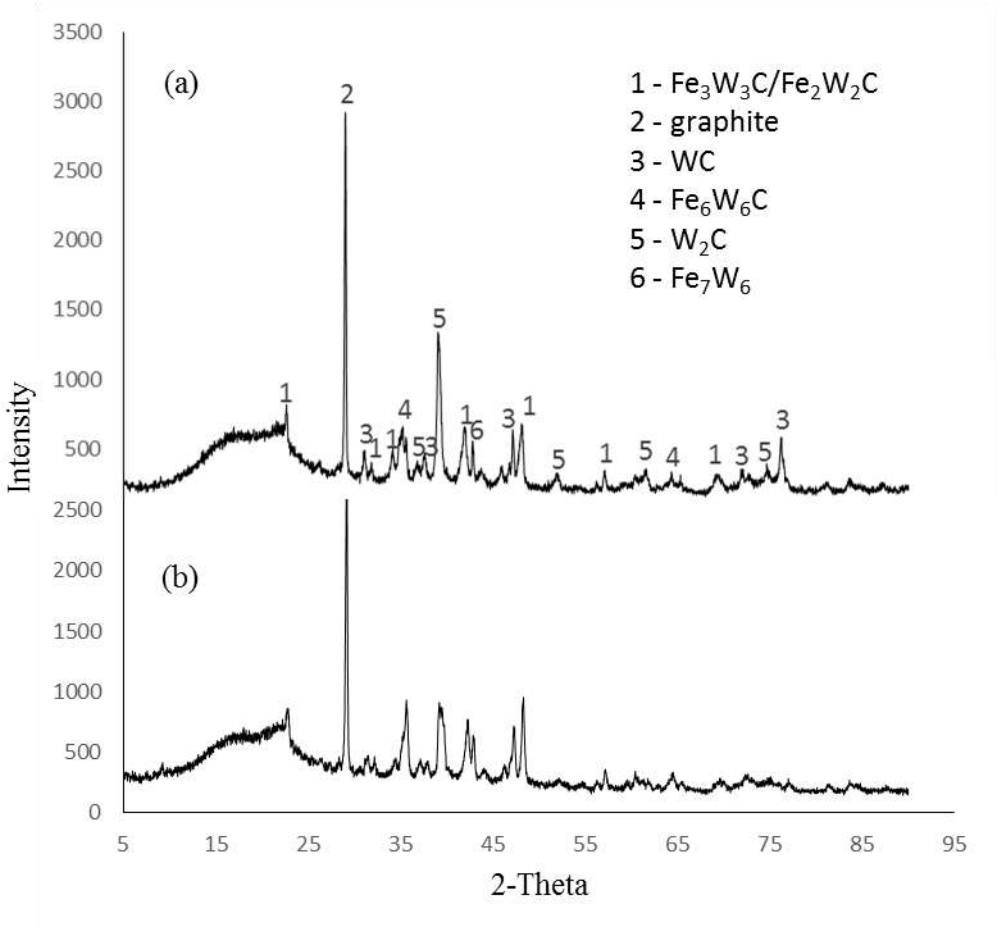

Figure 6-35: XRD spectrum of the thin wall samples at 3.2 mm/s; (a) 200 W, (b) 300 W.

Table 6-4: XRD phase results.

Laser power (W)	**Traverse speed (mm/s)**	**Powder feed rate (g/min)**	**Phases identified**
200	3.2	12.2	WC, W_2C, Fe_3W_3C, Fe_6W_6C, Fe_7W_6
300	3.2	12.2	WC, W_2C, Fe_3W_3C, Fe_6W_6C, Fe_7W_6
200	8.5	12.2	WC, W_2C, Fe_3W_3C, Fe_6W_6C, Fe_7W_6
300	8.5	12.2	WC, W_2C, Fe_3W_3C, Fe_6W_6C, Fe_7W_6
400	8.5	12.2	WC, W_2C, Fe_3W_3C, Fe_6W_6C, Fe_7W_6

The influence of the z-increment on the phases formed is shown *Figure 6-36*. When the z-increment was set equal to the layer thickness it led to an increase in the Fe_6W_6C and Fe_3W_3C peak intensity. The z-increment had the same effect as the laser power on the phases formed.

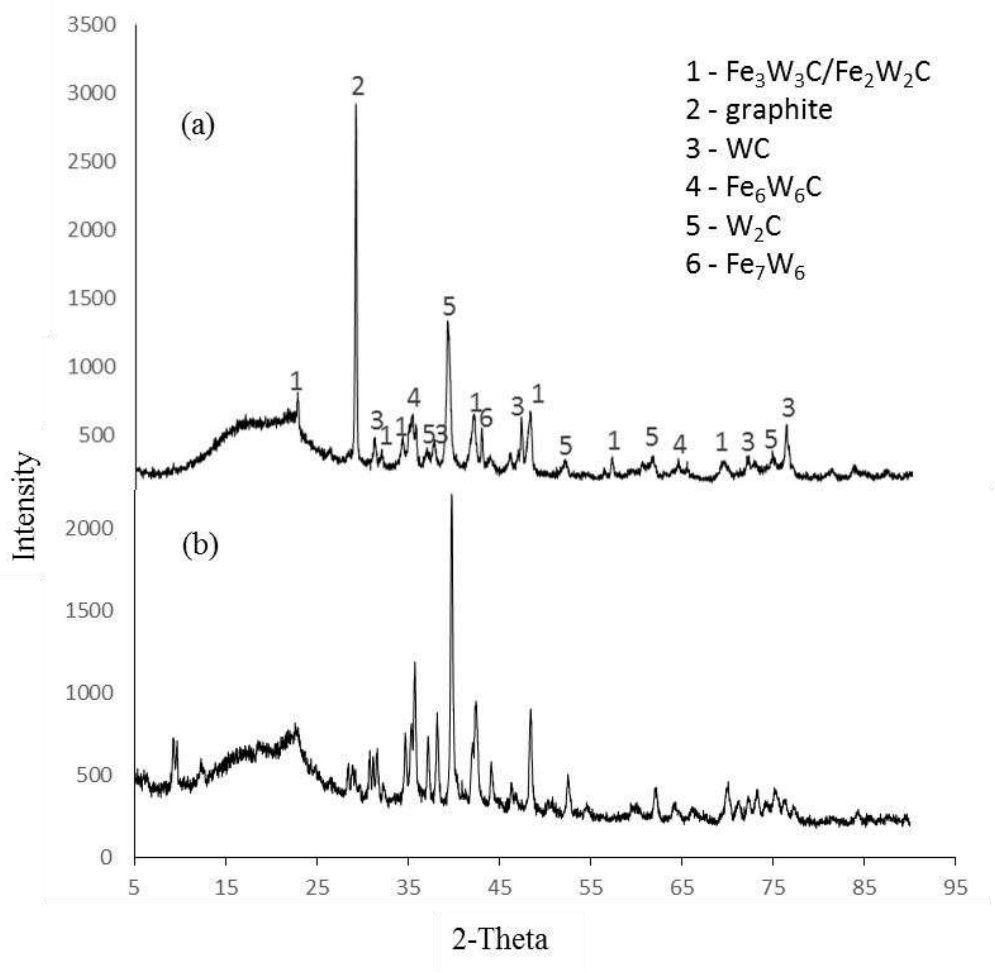

Figure 6-36: XRD spectrum of single wall samples at 200 W, 3.2 mm/s, 7.3 g/min; (a) z-increment of 0.2 mm, (b) z-increment of 0.167 mm.

6.3.2 Phases present in the FeCr cube sample

Figure 6-37 shows the XRD spectrum for the FeCr binder. Only two phases were observed α Fe and chromium carbides, Cr_7C_3.

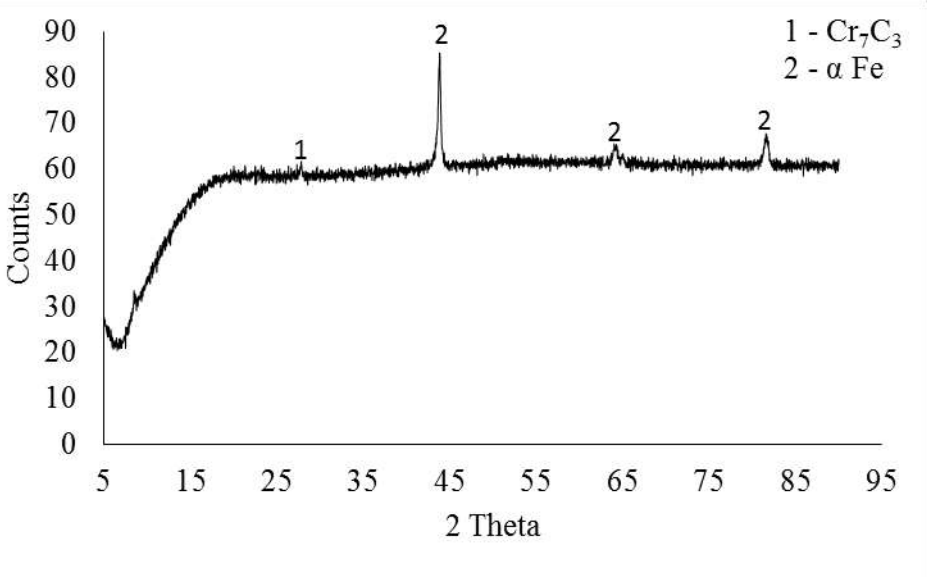

Figure 6-37: XRD spectrum for FeCr cube sample.

6.3.3 Phases present in the optimum cube sample

Figure 6-38 shows the XRD spectrum for the cube sample and the phase composition based on stoichiometric calculation is shown in *Table 6-5*. The Fe_6W_6C phase which was observed in the thin wall samples was also observed on the cube sample. Fe_6W_6C is a decomposition phase of Fe_3W_3C, from the reaction shown in Eq. 6-3:

$$5Fe_3W_3C \rightarrow 3WC + 2Fe_6W_6C + 3Fe \qquad \text{Eq. 6-3}$$

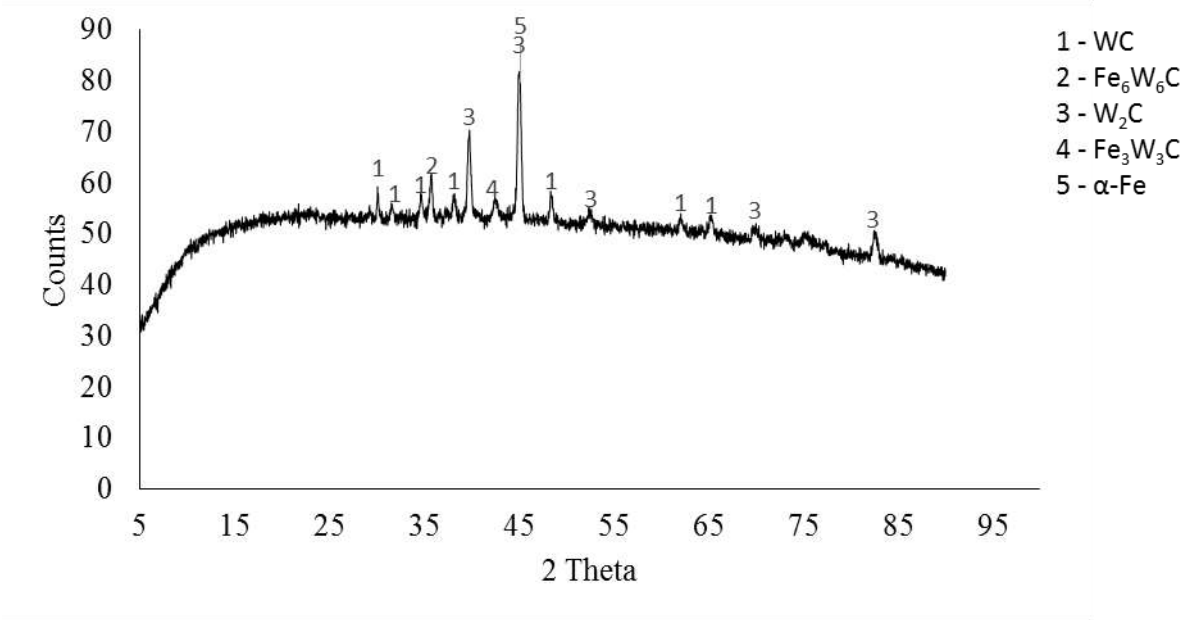

Figure 6-38: XRD spectrum of cube sample deposited at 200 W, 3.2 mm/s, 12.2 g/min.

Table 6-5: Calculated mass % of the different phases.

Compound	Chemical composition (wt.%)			
	W	C	Fe	Cr
WC	93.87	6.13	-	-
W_2C	96.84	3.16	-	-
Fe_3W_3C	75.44	1.64	22.92	-
Fe_6W_6C	76.07	0.83	23.11	-

6.4 Hardness Properties

6.4.1 Influence of process parameters on the thin wall sample hardness

Figure 6-39 shows the influence of laser power and traverse speed on the hardness of the matrix phase which comprised of FeCr and WC dissolution products. An increase in the laser power led to a decrease in hardness and an increase in the traverse speed resulted in an increase in hardness. A high laser power results in high heat input into the system and a slow cooling rate while an increase in traverse speed results in a decrease of the heat input into the system and hence a decrease in the WC dissolution.

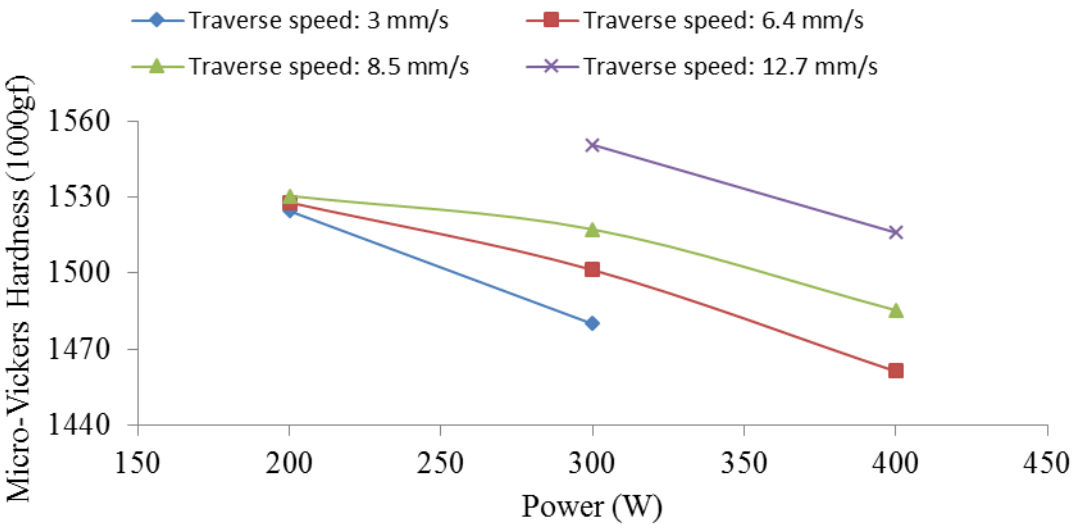

Figure 6-39: Influence of laser power on the micro-hardness of thin wall samples.

The Vickers macro-hardness measurement results using a load of 30 kgf are shown in *Figure 6-40*, the same trend as the micro-Vickers hardness results was observed. An increase in laser power led to a decrease in the hardness and increase in the traverse speed led to an increase in hardness. The macro-hardness was higher than the micro-hardness results because the hardness of the matrix is lower due to the use of a Fe-based binder.

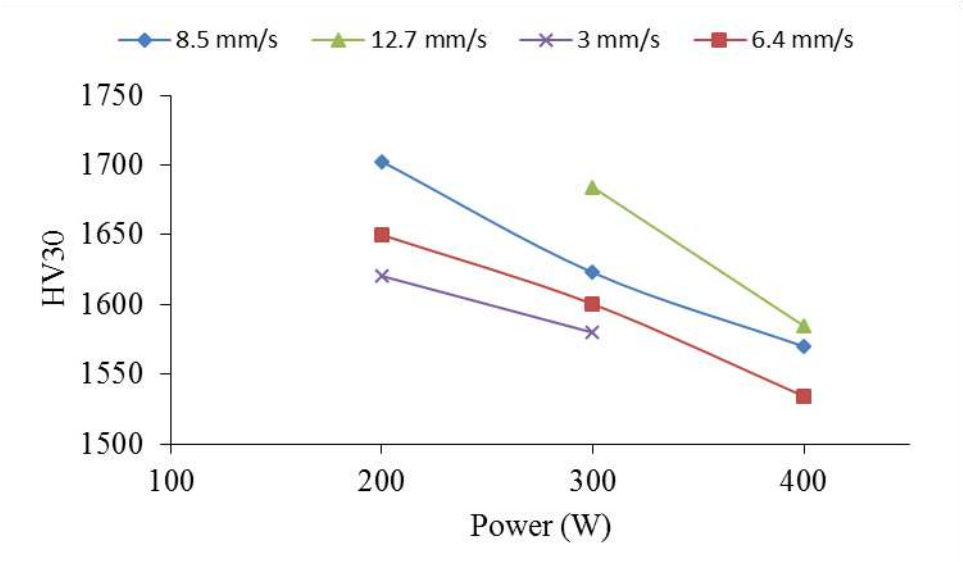

Figure 6-40: Influence of laser power on sample macro-hardness.

6.4.2 Hardness profile of the thin wall samples

Figure 6-41 and *Figure 6-42* present the micro-hardness profile of thin wall sample deposited at 300 W, 3.2 mm/s, 12.2 g/min and 200 W, 3.2 mm/s 12.2 g/min. The hardness profile for a laser power of 300 W, traverse speed of 3.2 mm/s and powder feed rate of 12.2 g/min showed that the hardness within the build was inhomogeneous and fluctuated between the ranges of 1200 – 1500 HV. However, the top surface showed a drop in hardness to values in the range of 1000 - 1012 HV. A drop in the hardness towards the top surface of the deposited samples was also observed at a laser power of 200 W, traverse speed of 3.2 mm/s and powder feed rate of 12.2 g/min. The micro-hardness throughout the built fluctuated between the ranges of 1200 – 1600 HV with the surface having a hardness in the range of 1077 – 1183 HV

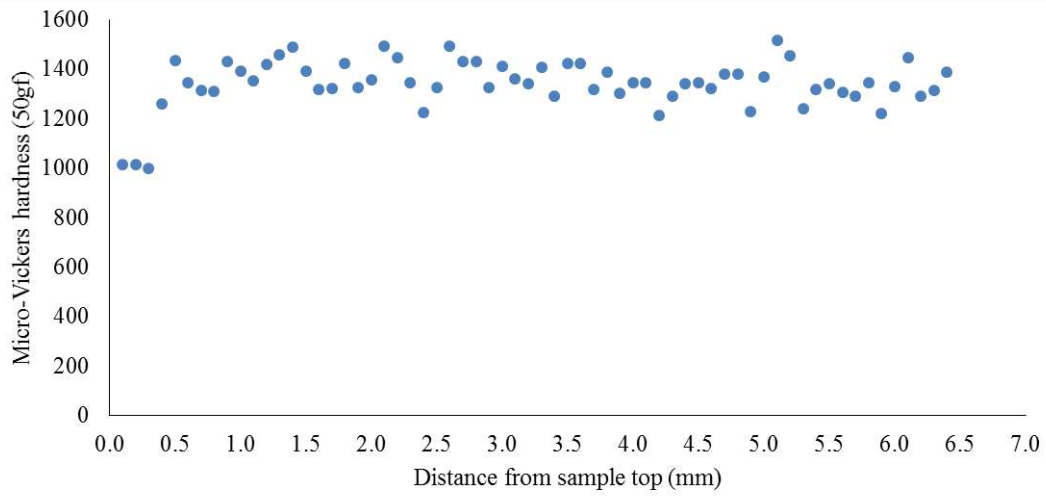

Figure 6-41: Micro-Vickers hardness profile at 300 W, 3.2 mm/s, 12.2 g/min.

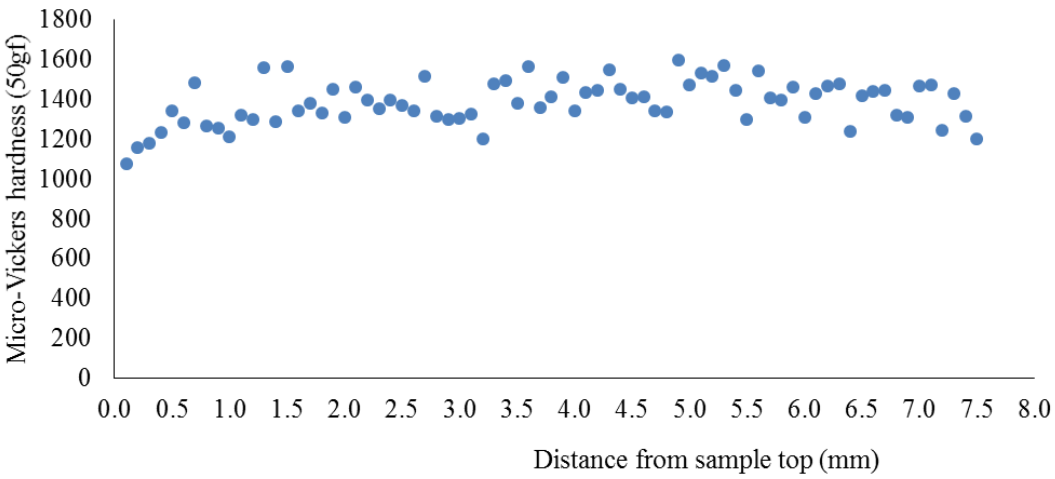

Figure 6-42: Micro-Vickers hardness profile at 200 W, 3.2 mm/s, 12.2 g/min.

6.4.3 Hardness of reaction phases in thin wall samples

Figure 6-43 and *Table 6-6* show the different phases and their hardness results. It was observed from the results that the spherical WC and W_2C particles had a higher hardness than the reaction product, M_6C phase. It can also be seen that the W_2C phase which forms a halo effect around the WC spherical phase had a higher hardness than the W_2C which has disintegrated from the spherical WC, and has formed a herringbone and granular structure within the matrix.

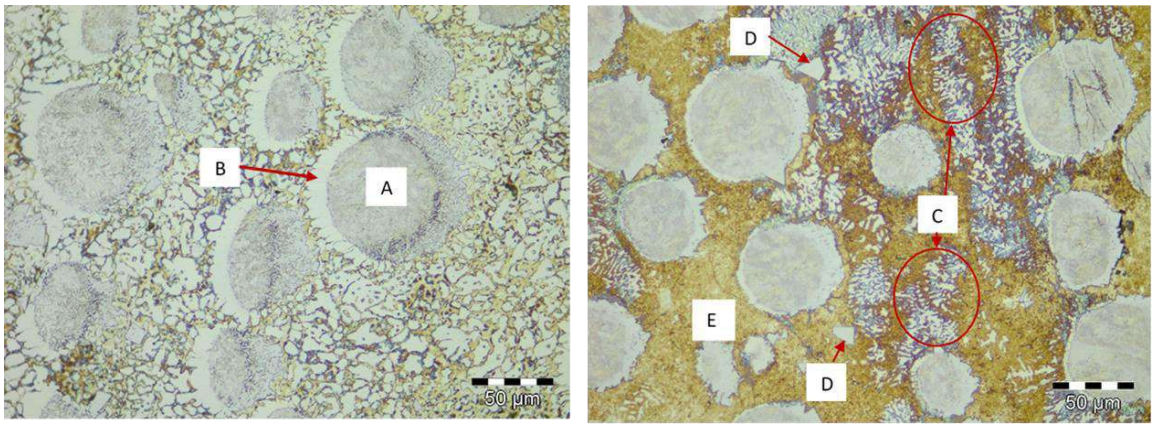

Figure 6-43: Phases for hardness measurements.

Table 6-6: Hardness of different phases.

Label	Phase	Vickers micro-hardness (50gf)
A	Spherical WC	2074.30 ± 38.40
B	W_2C (reaction halo)	2122.85 ± 74.85
C	W_2C(herringbone)	1532.90 ± 19.02
D	M_6C(trapezoidal phase)	1681.43 ± 29.67
E	FeCr (Matrix)	1292.20± 0.14

6.4.4 Hardness of the optimum cube sample

The hardness of the optimum cube sample was compared with the hardness of WC- 10 % FeCr samples manufactured using the sintering process to establish if the LENS® process can produce samples with comparable hardness to the sintering process. In addition the hardness of the optimum cube sample was compared with the hardness of the reference WC- 10 w.t% Co, to verify whether a FeCr binder can be used as a replacement for Co. *Table 6-7* shows the hardness results.

Table 6-7: Hardness of the optimum cube sample.

Hardmetal system	Hardness (HV30)
WC-10wt% FeCr (LENS®)	1441.73 ± 91.90
Comparison grades	
WC- 15 wt% FeCr (Sintered) [125]	1939
WC- 10 wt % Co (LENS®) [8]	1326±111
WC- 10 wt % Co (Sintered grade M10) [154]	1369

6.5 Fracture Toughness of the Cube Sample

Figure 6-44 shows multiple cracks at the corners of the hardness indents and on the surface of the diamond shaped indent for the optimum cube sample. All samples behaved in this manner hence, the fracture toughness could not be calculated in accordance with ISO 28079 [82]. Hardness indents were further made on cube samples deposited at 300 W 3.2 mm/s 10 g/min and 400 W 6.4 mm/s 12.2 g/min, however, multiple cracks originating from the indents were also observed.

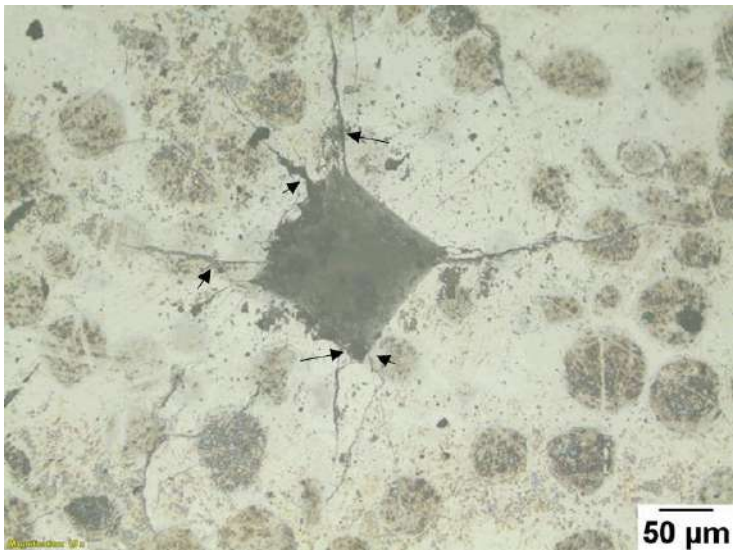

Figure 6-44: Palmaqvist indent showing multiple cracks originating away from the corners.

6.6 Effect of Laser Heat Input on the Surface Roughness of Thin Wall Samples

An analysis was done to investigate the influence of heat input on the surface roughness of the thin wall samples. The LENS® process is known as a near net shaped process with little post processing required [40]. Measurement of the surface roughness of the samples is required in order to establish whether post processing will be required. The heat input was calculated from Eq. 3-7. *Figure 6-45* shows that an increase in the heat input resulted in a decrease in the sample surface roughness. Laser power and traverse speed are significant parameters in the heat input expression.

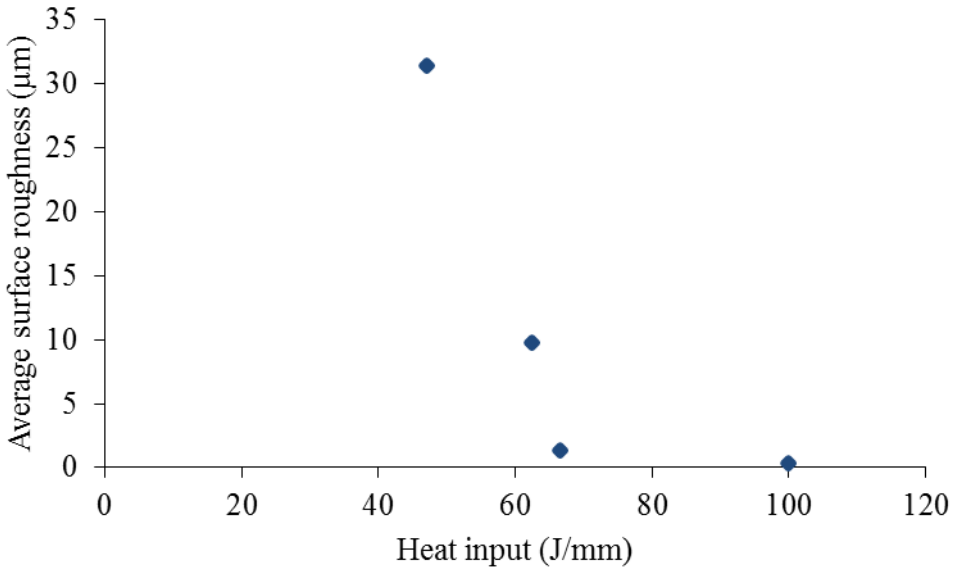

Figure 6-45: Influence of heat input on surface roughness.

6.7 Analysis of Thin Wall Thermal Profiles

Table 3-9 shows the experimental thermal conditions for thin wall samples. During the LENS® process the first layer was deposited for a length of 25.4 mm. The temperature across the length of the sample was established by calculating the temperatures at different distances away from the laser source for a single layer sample. As expected, the temperature close to the heat source was higher than that away from the heat source. Temperature was seen to increase with the deposition of subsequent layers with the first layer displaying the lowest temperatures. During the LENS® process the first layer is deposited on to a substrate which is at room temperature, the second layer is deposited on to the first layer which is still at high temperature. Continuous deposition of layers leads to a heat build-up whereby the last layer to be deposited experiences the highest temperatures. *Figure 6-46* shows the heat distribution away from the heat source, the material behind the heat source cooled down and the temperature of the heat source on the last layer deposited was enough to induce melting of the WC grains. This was observed in the microstructures where the top layer experiences partial melting and complete disintegration of the WC spherical grains.

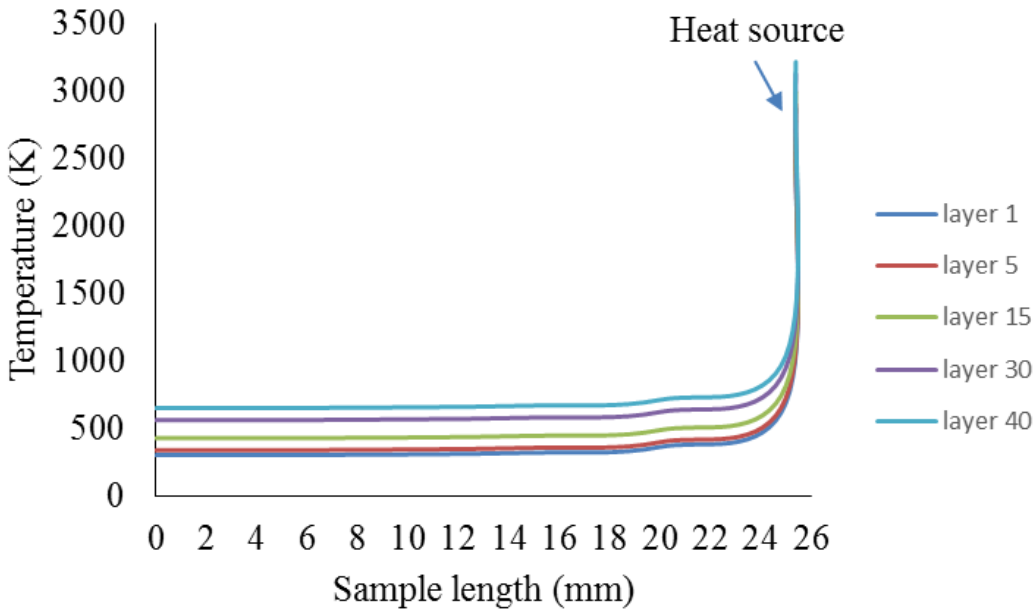

Figure 6-46: Temperature profile away from the heat source.

The temperature profile in is an affirmation that the hardness decreases from the first layer to the last layer deposited due to the heat build-up. The hardness and temperature profile across the sample layers are inhomogeneous. This affirms the inhomogeneous microstructure that was observed.

CHAPTER 7 Results and Analysis of Crack Restraining Methods

7.1 Introduction

This chapter presents the results and analysis of four crack restraining methods namely substrate preheating, laser re-melting, and buffering with a FeCr and Ni-alloy respectively. These methods were applied to the optimum cube sample described in Section 5.5. The influence of these methods on crack formation, hardness and phase formation are presented

7.2 Cube Sample without Crack Restraining

Figure 7-1 shows the LENS® deposited WC-FeCr hardmetal cube sample before the application of crack restraining techniques. No cracks were visually visible and this could have been due to the surface roughness of the sample.

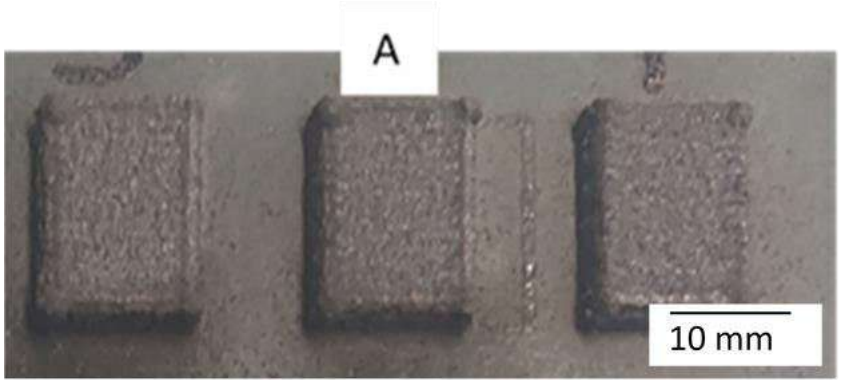

Figure 7-1: Sample A, LENS deposited sample at 200 W, 3.2 mm/s, 12.2 g/min without crack mitigation.

The cross section of the cube sample displayed vertical macro-cracks propagating from the top surface parallel to the sample build direction until the substrate/deposit interface. Horizontal secondary cracks originating from the main cracks were also observed, evidence of secondary cracking shows that the material was under high internal stresses [155]. Toe cracks were also observed between the deposited sample and the substrate interface. *Figure 7-2* shows the cracks on the cross section of the cube sample.

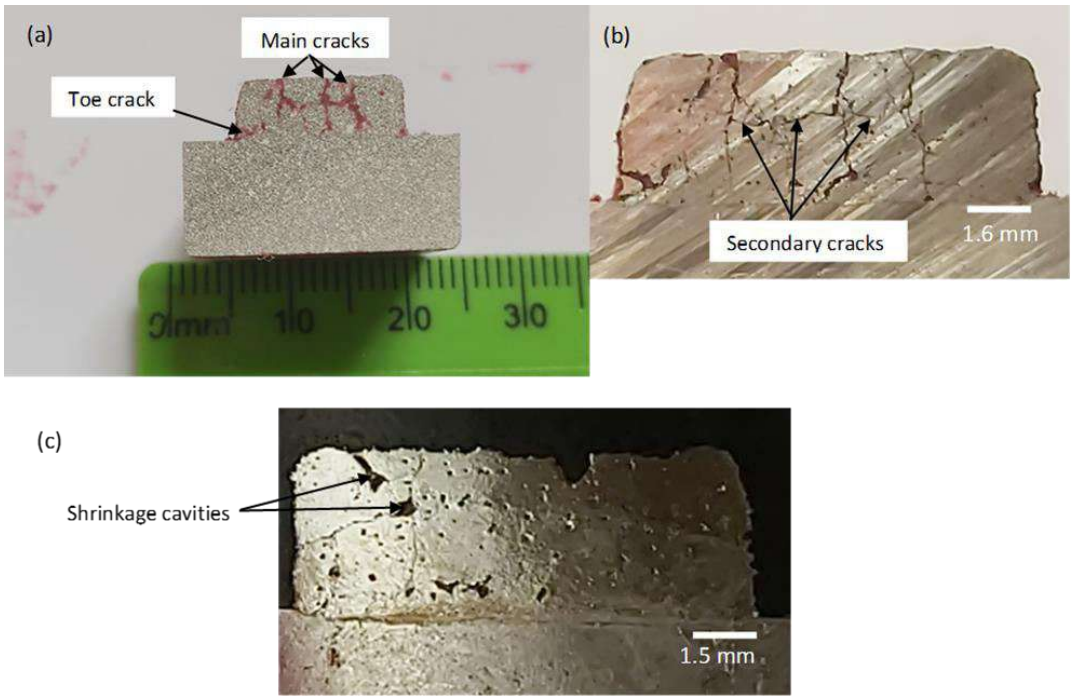

Figure 7-2: Cracks on cube sample (a) Dye penetrant tested sample, (b) As-sectioned cross section, (c) As-polished cross section.

7.3 Effect of FeCr Buffer Layer on Crack Formation

Figure 7-3 shows the WC-FeCr hardmetalcube sample deposited with a buffer layer. The surface profile showed a balling effect on the contour wall, with the contour achieving higher height than the rest of the build. The use of a FeCr buffer layer (*Figure 7-5*) led to a slight increase in the number of main cracks, however the secondary cracks reduced and the cracks observed were perpendicular to the substrate-buffer layer interface. The FeCr buffer layer showed no defects and displayed good fusion with both the substrate and WC-FeCr hardmetal (*Figure 7-6*).

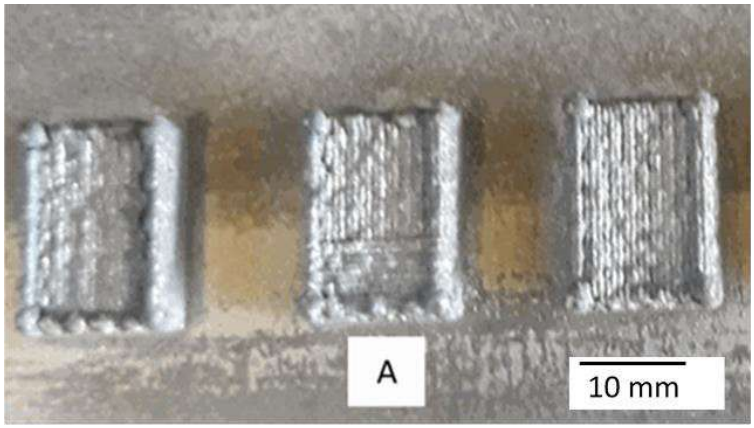

Figure 7-3: Sample A deposited with a FeCr buffer layer.

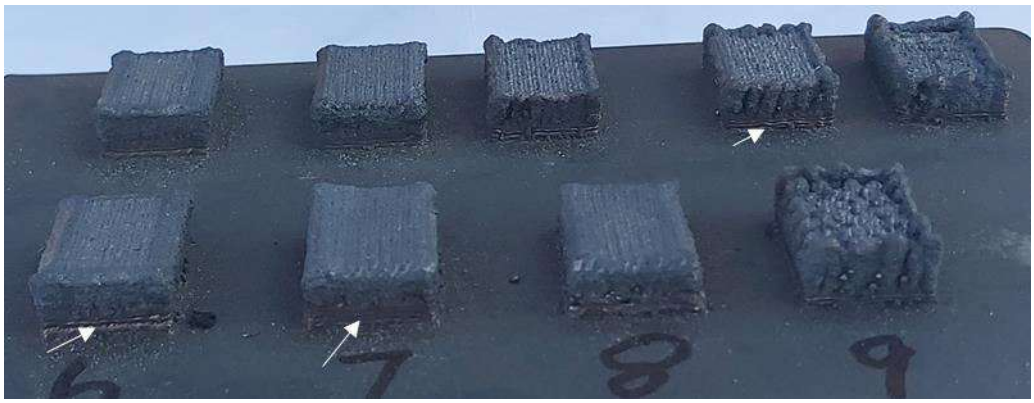

Figure 7-4: Ni buffer layer shown by the arrows.

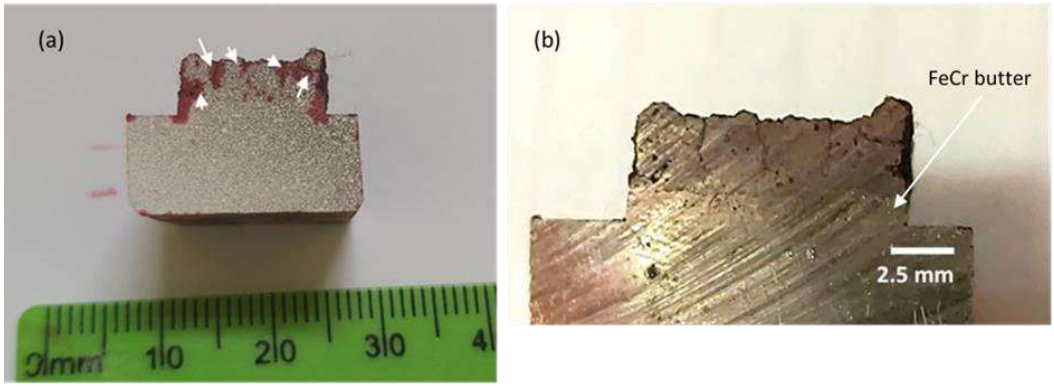

Figure 7-5: Ni-alloy buffer; (a) dye penetrant sample, (b) macro-image showing cracks.

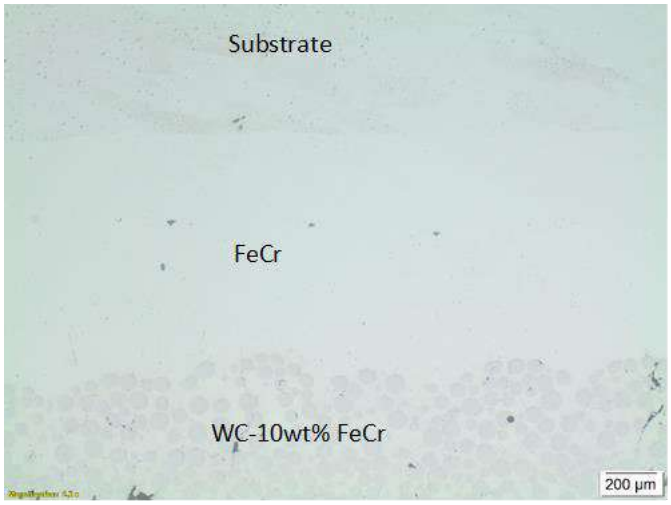

Figure 7-6: Micrograph of the FeCr buffer layer.

7.4 Effect of Ni-Alloy Buffer Layer on Crack Formation

Figure 7-7 shows the deposed cube sample with a Monel 400 (Ni alloy) buffer layer. No surface cracks or open pores were observed, however, the surface and shape profile showed evidence of balling on the contours. The buffer layer had no influence on the main cracks (which were visually counted) as the same number of cracks were present with or without the Ni-alloy buffer layer, however there was a reduction in the formation of secondary cracking (*Figure 7-8*). A micrograph of the Ni-alloy buffer layer displayed pores, low melting inclusions (shown with arrows) and cracks (*Figure 7-9*).

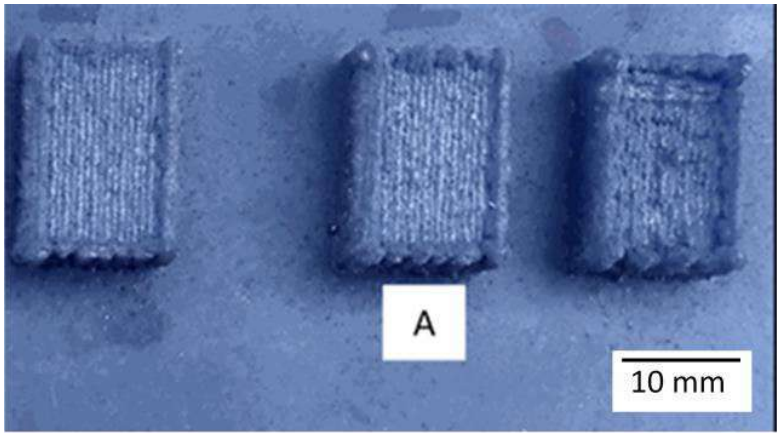

Figure 7-7: Sample A deposited with a Ni-alloy buffer layer.

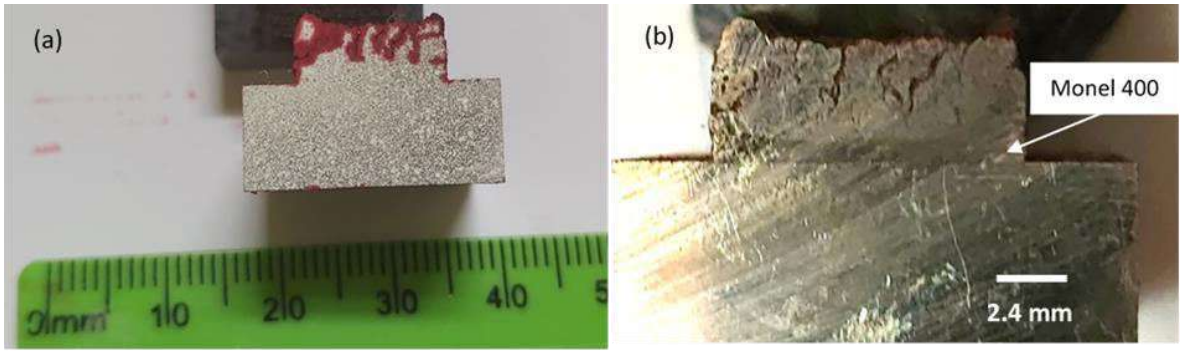

Figure 7-8: Ni-alloy buffer; (a) dye penetrant sample, (b) macro-image showing cracks.

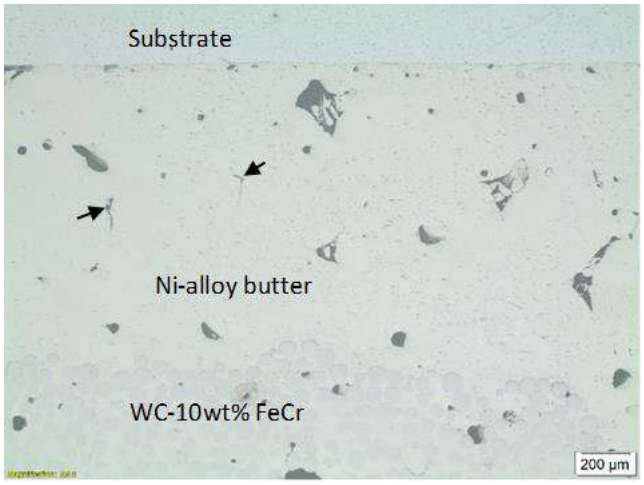

Figure 7-9: Micrograph of the Ni-alloy buffer layer with arrows showing inclusions.

7.5 Effect of Laser Re-Melting On Crack Formation

Laser re-melting was carried out by heating the sample surface with the laser without the addition of powder. *Figure 7-10* shows the surface morphology of the deposited samples before and after one and three layers of laser re-melting. Laser re-melting resulted in an improved surface appearance which visually appeared smoother with reduced edges on the contours and with less visibility of the scanning pattern than the samples without laser re-melting. A three layer re-melting technique had the most impact on improved surface appearance in comparison to a one layer re-melting technique due to more heat application and hence increased melting of un-melted powder particles. The cross section of the cube sample displayed cracks which were perpendicular to the deposit-substrate interface, a reduction of secondary cracks was observed in comparison to the sample deposited without any crack restraining techniques (*Figure 7-11*). The one layer re-melting led to lack of fusion cracks along the interface. One layer laser re-melting had no influence on the cracks as the number of cracks were the same with samples without laser re-melting. However, a three-layer laser re-melting technique resulted in a reduced number of cracks.

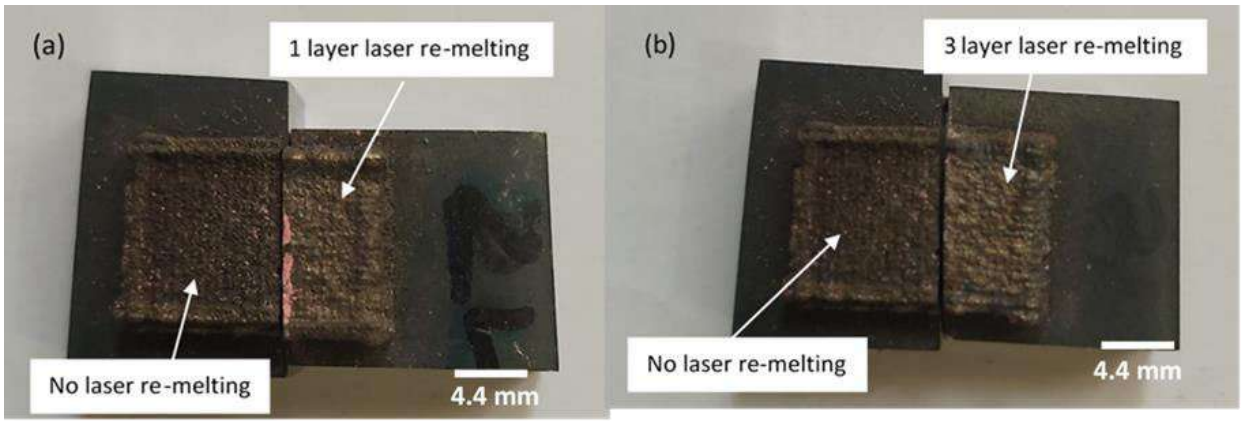

Figure 7-10: Effect of laser re-melting, (a) and (c) 1 layer re-melting; (b) and (d) 3 layers re-melting.

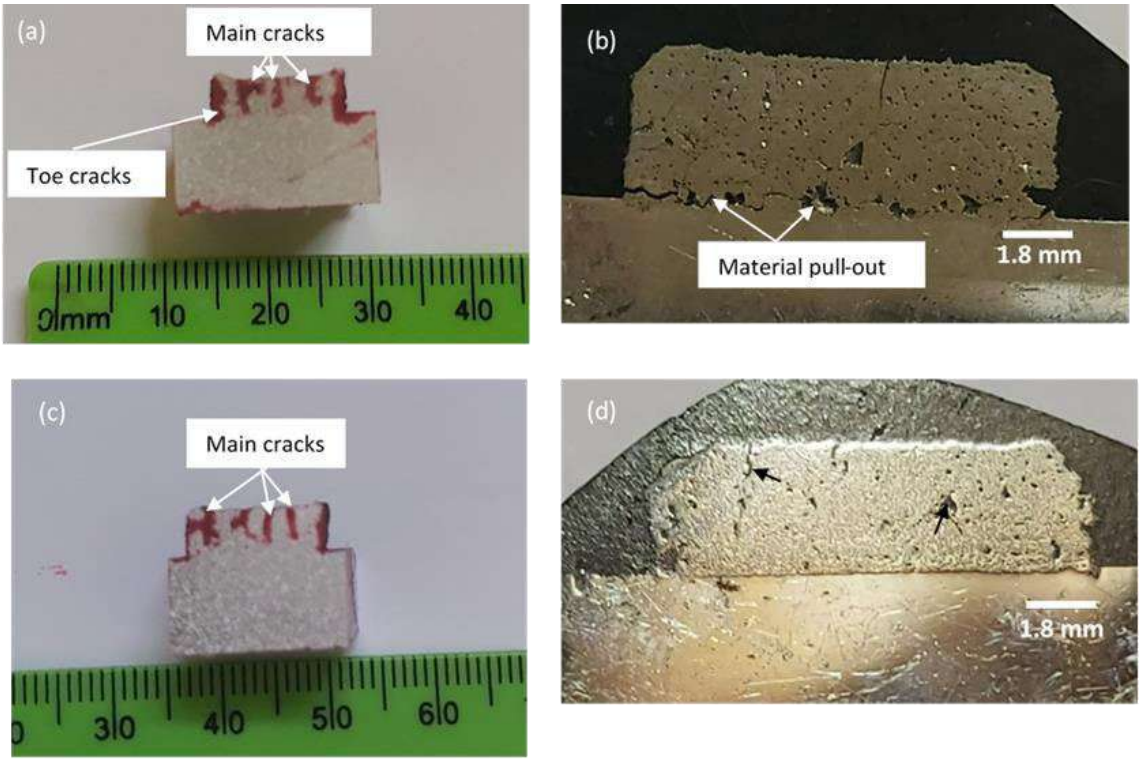

Figure 7-11: Effect of laser re-melting, (a) and (b) 1 layer re-melting; (c) and (d) 3 layers re-melting.

7.6 Effect of Preheat on Crack Formation

Figure 7-12 shows the dye penetrant and macro-image cracks on the preheated sample. There was a reduction in the number of main cracks in comparison to the samples which did not undergo preheating and no secondary cracking was observed.

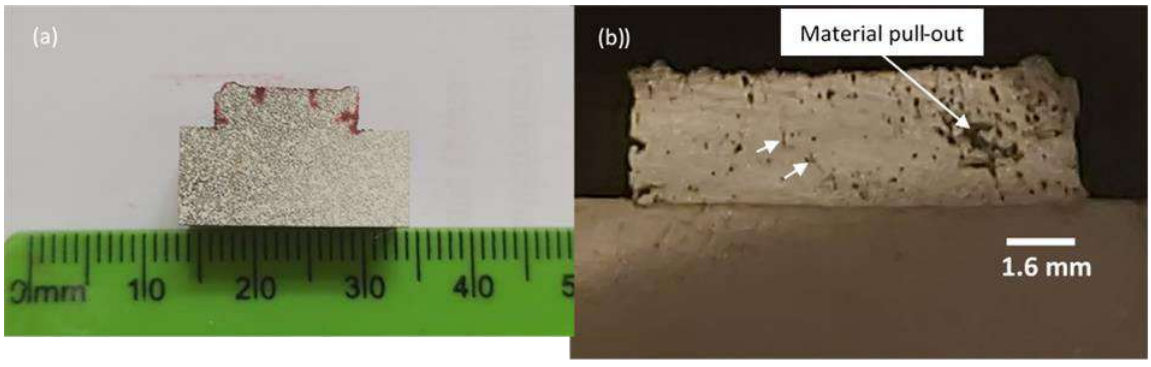

Figure 7-12: Preheat at 250 °C; (a) dye penetrant sample, (b) macro-image.

7.7 Comparison of Crack Restraining Methods

7.7.1 Crack analysis

Table 7-1 presents a summary of the effect of the crack restraining methods on the formation of cracks. None of the crack restraining methods led to crack free samples. However, preheating to 250 °C and three layers of laser re-melting resulted in a decrease in the number of cracks. All the crack restraining methods reduced the secondary cracking but the main cracks were still present.

Table 7-1: Influence of crack restraining methods on cracks.

Samples deposited at 200W, 3.2mm/s, 12.2 g/min	**Nr. of main cracks**
As deposited	4
FeCr (AISI 420) buffer	5
Monel 400 (Ni alloy) buffer	4
1 layer laser re-melting	4
3 layer laser re-melting	3
Preheating the substrate to 250 °C	3

7.7.2 Effects of crack restraining methods on hardness

Hardness measurement were carried out at random selected points. *Figure 7-13* shows that laser re-melting led to a drop in the average hardness, the hardness of the top re-melted layers could not be established as upon indentation the surface shattered and led to numerous cracks. Hardness also decreased with the use of the FeCr buffer layer. Preheating and the use of a Ni-alloy buffer layer led to an increase in hardness.

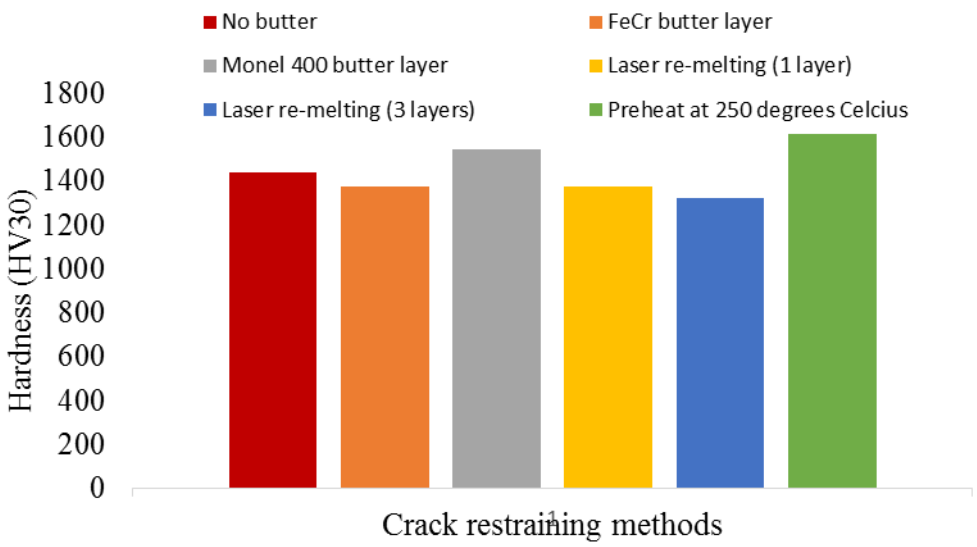

Figure 7-13: Influence of crack restraining methods on hardness.

7.7.3 Effects of crack restraining methods on phase formation

Figure 7-14, shows the XRD spectrums of the phases present in the crack restraining samples and these were compared with the sample without any crack restraining method. The use of a Ni-alloy buffer layer led to NiCu peaks with no secondary chromium carbide formation. The FeCr buffer layer and preheated sample led to the formation of Cr_7C_3 peaks. The peaks for the 3 layers laser re-melting was similar to the sample without the application of crack restraining techniques. The 1 layer laser re-melting peaks were not included as it was the same as the 3 layers laser re-melting.buffer

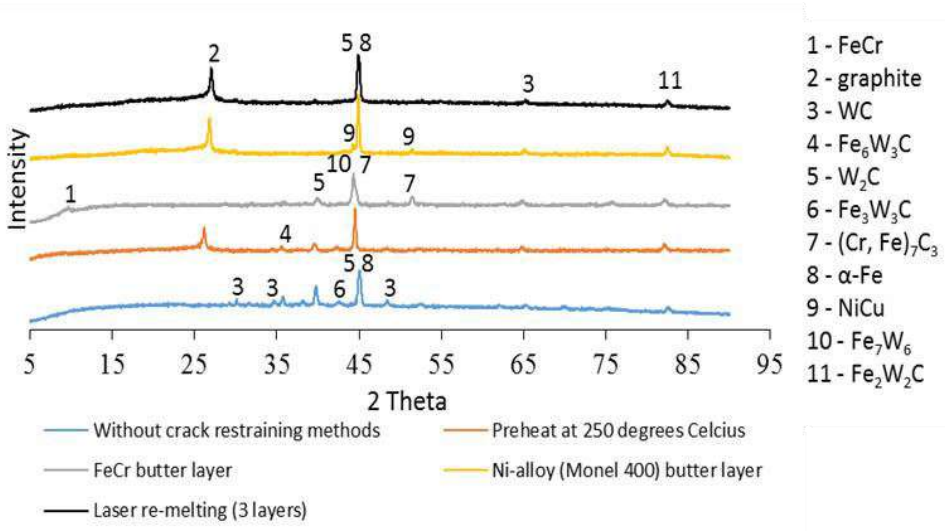

Figure 7-14: XRD spectra of the different crack restraining methods.

CHAPTER 8 Rotary Burr Prototype Results and Analysis

8.1 Introduction

In this chapter the optimum cube sample parameters established in Chapter 5 were used to fabricate a WC-FeCr hardmetal prototype rotary burr using the LENS® technology. A 3D CAD model of the burr was made and two burrs were fabricated, with and without substrate preheating. The rotary burr was manufactured in a three-step process (*Figure 8-1*) without the use of fixtures, compared to the nine-step conventional process (*Figure 8-2*). The LENS® process has been reported to reduce the manufacturing steps in the production of hardmetals in comparison to conventional sintering processes [156]. The shorter manufacturing times associated with the LENS® process has been also been report in similar studies [156] [157]. A finite element analysis (FEA) method under static conditions was used to understand the possible stresses acting on the burr and geometrical stress raisers during simulated operation. The initial performance of the prototype burr was carried out by conducting field testing and comparing it to conventionally manufactured hardmetal burrs.



Figure 8-1: LENS® process flow for the manufacture of the prototype burr.

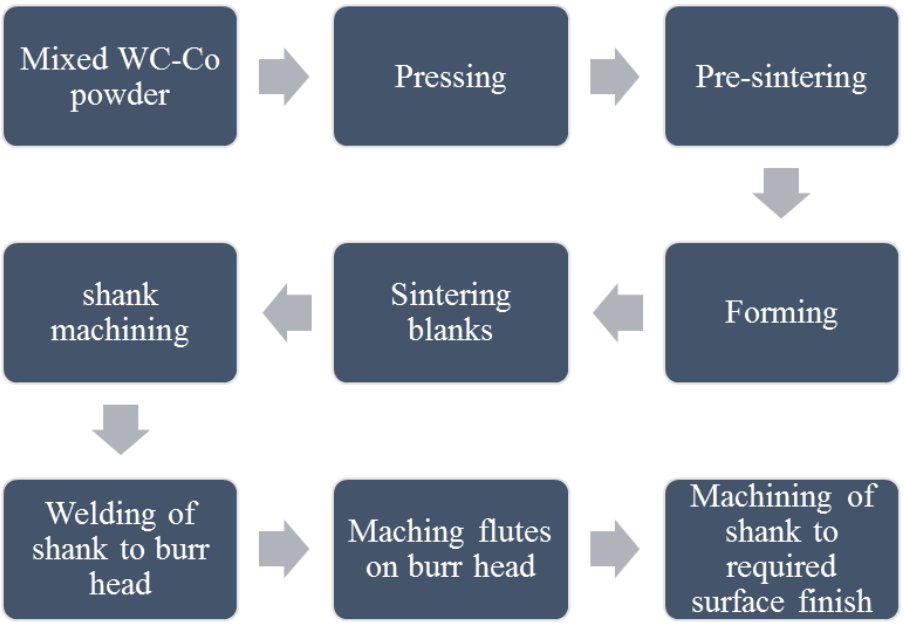

Figure 8-2: Process flow in the conventional manufacturing of hardmetal burrs [158].

8.1 CAD Model of the Rotary Burr

Figure 8-3 to *Figure 8-5* shows the CAD model of the cylindrical rotary burr at different views.

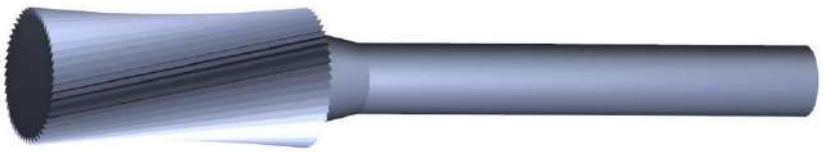

Figure 8-3: Side view of the cylindrical rotary burr.



Figure 8-4: Offset front view of the burr on the shank.

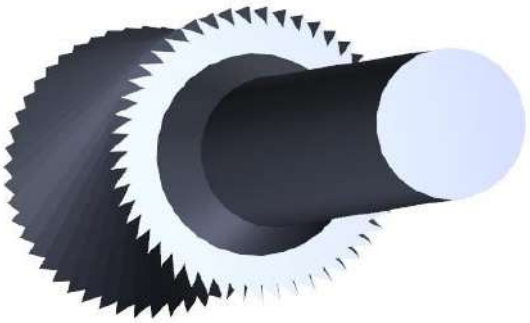

Figure 8-5: Shank view of the cylindrical rotary burr.

8.2 LENS® Deposition of a Cylindrical Rotary Burr

Figure 8-6 shows the LENS® fabrication of cylindrical rotary burr and *Figure 8-7* and *Figure 8-8* shows the cylindrical burrs with and without preheat. The fabrication time per burr was 04 h 04 min 30 sec and the cylindrical rotary burr consisted of 351 layers. The flutes on the burr where not discernable in comparison to the conventionally manufactured rotary burrs and this was due to the rougher surface finish imparted by the LENS® process. The powder utilization of this process was calculated by weighing the initial amount of powder used for the deposition process and the amount of powder which was not deposited into the molten pool. The powder utilization of the process was calculated to be 50.2%, however it still needs to be explored whether the powder can be re-used.



Figure 8-6: LENS fabricated cylindrical rotary burr.

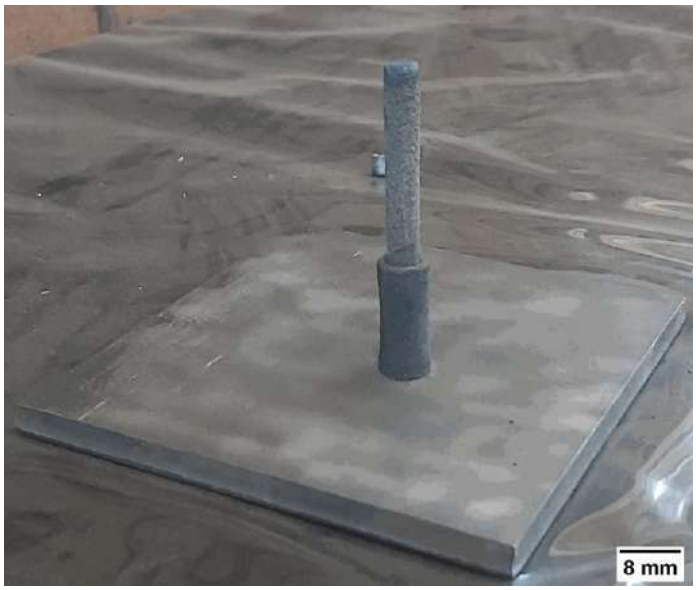

Figure 8-7: LENS® fabricated cylindrical rotary burr without preheat.



Figure 8-8: LENS® fabrication of a cylindrical rotary burr with preheat of 250°C.

The cylindrical rotary burr which was deposited on a preheated substrate fractured during removal from the substrate. To verify if indeed the LENS® process is a near-net shape process the dimensions of the burr without preheat were measured and compared with the CAD model dimensions and a sintered WC-Co cylindrical burr. *Table 8-1* shows the dimensions of the burrs. The shank and burr diameter together with the burr length deviated from the CAD model by 1.61, 0.26 and 1.51 mm respectively, this shows that post machining processes are required following LENS® fabrication.

Table 8-1: Dimensions of the LENS® fabricated and sintered WC burrs.

Dimensions	Shank diameter (mm)	Burr diameter (mm)	Burr length (mm)
CAD model dimensions	6	12	25+5(to accommodate removal from substrate)
LENS® deposited WC 10 wt.% FeCr burr	7.26	11.74	26.51
Sintered WC-Co burr	6.04	11.99	25.04

8.3 Finite Element Analysis (FEA)

In order to simulate the stress raisers on the geometrical surface of the rotary burr at static conditions the torque and maximum shear stress acting on the burr during field testing was calculated using Eq. 3-9 to Eq. 3-13. The shear stress acting on a concentrated area was calculated to be 6.84 MPa. The finite element model of the cylindrical rotary burr is shown in *Figure 8-9*. The properties of the WC-FeCr hardmetal used in the FEA analysis can be found in Section 3.5.4. *Figure 8-10* shows the load and boundary conditions of the cylindrical rotary burr.

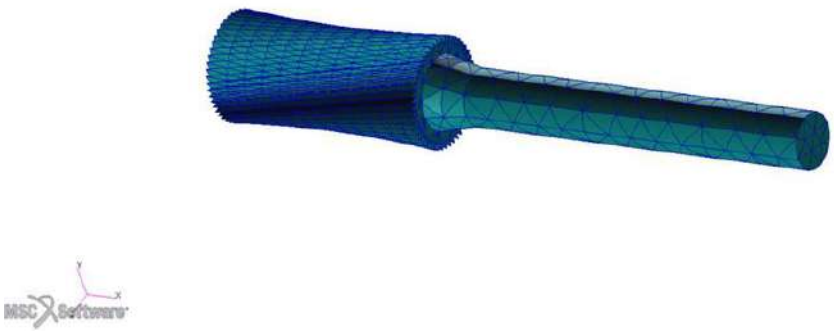

Figure 8-9: Finite element model of the cylindrical rotary burr.

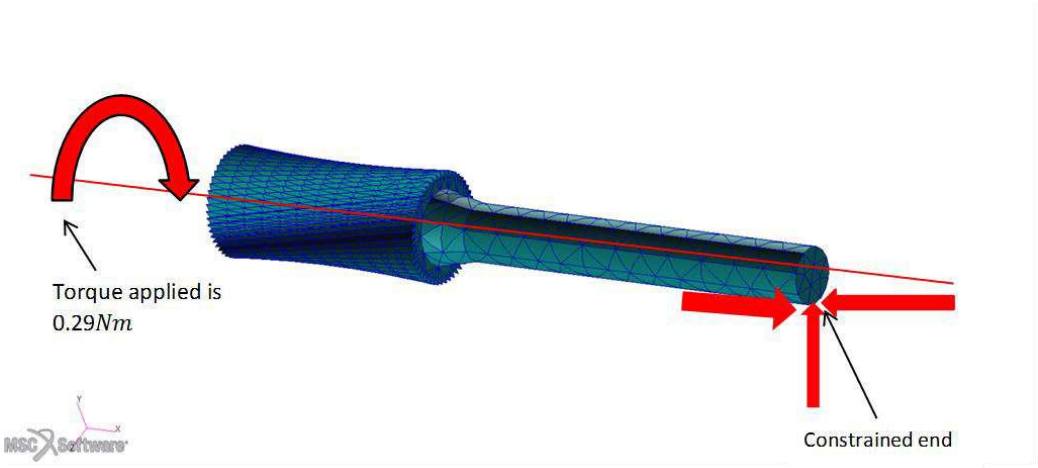

Figure 8-10: Applied operational loads and boundary conditions.

Figure 8-11 shows the stress distribution throughout the burr and the stress concentration was found to be at the fillet junction area (transition between the burr and shank). This means that if failure should occur, the highly stressed part would be the first to fail.

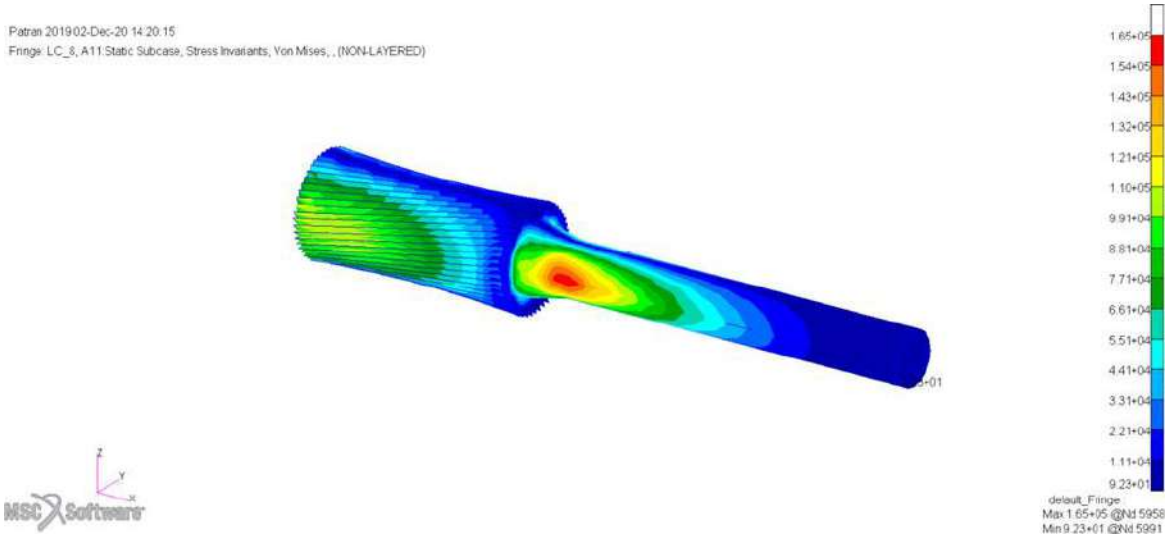

Figure 8-11: Von Mises stress due to imposed load.

8.4 Field Testing of the Prototype Burr

A field test of the as-built WC-FeCr hardmetal prototype cylindrical rotary burr fabricated by the LENS® process was conducted by measuring the performance based on the removal of weld metal made from AWS A5.1 E7018-1 electrode. In industry,

during refurbishment/repair of various components through welding, it is a requirement to remove pre-existing welds using burrs. The performance was compared with conventionally manufactured hardmetal burrs. *Figure 8-12* shows the built-up weld requiring machining.

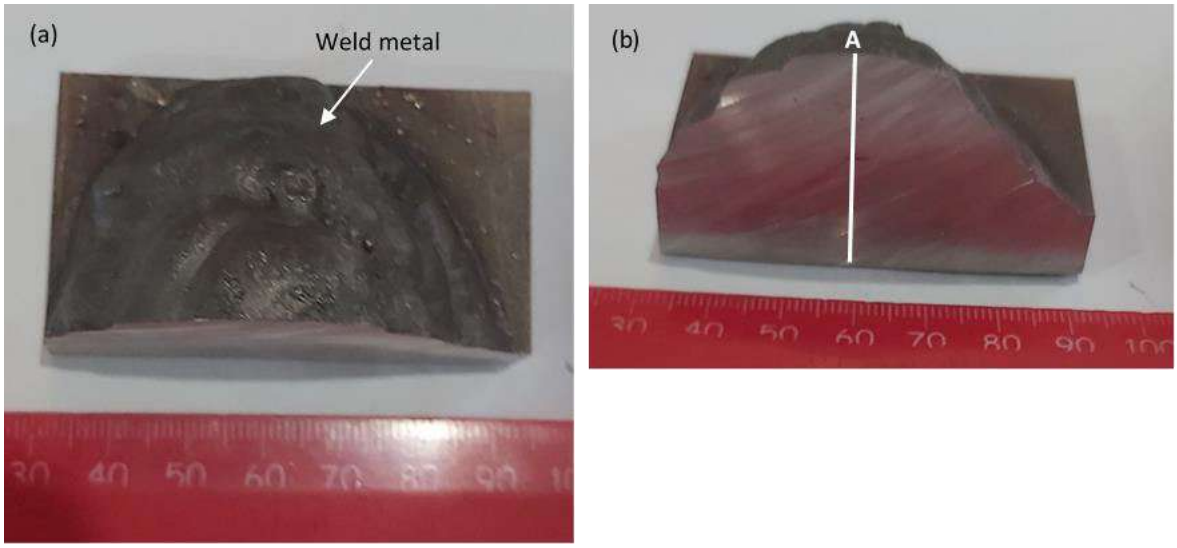

Figure 8-12: (a) Pre-existing weld area for machining, (b) measurement of the amount of material removed by the burr on surface A.

Figure 8-13 shows the performance of the prototype burr in comparison to the sintered burr, in machining pre-existing welds. The LENS® fabricated WC-FeCr hardmetal burr failed after machining off 0.22 mm of weld in 2 minutes. The sintered burr did not fail and testing was stopped after 5 minutes. *Figure 8-14* shows the machined weld.

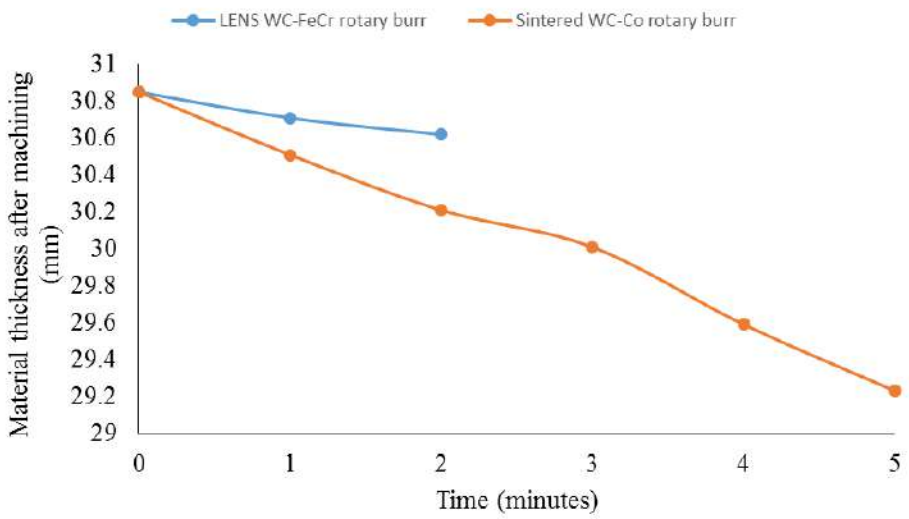

Figure 8-13: Machining performance of LENS® fabricated and sintered cylindrical rotary burrs.

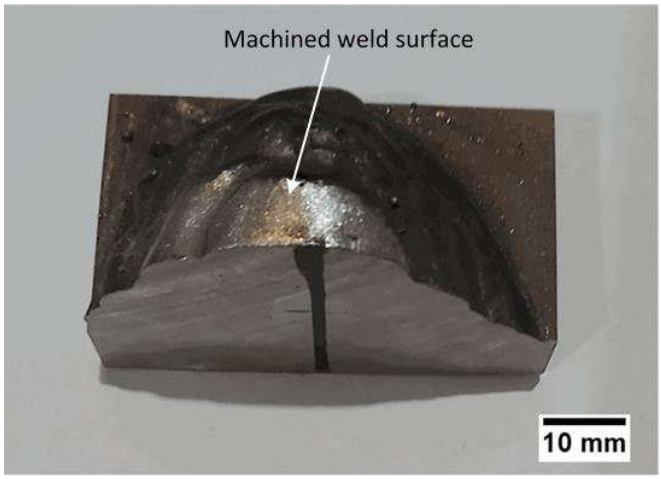

Figure 8-14: Machined weld surface.

The failure of the LENS® fabricated WC-FeCr hardmetal burr was a three point brittle fracture and the fracture occurred at the change in thickness between the burr and the shank as simulated by the FEA analysis. During machining the LENS® fabricated rotary burr experienced vibration in comparison to the sintered burr and this was due to the rougher surface finish imparted by the LENS® process. *Figure 8-15* shows the fractured LENS® fabricated cylindrical rotary burr, *Figure 8-16* and *Figure 8-17* shows the fracture surface.



Figure 8-15: Fracture of LENS® cylindrical rotary burr.



Figure 8-16: Fracture surface of LENS® fabricated rotary burr.

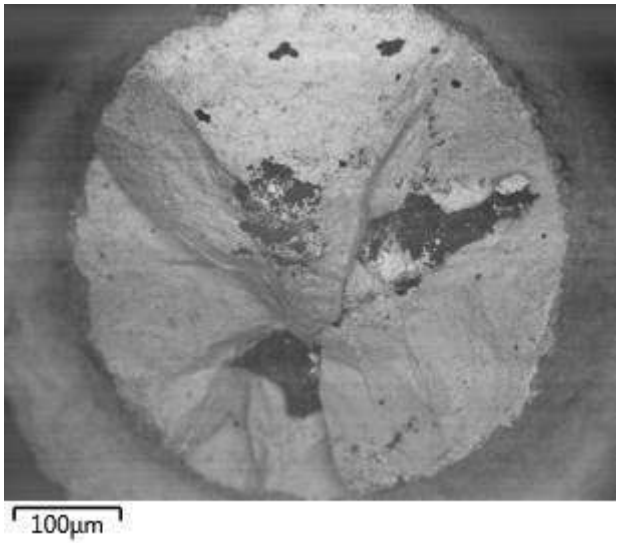

Figure 8-17: Fracture surface of the rotary burr

CHAPTER 9 Discussion

9.1 Introduction

This chapter presents a detailed discussion of all materials and processes studied as based on the results in Chapters 4 to 8. It begins with a discussion on the characteristics of the feedstock powders and how this influenced the deposition process and alloy process. It is followed by a study of the feasibility of the LENS® process to deposit thin wall samples and attaining optimal process parameters which were used to deposit a cube sample. The influence of process parameters on sample profile and porosity, regression analysis and the different types of optimization

techniques is discussed. The influence of process parameters on the microstructure and mechanical properties will also be discussed together with the correlation between the microstructure, hardness and sample thermal profile. Comparisons are drawn between the LENS® process and conventional sintering processes based on optimum cube sample densification and hardness. The effect of the different crack restraining methods on the ability to produce crack free samples will be looked into and the chapter will end with a discussion into the feasibility of fabricating a prototype component and field test performance results.

9.2 Influence of Feedstock Powders on Deposition Process and Composite Properties

The nominal powder particle size of the feedstock powders (*Table 4-1*) was similar to the particle size stated by the suppliers (Section 3.2), and complied with the LENS® machine powder size requirements which specify a range from 38 – 150 µm [41]. The slight difference between the measured and stated PSD as per suppliers material certificate was due to the different measurement methods namely laser diffraction and sieve analysis. The PSD of the blended WC-10wt% FeCr showed no agglomeration or fragmentation, and complied with the LENS® machine particle size requirements. The blended powder resembled the WC powder in terms of particle size because the mixture was predominately WC.

The WC powder had a spherical morphology (*Figure 4-2*) and the FeCr powder had a spheroidal and spherical morphology with the presence of smaller satellites attached to the main particles (*Figure 4-3*). The presence of satellites is attributed to the gas atomization during powder production whereby the heat capacity of the gas is lower than that of water causing an increase in the solidification time [159]. During the LENS® process or any AM process, powder morphology is important as it determines the ease at which powder can be deposited at the point of use. Irregular particle sizes not only have an impact on the flowability characteristics during AM deposition but it can cause damage and blockage to the powder delivery system [41] [46] [47]. Elemental contamination in the form of iron, calcium, potassium and other elements was evident on the WC feedstock powder (*Figure 4-5*). These elements were not

reported on the supplier's material certificate and thus the cause could not be established because powder contamination results from numerous aspects such as powder casting, packaging and even sample preparation. No contamination was observed on the FeCr powder and the chemical analysis results (*Figure 4-6*) were similar to the supplier's material certificate. A close to homogenous mixture of the blended WC-10wt% FeCr was attained (*Figure 4-4*) and chemical composition similar to the stoichiometric calculations (*Table 4-2*). The backscattered electron image showed a brighter WC in comparison to the FeCr powder. Backscattered electron image signals are dependent on the mean atomic number which allows phases with different atomic numbers to be recognised, as a result heavier elements backscatter more efficiently and appear brighter than lighter elements [148].

X-ray diffraction was done on the powders to identify the phases present. The phases present in the WC powder were WC, W_2C and elemental W where W_2C is a decarburisation phase of WC (*Figure 4-8*), these phases have been reported in other studies where the feedstock powder was characterized [70] [160] [161]. An α-Fe phase was detected from the FeCr powder (*Figure 4-10*) and the WC-10wt% FeCr powder, had the presence of cementite (Fe_3C), WC, W_2C and α-Fe. The Fe_3C phase is expected in a Fe-Cr-C system [132], however the peak was higher in the WC-10wt% FeCr than in the FeCr powder which was due to the high affinity Fe has for carbon. Chromium was not detected due to the low amount, however it was detected during EDS analysis (*Figure 4-7*).

The % porosity of the WC and FeCr was 0.55 ± 0.26 and 0.55 ± 0.16% respectively (*Figure 4-11*and *Figure 4-12*). Porosity measurements of the feedstock powders is important as it is a contributing factor to the porosity of AM fabricated parts. The disadvantage of inherent porosity not only affects the porosity of the bulk component but it also leads to cracking as it acts as a stress raiser.

9.3 Influence of Deposition Parameters on WC-FeCr Hardmetal Sample Height and Porosity

The optimum deposition parameters to produce a cubed WC-FeCr hardmetal sample were determined by using a full factorial Design of Experiments approach which started with the production of thin wall specimens with sample height and porosity being used for benchmarking because sample height shows that deposition has occurred and that substrate fusion took place through powder catchment by the molten pool. Porosity is also an important aspect which has a direct influence on the mechanical properties and the densification of the component. It determines whether the component will be able to operate in its intended function as pores are stress raisers and initiation points for failure.

Thin wall samples were successfully deposited with process parameters ranging as follows; laser power of 200 – 400 W, traverse speed of 3.2 – 12.7 mm/s and a powder feed rate of 7.3 – 12.2 g/min. The stand-off/working distance was set at 8 mm which was the focal length of the laser and the z-increment was varied between the layer thickness and 0.2 mm, 40 layers were deposited, hence it was expected for the samples to have a height of 8 mm in accordance to Eq. 3-6 in order to maintain a constant working distance. To establish an optimal set of process parameters the effects of laser power, traverse speed, powder feed rate and the z-increment on the sample height and porosity were analysed and it was established that an increase in the laser power and powder feed rate led to an increase in sample height, while an increase in the traverse speed led to a decrease in the sample height (*Figure 5-3* to *Figure 5-8*). A z-increment equal to the layer thickness also led to an increase in the sample height (*Figure 5-24*). It is clear that sample height is dependent on the heat input (Eq. 3-7) because the heat input is a function of both laser power and traverse speed. An increase in the laser power leads to an increase in the heat input and hence more heat is available for melting the powder leading to an increase in the molten pool and hence sample height upon cooling. An increase in the traverse speed leads to a decrease in the heat input, hence less heat is available for melting the powder leading to a reduction in the molten pool size and lack of height attainment. At high traverse speeds there is less time for powder-laser interaction, and this leads to fast cooling rates [162] [163] [164], and less time for the formation of the molten pool. An increase in the powder feed rate increases the powder interaction with the laser leading to more powder catchment into the molten pool and hence an increase in sample height, this has also been reported in similar studies [70]. The fact that a z-increment equal to the layer thickness resulted in

an increase in sample height shows that there was enough heat to melt the powder, and more powder was introduced into the molten pool. The z-increment is critical in preventing a defocused laser and if an incorrect z-increment is set not all the powder will be captured in the molten pool. A correct z-increment ensures that the laser head does not trail away from the sample leading to an increase in the work distance [58], in contrast it also ensures that the sample being deposited does not crash into the laser head, thus leading to a decrease in the work distance.

The porosity formation in the thin wall samples was, however contrary to the sample height. It was established that the porosity with a circularity range of 0 – 0.5 decreased with an increase in the laser power and the porosity with a circularity range of 0.51 – 1 increased with an increase in laser power (*Figure 5-13* and *Figure 5-14*). At low laser power lack of fusion porosity forms due to insufficient heat to melt the powders and an increase in the laser power would reduce the porosity [68], hence the pores with a circularity range of 0 – 0.5 were classified as lack of fusion porosity. An increase in the laser power leads to the formation of gas pores [66] [68], hence the porosity with a circularity range of 0.51 - 1 was classified as gas porosity. At high laser powers the molten pool behaves erratically with spatters and the high heat input results in a decrease in the surface tension in the center of the pool. This thus leads to a Marangoni effect where the center of the molten pool has a low surface tension compared to the surrounding molten material; this then leads to a divergent fluid flow and easy entrapment of gases leading to gas porosity [66]. In an effort to understand whether these gas pores were due to gas entrapment from the molten pool dynamics or from keyhole porosity which is formed at high power densities leading to deeper penetration, the aspect ratio of the porosity at different circularity ranges was calculated and the porosity which increased with an increase in laser power had the lowest aspect ratio (*Figure 5-15* and *Figure 5-16*). Keyhole porosity has a high aspect ratio [165], hence these pores were due to gas entrapment. The porosity with a low circularity had the highest aspect ratio and this was attributed to the presence of cracks.

An increase in the powder feed rate led to an increase in porosity (*Figure 5-20* to *Figure 5-22*), due to insufficient energy available to melt all the powder, and leading to lack of fusion porosity. In addition high powder feed rates tend to shield the molten pool from

the laser beam retarding heat input into the deposition zone thus leading to increased lack of fusion porosity as more particles are not melted. Studies have shown that an increase in the powder feed rate leads to lack of fusion porosity [66] [67].

An increase in the traverse speed led to a decrease in the measured porosity with a circularity of 0-0.79. This is because an increase in the traverse speed leads to less powder being deposited into the molten pool. Since an increase in the powder feed rate results in an increase in porosity due to lack of fusion, it is therefore expected that less powder will lead to a decrease in porosity. It thus becomes clear that a reduced powder feed rate has more effect on the lack of fusion porosity than the overall heat input [66] [68]. However, the porosity was seen to increase again at a traverse speed of 8.5 mm/s, and this was due to insufficient heat input resulting in less melt pool stability and lack of fusion porosity. This effect of traverse speed on porosity has been reported and it has been shown that there is a process window at which the porosity in a sample decreases [68] [166] which can be best described by *Figure 2-21*. The porosity with a circularity of 0.81-1 was seen to decrease with an increase in the traverse speed as expected because gas porosity forms with an increase in heat input. .An increase in the traverse speed leads to a decrease in the heat input and hence result in a reduction in the porosity.

A z-increment equal to the layer thickness led to an increase in the porosity with a circularity of 0 – 0.5 when compared to a z-increment of 0.2 mm (*Figure 5-25* to *Figure 5-27*). OM observation (*Figure 5-28* to *Figure 5-30*), showed keyhole porosity, which is formed at high power densities, leading to deeper penetration and formation of a molten pool hole. The molten pool hole acts as a blackbody and absorbs the heat from the laser beam, thus reducing the heat available for melting more powder. This results in the formation of keyhole porosity [167].

The mean % porosity analysis (*Figure 5-23*) showed that porosity increased with an increase in laser power, powder feed rate and a decrease in the traverse speed. It was observed that an increase in sample height led to an increase in the porosity of the samples which follows the trend in published literature [166] [168].

The analysis results show that laser power, traverse speed, powder feed rate and z-increment all have an impact on whether a defocused laser beam will be formed. The working distance (distance between the laser deposition head and substrate) has to be adjusted to maintain a focused beam by taking all parameters into consideration. A deviation in the set working distance leads to the formation of a defocused laser beam, which arises when the working distance is above or below the focal plane of the laser. A defocused laser beam leads to reduced laser intensity [58]. An increase in the traverse speed led to an increase in the working distance because the height attained was not enough to maintain the set working distance, this in turn led to a defocused laser beam with lower heat intensity and less alignment of the powder with the laser beam, this then led to no deposition. The observed influence of the laser power traverse speed and powder feed rate on sample height agree with studies done using the AM process [58] [70] [169] [170] [171]. A z-increment equal to the layer thickness ensured a constant working distance and hence the highest laser intensity. This however led to keyhole porosity and the formation of a defocused laser by using a z-increment of 0.2 mm was more appropriate in reducing the porosity.

Process parameter optimization was carried out in a two-step process, firstly height optimization was done by means of an ANOVA regression analysis and generalized reduced gradients (GRG) non-linear optimization, in order to attain a sample height close to 8 mm. Numerous regression analysis techniques were used to attain a model that offered the best fit for experimental data because evaluation based on the coefficient of determination (R^2) was seen to be inadequate since high order terms tend to artificially inflate it [172]. Three regression models namely linear, quadratic and exponential were evaluated and the quadratic model showed the highest R^2 value. According to this analysis the quadratic regression model offered the best fitment for the experimental data, however through statistical hypothesis analysis and residual analysis it was shown that the exponential regression model showed the best fitment and that the quadratic model artificially inflated R^2. The exponential model displayed a more normal residual distribution in comparison to the quadratic model (*Figure 5-9* and *Figure 5-10*) and the residual plots also graphically showed that the exponential regression model had errors which were randomly distributed across the horizontal axis (*Figure 5-11*), which proved that the model was adequate [172]. The relationship between laser power, traverse speed and powder feed rate with sample was

mathematically represented by an exponential regression model (Eq. 5-1). Through optimization it was shown that the optimum parameter set that would yield a sample height of 8 mm was 200 W 3.2 mm/s and 12.2 g/min, however these parameters were not included in the DoE. For verification purposes the DoE was extended to include these parameters and it was experimentally proven that these parameter led to the deposition of a sample with a height of 7.92mm, the closest to the required height. It was concluded that these would be the optimum parameters that would yield the required height.

In as much as it is important to attain the required sample height during LENS® manufacturing, sample porosity is also important, hence it becomes imperative to optimize both height and porosity. The second optimization process included maximizing the height while minimizing the porosity. The optimization of sample height was an important step in refining the data for further optimization based on porosity, as only samples that attained 50% of the required height were further analysed for porosity. Porosity could not be modelled using a regression analysis because of the scattering of data, hence a multi-objective optimization (MOO) technique was used to model both porosity and height. A set of Pareto non-dominated optimum solutions were established (*Table 5-7*) and the single objective and multi-objective optimization processes yielded the same optimum parameters (200 W, 3.2 mm/s, 12.2 g/min).

Cube samples were deposited using the optimum Pareto solutions and the parameter set that displayed the lowest porosity was 200 W, 3.2 mm/s, 12.2 g/min. It was then clear from all the optimization and techniques that this was the optimum parameter set for the LENS® deposition of WC-FeCr hardmetals. The density of the optimum cube samples was found to be higher than sintered WC-FeCr hardmetals [124] but lower than the conventionally manufactured WC-Co hardmetals [83]. This shows that with process refinement the LENS® process may be applicable to the production of WC-Fe hardmetals. Currently there are no standards for the acceptable level of porosity in additive manufactured parts.

9.4 Microstructure of LENS® Manufactured WC-FeCr Hardmetals

Metallographic examination of both the thin wall samples and the optimum cube sample revealed that the initial dissolution of WC spherical grains led to the formation of equiaxed and columnar grains which formed a reaction zone in a form of a halo effect around the spherical WC edges (*Figure 6-2* and *Figure 6-24*), this dissolution structure has been reported in AM deposited WC-Ni and WC reinforced iron hardmetal systems [73] [74] [160] [173] [174]. The reaction zone phase had a bright color because it was rich in tungsten, a higher hardness than the WC spherical grain (*Table 6-6*) and was identified as W_2C through chemical and phase analysis, this is a carbide of the W-C system and forms as a result of decarburization of WC. This W_2C phase was also observed in the phase analysis of the WC feedstock powder (*Figure 4-8*), hence it can be seen that with the application of heat the spherical WC/W_2C dissociated and W_2C was the phase to form the reaction zone. Since W_2C has a high tungsten content it is expected that it will have a higher hardness than WC [175]. The reaction zone was seen to increase with laser power and hence heat input, at high heat inputs there is enough energy for the WC to interact with the molten FeCr binder and thus giving rise to reaction phases.

A microstructural and solidification profile along the build from the substrate to the last deposition layer of the single walls and optimum cube sample showed an inhomogeneity in the microstructure. A herringbone structure which is also called a dendritic structure was observed at the bottom of the samples in the matrix and was due to coalescence of the W_2C columnar grains in the matrix (*Figure 6-1*, *Figure 6-2*, *Figure 6-25* and *Figure 6-26*). The herringbone phase was seen to have a lower concentration of W in comparison to the halo W_2C., this was due to its higher iron (Fe) content (*Figure 6-2* and *Table 6-3*). The formation of the herringbone structure has been reported in the additive manufacturing and cladding of WC-Ni, and metal matrix composite hardmetals [73] [74] [126] [175] [176]. Herringbone/dendritic structures are solidification products that form from the heterogeneous solidification of an alloy. Solidification in the LENS® deposition is a heterogeneous process because it starts on existing surfaces, i.e. the substrate requires a lower surface energy to form a stable nucleus, because the surface area of the nucleus that is in contact with the surrounding molten metal is less.. During heterogeneous solidification, two main structures form, namely equiaxed grains which grow equally in all directions and columnar grains which are long thin grains which are formed when the metal solidifies in the presence

of a steep temperature gradient [61]. During heterogeneous solidification a temperature gradient (G) exists between the interface and deposits leading to an unstable solidification which leads to the development of dendritic solidification structures. The temperature gradient (G) is maximum at the substrate-deposit interface and minimum at the center of the deposit and this is because during solidification the substrate acts as a heat sink, hence the temperature of the molten pool is the lowest at the fusion line and rises towards the center. Solidification starts at the interface and proceeds upwards towards the top of the sample build direction. The accumulation of elements/solutes ahead of the solidification front leads to the super-cooling of the liquid in front of the solidification front, this leads to the formation of the dendritic/herringbone structure. The stability of the substrate-molten pool interface is described by Eq. 9-1 [61].

$$\frac{G_l}{R} = \frac{m_L C_o}{D_L k}(1-k) \qquad \text{Eq. 9-1}$$

Where: G_l is the liquid temperature gradient, R is the solidification rate, m_L is the slope of the liquidus line, C_o is the nominal composition of the alloy,D_L is the diffusion rate within the liquid and k is the equilibrium portioning coefficient.

As long as $\frac{G_l}{R}$ at the interface is equal or greater than the right-hand side of Eq. 9-1 a planar solidification front will take place, however if the ratio is less than the right-hand side the liquid ahead of the interface will be super-cooled and a dendritic/herringbone structure will form. It becomes clear that a herringbone structure will form at high solidification rates which are mostly experienced at the substrate-molten pool interface due to the heat sink of the substrate. The different types of solidification structures formed as function of G_L and R are shown in *Figure 9-1*, and as observed in the WC-FeCr hardmetal microstructure a columnar herringbone microstructure was formed.

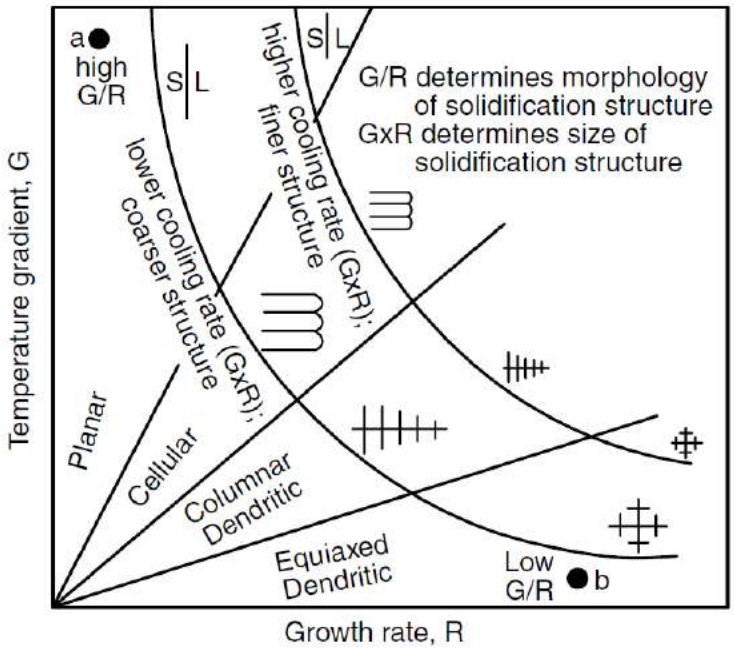

Figure 9-1: Solidification structures as a function of temperature gradient and solidification/growth rate [177].

Carbon-deficient η-phases having trapezoidal and strip morphology were also observed and were seen to originate from the edges of the WC grains as well (*Figure 6-1* and *Figure 6-27* to *Figure 6-29*). The η-phases were observed throughout the center matrix of the hardmetal but were more predominant at the top of the samples. The fabrication of WC-FeCr hardmetals led to the precipitation of dissolution phases upon cooling, phase analysis showed these phases to be Fe_3W_3C, Fe_6W_6C and Fe_7W_6, according to Alvarez *et al.* [178], the formation of M_6C is produced by a carbon deficiency in the WC-Fe system. It was also observed that the intensity of Fe_3W_3C at position 42.1° increased with laser power, concurrently heat input. M_6C are eta (η) carbides that are hard, brittle and undesirable however it has been reported that the presence of these phases may lead to improved wear properties provided that the carbon content of the hardmetal is not below the stoichiometric values and provided that small phases with a large distribution are formed [179]. According to Upadhyaya [20], M_6C carbides form from the eutectic reaction:

$$liquid \rightarrow M_6C + WC \qquad \text{Eq 9-2}$$

This shows that M_6C carbides form at cooling of mixtures; hence carbon has to be added slightly above its stoichiometric value in order to avoid the η-phase; however at high carbon additions graphite will form. $M_{12}C$ carbides are low temperature modifications of M_6C carbides [20]. The reason why the XRD peak of the M_6C carbides namely Fe_3W_3C increased with laser power is because, at high heat inputs slow cooling occurs thus allowing for carbon to diffuse out of the WC structure (decarburization) due to elements that have a high affinity for C, such as Fe and Cr, this causes a carbon deficiency which leads to the formation of the η-phase. The formation of the η-phase has been reported in the sintering of hardmetals where the formation is more prevalent in WC-Fe hardmetals due to the narrow carbon window [20] [116]. Laser deposition is known as a rapid manufacturing process with higher cooling rates hence the formation of the η-phase may not be expected as the powder does not spend a long time at high temperatures, however this research and studies done on the laser deposition of hardmetals [73] [74] [175] have shown that the formation of the η-phase occurs in laser based processes.

The matrix to which the precipitation of reaction phases occurred had a darker color than the WC grains and comprised of an austenitic-martensitic microstructure, this microstructure was verified by the microstructure obtained for the LENS® deposition of FeCr using the optimum parameters obtained in section 5.5. Retained austenite and lathe martenite were the phases observed (*Figure 6-20* and *Figure 6-21*) and the phases identified were α-Fe and Cr_7C_3 which are the phases expected in a Fe-Cr-C system [132], the carbide phases are classified as $M_{23}C_6$, however chromium carbides were not detected in the WC-FeCr hardmetals due to the low concentration of Cr. The phases identified correlates with those reported in WC-FeCr hardmetals fabricated using the sintering process [116].

The top layers (final deposited layers) were composed of a bright surface zone which was seen to increase with laser power and a decrease in the traverse speed (*Figure 6-5* to *Figure 6-7* and *Figure 6-13*). A z-increment equal to the layer thickness was also seen to result in an increase in the bright surface zone layer (*Figure 6-16*). It is clear from the results that the bright surface zone was heat dependent, and an increase in heat input resulted in an increase in the dissolution of WC and evaporation of the binder phase (*Figure 6-3* and *Table 6-1*) as this region was rich in WC. The heat input imparted

by the IPG fiber laser beam follows the Gaussian source distribution where the highest heat intensity is at the center of the beam. The melting temperature of Fe is 1538 °C, and turns into a gas at 2862 °C, while the melting temperature of WC is 2870 °C. Since the WC particles partly melts in the top layers of the deposited sample, it is more likely that the evaporation temperature of Fe was reached. During deposition there is a heat built up as the sample height increases because each layer is deposited onto the previous layer which is still at temperatures above room temperature, this can either form a temper effect or re-melting of the previous layers. The top layers are thus experiencing a higher energy intensity leading to metal evaporation, this was shown in the thermal profile of the thin wall samples deposited at optimum parameters were established using the Rosenthal heat flow equations and it was graphically shown that there is a heat-build from the substrate to the top layers during deposition. It was also shown that the temperatures at the laser heat source were enough to cause melting and decomposition of WC. At high temperatures there is an increase in the dissolution of WC and the FeCr binder phase experiences a decrease in the martensitic start (Ms) temperature resulting in an increase in the austenitic phase field. (*Figure 6-46*). In addition, during deposition at high laser powers these layers tend to form spatter because of the erratic molten pool caused by a high heat input and thus gives rise to entrapment of gases and hence porosity.

The observation of the microstructure variation and thermal profile across the sample height correlated with the hardness profile as it was seen to decrease from the first deposited layer to the last layer (*Figure 6-41* and *Figure 6-42*), this has been reported in similar studies on the laser based additive manufacturing of hardmetals [8] [79]. The heat build-up during the deposition of subsequent layers was the reason for the decrease in hardness. Grain growth also occurs leading to a decrease in mechanical properties including hardness. The surface roughness of the deposited thin wall samples decreased with an increase in heat input because un-melted powder which was attached to the sample was now melted and formed more uniform sample profile. The hardness was dependent on the process parameters with an increase in laser power resulting in a reduction in hardness. The hardness of optimum cube LENS® fabricated WC-FeCr hardmetal samples was superior to LENS® deposited WC-10wt.% Co and sintered WC-10wt% Co (*Table 6-7*).

An increase in the heat input from 47 to 67 J/mm led to a decrease in the sample surface finish of the thin wall samples from 31.4 to 1.3 µm. At high heat inputs more powder is melted and no adherence of un-melted powder on the sample surface occurs. It was also reported in a study by Rosli *et al*. [180] that an increase in the heat input from 142 J/mm to 207 J/mm led to a smoother surface finish. A rough surface finish has become a limiting factor of additive manufactured parts in the as-built form [181] [182], and hence fine grinding will be a requirement following fabrication.

9.5 Influence of Crack Restraining Methods on Crack Prevention During Deposition

All WC-FeCr hardmetal thin wall samples and the optimum cube sample fabricated using the LENS® process displayed the presence of cracks. Thermal residual stresses and a mismatch in the coefficient of thermal expansion (CTE) between WC, the matrix phase and substrate are the main cause of cracking in the laser deposition of hardmetals and metal matrix composites (MMC) [78] [80]. In this research study four crack restraining methods were used, namely substrate preheating, laser re-melting, FeCr buffer layer and Ni-alloy buffer layer in an attempt to see which method would reduce the thermal residual stresses.

All crack restraining methods led to a reduction in the secondary cracks which originated from the main cracks (*Figure 7-5*, *Figure 7-8*, *Figure 7-11* and *Figure 7-12*). Substrate preheat and three layer laser re-melting were the only methods that led to the reduction of the main cracks (*Table 7-1*). Substrate preheating reduces the thermal gradient between the substrate-molten pool interface thereby reducing the cooling rate and hence the thermal residual stresses. Mild steel has a high thermal conductivity hence high heat inputs would be required to form a metallurgical bond between the substrate and deposit, hence preheating the substrate will assist in the heat build-up. The application of substrate preheating has been seen to reduce cracks [183] [184] [185] [186]. In as much as preheating led to the reduction in the main cracks it also led to an increase in sample hardness and the formation of chromium carbides (*Figure 7-13* and *Figure 7-14*). Substrate preheating leads to an increase in the heat of the molten pool through heat build-up and increases the tendency of forming dissolution products.

Substrate preheating increases hardness due to the formation and uniform distribution of carbides [187]

Laser re-melting resulted in an improved surface appearance which visually appeared smoother with reduced edges on the contours and with less visibility of the scanning pattern than the samples without laser re-melting. During laser re-melting the top layers of the sample are heated and melted without the addition of powder, this then leads to the melting of the initial un-melted powder particles on the surface and re-melted material flow from peaks to valleys under surface tension [78] [188] [189]. Not only is laser re-melting used to improve the surface quality of laser deposited samples but it can also be used as an in-situ post heat treatment process to retard crack growth and reduce cracks [190] [191]. Laser re-melting increases the overall temperature of the LENS® fabricated WC-10wt%FeCr sample with the top layers experiencing the highest temperature, this increase in temperature results in slower cooling rates thus decreasing the thermal residual stresses [192]. Laser re-melting and the application of the FeCr buffer layer resulted in a decrease in hardness of the WC-FeCr hardmetal samples. The 3 layer re-melting process was seen to have a stronger impact on hardness reduction more so than the 1 layer re-melting process. Laser re-melting results in increased WC dissolution leading to a reduction in hardness. This is in agreement to the results obtained by Dai et al. [78] and Leunda et al. [79].

The Ni-alloy buffer layer had no influence on the number of main cracks, however there was a reduction in the formation of secondary cracking. The Ni-alloy buffer layer with a CTE of 14.5 x 10-6 $°C^{-1}$ which exceeds that of the substrate and the WC-FeCr hardmetal was used. The reason of usage is because the Ni-alloy has a yield strength of 240 MPa [44] which is lower than that of FeCr which is 532 MPa [45], which means that the Ni-alloy will be able to absorb the plastic strain during deposition and will absorb the plastic strain in the WC-FeCr hardmetal. In addition the Ni-alloy has a lower thermal conductivity than mild steel hence a slower cooling rate will be imparted by the buffer layer and hence a reduction in the thermal residual stresses. The use of Ni-alloys as a buffer layer has been extensively used in order to reduce the thermal residual stresses by applying a bond coat material that has a coefficient of thermal expansion which is intermediate between the substrate and the material to be deposited [79] [193]. Leunda et al. [79], also discovered that the use of a

NiCr buffer layer was not sufficient in avoiding cracks in hardmetals. Hardness was seen to increase when the Ni-alloy buffer was used, Winarto et al. [193] and Nagentrau et al. [187] and Stanciu et al. [25] also indicated that hardness of Ni buffered coatings increased with the application of substrate preheat and this was attributed to the distribution of carbides within the coating.

The use of a FeCr buffer layer was used to attain compatibility with the binder phase in LENS® deposited WC-FeCr hardmetal samples and to ensure that the coefficient of thermal expansion was similar to that of the deposited material. A WC-FeCr hardmetal, FeCr alloy and mild steel material have CTE's of 7 x 10-6 °C-1 [40], 10.25 x 10-6 °C-1 and 11.7 x 10-6 °C-1 [41], respectively. A buffer layer having an intermediate CTE between the substrate and the deposited material reduces the thermal residual stresses and hence reduce susceptibility to crack formation [42]. Even though the FeCr buffer layer had an intermediate CTE it was observed that it had no influence of on the main cracks but led to a reduction in the secondary cracks. FeCr alloys namely AISI 420 are fracture sensitive and have microstructures composed of brittle martensite and retained austenite following laser deposition [43]. During deposition of subsequent layers (in-situ heat treatment) the martensite may transform to tempered martensite thus imparting ductility hence the ability to reduce secondary cracks.

9.6 Assessment of Prototype WC-FeCr Hardmetal Rotary Burr

The fabricated rotary burr had a rough surface finish in comparison to the conventional burr, and due to this the design flutes where not discernable, it thus becomes clear that post-processing fine grinding is required following deposition, as the surface finish of burrs needs to be 0.8 µm [158]. In addition the part accuracy was not compliant with the 3D CAD model input dimensions (*Table 8-1*), further showing that the prototype requires final machining in order to achieve accurate dimensions and acceptable surface finish for field work.

FEA analysis of the rotary burr was conducted to understand the stress concentration acting on the burr during static conditions, and it was established that the fillet junction which connects the shank and the burr head acted as a stress raiser and

experienced the highest stresses. Sharp corners and fillet radii will have high internal stresses because of the abrupt change in shape, in order to mitigate this a large fillet radius should be incorporated in the 3D CAD model so that the internal stresses gets ample space to be redistributed evenly. During the cylindrical rotary burr performance analysis, failure occurred at the fillet junction as predicted by the FEA analysis after 2 minutes of machining 0.22 mm of an AWS A5.1 E7018-1 weld. During machining vibrations from the LENS® fabricated burr were experienced and this was attributed to the surface roughness and the fracture was a brittle three-point fracture (*Figure 8-16*). The fracture was of a brittle mode as there was no evidence of plastic deformation. This clearly showed that only low fracture energy was required for the failure to occur. The point of origin of the fracture could not be determined, however the cause of fracture was attributed to the internal porosity (Section 5.5) and inherent cracks in the material (CHAPTER 7). The conventionally manufactured WC-Co burr outperformed the LENS® manufactured WC-FeCr prototype burr, however the prototype failed at the shank and not the burr, this requires further improvement into the burrs material properties. In addition the LENS® process had a low powder efficiency with the powder utilization of 50.2%, hence the process feasibility will also depend on the ability to recycle the powder, this was also reported by Xiong et al. [156].

CHAPTER 10 Conclusions and Recommendations

10.1 Introduction

The aim of this study was to investigate the feasibility of using the LENS® technology to manufacture hardmetals having a martensitic steel binder. The use of this technology in the manufacture of hardmetals is yet to be adopted on a commercial level and currently there is limited published research available. The research undertaken in the current study will add to the scientific knowledge base and according to the author's knowledge it is the first time that this technology has been applied to WC-FeCr hardmetals. The results of this research should assist in promoting the concept of additive manufacturing and the use and development of alternative Fe-based binders in the hardmetal industry.

The DOE statistical modelling and optimization techniques showed that WC-FeCr hardmetals can be manufactured using the LENS® technology. The optimized process parameters were a laser power of 200 W, traverse speed of 3.2 mm/s, powder feed rate of 12.2 g/min and z-increment of 0.2mm, however, some porosity was still present.
It was also established that as-deposited samples had a microstructural and mechanical variation across the sample build and this was evidence enough that in order to achieve a homogeneous structure following the LENS® deposition process, post heat treatment will be required for stabilization and to establish homogeneity in the structure. The average hardness of LENS® fabricated WC-FeCr hardmetal was seen to be higher than that of sintered WC-10wt% Co. In as much as cracks were still present even after the application of crack restraining methods namely; laser re-melting, buffering and preheating, crack reduction was evident. Secondary cracks (originating from the main cracks) were mitigated, however the main cracks could only be reduced.

A WC-FeCr hardmetal prototype cylindrical rotary burr was fabricated using the LENS® technology. The limitations of the fabricated burr included the rough surface finish which led to vibrations during testing and the early failure which was possibly due to inherent material defects. The conventionally manufactured WC-Co cylindrical rotary burr outperformed the LENS® prototype, however the LENS® component showed potential as the rotary burr failed at the shank and not the burr head

10.2 Recommendations for future research

A comprehensive residual stress study to understand the mechanisms behind crack initiation and propagation is proposed together with crack restraining methods that will ensure the fabrication of crack-free samples.

Investigations into post-processing techniques such as hot isostatic pressing and post heat treatment is required in order to form a homogeneous microstructure, to remove porosity and increase the density of the hardmetals.

A study into possible powder recycling during deposition in order to increase powder utilization.

REFERENCES

[1] T. Sudarshan and T. Srivatsan, Additive Manufacturing: Innovations, Advances, and Applications, New York: Taylor & Francis Group, 2016.

[2] Sciaky, [Online]. Available: http://www.sciaky.com/additivemanufacturing/. [Accessed 6 January 2017].

[3] P. Robert and R. Nicholas, "RPM Innovations, Inc," January 2007. [Online]. Available: http://www.rpmandassociates.com/RPMILaserDepositionTechnologyAdvancesAdditiveManufacturingAndRepair.aspx. [Accessed 13 Feburary 2017].

[4] D. M. Keicher, J. L. Jellison, J. A. Romero, D. H. Aboott and L. P. Schanwald, "Towards a Reliable Laser Spray Powder Deposition System Through Process Characterization," *Proceedings of the 27th International SAMPE Technical Conference,* vol. 27, pp. 1029-1039, 1995.

[5] S. N. Joshi and U. S. Dixit, "Laser Based Manufacturing," in *5th International and 26th all India Manufacturing Technology, Design and Research Conference*, India, 2014.

[6] PRNewswire, "Tungsten Market Looks to Rebalance in 2017," 20 January 2017. [Online]. Available: http://www.prnewswire.com/news-releases/tungsten-market-looks-to-rebalance-in-2017-611302275.html. [Accessed 9 February 2017].

[7] "National Science Foundation," [Online]. Available: https://www.nsf.gov/awardsearch/showAward?AWD_ID=0423695...false. [Accessed 13 February 2017].

[8] Y. Xiong, J. Smugeresky, L. Ajdelsztajn and J. Schoenung, "Fabrication of WC-Co Hardmetals by Laser Engineered Net Shaping," *Materials Science & Engineering: A,* vol. 493, no. 1-2, pp. 261-266, 2008.

[9] W. Lyons, G. Plisga and M. Lorenz, Standard Handbook of Petroleum and Natural Gas Engineering, London: Elsevier, 2015.

[10] S. Hanyaloglu, B. Aksakal and S. Sen, "An indentation and Stress Analysis of

WC/Fe-Mn Hardmetal," *Indian Journal of Engineering and Materials Sciences,* vol. 10, no. 3, pp. 229-235, 2003.

[11] N. T. Program, "Toxicology Studies of Cobalt Metal in F344/N Rats and B6C3F1/N Mice and Toxicology and Carcinogenesis Studies of Cobalt Metal in F344/NTac Rats an B6C3F1/N Mince: Inhalation Studies," U.S Department of Health and Human Services, United States of America, 2014.

[12] K. B. Shedd, E. A. McCullough and D. I. Bleiwas, "Global Trends Affecting the Supply Security of Cobalt," *Mining Engineering,* vol. 69, no. 12, pp. 37-42, 2017.

[13] I. J. Shon, I. K. Jeong, I. Y. Ko, J. M. Doh and K. D. Woo, "Sintering Behaviour and Mechanical Properties of WC-10Co, WC-10Ni and WC-10Fe Hard Materials Produced by High Frequency Induction Heated Sintering," *Ceramics International,* vol. 35, no. 1, pp. 339-344, 2009.

[14] J. Richter and R. Michalik, "Corrosion Resistance of WC-Co and WC-Ni Type Sintered Carbides in Acetic Acid Water Solution," *Materials and Corrosion,* vol. 70, no. 1, pp. 128-134, 2018.

[15] E. J. Wentzel and C. Allen, "Erosion-Corrosion Resistance of Tungsten Carbide Hardmetals with Different Binder Compositiions," *Wear,* Vols. 181-183, pp. 63-69, 1995.

[16] L. Toller, S. Jacobson and S. Norgen, "Life Time of Cemented Carbide Inserts with Ni-Fe Binder in Steel Turning," *Wear,* pp. 1822-1829, 2017.

[17] K. Schroter, "Hardmetal Alloy and The Process of Making Same". United States of America Patent 1,549,615, 11 August 1925.

[18] V. P. Astakhov, Drills: Science and Technology of Advanced Opertions, London: Taylor and Francis Group, 2014.

[19] A. Kurlov and A. Gusev, Tungsten Carbides: Structure, Properties and Application in Hardmetals, Switzerland: Springer, 2013.

[20] G. S. Upadhyaya, Cemented Tungsten Carbides, Production, Properties and Testing, United States of America: Noyes Publications, 1998.

[21] E. Isakov, Cutting Data for Turning of Steel, New York: Industrial Press Inc, 2009.

[22] M. G. Andrews, Tungsten: The Story of an Indispensible Metal, Washington D.C: The Tungsten Institute, 1955.

[23] K. A. Brookes, "Half a Century of Hardmetals," *Metal Powder Report,* vol. 50, no. 12, p. 22, 1995.

[24] D. Mari, L. Miguel and C. Nebel, Comprehensive Hard Materials, United States of America: Elsevier, 2014.

[25] V. Stanciu, V. Vitry and F. Delaunois, "Tungsten Carbide Powder Obtained by Direct Carburization of Tungsten Trioxide Using Mechanical Alloying Method," *Journal of Alloys and Compounds,* vol. 659, pp. 302-308, 2015.

[26] T. Gong, P. Yao, X. Zuo, Z. Zhang, Y. Xiao, L. Zhao, H. Zhou, M. Deng, Q. Wang and A. Zhong, "Influence of WC Carbide Particle Size on the Microstructure and Abrasive Wear Behavior of WC–10Co–4Cr Coatings for Aircraft Landing Gear," *Wear,* vol. 362, pp. 135-145, 2014.

[27] Petrowiki, "Roller Cone Bit Design," [Online]. Available: https://petrowiki.spe.org/Roller_cone_bit_design. [Accessed 30 November 2018].

[28] J. Davis, ASM Speciality Handbook: Tool Materials, USA: ASM International, 1995.

[29] R. Kiepura and T. Weintraub, Powder Metallurgy, USA: ASM International, 1984.

[30] X. Wang, "Grain Growth, Densification and Mechanical Properties of Nanocrystalline Tungsten Carbide-Cobalt," Phd Thesis, University of Utah, Utah, 2008.

[31] Z. Fang, P. Maheshwari, X. Wang, H. Sohn, A. Griffo and R. Riley, "An Experimental Study of the Sintering of Nanocrystalline WC-Co Powders," *International Journal of Refactrory Metals an Hard Materials,* vol. 23, p. 251, 2005.

[32] M. Gupta, T. Srivatsan, C. Lim and R. Varin, Processing and Fabrication of Advanced Materials XIII, Singapore: Stallion Press (S) Pty Ltd, 2005.

[33] A. Bandyopadhyay and S. Bose, Additive Manufacturing, London: Taylor and Francis Group, 2016.

[34] L. Robinson and J. Scott, "Layers of Complexity: Making the Promises Possible for Additive Manufacturing of Metals," *Journal of Material Science,* vol. 66, no. 11, pp. 1-14, 2014.

[35] I. Gibson, D. W. Rosen and B. Stucker, Additive Manufacturing Technologies: Rapid Prototyping to Direct Digital Manufacturing, New York: Springer, 2014.

[36] L. D. Sturm, C. B. Williams, J. A. Camelio, J. White and R. Parker, "Cyber-Physical Vulnerabilities in Additive Manufacturing Systems: A Case Study Attach on the .STL File with Human Subjects," *Journal of Manufacturing Systems,* vol. 44, pp. 154-164, 2017.

[37] "Additive Manufacturing Technologies," ASTM F2792-12a, 2013.

[38] J. Zhang and Y.-G. Jung, Additive Manufacturing: Materials, Processes, Quantifications and Applications, Oxford: Butterworth-Heinemann, 2018.

[39] C. Atwood, M. Ensz, D. Greene, M. Griffith, L. Harwell, D. Reckaway, T. Romero, E. Schlienger and J. Smugeresky, "Laser Engineered Net Shaping (LENS™) a Tool for Direct Fabrication of Metal Parts," Sandia National Laboratories, Albuquerque, 1998.

[40] P. Popoola, G. Farotade, O. Fatoba and O. Popoola, Laser Engineering Net Shaping Method in the Area of Development of Functionally Graded Material for Aero Engine Applications - A Review, Pretoria: Intech, 2016.

[41] *LENS 850-R System Manual,* U.S.A: Optomec, 2011.

[42] M. L. Griffith, M. T. Ensz, J. D. Puskar, C. V. Robino, J. A. Brooks, J. A. Philliber, J. E. Smugeresky and W. H. Hofmeister, "Understanding the Microstructure and Properties of Components Fabrication by Laser Engineered Net Shaping," Sandia National Laboratories, Nashville, 2000.

[43] J. Ruan, T. E. Sparks, Z. Fan, J. K. Stroble, A. Panackal and F. Liou, "A Review of Layer Based Manufacturing Processes for Metals," University of Missouri, Rolla, 2006.

[44] J. W. Morris, "The Influence of Grain size on the Mechanical Properties of Steel," Lawrence Berkeley National Laboratory, California, 2001.

[45] M. Balazic, "Additive Manufacturing and 3D Printing LENS Technology," in *Additive Manufacuturing of Metal Components Conference*, Ordizia, 2013.

[46] S. T. Erdogan and D. W. Fowler, "Determination of Aggregate Shape Properties Using X-ray Tomographic Methods and the Effects of Shape on Concrete Rheology," International Centre for Aggregate Research, Texas, 2005.

[47] A. T. Sutton, C. S. Kriewall, M. C. Leu and J. W. Newkirk, "Powders for Additive Manufacturing Processes: Characterization Technique and Effects on Part Properties," in *Proceedings of the 27th Annual International Solid Freeform Fabrication Symposium - An Additive Manufacturing Conference*, Austin, 2016.

[48] W. J. Sames, F. A. List, S. Pannala, R. R. Dehoff and S. S. Babu, "The Metallurgy and Processing Science of Metal Additive Manufacturing," *International Materials Reviews,* vol. 61, no. 5, pp. 1-76, 2016.

[49] E. Hyrha, "Powder Recycling in Additive Manufacturing," Chalmers University of Technology, Department of Industrial and Material Science, Gothenburg, 2019.

[50] H. Freisse, "Process Development for Additive Manufacturing by DED," in *Additive Manufacturing Seminar*, Gothenburg, 2019.

[51] F. Mazzucato, S. Tusacciu, M. Lai, S. Biamino, M. Lombardi and A. Valente, "Monitoring Approach to Evaluate the Performance of a New Deposition Nozzle Solution for DED Systems," *Multidisciplinary Digital Publishing Institute: Technologies,* vol. 5, no. 29, pp. 1-13, 2017.

[52] S. Zekovic, R. Dwivedi and R. Kovacevic, "An Investigation of Gas-Powder Flow in Laser-Based Direct Metal Deposition," in *17th Solid Freeform Fabrication Symposium*, Texas, 2006.

[53] J. P. Davim, Lasers in Manufacturing, London: John Wiley & Sons Inc, 2012.

[54] A. J. Pinkerton, "An Analytical Model of Beam Attenuation and Powder Heating During Coaxial Laser Direct Metal Deposition," *Journal of Physics and Applied Physics,* vol. 40, p. 7323–7334, 2007.

[55] A. J. Pinkerton and L. Lin, "Modelling Powder Concentration Distribution From a Coaxial Deposition Nozzle for Laser-Based Rapid Tooling," *Journal of Manufacturing Science and Engineering,* vol. 126, pp. 33-41, 2004.

[56] J. Liu, L. Li, Y. Zhang and X. Xie, "Attenuation of Laser Power of a Focused Gaussian Beam During Interaction Between a Laser and Powder in Coaxial Laser Cladding," *Journal of Physics D: Applied Physics,* vol. 38, pp. 1546-1550, 2005.

[57] J. Wang, F. Han, S. Chen and W. Ying, "A Novel Model of Laser Energy Attenuation by Powder Particles for Laser Solid Forming," *International Journal of Machine Tools and Manufacture,* vol. 145, pp. 1-5, 2019.

[58] Y. Xiong, J. E. Smugeresky and J. M. Schoenung, "The Influence of Working Distance on Laser Deposited WC-Co," *Journal of Materials Processing Technology,* vol. 209, no. 10, pp. 4935-4941, 2009.

[59] A. F. Kaplan and J. Powel, "Spatter in Laser Welding," *Journal of Laser Applications,* vol. 23, no. 3, pp. 1-20, 2011.

[60] M. Fenech, M. Grech and J. C. Betts, "The In-Flight Temperature Variation and Dissolution of WC Powder Particles Producing an Fe-Cr-W-C System by Direct Laser Deposition," *Surface and Coatings Technology,* vol. 207, pp. 211-217, 2012.

[61] P. G. Pistorius, "Welding Metallurgy: Study theme 2.7 to 2.16," University of Pretoria: Faculty of Engineering, Built Environment and Information Technology, Pretoria, 2016.

[62] J. Mazumder, "Laser-Beam Welding," *ASM Handbook,* vol. 6, pp. 262-269, 1993.

[63] J. Sundqvist, "Licentiate Thesis: Heat Conduction Effects During Laser Welding," Lulea University of Technology, Department of Engineering Sciences and Mathematixs, Lulea, 2015.

[64] A. Sola and A. Nouri, "Microstructural Porosity in Additive Manufacturing: The Formation and Detection of Pores in Metal Parts Fabricated by Powder Bed Fusion," *Journal of Advanced Manufacturing and Processing,* vol. 1, no. 3, pp. 1-21, 2019.

[65] J. Clayton, "TCT Magazine," 30 October 2020. [Online]. Available: https://www.tctmagazine.com/additive-maufacturing-3d-printing-industry-insights/storage-pre-treatment-additive-manufacturing-metal-powder/. [Accessed 20 November 2020].

[66] G. K. Ng, A. E. Jarfors, G. Bi and H. Y. Zheng, "Porosity Formation and Gas Bubble Retention in Laser Metal Deposition," *Applied Physics A,* vol. 97, pp. 641-649, 2009.

[67] J. B. Ferguson, B. F. Schultz, A. D. Moghadam and P. K. Rohatgi, "Semi-

Empirical Model of Deposit Size and Porosity in 420 Stainless Steel and 4140 Steel Using Laser Engineered Net Shaping," *Journal of Manufacturing Processes,* vol. 19, pp. 163 - 170, 2015.

[68] H. Gong, K. Rafi, H. Gu, T. Starr and B. Stucker, "Analysis of Defects Generation in Ti-6Al-4V Parts Made Using Powder Bed Fusion Additive Manufacturing Processes," *Additive Manufacturing ,* Vols. 1-4, pp. 87-98, 2014.

[69] M. Tang, C. P. Pistorius and J. L. Beuth, "Prediction of Lack-of-Fusion Porosity for Powder Bed Fusion," *Additive Manufacturing,* vol. 14, pp. 39-48, 2017.

[70] Y. Xiong, J. Smugeresky, J. Lavernia and J. Schoenung, "Processing and Microstructure of WC-Co Hardmetals by Laser Engineered Net Shaping," in *2008 International Solid Freeform Fabrication Symposium*, Texas, 2008.

[71] Y. Xiong, M. Kim, O. Seo and J. M. Schoenung, "(Ti, W)C-Ni Hardmetals by Laser Engineered Net Shaping," *Powder Metallurgy,* vol. 53, p. 41, 2010.

[72] Y. Xiong, W. Hofmeister, Z. Cheng, J. Smugeresky, E. Lavernia and J. Schoenung, "In Situ Thermal Imaging and Three-dimensional Finite Element Modeling of Tungsten Carbide-Cobalt during Laser Depostion," *Acta Materialia,* vol. 57, pp. 5419 - 5429, 2009.

[73] C. Li, K. C. Chang, A. Yeh, J. Yeh and S. Lin, "Microstructure Characterization of Cemented Carbide Fabrication of Selective Laser Melting Process," *International Journal of Refractroy Metals and Hard Materials,* vol. 75, pp. 225-233, 2018.

[74] C. Li, K. Chang and A. Yeh, "On the Microstructure and Properties of an Advanced Cemented Carbide System Processed by Selective Laser Melting," *Journal of Alloys and Compounds,* vol. 782, pp. 440-450, 2019.

[75] E. Uhlmann, A. Bergmann and W. Gridin, "Investigation on Additive Manufacturing of Tungsten Carbide-Cobalt by Selective Laser Melting," in *15th Machining Innovaitons Conference for Aerospace Industry*, Berlin, 2015.

[76] J. A. Picas, Y. Xiong, M. Punset, L. Ajdelsztajn, A. Forn and J. M. Schoenung, "Microstructure and Wear Resistane of WC-Co by Three Consolidation Processing Techniques," *Int. Journal of Refractory Metals & Hard Materials,* vol. 27, p. 344–349, 2009.

[77] N. Ku, J. J. Pittari, S. Kilczewski and A. Kudzal, "Additive Manufacturing of

Cemented Tugsten Carbide with a Cobalt-Free Alloy Binder by Selective Laser Melting for High Hardness Applications," *The Journal of the Minerals, Metals and Materials Society,* vol. 71, pp. 1535-1542, 2019.

[78] Q. Dai, C. Luo and F. You, "Crack Retraining Methods And Their Effect On The Microstructure And Properties Of Laser Cladded W/Fe Coatings," *Materials,* vol. 11, pp. 1-13, 2018.

[79] J. Luenda, C. Soriano and C. Sanz, "Inner Walls Laser Cladding of WC Reinforced Ni Coating," in *Lasers in Manufacturing Conference*, Munich, 2015.

[80] J. Wang, L. Li and W. Tao, "Crack Initiaion and Propagaion Behaviour of WC Particles Reinforced Fe-Based Metal Matrix Composites," *Optics and Laser Technology,* vol. 82, pp. 170-182, 2016.

[81] S. Sheikh, R. M'Saoubi, P. Flasar, M. Schwind, T. Persson, J. Yang and L. Llanes , "Fracture Toughness of Cemented Carbides: Testing Methods and Microstructural Effects," *International Journal of Refractory Metals and Hard Materials,* vol. 49, pp. 153-160, 2014.

[82] "Hardmetals - Palmqvist Toughness Test," ISO 28079, 2009.

[83] W. Schubert, M. Fuggers, B. Witmann and R. Useldinger, "Aspects of Sintering of Cemented Carbides with Fe-Based Binders," *International Journal of Refactory Metals and Hard Materials,* vol. 49, pp. 110-123, 2014.

[84] T. B. Trung, H. Zuhailawati, Z. A. Ahmad and K. N. Ishihara, "Sintering Characteristics and Properties of WC-10AISI304 (Stainless Steel) Hardmetals with Added Graphite," *Material Science and Engineering A,* vol. 605, pp. 210-214, 2014.

[85] M. Tarraste, J. Kubarsepp, K. Juhani, A. Mere, M. Kolnes and M. Viljus, "Ferritic Chromium Steel as Binder Metal for WC Cemented Carbides," *International Journal of Refractory Metals and Hard Materials,* vol. 73, pp. 183-191, 2018.

[86] B. J. Marques, C. M. Fernandes and A. M. Senos, "Sintering Microstructure and Properties of WC-AISI304 Powder Composities," *Journal of Alloys and Compounds,* vol. 562, pp. 164-170, 2013.

[87] J. Davis, Nickel, Cobalt and Their Alloys, U.S: ASM International, 2000.

[88] W. Callister, Fundamentals of Materials Science and Engineering, New York: John Wiley and Sons, 2001.

[89] D. P. Alves, D. Blagoeva, C. Pavel and N. Arvanitidis, "Cobalt: Demand-Supply Balances in the Transition to Electric Mobility," Publication Office of the European Union, Luxembourg, 2018.

[90] "Intergrated Country Strategy: Democratic Republic of the Congo," ICS DRC, Democratic Republic of the Congo, 2018.

[91] Deloitte Sustainability, British Geological Survey , Bureau de Recherches Géologiques et Minières and Netherlands Organisation for Applied Scientific Re, "Study on the Review of the List of Critical Raw Material," European Commission, 2017.

[92] K. B. Shedd, "Mineral Commodities Summaries," U.S Geological Survey, 1999.

[93] K. B. Shedd, "Mineral Commodity Summaries - Cobalt," U.S Geological Surveys, 2015.

[94] W. Jonas, "Metals and Health: A Clinical Toxicological Perspective on Tungsten and Review of the Literature," *Military Medicine,* vol. 172, pp. 1002 -1005, 2007.

[95] D. G. Barceloux and D. Barceloux, "Cobalt," *Journal of Toxicology: Clinical Toxicology,* vol. 37, no. 2, pp. 201-216, 1999.

[96] F. Miranda, "Nickel in Hardmetals," 2003.

[97] J. Kim and S. Kim, "Coating Properties of WC-Ni Cold Spray Coating for the Application in Secondary Piping System of Nuclear Power Plants," *Transactions of the Korean Nuclear Society,* pp. 29-30, 2015.

[98] P. Mendeza, N. Barnesa, K. Bell, A. Steven and et al, "Welding Processes for Wear Resistant Overlays," *Journal of Manufacturing Processes,* vol. 16, no. 1, pp. 4-25, 2014.

[99] P. Goeuriot, F. Thevenot, N. Bouaoudja and G. I. Fantozzi, "Boron as Sintering Additive in Cemented WC-Co (or Ni) alloys," *Ceramics International,* vol. 13, pp. 99-103, 1987.

[100] C. M. Fernandes and A. M. Senos, "Cemented Carbide Phase Diagrams, A Review," *Internation Journal Refactrory Metals,* vol. 29, pp. 405-418, 2011.

[101] V. K. Sarin, D. Mari and L. Llanes, "Fundamentals and General Application of Hardmetals," in *Comprehensive Hard Materials*, UK, Elsevier, 2014, pp. 29-90.

[102] J. Garcia, V. C. Cipres, A. Blomqvist and B. Kaplan, "Cemented Carbide Microstructures: A Review," *International Journal of Refactory Metals and Hard Materials,* vol. 80, pp. 40-68, 2019.

[103] M. B. Stearns, Phase Diagrams, Lattice Constants and Elastic Moduli, Vols. 19a: 3d,4d and 5d Elements, Alloys and Compounds, Berlin: Springer, 1986.

[104] T. W. Penrice, "Alternative Binders for Hardmetals," *J.Mater. Shaping Technology,* vol. 5, pp. 35-39, 1987.

[105] "National Cancer Institute," 15 February 2019. [Online]. Available: https://www.cancer.gov/about-cancer/causes-prevention/risk/substances/nickel. [Accessed 18 October 2019].

[106] E. Union, "Official Journal of the European," vol. 51, p. 104, 2008.

[107] K. Schroter, "Method of Making Tools from Hard-Metal Alloys Produced by Sintering". United States of America Patent US1728909 A, 23 July 1926.

[108] M. Humenik, D. Moskowitz and A. Park, "Iron Bonded Tungsten Carbide". United States Patent US3384465A, 21 May 1968.

[109] D. Moskowitz, M. J. Ford and M. Humenik Jr., "High-Strength Tungsten Carbides," *Modern Developments in Powder Metallurgy,* pp. 225-234, 1971.

[110] P. Pistorius, "Material Science, Study Theme 3," University of Pretoria, Department of Materials Science and Metallurgical Engineering, Pretoria, 2007.

[111] R. Zhou, Y. Jiang and L. Dehong, "The Effect of Volume Fraction of WC Particles on Erosion Resistance of WC Reinforced Iron Matrix Surface Composties," *Wear,* vol. 255, pp. 134-138, 2003.

[112] C. M. Fernandes, L. M. Vilhena, C. M. Pinho, F. J. Oliveira, E. Soares, J. Sacramento and A. M. Senos, "Mechanical Characterization of WC - 10 wt% AISI 304 Cemented Carbides," *Material Scinece and Engineering A,* vol. 618, pp. 629-636, 2014.

[113] G. Wang, C. Xing, F. Tao, P. Ding and H. Zhongjia, "Enhancement in the Corrosion Resistance of WC Coatings by Adding a Fe-based Alloy in Simulated Seawater," *Science and Coating Technology,* vol. 305, pp. 62-66, 2016.

[114] L. Niu, Y. Xu and X. Wang, "Fabrication of WC/Fe Composite Coating by Centrifugal Casting Plus In-Situ Synthesis Techniques," *Surface and Coating Technology,* vol. 205, pp. 551-556, 2010.

[115] L. Prakash, "Development of Tungsten Carbide Hardmetal using Iron-Based Binder Alloys. Ph.D Thesis," Institute of Materials and Solid State Research, University of Karlsruhe, Karlsruhe, 1980.

[116] M. Tarraste, "Development of Cemented Carbides with High Chromium Iron Alloy Binder, PhD Thesis," Tallinn University of Technology, Tallin, 2008.

[117] A. 1. ASTM, "Austenitic Manganese Steel Castings," ASTM, 2017.

[118] G. Zhang, J. Xing and Y. Gao, "Impact Wear Resistance of WC/Hadfield Steel Composite and its Interfacial Characteristics," *Wear,* vol. 260, p. 728, 2005.

[119] S. Bhero, B. Nyembe and K. Lentsoana, "Common Failures of Hadfield Steel in Application," in *International Conference on Mining, Mineral Processing and Metallurgical Engineering*, Johannesburg, 2014.

[120] D. L. Lewellyn and R. Hudd, Steels: Metallurgy and Applications, Oxford: Butterworth-Heinemann, 1998.

[121] C. G. Windsor, J. G. Morgan and P. F. Buxton, "Heat Deposition into the Superconducting Central Column of a Spherical Tokamak Fusion Plant," *Nuclear Fusion,* vol. 55, no. 2, 2015.

[122] Z. Zhang, P. Farahmand and R. Kovacevic, "Laser Cladding of 420 Stainless Steel with Molybdenum on Mild Steel A36 by a High Power Direct Diode Laser," *Materials and Design,* vol. 109, pp. 686-699, 2016.

[123] S. Sakaguchi, S. Imasato, H. Ito and R. Nakamura, "Some Properties of Sintered WC-(Fe-Cr-C) Alloys," *Journal of the Japan Society of Powder and Powder Metallurgy,* vol. 36, no. 8, pp. 908-912, 1989.

[124] S. A. Humphry-Baker, J. M. Marshall, G. D. Smith and W. E. Lee, "Thermophysical Properties of Co-free WC-FeCr Hardmetals," in *19th Plansee Seminar International Journal of Refractory Metals and Hard Materials*, Oxfordshire, 2017.

[125] M. Tarraste, K. Juhani, J. Kubarsepp, J. Pirso and V. Mikli, "The effect of Cr and C on the Characteristics of WC-FeCr Hardmetals," in *European Powder*

Metallurgy Congress and Exhibition - Hard Materials, Denmark, 2015.

[126] J. F. Flores, A. Neville, N. Kapur and A. Gnanavelu, "Corrosion and Erosion-Corrosion Processes of Metal-Matrix Composites in Slurry Conditions," *Journal of Materials Engineering & Performance,* vol. 21, pp. 395-405, 2012.

[127] R. Calderon, C. Edtmaier and W.-D. Schubert, "Novel binders for WC-Based Cemented Carbides with High Cr Contents," *International Journal of RefractoryMetals and Hard Materials,* vol. 85, pp. 1-18, 2019.

[128] L. Barlow and M. Du Toit, "Effect of Austenitizing Heat Treatment on the Microstructure and Hardness of Martensitic Stainless Steel AISI 420," *Journal of Materials Engineering and Performance,* vol. 21, p. 1327–1336, 2012.

[129] C. Kose and R. Kacar, "The Effect of Preheat & Post Weld Heat Treatment on the Laser Weldability AISI 420 Martensitic Stainless Steel," *Materials and Design,* vol. 64, pp. 221-226, 2014.

[130] A. S. Kurlov and A. I. Gusev, "Tungsten Carbides and W-C Phase Diagram," *Inorganic Materials,* vol. 42, no. 2, pp. 156-163, 2006.

[131] B. Uhrenius, "Calculation of Phase Equilibria in the Fe-W-C System," *CALPHAD,* vol. 4, no. 3, pp. 173-191, 1980.

[132] G. Roberts, G. Krauss and R. Kennedy, Tool Steels, USA: ASM International, 1998.

[133] K. Bungardt, E. Kunze and E. Horn, "Investigation of the Structure of the Iron-Chromium-Carbon System," *Arch. Eisenhuttenwes,* vol. 29, p. 193, 1958.

[134] M. Bergstrom, "The Eta-Carbides in the Ternary System Fe-W-C at 1250 oC," *Material Science and Engineering,* vol. 27, pp. 257-269, 1977.

[135] C. B. Pollock and H. H. Stadelmaier, "The Eta Carbides in the Fe-W-C and Co-W-C Systems," *Metallurgical Transactions,* vol. 1, pp. 767-770, 1970.

[136] A. Ghabriel, H. Pastor, D. M. Deo, S. Basu and C. H. Allibert, New Experimental Data in the C-Fe-W, C-Co-W, C-Ni-W, C-Fe-Ni-W and C-Co-Ni-W Systems Application to Sintering Conditions of Partial Facttorial Experiments, Bonston: Springer, 1985.

[137] B. Uhrenius and S. Frondella, "An Experimental and Thermodynamic Study of Carbide/Austenite Equilibria in Fe-Cr-W-C alloys," *Material Science,* vol. 11,

no. 3, pp. 73-81, 1977.

[138] P. Gustafson, "The Thermodynamic Evaluation of the C-Cr-Fe-W System," *Metallurgical Transactions A,* vol. 19A, pp. 2547-2554, 1988.

[139] H. Goldschmidt, *Metallurgia,* vol. 56, pp. 17-26, 1957.

[140] N. Arthur, K. Malabi, P. Baloyi, H. Moller and S. Pityana, "Influence of Process Parameters on Layer Build-up and Microstructure of Ti6Al4V (ELI) Alloy on the Optomec LENS," Council of Scientific and Industrial Research, Pretoria, 2016.

[141] J. Antony, Design of Experiments for Engineers and Scientists, London: Elsevier, 2014.

[142] K. Deb, Multi-Objective Optimization Using Evolutioinary Algorithms, John Wiley & Sons, 2001.

[143] W. Pei, Z. Wei, C. Zhen, L. Junfeng, Z. Shuzhe and D. Jun, "Numerical Simulation and Parametric Analysis of Selective Laser Melting Process of AlSi10Mg Powder," *Applied Physics A 123(8),* vol. 123, no. 8, pp. 1-15, 2017.

[144] Pferd, 1 April 2014. [Online]. Available: https://www.pferd.com/images/WZH_22_202_en_72_dpi.pdf. [Accessed 28 October 2020].

[145] K. Liu, Tungsten Carbide, Croatia: InTech, 2012.

[146] M. Hrncirova, J. Pospisil and M. Spilacek, "Size Analysis of Solid Particles Using Laser Diffraction and Sieve Analysis," *Engineering Mechanics,* vol. 20, pp. 309-318, 2013.

[147] "Standard Guide for Metalographic Sample Preparation of Cemented Tungsten Carbides," ASTM B665.

[148] M. Kejzlar and M. Svec, "The Usage of Backscattered Electron in Scanning Electron Microscopy," 2014.

[149] "Hardmetals - Vickers Hardness Test," ISO 3878, 1983.

[150] R. Spiegler, S. Schmauder and L. Sigl, "Fracture Toughness Evaluation of WC-Co Alloys by Indentation Testing," *Journal of Hard Mater,* vol. 1, pp. 147-158, 1990.

[151] A. C373-88, "Standar Test Method for Water Absorption, Bulk Density, Apparent Porosity an Apparent Specific Gravity of Fired Whiteware Products,"

ASTM, 2006.

[152] D. Rosenthal, "The Theory of Moving Source of Heat and its Application to Metal Treatment," *Transactions of the AIME,* vol. 68, pp. 849-866, 1946.

[153] A. L. Schaeffler, "Construction Diagram for Stainless Steel Weld Metal," *Metal Progress,* vol. 85, no. 7, p. 680B, 1949.

[154] S. Luyckx and A. Love, "The Relationship Between the Abrasion Resistance and the Hardness of WC-Co Alloys," *The Journal of the South African Institute of Mining and Metallurgy,* vol. 104, no. 10, pp. 579-582, 2004.

[155] L. C. Canale, R. A. Mesquita and G. E. Totten, Failure Analysis of Heat Treated Steel Components, Ohio: ASM International, 2008.

[156] Y. Xiong, K. Lau, X. Zhou and J. M. Schoenung, "A Streamlined Life Cycle Assessment on the Fabrication of WC-Co," *Journal of Cleaner Production,* vol. 16, pp. 1118-1126, 2008.

[157] M. Hedges and N. Calder, "Near Net Shape Rapid Manufacture and Repair by LENS®," in *Proceedings of NATO AVT-139 Specialists Meeting on Cost Effective Manufacature Via Net Shape Processing*, Amsterdam, 2006.

[158] "Liyotools," 14 May 2017. [Online]. Available: http://liyotools.com/production-process-carbide-burrs/. [Accessed 22 October 2020].

[159] B. R. Dawes and R. Bowerman, "Introduction to Additive Manufacturing Powder Metallurgy Supply Chain," *Johnson Matthey Technology Review,* vol. 59, no. 3, pp. 243-256, 2015.

[160] Q. B. Nguyen, Z. Zhu, B. W. Chua, W. Zhou, J. Wei and S. M. Nai, "Develompment of WC-Inconel Composites Using Selective Laser Melting," *Archives of Civil and Mechanical Engineering,* vol. 18, pp. 1410-1420, 2018.

[161] V. K. Balla, S. Bose and A. Bandyopadhyay, "Microstructure and Wear Properties of Laser Deposited WC-12 % Co Composites," *Materials Science and Engineering A,* vol. 527, pp. 6677-6682, 2010.

[162] J. Kim and Y. Peng, "Temperature Field and Cooling rate of Laser Cladding with Wire Feeding," *Journal of Mechanical Science and Technology,* vol. 14, no. 8, pp. 851-860, 2012.

[163] A. Bagheri, N. Shamsaei and S. Thompson, "Microstructure and Mechanical

Properties of Ti-6Al-4V Parts Fabricated by Laser Engineered Net Shaping," in *ASME 2015 International Mechanical Engineering Congress and Exposition (IMECE)*, Texas, 2015.

[164] L. M, D. Yao, Y. Guan, Y. Duan and L. Yang, "Effect of Welding Speed and Post Quenchng on the Microstructure and Mechanical Properties of Laser-Welded B1500HS Joints," *Materials,* vol. 13, no. 4645, pp. 1-16, 2020.

[165] J. Zhou and H. L. Tsai, "Porosity Formation and Prevention in Pulsed Laser Welding," *Journal of Heat Transfer,* vol. 129, pp. 1014-1024, 2007.

[166] A. du Plessis, "Effects of Process Parameters on Porosity in Laser Powder Bed Fusion Revealed by X-ray Tomography," *Additive Manufacturing,* vol. 30, pp. 1-9, 2019.

[167] M. Bayat, A. Thanki, S. Mohanty, A. Witvrouw, S. Yang, J. Thorborg, N. S. Tiedje and J. H. Hattel, "Keyhole-Induced Porosities in Laser-Based Powder Bed Fusion (L-PBF) of Ti6Al4V: High-Fidelity Modelling and Experimental Validation," *Additive Manufacturing,* vol. 30, pp. 1-18, 2019.

[168] T. J. Jeon, T. W. Hwang, H. J. Yun and C. J. Van Tyne, "Control of Porosity in Parts Produced by a Direct Laser Melting Process," *Applied Sciences,* vol. 8, pp. 1-16, 2018.

[169] J. Kummailil, C. Sammarco, D. Skinner, C. A. Brown and K. Rong, "Effect of Select LENS Processing Parameters on the Deposition of Ti-6Al-4V," *Journal of Manufacturing Processes,* vol. 7, no. 1, pp. 42-50, 2005.

[170] M. L. Griffith, D. M. Keicher, C. L. Atwood, J. A. Romero, J. E. Smugeresky, L. D. Harwell and D. L. Greene, "Free Form Fabrication of Metallic Components Using Laser Engineered Net Shaping (LENS™)," in *Solid Free Form Fabrication Symposium*, Texas, 1996.

[171] P. A. Kobyn, E. H. Moore and S. L. Semiatin, "The Effect of Laser Power and Traverse Speed on Microstructure, Porosity, and Build Height in Laser-Deposited Ti-6Al-4V," *Scripta Materialia,* vol. 43, pp. 299-305, 2000.

[172] D. C. Montgomery and G. G. Runger, Applied Statistics and Probability for Engineers, United States of America: John Wiley and Sons, Inc, 2003.

[173] H. Cao, W. Ma, H. Chen, Q. Wang and Y. Wang, "Core-Rim Microstructure and Properties of WC/Ni Composites," *International Journal of Refactory metals an*

Hard Materials, vol. 78, pp. 170-177, 2019.

[174] D. Gu, J. Ma, H. Chen, K. Lin and L. Xi, "Laser Additive Manufactured WC Reinforced Fe-based Composites with Gradient Reinforcement/Matrix Interface and Enhanced Performance," *Composite Structure,* vol. 192, pp. 387-396, 2018.

[175] T. E. Abioye, "Laser Deposition of Inconel 625/Tungsten Carbide Composite Coatings by Powder and Wire Feedstock," University of Nottingham, PhD Thesis, United Kingdom, 2014.

[176] Y. Xianqing, Z. Chengjun, S. Xuefeng, H. Manping and M. Jianguo, "Microstructure Evolution of WC/Steel Composite by Laser Surface Re-Melting," *Applied Surface Science,* vol. 253, pp. 4409-4414, 2007.

[177] S. Kou, Welding Metallurgy, New Jersey: John Wiley and Sons, Inc, 2003.

[178] E. A. Alvarez, C. Gonzalez Oliver and J. L. Garcia, "Densification and Phase Formation Kinetics in Composite Materials of WC embedded in an Fe-Matrix," *Procedia Materials Science,* vol. 9, pp. 13-20, 2015.

[179] A. Formisano, F. C. Minutolo, A. Caraviello, L. Carrino, M. Durante and A. Langella, "Influence of Eta-Phase on Wear Behaviour of WC-Co Carbides," *Advances in Tribology,* pp. 1-6, 2016.

[180] N. A. Rosli, M. R. Alkahari, M. F. bin Abdollah, S. Maidin, F. R. Ramli and S. G. Herawan, "Review on Effect of Heat Input For Wire Arc Additive Manufacturing Process," *Journal of Materials Research and Technology,* Vols. 2127-2145, p. 11, 2021.

[181] J. C. Fox, S. P. Moylan and B. M. Lane, "Effect of Process Parameters on the the Surface Roughness of Overhang Structures in Laser Powder Bed Fusion Additive Manufacturing," *Procedia CIRP,* vol. 45, pp. 131-134, 2016.

[182] H. Hassanin, A. Elshaer, R. Benhadji, F. Modica and I. Fassi, "Surface Finish Improvement of Additive Manufactured Metal Parts," in *Micro and Precision Manufacturing*, Cham, Switzerland, Springer, 2017, pp. 145-164.

[183] A. O' Brien, Welding Handbook Volume 4: Materials and Application part 1, Miami: American Welding Society, 2011.

[184] J. Dowden and D. Lepski, The Theory of Laser Materials Processing: Heat and Mass Transfer in Modern Technology, Switzerland: Springer, 2017.

[185] C. I. John, Laser Processing of Engineering Materials: Principles, Procedures and Industrial Application, Amsterdam: Elsevier Butterworth-Heinemann, 2005.

[186] Z. Lestan, S. Klancnik, J. Balic and M. Brezocnik, "Modeling and Design of Experiments of Laser Cladding Process by Genetic Programming and Nondominated Sorting," *Materials and Manufacturing Processes,* vol. 30, no. 4, pp. 458-463, 2015.

[187] M. Nagentrau, A. L. Tobi, A. S. Omar and M. I. Ismail, "Preheat Treatment on the Tungsten Carbide Hardfacing: Microstructure Analysis," *Materials Science and Engineering,* vol. 505, pp. 1-11, 2019.

[188] S. Marimuthu, A. Triantaphyllou, M. Antar, D. Wimpenny, H. Morton and M. Beard, "Laser Polishing of Selective Laser Melted Components," *International Journal of Machine Tools Manufacturing,* vol. 95, pp. 97-104, 2015.

[189] Y. Zhao, J. Sun, K. Guo and J. Li, "Investigation on the Effect of Laser Remelting for Laser Cladding Nickel Based Alloys," *Journal of Laser Applications,* vol. 31, pp. 1-6, 2019.

[190] X. Zhao, H. Zhang and Y. Liu, "Effect of Surface Laser Remelting on the Fatigue Crack Propagation Rate of 40Cr Steel," *Results in Physics,* vol. 12, pp. 424-431, 2019.

[191] S. Zhou, Y. Xu, B. Liao, Y. Sun, X. Dai, J. Yang and Z. Li, "Effect of Laser Remelting on Microstructure and Properties of WC Reinforced Fe-based Amorphous Composite Coatings by Laser Cladding," *Optics and Laser Technology,* vol. 103, pp. 8-16, 2018.

[192] A. Sadhu, A. Choudhary, S. Sarkar, A. M. Nair, P. Nayak, S. D. Pawar, G. Muvvala, S. K. Pal and A. K. Nath, "A Study on the Influence Of Substrate Pre-Heating on Mitigation of Cracks in Direct Metal Laser Deposition of NiCrSiBC-60%WC Ceramic Coating on Inconel 718," *Surface & Coatings Technology,* vol. 389, pp. 1-14, 2020.

[193] W. Winarto, N. Sofyan and D. Rooscote, "Effect of Bond Coat and Preheat on the Microstructure, Hardness, and Porosity of Flame Sprayed Tungsten Carbide Coatings," in *Proceedings of the 3rd International Conference on Engineering, Technology, and Industrial Application*, Surakarta, Indonesia, 2017.

[194] F. Ning, "Microstructures and Mechanical Properties of Fe-Cr Stainless Steel

Parts Fabricated By Ultrasonic Vibration-Assisted Laser Engineered Net Shaping Process," *Materials Letters,* vol. 179, pp. 61-64, 2016.

[195] X. Wang, D. Deng, Y. Hu, F. Ning, H. Wang, W. Cong and H. Zhang, "Overhang Strucutre and Accuracy in Laser Engineered Net shaping of Fe-Cr Steel," *Optics and Laser Technology,* vol. 106, pp. 357-365, 2018.

[196] M. Izadi, A. Farzaneh, I. Gibson and B. Rolfe, "The effect of Process Parameters and Mechanical Properties of Direct Energy Deposited Stainless Steel 316," in *Solid Freeform fabrication Symposium - An Additive Manufacturing Conference*, Austin Texas, 2017.

[197] T. Durejko, M. Zietala, W. Polkowski and T. Czujko, "Thin Wall Tubes with Fe3Al/SS316L Graded Structure Obtained by Using Laser Engineered Net Shaping Technology," *Materials and Design,* vol. 63, pp. 766-774, 2014.

APPENDIX A Tungsten and Iron-Chromium LENS® Parameters from Literature

Table A-1: Process parameter mapping of LENS® deposited WC and FeCr alloys.

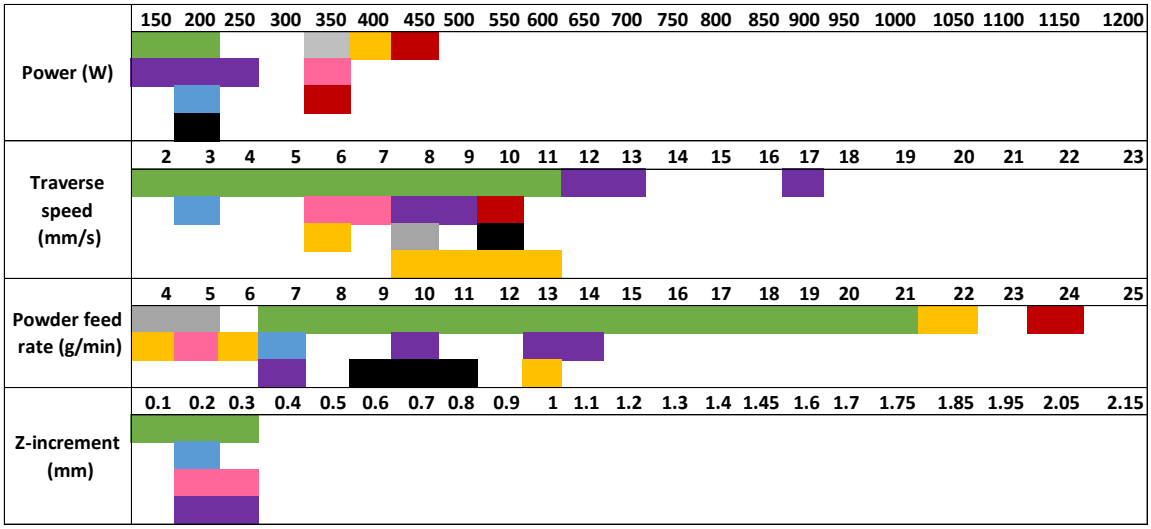

Table A-2: Colour coding for process parameter mapping.

LENS deposition of WC-Co hardmetals	
	Processing an microstructure of WC-Co hardmetals by laser engineered net shaping [70]
	Microstructure and wear properties of laser deposited WC–12%Co composite [161]
	Microstructure and wear resistance of WC–Co by three consolidation processing techniques [76]
LENS deposition of FeCr alloys	
	Microstructures and mechanical properties of Fe-Cr stainless steel parts fabricated by ultrasonic vibration-assisted laser engineered net shaping process [194]
	Overhang structure and accuracy in laser engineered net shaping of Fe-Cr steel [195]
	Semi-empirical model of deposit size and porosity in 420 stainless steel and 4140 steel using laser engineered net shaping [67].
	The effect of process parameters and mechanical properties of direct energy deposited stainless steel 316 [196]
	Thin Wall tubes with Fe3al/SS316L Graded Structure Obtained by Using Laser Engineered Net Shaping Technology [197]

APPENDIX B Cylindrical Rotary Burr Application and Design

Table B-1: Rotary burr applications and material groups [144].

Application	Material Group		
Deburring, chamfering, milling out for the preparation of build-up welding, machining of welded joints, machining of contours, cleaning cast material	Steel and cast steel	Non-hardened, non-heattreated steels up to 1,200 N/mm2 (< 38 HRC)	Construction steels, carbon steels, tool steels, non-alloyed steels, case-hardened steels, cast steel
		Hardened, heat-treated steels over 1,200 N/mm2 (> 38HRC)	Tool steels, tempering steels, alloyed steels, cast steel
	Stainless steel	Rust- and acid-resistant steels	Austenitic and ferritic stainless steels
	Non-ferrous metals	Soft non-ferrous metals, non-ferrous metals	Aluminium
			Brass, copper, zinc
		Hard non-ferrous metals	Aluminium alloys, brass, copper, zinc
			Bronze, titanium/titanium alloys, hard aluminium alloys (high Si content). Coarse stock Fine stock
			Nickel-based and cobalt-based alloys,(engine and turbine construction)
	Cast iron	Grey cast iron, white cast iron	Cast iron with flake graphite EN-GJL (GG), with nodular graphite/nodular cast iron EN-GJS (GGG), white annealed cast iron EN-GJMW, (GTW), black cast iron EN-GJMB (GTS)
Milling out, machining of contours	Plastics, other materials	Fibre-reinforced plastics (GRP/CRP) fibre content ≤ 40 %, fibre-reinforced plastics (GRP/CRP) fibre content > 40 %, thermoplastics	
Trimming, contour milling, cutting out holes			

Table B-2: Rotary burr design [144].

Cuts for universal applications	Application
Cut 1 (C according to DIN 8033) 	Machining of light metals, non-ferrous metals, steel and cast iron High stock removal
Cut 3 (MY according to DIN 8033) 	Machining of cast iron, steel < 60 HRC, stainless steel, nickel-based alloys and titanium alloys High stock removal,Good surface
Cut 3+ (MX according to DIN 8033) 	Similar to cut 3, but with cross cut machining of cast iron, steel < 60 HRC,stainless steel, nickel-based alloys and titanium alloys High stock removal
Cut 4 (MX according toDIN 8033) 	Machining of stainless steel, steel < 60 HRC and high-temperature resistant materials such as nickel-based and cobalt-based alloys High stock removal with short chips, good surface
Cut 5 (F according to DIN 8033) 	Fine machining of cast iron, steel< 60 HRC, stainless steel and high-temperature-resistant materials such as nickel-based and cobalt-based alloys Good surface

Table B-3: Recommended rotational speeds [144].

	Material group	
	Steel, cast steel	Stainless steel
Heat treatment	Hardened, heat-treated steels over 1,200 N/mm² (> 38 HRC)	Rust- and acid resistant steels
Material grade	Tool steels, tempering steels, alloyed steels, cast steel	Austenitic and ferritic stainless steels
Application	Coarse stock removal	Coarse stock removal
Cut	3, 3 PLUS, 4	3, 3 PLUS, 4
Cutting speed	450-600 m/min	250–450 m/min

Table B-4: Rotational speed based on burr diameter [144].

Burr dia. [mm]	Cutting speed [m/min]	
	450	600
	Rotational speed [RPM]	
1.5	95,000	127,000
2	72,000	95,000
3	48,000	64,000
4	36,000	48,000
6	24,000	32,000
8	18,000	24,000
10	14,000	19,000
12	12,000	16,000
16	9,000	12,000
20	7,000	10,000
25	6,000	8,000

APPENDIX C ANOVA Regression Analysis

Table C-1: Quadratic regression model for sample height.

Regression Statistics	
Multiple R	0.97932919
R Square	0.95908566
Adjusted R^2	0.93742513
Standard Error	0.44779785
Observations	27

ANOVA

	df	*SS*	*MS*	*F*	*Significance F*
Regression	9	79.90882897	8.878759	44.27803	4.81243E-10
Residual	17	3.408889549	0.200523		
Total	26	83.31771852			

	Coefficients	*Standard Error*	*t Stat*	*P-value*	*Lower 95%*	*Upper 95%*
Intercept	3.871999	4.409283193	0.878147	0.392106	-5.43077536	13.1747734
Power (W)	0.01807175	0.012716171	1.421163	0.173354	-0.00875703	0.04490053
Speed (mm/s)	-0.951343	0.450445711	-2.112	0.049788	-1.90170039	-0.00098564
Feedrate (g/min)	-0.2621145	0.638377112	-0.4106	0.686498	-1.60897249	1.08474346
Power^2	-9.556E-06	1.82813E-05	-0.5227	0.607931	-4.8126E-05	2.9015E-05
Speed^2	0.07304082	0.020789411	3.513366	0.002666	0.029178992	0.11690264
feedrate^2	0.06553822	0.030829913	2.1258	0.048472	0.000492794	0.13058365
Power X Speed	-0.0008563	0.000399933	-2.14108	0.047052	-0.00170007	-1.2503E-05
Speed X Feed rate	-0.0634061	0.016295544	-3.89101	0.001174	-0.09778673	-0.02902555
Power X Feed rate	0.00030529	0.000526712	0.579623	0.569771	-0.00080597	0.00141656

Table C-2: Multiple linear regression model for sample height.

Regression Statistics	
Multiple R	0.932504581
R Square	0.869564793
Adjusted R Square	0.852551506
Standard Error	0.687388373
Observations	27

ANOVA

	df	*SS*	*MS*	*F*	*Significance F*
Regression	3	72.45015469	24.15005	51.11092	2.48796E-10
Residual	23	10.86756383	0.472503		
Total	26	83.31771852			

	Coefficients	*Standard Error*	*t Stat*	*P-value*	*Lower 95%*	*Upper 95%*
Intercept	-0.38060573	0.94149064	-0.40426	0.689757	-2.328227505	1.567016
Power (W)	0.007488889	0.00162019	4.622229	0.000119	0.004137271	0.0108405
Speed (mm/s)	-0.41865454	0.050125864	-8.35207	2.03E-08	-0.522347795	-0.314961
Feed rate (g/min)	0.520691139	0.066015738	7.887379	5.47E-08	0.384127181	0.6572551

Table C-3: Exponential regression model for sample height.

Regression Statistics	
Multiple R	0.967248588
R Square	0.93556983
Adjusted R Square	0.927165895
Standard Error	0.166357453
Observations	27

ANOVA

	df	*SS*	*MS*	*F*	*Significance F*
Regression	3	9.242709374	3.080903	111.3252	7.72369E-14
Residual	23	0.636520452	0.027675		
Total	26	9.879229826			

	Coefficients	*Standard Error*	*t Stat*	*P-value*	*Lower 95%*	*Upper 95%*
Intercept	-0.277163038	0.227853702	-1.21641	0.236166	-0.748514332	0.1941883
Power (W)	0.002822328	0.000392108	7.197829	2.5E-07	0.002011191	0.0036335
Speed (mm/s)	-0.149981731	0.012131149	-12.3634	1.22E-11	-0.175076925	-0.1248865
Feedrate (g/min)	0.181681545	0.015976718	11.37164	6.42E-11	0.148631186	0.2147319

APPENDIX D PUBLICATIONS AND CONFERENCES

Emma Molobi, Natasha Sacks, Maritha Theron, Feasibility of Using Laser Enabled Net Shaping to Manufacture WC-Fe Alloys, *Proceedings of Euro PM2018*., ISBN 978-1-899072-50-7, (2018).

E. Molobi, B Davoren, N. Sacks and M. Theron, Laser Engineered Net Shaping Technology For WC-Based Materials, 19th Annual Conference, Additive Manufacturing, Rapid Product Development Association of South Africa, 2018.

Emma Molobi, Natasha Sacks, Maritha Theron, Influence of z-increment on the build height, porosity and microstructure of laser deposited WC-10wt%FeCr thin walls, *Proceedings of Euro PM2021,* (2021).

Emma Molobi, Natasha Sacks, Maritha Theron, Direct Energy Deposition of a Cemented Tungsten Carbide Rotary Burr Prototype, The 22nd Annual International Conference, Rapid Product Development Association of South Africa, 2021 – (Paper under review).